SPIN DEPENDENT TOTAL CROSS-SECTION MEASUREMENTS, $\Delta\sigma_L$, $\Delta\sigma_T$, IN P-P SCATTERING BETWEEN 200 AND 520MeV.

JEREMY PAUL STANLEY

BEDFORD COLLEGE

This thesis is submitted for
the degree of
Doctor of Philosophy
in the
University of London

March 1983

ABSTRACT

The differences $\Delta\sigma_L$ ($\Delta\sigma_T$) between proton-proton total cross sections for longitudinal (transverse) spin states parallel and antiparallel to the incident beam momentum have been measured at the TRIUMF laboratory from 200 to 520MeV.

A beamline was designed to produce a transverse or longitudinal polarization from the vertically polarized beam extracted from the cyclotron. The polarization of the beam was measured using a polarimeter which had been previously calibrated to $\pm 1.5\%$. The polarization of the dynamically polarized butanol target was monitored by an NMR system under microprocessor control. In addition, multiwire proportional chambers detected elastically scattered protons and enabled an independent value of the target polarization to be calculated. Careful attention was paid to the removal of systematic effects by taking data with different combinations of beam and target polarizations. The beam transmitted through the target was detected by six closely spaced circular scintillation counters. The transmission ratios were corrected for Coulomb-Barrier and Coulomb-Nuclear interference effects before final total cross sections were evaluated.

Values of $\Delta\sigma_L$ ($\Delta\sigma_T$) were measured at six (seven) energies. At the two lowest energies (203 and 325MeV), where inelasticity is zero or negligible, excellent agreement was obtained with phase shift predictions. The results were incorporated into a phase shift analysis.

CONTENTS

PAGE

FIGURES

TABLES

ACKNOWLEDGEMENTS

I wish to thank all the members of the BASQUE group for their invaluable help; Dave Axen, David Bugg, Tony Clough, Martin Comyn, John Edgington, Denis Healey, George Ludgate, Rick Shypit, Nigel Stevenson and Noel Stewart.

My sincerest thanks to Ann Tucker for typing this thesis and for the encouragement and support she has given me. I also wish to thank my father, Eric Stanley, for checking the manuscript.

I would like to thank David Bugg for his diligent checking of the numerical calculations contained in this thesis.

My special thanks go to Noel Stewart for all his help over the last four years.

I DEDICATE THIS THESIS TO

ANN

CHAPTER 1 AN INTRODUCTION TO THE EXPERIMENT

The availability of both polarized proton beams and polarized hydrogen targets of substantial polarization (>60%) has allowed a study of total cross sections in pure spin states.

A set of experiments, performed at the Argonne National Laboratory, measured the differences in total cross sections between states with antiparallel and parallel alignments of the beam and target polarizations. The polarizations were aligned along and transverse to the beam momentum defining $\Delta\sigma_L$ and $\Delta\sigma_T$ respectively.

$$\Delta\sigma_L = \sigma\ (\rightleftarrows) - \sigma\ (\rightrightarrows) \tag{1.1}$$

$$\Delta\sigma_T = \sigma\ (\uparrow\downarrow) - \sigma\ (\uparrow\uparrow) \tag{1.2}$$

where σ denotes a total cross section, the upper or first arrow, in the brackets, indicates the target polarization direction, the other that of the beam. Rotational invariance of space demands the equivalence of states when both target and beam spins are reversed, ($\uparrow\downarrow \equiv \downarrow\uparrow$, $\uparrow\uparrow \equiv \downarrow\downarrow$).

The Argonne measurements of $\Delta\sigma_L$($\Delta\sigma_T$) were in the laboratory momentum range 1 - 6, (1 - 4)GeV/c. In the range 1 - 2GeV/c, the $\Delta\sigma_L$ data showed a suprisingly rich momentum dependence. This structure has been investigated using both phase shift and dispersion analyses.

1.1 The Nucleon - Nucleon Interaction

Some of the general features of the Nucleon - Nucleon (N-N) interaction can be deduced from the properties of nuclei. It is immediately clear that the nuclear force is attractive, and sufficiently strong to overcome coulomb repulsion. The binding energy per nucleon goes to a constant value on increasing the atomic number A. The nuclear force is not, therefore, long-range like the coulomb force. If it were, the binding energy would increase with increasing A. The binding energy per particle only increases by approximately 1MeV on going from ^{4}He up to heavy nuclei. This indicates a kind of saturation is nearly reached by the time four particles are put together, and that the range of the N-N force is roughly equal to the radius of the alpha particle. The similar binding energies of ^{3}He and ^{3}H suggest that the interaction is also charge independent.

The nuclear radius, R, obeys the relation,

$$R = r_o A^{1/3} \qquad 1.1.1$$

where A is the atomic number and r_o is a constant. There is, therefore, some form of repulsive core in the N-N interaction that prevents collapse of all the nucleons to the range of the nuclear force. The constant r_o has been found to be approximately 1.5fm.

In 1935, Yukawa (1.1) proposed that the N-N force was mediated by the exchange of a virtual particle of finite mass, which accounted for the finite range of the force. Heisenberg's uncertainty principle allows for an energy conservation violation of Δ E for a time Δt through the relation,

$$\Delta E \Delta t = \hbar \qquad 1.1.2$$

where $\hbar$ is the Planck constant $/2\pi$. If the virtual particle travels at the speed of light, c, the maximum range of the force is $\hbar/mc$, where m is the mass of the particle. From the range of the N-N force of approximately 1.5fm, the mass of the virtual particle was expected to be approximately 150MeV.

Early experiments using cosmic radiation had discovered the μ-meson with a mass of approximately 106MeV. This was erroneously identified as the Yukawa meson, however, its properties were not those of the expected meson. The Yukawa, or π-meson (pion) was finally discovered in 1947 (1.2). The π meson was found to have three charge states, π°, $\pi^{\pm}$; to have zero spin and negative parity, ($T = 1$, $J^{P} = 0^{-}$). Its three charge states allow it to mediate the n-n, p-p and n-p interactions. In one pion exchange, (OPE), only the π° of mass approximately 135MeV mediate the n-n and p-p interaction, while in the n-p system, the π^{+} and π^{-}, of mass approximately 140MeV, may also be exchanged. The long-range component of the N-N interaction is calculated using one pion exchange.

Unfortunately, the only bound n-p state is that of the deuteron. To provide extra data on the N-N interaction, a set of scattering experiments were required. In the late '50s and early '60s, experiments were performed using proton beams at energies up to approximately 450MeV, obtained from linacs and cyclotrons. The data could be represented by exchanges of a range of mesons, the π and η pseudoscalars, and the ρ and ω vector mesons ($J^P = 1^-$).[1.3] These mesons were necessary to explain the spin-spin, spin-orbit, tensor and short range repulsion forces.

One approach of representing the N-N interaction is that of phenomenological scattering potentials. The interaction cannot be represented by a single potential as the N-N interaction is dependent on the momentum, the separation and the spin and angular momentum of the nucleons. The most well known are the Hamada-Johnston, Reid and the Paris potentials. The most modern potential is that of the Paris group; this uses calculated OPE + 2π + ω exchange for separations greater than 0.8fm. For separations less than these they join to a phenomenological potential.

Phase shift analysis is another method of representing the N-N interaction. The interaction is expressed by the change in phase and magnitude of spherical waves, representing the incident particle, it imposes when the particle is scattered by an N-N interaction. The OPE potential is used to determine and fix the phases of the higher partial waves, representing the long range component of the interaction, before phase shift analysis fits to the scattering data are preformed. Scattering data has tended to group around a number of energies. Two types of phase shift analysis fits are used; an energy independent phase shift analysis ignores results obtained at nearby energies, whereas an energy dependent analysis demands a smooth variation of fit parameters with changing energy. A review of current phase shift analyses is given by Bryan [1.4].

Only a brief resume of the N-N interaction is included here. A more comprehensive review is contained in many publications.[1.5] [1.6] [1.7] and [1.8].

The meson factories eg TRIUMF, SIN and LAMPF, have now provided sufficiently accurate and complete scattering data to yield good phase shift solutions up to 600MeV for p-p [1.9] and 500MeV for n-p.

The elastic scattering data has accurately determined the phase shifts. However, these data are relatively insensitive to the values of the elasticity parameters. The elasticity parameters can be calculated based upon NN-NΔ (1230) via π and ρ exchange [1.10]. Information on them also comes from measurements of the total cross section , $\Delta\sigma_L$ and $\Delta\sigma_T$ allowing comparison of calculated and measured values.

1.2 Previous $\Delta\sigma_L$ and $\Delta\sigma_T$ Measurements.

1.2.1 $\Delta\sigma_T$ Measurements

The first measurement of $\Delta\sigma_T$ was performed by E Parker et al [1.11] in 1973. The experiment was performed at the Argonne National Laboratory using the Zero Gradient Synchrotron (ZGS) accelerator. Only one incident momentum, 3.5GeV/c was considered. The result, 1.8 ±2.0mb, was consistent with an equal cross section in the parallel and antiparallel states. The total cross section is approximately 43mb at this energy.

A second set of experiments, using the ZGS accelerator, were carried out by W de Boer et al [1.12]. These measurements had an experimental error reduced by a factor of 30, compared to the previous measurement. This reduction in error allowed a clear difference to be seen between the parallel and antiparallel cross sections. Four incident momenta were used; 2, 3, 4 and 6GeV/c. The results are listed in table 1.1 and plotted on fig 1.1. They were all non zero and positive.

The energy of the $\Delta\sigma_T$ results was extended down to 1.2GeV/c by K Biegert et al [1.13]. Five measurements were made up to 2.5GeV/c. A repeat of the measurement at 2GeV/c agreed with the previous measurement [1.12].

The value of $\Delta\sigma_T$ has a minimum at 1.5GeV/c rising to $\sim$6.0mb at 2.0GeV/c then falling to small values at higher momentum, see fig1.1 and table 1.1.

1.2.2 $\Delta\sigma_L$ Measurements

During 1977, the first results of a series of measurements of $\Delta\sigma_L$ at the Argonne Laboratory were published in two papers by I P Auer et al [1.14] [1.15]. The first covered the momentum range 1.2 up to 2.5GeV/c, where five measurements were made. In this range, $\Delta\sigma_L$ was seen to have a remarkable energy dependence with the value at

TABLE 1.1

ARGONNE $\Delta\sigma_T$ RESULTS

P (GeV/c)	$\Delta\sigma_T$ (mb)	ref
1.2	4.38 ± 0.27	1.13
1.5	3.00 ± 0.26	1.13
1.75	4.55 ± 0.25	1.13
2.0	6.21 ± 0.15	1.13
	5.79 ± 0.93	1.12
2.5	2.20 ± 0.31	1.13
3.0	0.76 ± 0.26	1.12
4.0	0.72 ± 0.36	1.12
6.0	0.34 ± 0.07	1.12

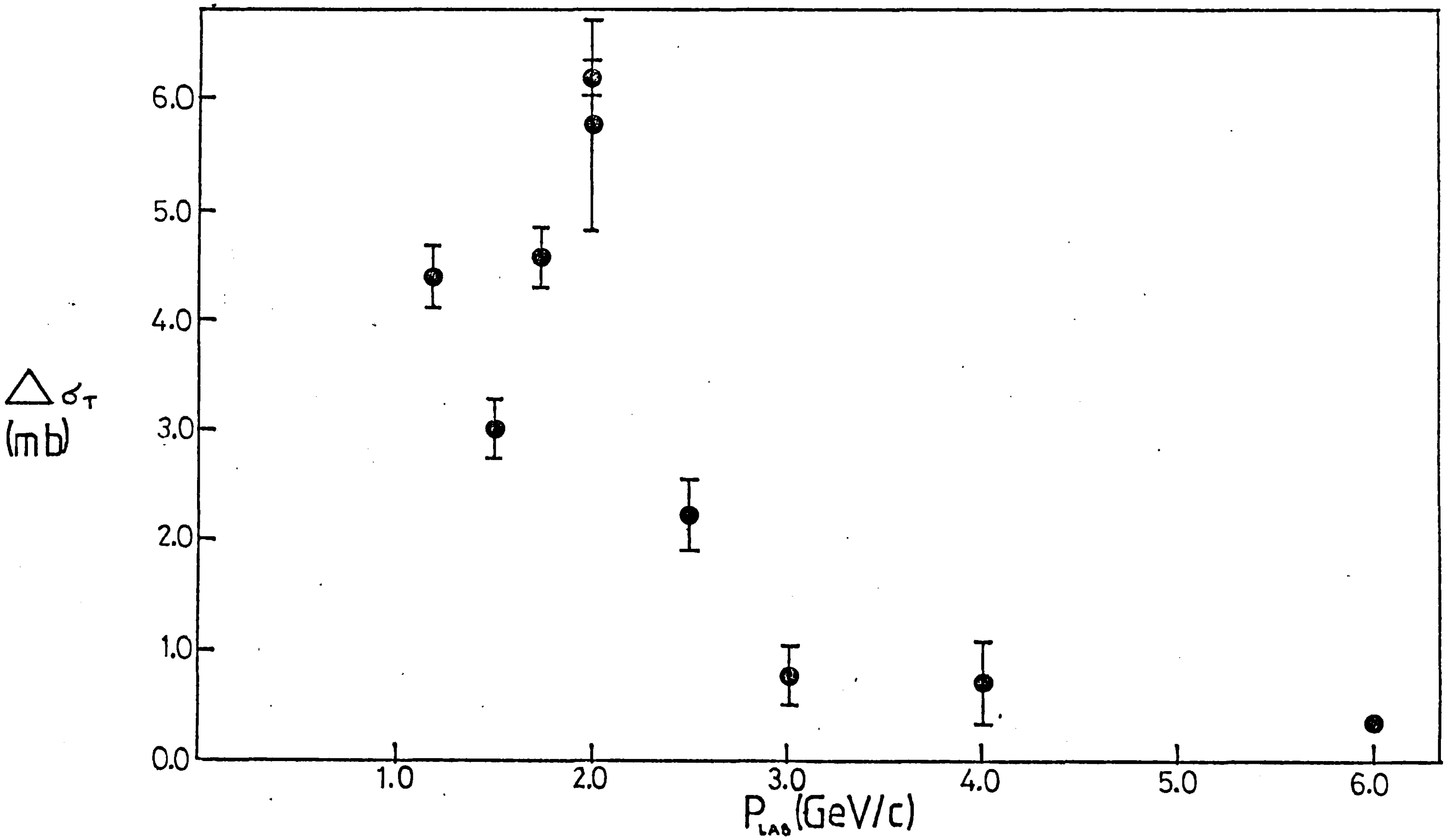

FIGURE 1.1 ARGONNE $\Delta\sigma_T$ RESULTS

1.47GeV/c being larger than a third of the total cross section. In the second paper two results were presented for 3 and 6GeV/c.

A further set of seven measurements were made in the momentum range 1 to 2.25GeV/c [(1.16)], to investigate the structure seen at approximately 1.5GeV/c. The results confirmed the earlier measurements and introduced a peak centred at approximately 1.17GeV/c. The $\Delta\sigma_L$ results are tabulated in table 1.2 and plotted in fig 1.2.

An explanation for the prominent bump-dip structure in the data between 1 and 2GeV/c, was clearly called for. In the energy range of the data, phase shift analysis offers a suitable investigatory tool.

1.3 Phase Shift Analysis

The result of a phase shift analysis of the N-N scattering data is a representation of the interaction by a set of phase shifts and elasticity parameters of scattered partial waves.

Consider the scattering of two spin-less particles. The target is at the origin of the Z axis. The incident beam is moving along the Z axis, it is represented by an incident set of plane waves, ψ_{INC}, ignoring the time dependence,

$$\psi_{INC} = e^{ikz} \qquad 1.3.1$$

where K is the wave number given by the relation,

TABLE 1.2

ARGONNE $\Delta\sigma_L$ RESULTS

P (GeV/c)	$\Delta\sigma_L$ (mb)	ref
1.0	-16.2 ± 0.2	1.16
1.1	-9.75 ± 0.16	1.16
1.17	-7.63 ± 0.28	1.14
1.3	-13.12 ± 0.10	1.16
1.47	-16.00 ± 0.11	1.14
1.58	-13.83 ± 1.04	1.16
1.69	-12.48 ± 0.12	1.14
1.71	-12.37 ± 0.14	1.16
1.97	-8.80 ± 0.19	1.16
2.10	-6.74 ± 0.12	1.16
2.25	-5.29 ± 0.07	1.16
2.49	-3.38 ± 0.10	1.14
2.97	-2.28 ± 0.10	1.15
6.00	-1.04 ± 0.09	1.15

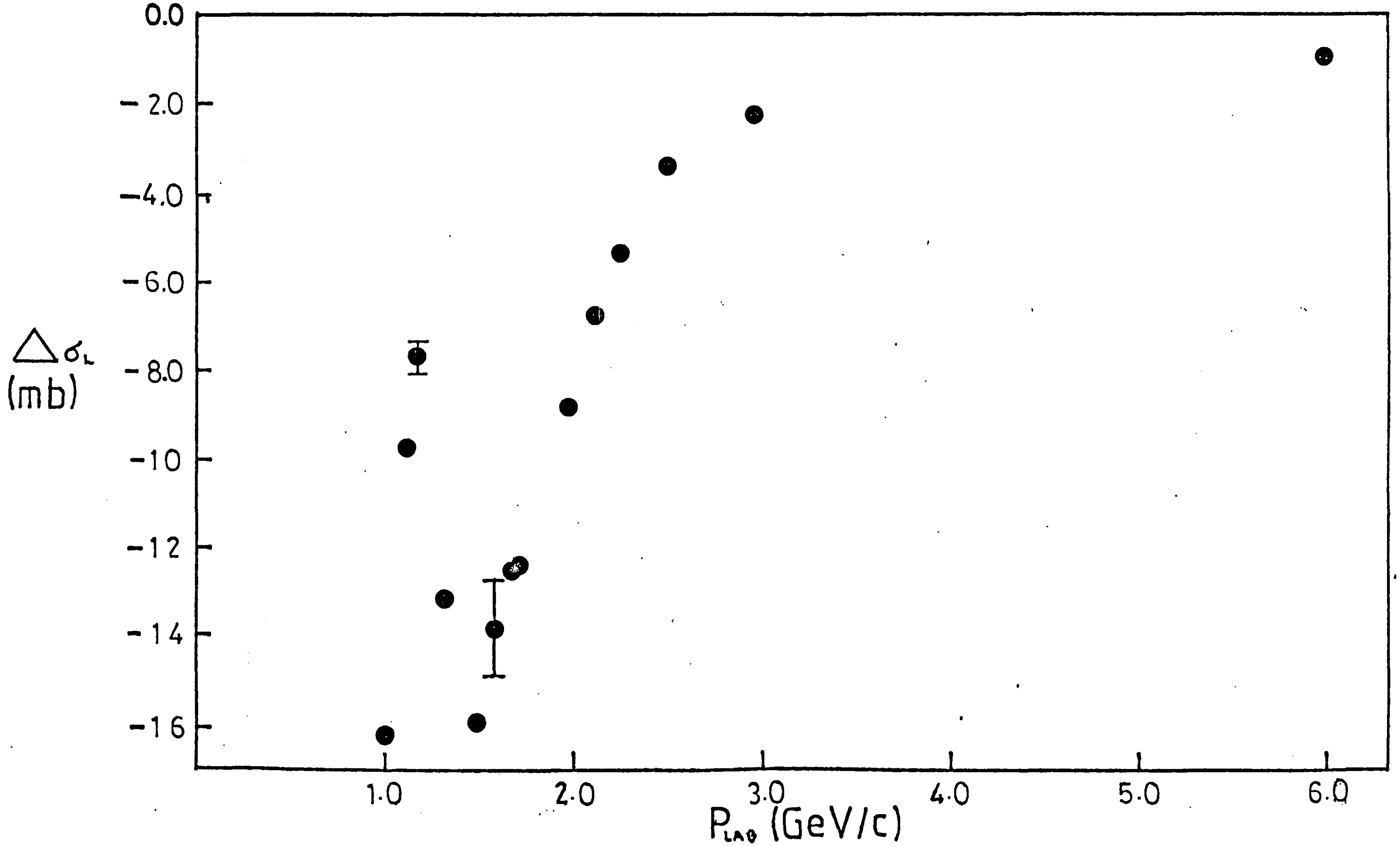

FIGURE 1.2 ARGONNE $\Delta\sigma_L$ RESULTS

$$k = P_{cm}/\hbar \qquad 1.3.2$$

where P_{cm} is the particle's centre of mass momentum. The incident wave function is normalized to give a density of one particle per unit volume.

$$|\psi_{INC}|^2 = 1 \qquad 1.3.3$$

If the particles are moving with velocity v, the incident flux is v particles per second.

It is shown in Mott and Massey (1.17) that a plane wave can be considered as a coherent superposition of spherical waves, which at large separation from the origin have an asymptotic form

$$\psi_{INC} = \frac{1}{2ikr} \sum_{l}^{\infty} (2l+1)\, i^{l}\, P_L\,(\cos\theta) \left\{ e^{i(kr-\frac{1}{2}l\pi)} - e^{-i(kr-\frac{1}{2}l\pi)} \right\} \qquad 1.3.4$$

where r is the distance from the origin, l is the orbital angular momentum quantum number, θ is the centre of mass scattering angle, and $P_l\,(\cos\theta)$ is the l^{th} order Legendre polynomial. The first (second) exponential term in the curly brackets represents a set of outgoing (incoming) spherical waves centred on the origin.

The effect of the N-N interaction is to modify the l^{th} outgoing spherical, or partial wave, by a multiplying factor $\eta_l e^{2i\delta_l}$; δ_l is a real phase shift which is positive (negative) for an attractive (repulsive) scattering potential. η_l, is another real number, the elasticity. This allows for absorption of the l^{th} partial wave.

The elasticity is constrained to lie between 0 and 1. For purely elastic (inelastic) scattering of the l^{th} partial wave $\eta_l = 1$ (0).

From equation 1.3.4 the wave function now representing the elastically scattered particles, ψ_{SCAT}, is

$$\psi_{SCAT} = \frac{e^{ikr}}{2ikr} \sum_{l} (2l+1)\, P_L\,(\cos\theta)\,(\eta_l e^{2i\delta_l} - 1) \qquad 1.3.5$$

The term $(\eta_l e^{2i\delta_l} - 1) / 2i$ contained in equation 1.3.5 is conventionally defined as the transition amplitude, R_l . The relation between η_l, δ_l and R_l can be shown by plotting the transition amplitude in the complex plane, fig 1.3 . The circle of radius $\frac{1}{2}$, the unitary circle, represents elastic scattering. All other possible values of R_l lie inside this circle. The point representing R_l is fixed by being a distance $|R_l|$ from the origin and at a distance $\frac{1}{2}$ from the point $\frac{1}{2}$ for purely elastic scattering.

The scattered wave function may be written in another way to define the scattering amplitude, $f(\theta)$,

$$\psi_{SCAT} = \frac{e^{ikr}}{r}\, f(\theta) \qquad 1.3.6$$

where

$$f(\theta) = \frac{1}{k} \sum_{l} (2l+1)\, P_l\,(\cos\theta)\, R_l \qquad 1.3.7$$

From the calculation of the flux of ψ_{SCAT} through the solid angle $d\Omega$ one obtains the differential cross section for elastic scattering.

$$\frac{d\sigma}{d\Omega} = |f(\theta)|^2 \qquad 1.3.8$$

Cross sections are obtained by integrating the differential cross section over the whole solid angle of 4π steradians,

$$\sigma_{ELASTIC} = \frac{4\pi}{k^2} \sum_{l} (2l+1)\, |R_l|^2 \qquad 1.3.9$$

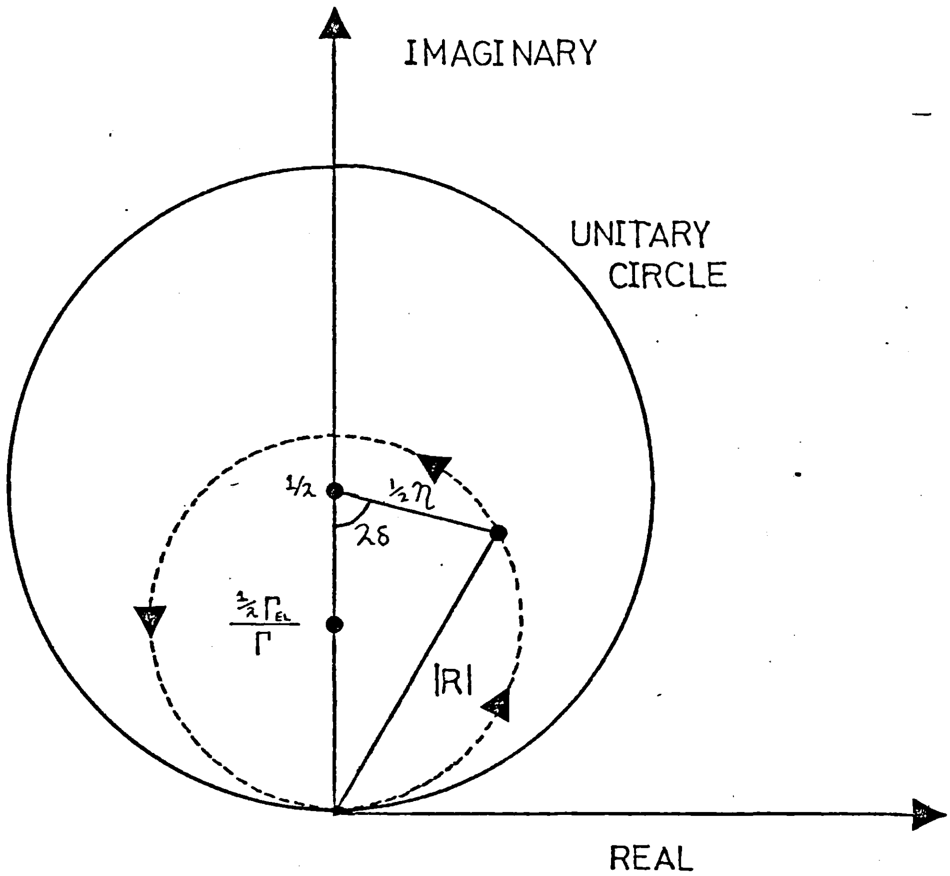

----- trajectory of ideal resonance

FIGURE 1.3 TRANSITION AMPLITUDE, R, PLOTTED IN THE COMPLEX PLANE

The inelastic cross section is given by

$$\sigma_{\text{INELASTIC}} = \frac{\pi}{k^2} \sum_{l} (2l+1)\,(1-\eta_l^2) \qquad 1.3.10$$

The total cross section is obtained by addition of the elastic and inelastic cross sections,

$$\sigma_{\text{TOT}} = \frac{4\pi}{k^2} \sum_{l} (2l+1)\,\text{Im}R_l \qquad 1.3.11$$

1.4 Phase Shift Analysis With Spin

A system of two interacting fermions such as protons must, according to the Pauli principle, be described by an overall antisymmetric wave function with respect to interchange of the particles.

Two interacting protons form an isospin triplet state which is a symmetric wave function, the combination of the space and spin wave functions must, therefore, be antisymmetric. This leads to states of singlet spin with even l, and triplet spin with odd l. Using spectroscopic notation, $^{2S+1}L_J$, where S is the total spin, L is the total orbital angular momentum, (where L = S,P,D,F,G,H are used for l = 0,1,2,3,4,5 etc) and J is the total angular momentum. The only partial waves involved in p-p scattering are shown in fig 1.4.

In collision processes, involving two nucleons, total angular momentum, total spin, and parity are conserved. The spin scattering matrix is therefore diagonal in these quantum numbers. To allow for

J \ L	S 0^+	P 1^-	D 2^+	F 3^-	G 4^+	H 5^-	I 6^+
0	${}^1S_{0^+}$	${}^3P_{0^-}$					
1		${}^3P_{1^-}$					
2		${}^3P_{2^-}$ $\bar{\varepsilon}_2$	${}^1D_{2^+}$	${}^3F_{2^-}$ $\bar{\varepsilon}_2$			
3				${}^3F_{3^-}$			
4				${}^3F_{4^-}$ $\bar{\varepsilon}_4$	${}^1G_{4^+}$	${}^3H_{4^-}$ $\bar{\varepsilon}_4$	
5						${}^3H_{5^-}$	
6						${}^3H_{6^-}$ $\bar{\varepsilon}_6$	${}^1I_{6^+}$
7							

FIGURE 1.4 CLASSIFICATION OF P-P STATES (SPECTROSCOPIC NOTATION)

the non-conservation of states with the same J,S and parity, but with different total orbital angular momentum L, eg $^3P_2$ and $^3F_2$, non-diagonal elements exist in the spin scattering matrix. The spin scattering matrix, S,[1.18] is given by,

$$S = \begin{bmatrix} R_J & 0 & 0 & 0 \\ 0 & R_{JJ} & 0 & 0 \\ 0 & 0 & R_{J-1,J} & R^J \\ 0 & 0 & R^J & R_{J+1,J} \end{bmatrix} \qquad 1.4.1$$

The transition amplitudes R_J, refer to singlet states with even J, even parity, L = J. The matrix element R_{JJ} relates to states with odd J, odd parity, L = J. The mixing of states with the same J,S and parity, but different L is achieved by using diagonal elements $R_{J\pm,J}$ and the off-diagonal element R^J. The most usual parameterization of the mixing is in terms of bar phase shifts and mixing parameters [1.19] $\bar{\varepsilon}_2$ for $^3P_2$ - $^3F_2$, $\bar{\varepsilon}_4$ for $^3F_4$ - $^3H_4$ etc. The transition amplitudes are defined in table 1.3

1.5 Range of Partial Waves

It is important to determine the number of partial waves involved in a scattering experiment, and hence determine the range of the summation in, for example, equation 1.3.4. The number is dependent upon the incident momentum and the range of the nuclear force. Classically, the highest angular momentum, l_{MAX}, involved in the scattering is,

$$l_{MAX}\hbar = b\,p_{CM} \qquad 1.5.1$$

TABLE 1.3

TRANSITION AMPLITUDES

SINGLET $$R_J = (\eta_J e^{2i\delta_J} - 1)/2i$$

TRIPLET

$$\left\{ \begin{array}{l} R_{J,J} = (\eta_{JJ} e^{2i\delta_{J,J}} - 1)/2i \\ R_{J\pm1,J} = \eta_{J\pm1,J} \cos \bar{\varepsilon}_J \, e^{2i\delta_{J\pm1,J}} \\ R^J = i(\eta_{J+1,J}\,\eta_{J-1,J})^{1/2} \sin 2\bar{\varepsilon}_J \, e^{i(\delta_{J+1,J}+\delta_{J-1,J})} \end{array} \right.$$

where b is the range of the N-N force and p_{cm} is the centre of mass momentum of the incident particle. For an incident proton of 520MeV, $p_{cm} \sim 500$MeV/c, equation 1.5.1 shows angular momentum states up to at least $l = 5$ must be considered. This simple model illustrates that the high l partial waves give information on the long range nuclear forces, whilst those of low l give information on the more complex short range forces.

The long range force is well understood in terms of OPE. From a comparision of phase shift analysis and OPE predictions for phase shifts, it is found that good agreement is found for partial waves with $l > 7$ for p-p and $l > 6$ for n-p [1.20].

To improve the stability of the results from phase shift fits, the phase shifts for high partial waves are set equal to the OPE predictions. It is important not to fix too many, or too few phase shifts, as this will distort the result of the phase shift fits. The BASQUE phase shift analysis program [1.9] assumes OPE calculated values for $l > 7$ for the p-p interaction, ${}^1I_6$ and $\overline{\varepsilon}_6$ are set equal to OPE + HBE ($2\pi, \rho, \omega$) values, using for the latter predictions of Vinh Mau et al [1.21]. The H waves and $\overline{\varepsilon}_4$ are constrained by including in the χ^2 minimization in the phase shift fitting program, terms of the form,

$$(\text{experimental phase} - \text{theory})^2 / \text{error}^2$$

where the error is a generous estimate of the theoretical error.

1.6 Coulomb Effects

The phase shifts defined previously for the p-p system, include both nuclear and coulomb contributions. To reveal the nuclear interaction effects, the coulomb contribution has to be subtracted out.

The full scattering amplitude, f, can be split into two contributions

$$f = f_c + f_N \qquad 1.6.1$$

where f_c is the coulomb contribution and f_N is the remainder. For one partial wave, and ignoring spin effects, the amplitude fc is given by

$$f_c = (e^{2i\xi} - 1) / 2i \qquad 1.6.2$$

where ξ is the coulomb phase shift (1.9). The second contribution to the full scattering amplitude is,

$$f_N = e^{2i\xi} \left[\eta \exp 2i \left(\delta + \Delta + i\phi \right) - 1 \right] / 2i \qquad 1.6.3$$

where δ and η are the true nuclear phase shifts and elasticity parameters respectively. Δ and ϕ are the coulomb barrier corrections. These allow for the effect of distortion to the incoming and outgoing waves by the coulomb potential. The values of Δ and ϕ can be calculated from the prescription of the Graz group(1.22). The values of ξ, Δ and ϕ allow the coulomb contributions to nuclear scattering parameters to be evaluated.

1.7 Resonant Partial Waves

A scattering process may take place through the formation of a Briet Wigner resonant state. The properties of this state determine many features of the process, in particular the energy variation of phase shift parameters.

The short-lived resonant state is represented by a complex energy, $E_0 - \frac{i}{2}\Gamma$. E_0 is the central energy and Γ is the level width, which is related to the mean life time, τ, of the resonance.

$$\Gamma = \hbar / \tau \tag{1.7.1}$$

Ignoring spin, and assuming the scattering takes place through a single resonant level formed by one partial wave, then dropping the l suffix, the transition amplitude is given by,(1.23)

$$|R|^2 = \frac{\frac{1}{4}\Gamma_{EL}^2}{(E-E_0)^2 + \frac{1}{4}\Gamma^2} \tag{1.7.2}$$

where Γ_{EL} is the elastic partial width. A second number required to fix the real and imaginary parts of the complex R is provided by the elasticity η, given by,

$$\eta^2 = 1 - \frac{\Gamma_{EL}(\Gamma - \Gamma_{EL})}{(E-E_0)^2 + \frac{1}{4}\Gamma^2} \tag{1.7.3}$$

The transition amplitude can be written as a complex quantity,

$$R = \frac{\frac{1}{2}\Gamma_{EL}\left[(E-E_0) + \frac{i}{2}\Gamma\right]}{(E-E_0)^2 + \frac{1}{4}\Gamma^2} \tag{1.7.4}$$

The above is the standard Briet Wigner resonance formula. It shows that the trajectories of the transition amplitude in the complex plane are affected by the existance of an intermediate state.

The trajectory of an ideal resonance is shown as the dotted line on fig 1.3. On increasing the energy towards the resonance, the representative point moves anticlockwise round a circle of radius $\Gamma_{EL}/2\Gamma$, centred on the point $i\Gamma_{EL}/2\Gamma$. On moving round the circle both η and δ change. At the resonant energy, for the case $\Gamma_{EL}/\Gamma > \frac{1}{2}$, δ goes through 90°, η is a minimum and R is purely imaginary. If $\Gamma_{EL}/\Gamma < \frac{1}{2}$ then δ goes through 0° at the resonant energy.

The situation represented in fig 1.3 is an ideal case. In reality the resonance structure is superimposed upon a background which may or may not be a smooth function of energy. The resonance parameters obtained from the transition amplitude plots can therefore be affected by the representation of the background subtracted from the data.

Relating equation 1.7.2 and 1.7.3 with 1.3.9, 1.3.10 and 1.3.11 one obtains expressions for the elastic, inelastic and total cross sections in terms of the elastic and total widths of the resonance,

$$\sigma_{ELASTIC} = \frac{\pi}{k^2}(2l+1)\frac{\Gamma_{EL}^2}{(E-E_0)^2 + \frac{1}{4}\Gamma^2} \qquad 1.7.5$$

$$\sigma_{INELASTIC} = \frac{\pi}{k^2}(2l+1)\frac{\Gamma_{EL}(\Gamma-\Gamma_{EL})}{(E-E_0)^2 + \frac{1}{4}\Gamma^2} \qquad 1.7.6$$

$$\sigma_{TOT} = \frac{\pi}{k^2}(2l+1)\frac{\Gamma_{EL}\Gamma}{(E-E_0)^2 + \frac{1}{4}\Gamma^2} \qquad 1.7.7$$

The above equations show that the existance of a resonance can be indicated by structure in the cross section.

1.8 Spin Dependent Observables

A spin dependent observable is measured in a scattering experiment where the polarization of at least one of the Beam, Target, Scattered or Recoil (B,T,S and R) particles is determined.

A coordinate system is defined using two unit vectors, $\underline{k}_i$ and $\underline{k}_f$ aligned along the direction of the incident and scattered particles. A unit normal to the scattering plane is defined as $\underline{n} = \underline{k}_i \times \underline{k}_f$. The polarization, $\langle\sigma\rangle$, of any of the particles in the reaction is written in terms of the unit vectors $\underline{n}$; $\underline{l}$ parallel to its direction; and $\underline{s} = \underline{n} \times \underline{l}$ transverse to its direction and in the scattering plane, fig 1.5.

In a general spin measurement one can determine an intensity, $I(\langle\sigma_B\rangle, \langle\sigma_T\rangle : \langle\sigma_S\rangle, \langle\sigma_R\rangle)$. For an experiment employing a polarized beam and target, the cross section is, (1.24)

$$I = I_0 \left(1+P_B I(n,o;o,o) + P_T I(o,n;o,o) + P_B P_T I(B,T;o,o)\right) \quad 1.8.1$$

where I_0 is the spin averaged cross section. The last term implies a sum over components of the beam polarization, P_B, and the target polarization, P_T. A list of spin dependent observables is given in table 1.4.

The polarization parameter P, $I(n,o;o,o)$ or $I(o,n;o,o)$ is, for example, evaluated in an experiment where the beam or target is polarized with a component along n. The difference in intensity when the polarization is up (+ n) and down (- n) is measured, from equation 1.8.1

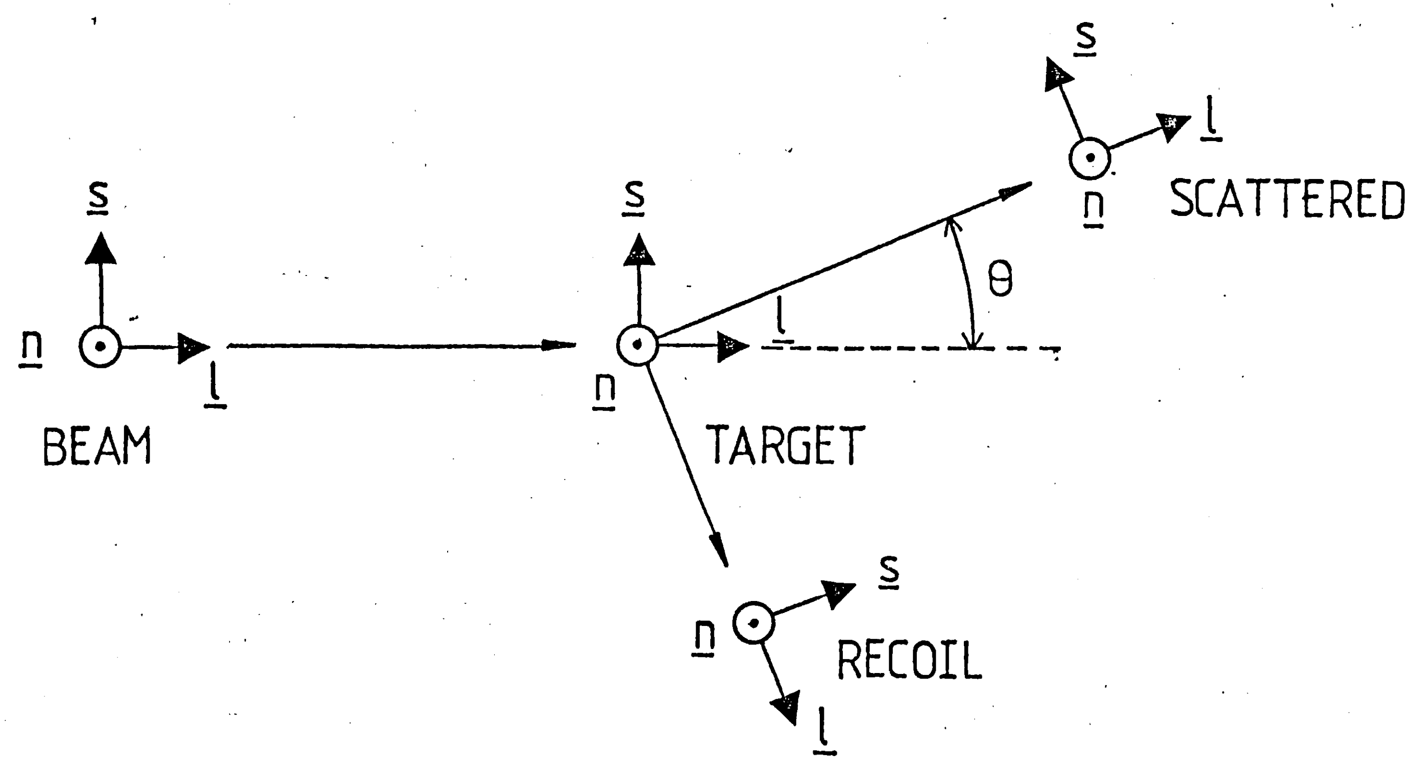

FIGURE 1.5 SCATTERING COORDINATE SYSTEM

OBSERVABLE	DESCRIPTION	SYMBOL
I (o,o;o,o)	CROSS SECTION	σ
I (n,o;o,o) I (o,n;o,o)	POLARIZATION PARAMETER	P
I (i,j;o,o)	SPIN-SPIN CORRELATION PARAMETER	A_{ij}
I (o,i;o,j)	DEPOLARIZATION, OR WOLFENSTEIN PARAMETER	D_{ij}
I (i,o;o,j)	SPIN-TRANSFER PARAMETER	K_{ij}
I (i,j;o,k)	TRIPLE-SPIN CORRELATION PARAMETER	H_{ijk}

TABLE 1.4 SPIN DEPENDENT OBSERVABLES

for a polarized beam experiment, monitoring at an angle θ ,

$$I(\pm) = I_0(1 \pm P_B P(\theta)) \qquad 1.8.2$$

leading to an asymmetry, ε ,

$$\varepsilon(\theta) = \frac{I(+) - I(-)}{I(+) + I(-)} = P_B P(\theta) \qquad 1.8.3$$

From the value of ε and the known beam polarization P can be evaluated.

The spin dependent observables can be expressed in terms of their constituent partial waves. A particularly elegant way to do this is via helicity amplitude formalism developed by Jacob and Wick[1.25]. In this representation a particle is labelled by a helicity quantum number. This is + (-) $\frac{1}{2}$, if the particle's spin is parallel (antiparallel) to its momentum. There are five independent helicity amplitudes, $\phi_i(\theta)$, $i = 1 - 5$, given by,[1.24]

$$\begin{aligned}
\phi_1(\theta) &= \langle +\tfrac{1}{2}, +\tfrac{1}{2}; +\tfrac{1}{2}, +\tfrac{1}{2} \rangle \\
\phi_2(\theta) &= \langle +\tfrac{1}{2}. +\tfrac{1}{2}; -\tfrac{1}{2}, -\tfrac{1}{2} \rangle \\
\phi_3(\theta) &= \langle +\tfrac{1}{2}. -\tfrac{1}{2}; +\tfrac{1}{2}, -\tfrac{1}{2} \rangle \\
\phi_4(\theta) &= \langle +\tfrac{1}{2}. -\tfrac{1}{2}; -\tfrac{1}{2}; +\tfrac{1}{2} \rangle \\
\phi_5(\theta) &= \langle +\tfrac{1}{2}. +\tfrac{1}{2}; +\tfrac{1}{2}; -\tfrac{1}{2} \rangle
\end{aligned}$$

where θ is the centre of mass scattering angle, and the notation used is $\langle S,R;B\ T \rangle$. The relation between the helicity amplitudes and the partial waves is given in appendix A.[1.24].

In table 1.5 a list of observables are given in terms of the helicity amplitudes[1.3].

OBSERVABLE	HELICITY AMPLITUDES
σ^{TOT}	$(2\pi/p_{CM}^2)\,\mathrm{Im}[\phi_1(0)+\phi_3(0)]$
$\Delta\sigma_L^{TOT}$	$(4\pi/p_{CM}^2)\,\mathrm{Im}[\phi_1(0)-\phi_3(0)]$
$\Delta\sigma_T^{TOT}$	$-(4\pi/p_{CM}^2)\,\mathrm{Im}\,\phi_2(0)$
σ	$[\lvert\phi_1\rvert^2+\lvert\phi_2\rvert^2+\lvert\phi_3\rvert^2+\lvert\phi_4\rvert^2+4\lvert\phi_5\rvert^2]/2p_{CM}$
P	$\mathrm{Im}[(\phi_1+\phi_2+\phi_3-\phi_4)^*\phi_5]/\sigma p_{CM}$
A_{NN}	$\mathrm{Re}[(\phi_1^*\phi_2-\phi_3^*\phi_4)+2\lvert\phi_5\rvert^2]/\sigma p_{CM}$
A_{SS}	$\mathrm{Re}[\phi_1^*\phi_2+\phi_3^*\phi_4]/\sigma p_{CM}$
A_{SL}	$\mathrm{Re}[(\phi_1+\phi_2-\phi_3+\phi_4)^*\phi_5]/\sigma p_{CM}$
A_{LL}	$[-\lvert\phi_1\rvert^2-\lvert\phi_2\rvert^2+\lvert\phi_3\rvert^2+\lvert\phi_4\rvert^2]/2\sigma p_{CM}$

TABLE 1.5 SPIN DEPENDENT OBSERVABLES IN TERMS OF HELICITY AMPLITUDES

1.9 Discussion of Argonne Results

The effect of a Briet Wigner resonance is to introduce structure into the variation of cross section as a function of energy. A resonance is not the only process that can create structure. The superposition of several non-resonant partial waves or the opening of an inelastic channel, can have the same effect. A true indication as to the origin of the structure is obtained by a study of both real and imaginary components of the scattering amplitudes.

The measurements of total cross sections give information only on the imaginary components of the scattering amplitude. Dispersion analysis can be used to give the real components of the scattering amplitudes from the imaginary components (1.26)(1.27).

A dispersion analysis was performed by W Grein and P Kroll (1.28) on the two forward amplitudes F_2 and F_3 given by,

$$F_2 = \frac{P_L}{P_{cm}^2} \phi_2(0) \qquad 1.9.1$$

$$F_3 = \frac{P_L}{P_{cm}^2} \left(\phi_1(0) - \phi_3(0) \right) \qquad 1.9.2$$

where P_L (P_{cm}) is the laboratory (centre of mass) momentum. Using equations 1.9.1 and 1.9.2 and the results in table 1.5,

$$\Delta\sigma_L = \frac{4\pi}{P_L} \operatorname{Im} F_3 \qquad 1.9.3$$

$$\Delta\sigma_T = \frac{-4\pi}{P_L} \operatorname{Im} F_2 \qquad 1.9.4$$

The amplitudes F_2 and F_3 can be expressed in terms of partial wave amplitudes,[1.3]

$$(P^2{}_{cm}/P_L)\ F_3 = \sum_J \left\{ (2J+1) R_J + R_{J+1,J} - R_{J-1,J} + 4\sqrt{J(J+1)}\, R^J - (2J+1) R_{JJ} \right\} \quad 1.9.5$$

$$(P^2{}_{cm}/P_L)\ F_2 = \sum_J \left\{ -(2J+1) R_J + J R_{J-1,J} + (J+1) R_{J+1,J} + 2\sqrt{J(J+1)}\, R^J \right\} \quad 1.9.6$$

W Grein and P Kroll used the Argonne $\Delta\sigma_L$ and $\Delta\sigma_T$ data in their dispersion analysis. The results for ReF_2 and ReF_3 are shown in fig 1.6, together with ImF_2 and ImF_3 over the laboratory energy range 0.1 - 7GeV. The peak at 0.6GeV in the Argonne $\Delta\sigma_L$ data leads to S shaped structure in ReF_3 extending down to 210MeV. The authors find indications of the existence of two resonances, one in a spin-singlet state (m = 2390MeV) and one in an uncoupled triplet state (m = 2320MeV). The real part of F_3 derived using dispersion relations is however, in disagreement with secure phase shift predictions.[1.29,31]

The energy range of the Argonne results for $\Delta\sigma_L$ and $\Delta\sigma_T$ is overlapped by four separate phase shift analyses; Arndt et al [1.29] (< 800MeV), BASQUE [1.30] (< 600MeV), Bystricky et al [1.31] (< 750MeV) and Hoshizaki [1.32] (500 - 2500MeV). The elastic scattering data is sufficient to yield good phase shift solutions up to approximately 600MeV. The outcome is that the four solutions agree very closely on the elastic phase shift parameter, δ , and disagree on the elasticity parameters, η , to which the elastic data are rather insensitive.

The imaginary component of the scattering amplitude is, from equation 1.3.7.

$$\text{Im} f(\theta) \propto 1 - \eta \cos 2\delta \qquad 1.9.7$$

The phase shifts are generally small, the imaginary components of the scattering amplitudes are, therefore, sensitive to values of the elasticity. $\Delta\sigma_L$ and $\Delta\sigma_T$ are dependent on the imaginary components of $f(\theta)$ and thus yield information on the elasticity parameters.

Previous to the data on $\Delta\sigma_L$ and $\Delta\sigma_T$ becoming available, all the elasticity was put into the $^1D_2$ partial wave. This was to allow for $p\text{-}p \rightarrow n\Delta^{++}$ from an incident $^1D_2$ state. The value of $\eta\,(^1D_2)$ was fixed by the total cross section. Although this approach introduces little error into real parts of the phase shift, it gives misleading predictions for $\Delta\sigma_L$ and $\Delta\sigma_T$. To incorporate $\Delta\sigma_L$ and $\Delta\sigma_T$ results into a phase shift analysis, freedom in elasticity parameters is introduced.

In order to reproduce the rise in $\Delta\sigma_L$ up to 600MeV, it is necessary to put the maximum inelasticity in the $^1D_2$ partial wave. This conclusion follows from the partial wave decomposition of F_3. The coefficient (2J+1) ensures that the dominant partial waves are R_J and R_{JJ} (as R^J is small). To allow for the rise in $\Delta\sigma_L$ the inelasticity in R_{JJ} eg. $^3F_3$ must be small, but above 600MeV this elasticity must rise rapidly to account for the descent of $\Delta\sigma_L$.

All the phase shift analysis fits incorporating the $\Delta\sigma_L$ data have as common the trends in $^1D_2$ and $^3F_3$ elasticities. Three of the analyses allow freedom in more than three η parameters, whereas the BASQUE phase shift analysis allows freedom in only ${}^1D_2$, ${}^3F_3$ and ${}^3F_2$, taking other values from OPE calculations.

The effect of fitting the $\Delta\sigma_L$ data is shown by Bugg [(1.30)] to cause inelasticities in ${}^1D_2$ that are in conflict with expected values.

A common problem of all the phase shift analyses is the disagreement between their predicted Re F_3 and those of the dispersion analysis. BASQUE phase shift predictions of Re and Im F_2 and F_3 are shown on fig. 1.6. Re parts are from a solution fitting $\Delta\sigma_L$ and $\Delta\sigma_T$. Im parts are from a solution using η parameters from OPE calculations and omit $\Delta\sigma_L$ and $\Delta\sigma_T$ results. No manipulation of the η parameters secures agreement between phase shift predictions and the dispersion analysis derived Re F_3.

If the structure in Im $F_{2,3}$ in the range 380-800MeV is bypassed[(1.30)] then the resulting dispersion analysis gives the dotted curves for Re $F_{2,3}$ shown on fig. 1.6. The latter give much better agreement with the phase shift solutions.

The structure in $\Delta\sigma_L$ has, in the phase shift analysis of Hoshizaki [(1.32)] and Arndt[(1.33)], been interpreted as caused by dibaryon resonances. In the analysis of Hoshizaki, which incorporated the values of Re $F_{2,3}$ from the dispersion analysis of Grein and Kroll[(1.28)], resonant behavior was seen in ${}^1D_2$ (${}^3F_3$), at M = 2.17 (2.22)GeV, see fig 1.7. The phase shift analysis of Arndt shows indications of resonances in ${}^1D_2$ and ${}^3F_3$, see fig 1.8.

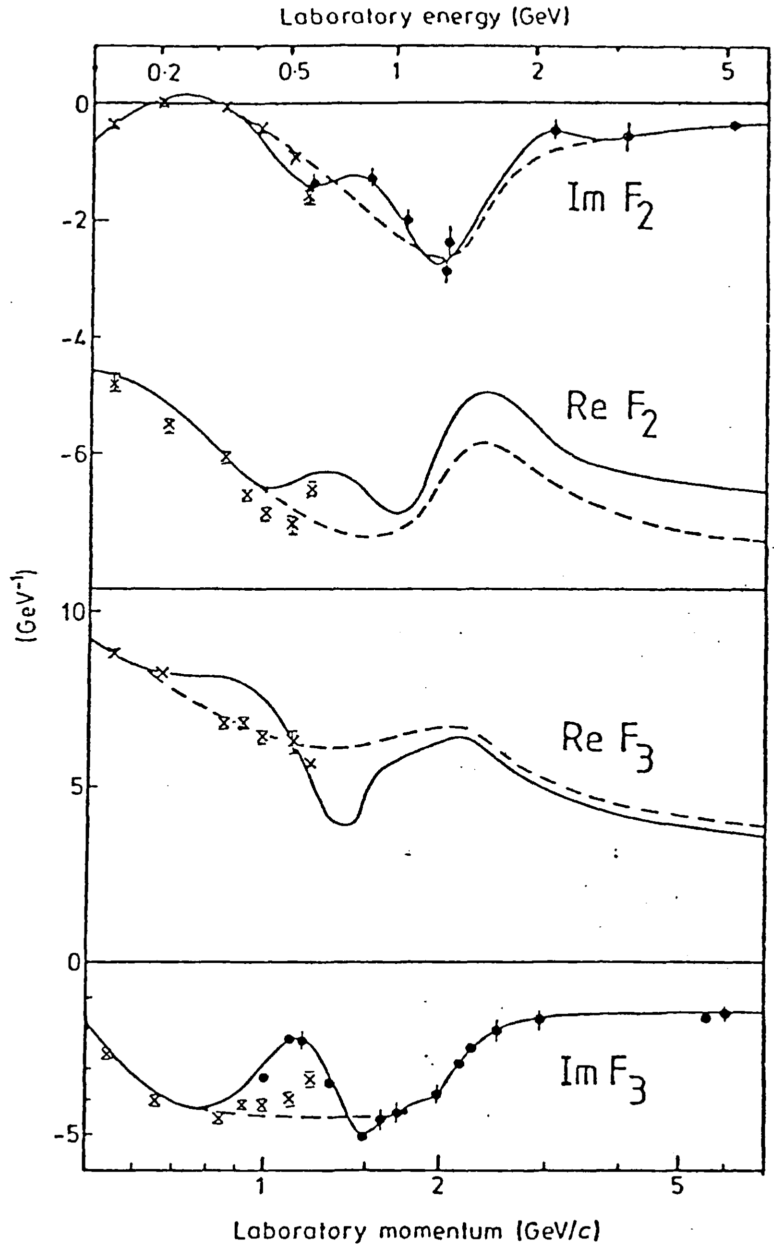

FIGURE I.6 REAL AND IMAGINARY PARTS OF THE AMPLITUDES F_2 AND F_3 FULL AND BROKEN CURVES ARE ALTERNATIVE FITS TO ImF_2 AND ImF_3, THE CORRESPONDING CURVES FOR THE REAL PARTS ARE CALCULATED FROM DISPERSION RELATIONS. FULL CIRCLES ARE EXPERIMENTAL DATA (REF. 1.11-1.16) AND CROSSES ARE FROM BASQUE PHASE SHIFT SOLUTIONS

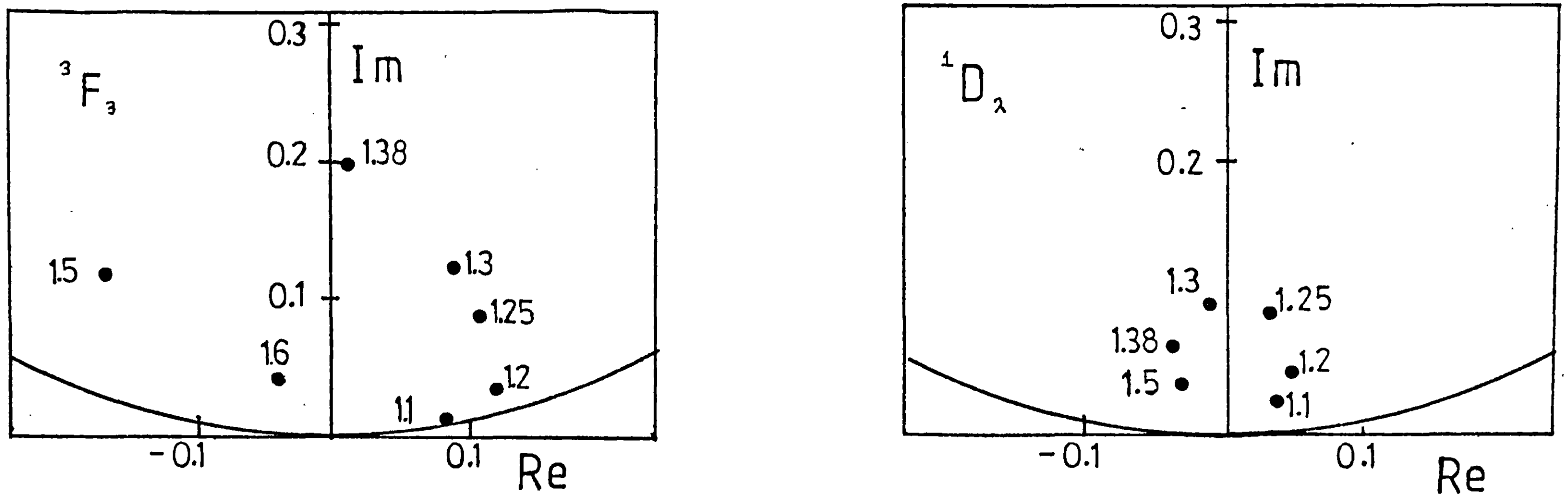

FIGURE 1.7 ARGAND DIAGRAMS OF THE $^3F_3$ AND $^1D_2$ PARTIAL WAVES FROM THE PHASE SHIFT ANALYSIS OF HOSHIZAKI. POINTS ARE IN GEV/C

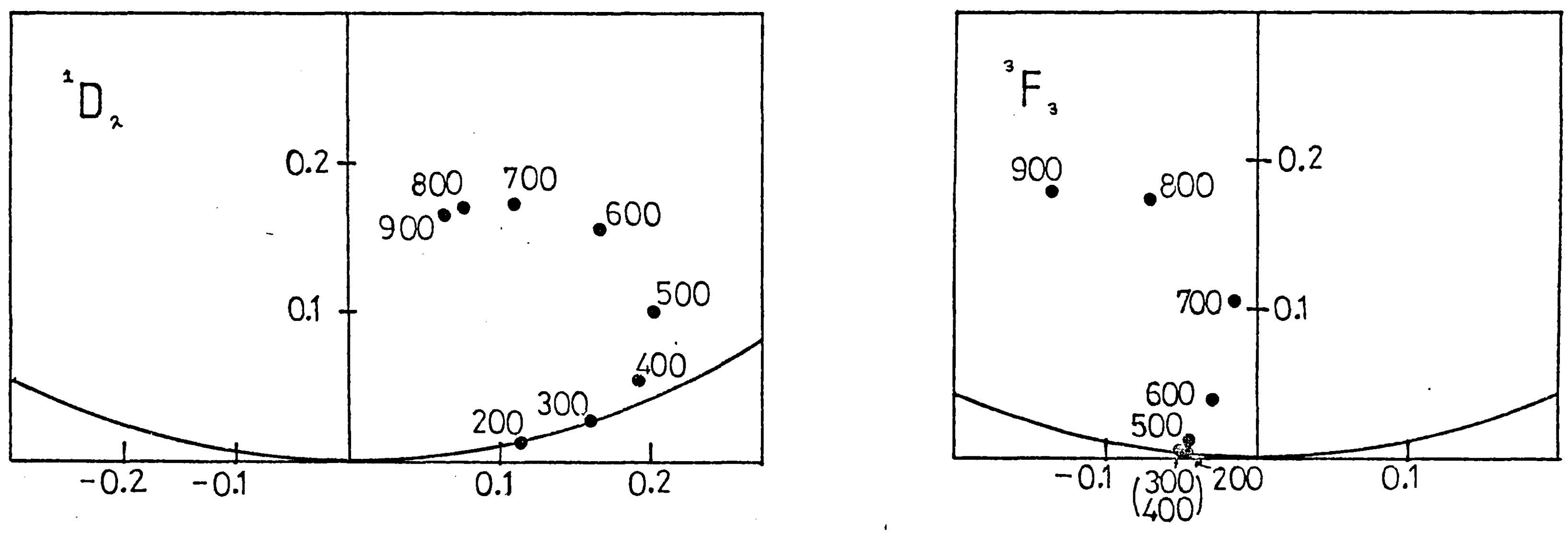

FIGURE 1.8 ARGAND DIAGRAMS OF THE $^1D_2$ AND $^3F_3$ PARTIAL WAVES FROM THE ENERGY DEPENDENT PHASE SHIFT ANALYSIS OF ARNDT. POINTS ARE IN MeV.

In conclusion, the structure in $\Delta\sigma_L$, results in values of ReF_3 in contradiction to phase shift predictions, specifically at 325, 380 and 425MeV. Phase shift fits to the $\Delta\sigma_L$ data also necessitate inelasticities in partial waves at variance to expected values. The structure has also been interpreted as indicating dibaryon resonances. It was therefore desirable to have an independent check on the data and to extend the measurements down to an energy below, or about π production threshold , where inelasticities are negligible and the phase shift predictions can be checked against the experimental results.

CHAPTER 2

REQUIREMENTS OF AN EXPERIMENT TO MEASURE $\Delta\sigma_L$ AND $\Delta\sigma_T$

The BASQUE group have performed several N-N scattering experiments at the TRIUMF Laboratory, at the University of British Colombia, in Vancouver. TRIUMF has a variable energy cyclotron, able to supply polarized protons over the energy range 200 to 520MeV. The main objective of the experiments performed by the BASQUE group, had been the determination of accurate n-p elastic amplitudes. The experiments measured three Wolfenstein parameters (2.1), D_t, R_t and A_t (2.2)(2.3), differential and total cross sections (2.4)(2.5), and the polarization parameter P (2.2). Measurements of D, R, R′ and P (1.9) were also made for p-p scattering.

In 1979 the BASQUE group proposed to continue their work on the N-N interaction by a set of measurements of $\Delta\sigma_L$ and $\Delta\sigma_T$. The measurements were to be performed at the five energies where the earlier N-N work had been performed, namely 210, 325, 380, 425 and 515MeV. Two extra energies, 460 and 500MeV, were to be added to give a more complete overlap with the previous Argonne data. Measurements at these energies would allow inclusion of the results into the BASQUE phase shift analysis. The results below the π production threshold could be compared with phase shift predicted values.

2.1 Total Cross Section Measurements

A beam of protons incident upon a target undergoes both scattering and absorption. The number of protons transmitted, N, after transversing a target of length, L, is

$$N = N_o e^{-nL\sigma} \qquad 2.1.1$$

where N_o is the incident number of particles, σ is the total cross section and n is the particle density of the target. A total cross section is obtained from an experiment counting the number of beam particles incident, and those transmitted by a target of known length and density.

The apparent cross section is a function of the half angle, θ, subtended by the counter detecting the transmitted beam. This variation is shown schematically in fig 2.1. At small angles the apparent cross section is a rapidly varying function of θ, the section A-B on fig 2.1. This effect arises from multiple coulomb scattering of the protons in the target. The multiple coulomb scattering is described by Rossi and Greisen [2.6]. They describe the distribution as being gaussian in form with a standard deviation, θ_{RMS} in radians given by

$$\theta_{RMS} = \frac{15}{p_{LAB}\beta}\left(\frac{L}{L_R}\right)^{1/2} \qquad 2.1.2$$

where p_{LAB} is the incident proton momentum in MeV/c, βc is its velocity, L the target length and L_R is the target's radiation length. A small number of protons undergo single coulomb scattering through a large angle, which superimposes a long tail onto the gaussian distribution of multiple coulomb scattered events.

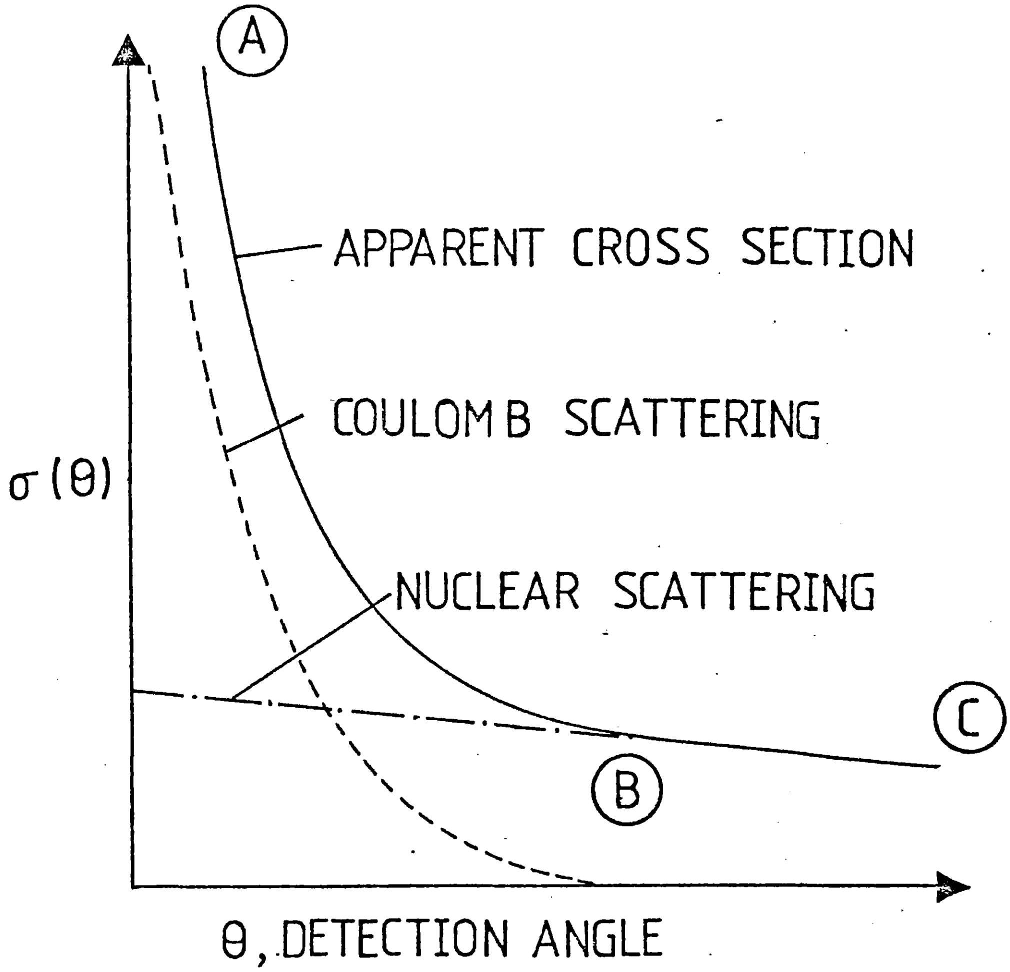

FIGURE 2.1 VARIATION OF MEASURED CROSS SECTION AS A FUNCTION OF DETECTION ANGLE (SCHEMATIC)

For the target material to be used in this experiment, Butanol-water spheres, L_R is approximately 40cm, the effective length of the target material was approximately 1.35cm. At the lowest (highest) incident proton momentum of approximately 650 (1120)MeV/c the value of Θ_{RMS} is 0.78^o (0.30^o). A measurement of a nuclear cross section must use a counter subtending an angle of greater than Θ_{RMS}.

In the region B-C a counter monitoring the transmitted beam now encompasses virtually all the coulomb scattered events. The change in apparent cross section in this region is, therefore, due to nuclear scattering. A cross section measurement made in this region would, however, underestimate the total cross section. To obtain the total cross section, a number of cross section measurements are made in the region B-C and the results are extrapolated under the coulomb peak to zero angle. A total cross section measured in this way is called a 'good geometry' measurement.

When a transversly polarized beam is used in conjunction with a transversly polarized target the effect is to alter the measured cross section. From the definition of $\Delta\sigma_T$, equation 1.2, a term $-\frac{1}{2}P_BP_T\Delta\sigma_T$ is introduced. The measured cross section σ is now given by

$$\sigma = \sigma_o - \tfrac{1}{2}P_BP_T\Delta\sigma_T \qquad 2.1.3$$

where σ_o is the unpolarized cross section. The factor P_BP_T is positive (negative) when the polarizations are aligned parallel (antiparallel).

In reality a polarized target contains not only polarized hydrogen nuclei but also unpolarized more complex nuclei. The total cross section consists of three components; σ_H arising from unpolarized hydrogen; $-\frac{1}{2}P_B P_T \Delta\sigma_T$ from the polarized hydrogen, and σ_B from the remaining non-hydrogen nuclei in the target. The transmission of the target, t(↑↑) for parallel alignment of P_B and P_T is, therefore given by

$$t(\uparrow\uparrow) = \frac{N(\uparrow\uparrow)}{N_o(\uparrow\uparrow)} = e^{-n_B\sigma_B L}\, e^{-n_H L\left(\sigma_H - \frac{P_B(\uparrow)P_T(\uparrow)\Delta\sigma_T}{2}\right)} \qquad 2.1.4$$

for the antiparallel alignment,

$$t(\uparrow\downarrow) = \frac{N(\uparrow\downarrow)}{N_o(\uparrow\downarrow)} = e^{-n_B\sigma_B L}\, e^{-n_H L\left(\sigma_H - \frac{P_B(\downarrow)P_T(\uparrow)\Delta\sigma_T}{2}\right)} \qquad 2.1.5$$

whence, from equations 2.1.4 and 2.1.5,

$$\tanh \frac{L n_H \overline{P}_B P_T \Delta\sigma_T}{2} = \frac{t(\uparrow\uparrow) - t(\uparrow\downarrow)}{t(\uparrow\uparrow) + t(\uparrow\downarrow)} \qquad 2.1.6$$

where $\overline{P}_B = \left[P_B(\uparrow) - P_B(\downarrow)\right]/2$, leading to

$$\Delta\sigma_T = \frac{\Delta t \; 1.0079}{\overline{t} n_H \overline{P}_B P_T L} \qquad 2.1.7$$

(an approximation good to 1 in 500000)

where $\Delta t = t(\uparrow\uparrow) - t(\uparrow\downarrow)$ 2.1.8

and $\overline{t} = \left(t(\uparrow\uparrow) + t(\uparrow\downarrow)\right)/2$ 2.1.9

The factor 1.0079 allows for the atomic weight of hydrogen. A similar expression is obtained for $\Delta\sigma_L$. A value of $\Delta\sigma_L$ or $\Delta\sigma_T$ is, therefore obtained from performing two transmission experiments; one with beam and target polarizations parallel and one with beam and target alignments antiparallel.

2.2 Beam Polarization Precession

A measurement of both $\Delta\sigma_L$ and $\Delta\sigma_T$ requires a beam polarized both parallel and transverse to the beam momentum at the target position. The beam extracted from the TRIUMF cyclotron has its polarization aligned transverse (vertical plane) to the beam. A new beamline, BL4C, was designed to precess the extracted vertical beam polarization into the longitudinal direction over the accessible energy range 200 to 520MeV. BL4C also had to be able to deliver the transversly polarized beam extracted from the cyclotron to the target.

2.2.1 Solenoidal Magnetic Fields

A proton beam with a spin component perpendicular to its momentum, travelling axially through a solenoid, will have this spin component rotated by an angle ϕ_s. For a solenoid with a field integral $\int \underline{B}.d\underline{l}$ the angle ϕ_s is given by (2.7)

$$\phi_s = \frac{2\mu_p \mu_N}{\gamma_{LAB}\beta_{LAB} c\hbar}\int \underline{B}.d\underline{l} \qquad 2.2.1$$

where $\mu_p = 2.793$, μ_N is the nuclear magneton $= \frac{e\hbar}{2m_p c}$

e is the electronic charge, m_p the mass of the proton and c the velocity of light. βc is the proton's velocity,

2.2.2 Bending Magnet Fields

For a bending magnet the rotation of the spin direction, ϕ_B, relative to the direction of the proton is (2.8)

$$\phi_B = (\mu_p - 1)\,\gamma_{LAB}\,\Theta_B \qquad 2.2.2$$

where Θ_B is the angle of beam deflection caused by the bending magnet.

A longitudinal polarization can be obtained from the extracted vertically polarized beam by using a solenoid-bending magnet combination, fig 2.2. The vertically polarized beam first traverses a solenoid energised to produce a field integral giving a $\phi_S = \pm 90^\circ$. The emergent beam is still polarized transverse to the beam momentum, but now lies in the horizontal plane. The beam is then incident into a bending magnet which bends it through an angle Θ_B. This angle is ideally such that $\phi_B = 90^\circ$, this being the case, the emergent beam is longitudinally polarized.

If the solenoid is not energised the beam polarization is unaffected by the bending magnet and it is delivered to the target vertically polarized.

The polarization precession angle for both a solenoid and a bending magnet is dependent upon the incident energy of the proton. To acheive a precession angle of 90° requires the changing of the field integral for each incident energy for a solenoid, and the changing of the bend angle for a bending magnet. The former is easily acheived, but the latter is impractical for this experiment.

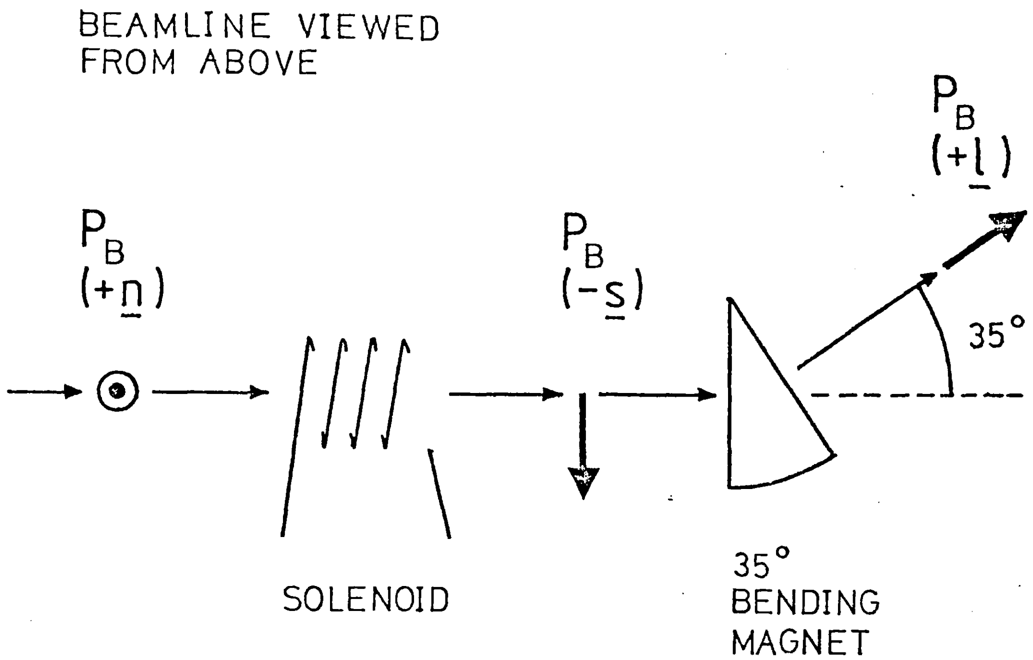

FIGURE 2.2 SOLENOID-BENDING MAGNET COMBINATION USED TO ACHIEVE A LONGITUDINAL POLARIZATION FROM AN INITIALLY VERTICALLY POLARIZED BEAM

To obtain a purely longitudinally polarized beam requires a bend angle of 41.4^{o} (32.3^{o}) for an incident proton energy of 200 (520)MeV. This change in bending angle necessitates the moving of all beam elements downstream of the bending magnet for each change in energy. A compromise bend angle of 35^{o} was chosen. This gave the best longitudinally aligned beams at the higher energies. In the worst case the longitudinal component of beam spin was reduced by approximately 3% at 200MeV. The fixed bend angle introduces a transverse component into the beam polarization.

2.3 Dynamically Polarized Target

The most important single element in the beamline was the polarized target. A dynamically polarized target was obtained from Liverpool University. It provided a target cell 2.4cm in length and 1.5cm in diameter, that could be polarized vertically or horizontally [2.9].

A dynamically polarized target utilizes low temperatures and strong magnetic fields, combined with microwave pumping to obtain sizeable proton polarizations [2.10] [2.11].

An assembly of protons in a magnetic field, B, have two preferred directions of orientation. Preferrentially, the proton's magnetic moment is aligned parallel to the field, the position of lowest energy. The thermal energy of the system KT, where K is the Boltzman Constant and T is the absolute termperature, determines the population of the two levels. The thermal equilibrium polarization, P_{TE}, of the system is given by

$$P_{TE} = \tanh\left(\frac{\mu_p \mu_N B}{2KT}\right) \qquad 2.3.1$$

At typical operating conditions of the target P_{TE} for protons is approximately 0.3%.

Dynamic polarization utilizes the much larger thermal equilibrium polarization of electrons, due to their large magnetic moment, 660 times that of the protons. At typical operating conditions P_{TE} for electrons is almost 100%.

The protons to be polarized are the nuclei of hydrogen in butanol. Mixed with the butanol is a small quantity of a paramagnetic impurity, eg a chromium compound. The magnetic field polarizes the unpaired electrons of the chromium atoms, which can then form temporary pairs with the hydrogen nuclei. There are only two possible combinations of spin, proton and electron spins parallel and antiparallel. Application of microwave power to the system can induce spin flips. Inducing the flipping of both spins in one of the parallel or antiparallel alignments then polarizes the protons and depolarizes the electrons. When the temporary pair breaks up, the electrons are readily repolarized. The flipping of parallel or antiparallel pairs requires slightly different energy and so the polarization direction can be chosen by the frequency of the applied microwave power. To ensure that only one transition is on resonance, the temperature and magnetic field must be constant throughout the target volume.

2.4 Target Polarization Measurements

The normalization of $\Delta\sigma_T$ and $\Delta\sigma_L$ depends on the absolute normalization of P_T. The target incorporated a NMR monitoring system. The calibration of the NMR system is such that it has, normally, an absolute uncertainty of approximately 4%.

A valuable improvement of this experiment over previous measurements of $\Delta\sigma_L$ and $\Delta\sigma_T$ was the incorporation of a nuclear physics experiment to independently determine the target polarization.

2.4.1 NMR Monitor

The target polarization was monitored by a constant current, series tuned, Q meter. A coil wrapped around the target applied a radiofrequency field perpendicular to the main applied magnetic field. The resonant frequency of this circuit is adjusted, by a variable capacitor, to be the same as the nuclear resonance frequency, ν. This frequency supplies an energy equal to the energy separation of the parallel and antiparallel alignment of the proton's spin, with the magnetic field, from equation 2.3.1, ν is given by

$$\nu = \frac{\mu_p \mu_N B}{h} \qquad 2.4.1$$

Application of a radiofrequency field of this frequency, causes a fraction of the protons to flip from one alignment to the other. The target polarization is deduced from measurements of the effect of the proton transitions on the electrical characteristics of the tuned circuit.

The impedance of the Q circuit includes a term proportional to χ [2.11], where χ is the susceptibility of the target. The susceptibility is frequency dependent and complex,

$$\chi(f) = \chi'(f) - i\chi''(f) \qquad 2.4.2$$

χ' is the elastic or dispersive term and χ'' is the absorptive part. At the resonant frequency, the susceptibility becomes highly imaginary. The area under the absorptive signal is proportional to the nuclear polarization,[2.11]

$$P_T \propto \int_0^{\infty} \chi''(f)\, df \qquad 2.4.3$$

where f is the frequency. The effect of the polarized protons is to produce a change in impedance around the nuclear magnetic resonance frequency. This change in impedance is measured by applying a frequency swept, radiofrequency voltage to the tuned circuit and detecting the change in voltage with frequency.

It is not possible to calculate the constant of proportionality in equation 2.4.3 , and so the constant is found experimentally. When the protons are in thermal equilibrium at a known temperature, the polarization is calculable using equation 2.3.1. At thermal equilibrium the nuclear polarization is very small, approximately 0.3%, large coil currents therefore, cannot be used as these will distort the polarization and lead to false readings. These low currents coupled with the small polarizations lead to low outputs and thus poor signal to noise ratios.

The inherently poor determination of the proportionality constant and the uncertainties of the temperature at which the thermal equilibrium measurements are made, lead to an overall uncertainty in the absolute calibration of the NMR deduced polarizations of the order of 4%.

The variation of the impedance depends upon the magnitude of χ and therefore incorporates a small unwanted χ' term. This dependence is removed by employing a phase sensitive detector which measures only the absorptive component of the complex susceptibility. The NMR module used to measure the target polarization, employed both phase and magnitude monitors. The magnitude detector is used to aid setting-up of the system, the phase sensitive detector is then used for polarization measurements.

2.4.2 Target Monitor Counters

In the $\Delta\sigma_T$ configuration the general expression for an intensity measurement when a polarized beam and target are used is obtained from equation 1.8.1 .

$$I(\theta) = I_o(\theta)\Big(1 + P_B P(\theta) + P_T P(\theta) + P_B P_T A_{NN}(\theta)\Big) \qquad 2.4.4$$

where θ is the scattering angle. By combining intensity data measured from runs with reversed beam or target polarizations to eliminate the unknown term $I_o(\theta)$, the target polarization can be obtained. The combining of runs with opposite target polarizations but the same beam spins, is less prone to systematic errors as shown in section 5.4.

To obtain an absolute value of P_T the counters monitoring the intensity have to view an angular range where $P(\theta)$ and $A_{NN}(\theta)$ are known absolutely over the whole energy range. $P(\theta)$ at 24^o_{LAB} has been determined to ±1.5% by a previous BASQUE experiment (2.12) in the range 200 to 520MeV. The appropriate values of A_{NN}, around 24^o_{LAB} can be predicted by the BASQUE phase shift analysis with estimated maximum errors of ±2% at 200MeV rising to ±5% at 520MeV. The target monitors were therefore to monitor around 24^o_{LAB}.

In the $\Delta\sigma_L$ configuration for a purely longitudinal polarized beam and target, the number of scattered protons is given by

$$I(\theta) = I_o(\theta)\left(1 + P_B P_T A_{LL}(\theta)\right) \qquad 2.4.5$$

The situation is, however, complicated by the variation of the precession angle of the spin with energy, due to the fixed bend angle of 35^o. This introduces an extra component dependent on A_{SL},

$$I(\theta) = I_o(\theta)\Big(1 + P_B P_T\left(\sin\phi_\theta A_{LL}(\theta) + \cos\phi_\theta A_{SL}(\theta)\right)\Big) \qquad 2.4.6$$

where ϕ_θ is the precession angle caused by the 35^o bend. The largest contribution to the term dependent on $P_B P_T$, in the equation is from A_{LL} as ϕ_θ is approximately 90^o.

In the $\Delta\sigma_L$ configuration the target has a total opening angle of 100^o in the horizontal plane. The opening angle is restricted by the support structure of the magnetic coils. This geometry leads itself to monitoring of the scattered and recoil protons at 90^o centre of mass (C M), using a double arm monitor. The value of

A_{LL} at $90^{o}_{C\,M}$, however, becomes small at the higher energies. At 520MeV the value is approximately 0.18, while at 200MeV it is approximately 0.84. The small value at the higher energies leads to a small change in scattered intensity on reversal of P_B or P_T.

To improve the determination of P_T, protons scattered at approximately $70^{o}_{C\,M}$ were to be monitored. At this angle the value of A_{LL} is approximately double that at $90^{o}_{C\,M}$, for energies greater than 460MeV, with an equivalent decrease in percentage error of A_{LL}. The values of A_{LL} at 70^{o} and $90^{o}_{C\,M}$ are listed in table 2.1, for the six energies at which $\Delta\sigma_L$ was eventually measured.

To monitor the scattered protons at approximately $70^{o}_{C\,M}$ the target structure was rotated by 12^{o}. The target cell, however, remained aligned along the beamline axis.

This 12^{o} rotation leads to a 2% decrease in absolute longitudinal polarization of the target. It also introduces an extra term into the intensity formula arising from an A_{SS} component. The rotation also changes the coefficients of both A_{LL} and A_{LS}. The target coils were rotated to the left looking down the beamline, so the forward monitor was to the right of the beamline. The intensity is now given by

$$I(\theta) = I_o(\theta)\Big(1 + P_B P_T\big(\alpha A_{LL}(\theta) - \beta A_{SS}(\theta) + \gamma A_{SL}(\theta)\big)\Big) \qquad 2.4.7$$

where $\alpha = \sin\phi_B \cos 12^{o}$

$\beta = \cos\phi_B \sin 12^{o}$

$\gamma = \cos(\phi_B + 12^{o})$

BEAM ENERGY (MeV)	$A_{LL}(70)$	$A_{LL}(90)$
202.7	0.859	0.837
325.1	0.715	0.643
419.5	0.351	0.220
455.7	0.297	0.169
497.1	0.320	0.183
515.2	0.307	0.176

TABLE 2.1 PHASE SHIFT PREDICTIONS OF A_{LL} AT $70^{o}{}_{CM}$ AND $90^{o}{}_{CM}$ WITH MAXIMUM ERRORS OF APPROXIMTELY $\pm$ 0.006

Taking intensity data with both beam polarizations with P_T fixed, allows the term $I_o(\theta)$ to be eliminated. The phase shift predictions of A_{LL}, A_{SS} and A_{SL} are then used to calculate the value of P_T.

The intensity of hydrogen events, I_H, scattered into a counter subtending a solid angle, $\Delta\Omega$, to the target of length, L, and hydrogen density, ρ_H, is given by

$$I_H = I_o \left(\frac{\partial\sigma}{\partial\Omega}\right) N_A \Delta\Omega L \rho_H \tag{2.4.8}$$

where $\left(\frac{\partial\sigma}{\partial\Omega}\right)$ is the differential cross section for p-p scattering:

N_A is the Avogadro constant. In the energy range 200 to 520MeV the differential cross section at θ_{LAB} ; around 35^o ; is approximately constant at 16mb/sterad. The target cell was approximately 2.4cm long and the expected hydrogen density was 0.07gm/cm^3. Using an incident beam rate of 10^5 sec^{-1} the forward scattered intensity from hydrogen events was expected to be

$$I_H \sim 160\, \Delta\Omega \mathrm{sec}^{-1} \tag{2.4.9}$$

The target structure allows a nearest approach for a counter of approximately 38cm. At this position a 1cm^2 counter would have a count rate of approximately 400 per hour. To give acceptable rates, therefore, large counters were required.

Large monitors count true p-p elastic and quasi elastic events. This background contamination needs to be subtracted out, requiring the use of high resolution counters. The experiment used

20cm square delay line wire chambers to detect both the forward and recoil protons. The chambers had 2mm wire spacing in both the horizontal and vertical planes. The background contamination could be removed by an offline analysis.

In the $\Delta\sigma_T$ configuration, two double arm monitors could be incorporated; for $\Delta\sigma_L$ the target geometry permitted only one double arm monitor to be fitted.

2.5 Beam Polarization Measurements

The measured intensity at an angle θ for a transversly polarized beam, scattered from an unpolarized target is, from equation 1.8.1

$$I(\theta) = I_o(\theta)\ (1 + P_B P(\theta)) \qquad 2.5.1$$

The sign of $P(\theta)$ is defined as positive (negative) for an event involving a forward scatter to the left (right), looking down the beamline. The monitor of beam polarization to be used in this experiment monitored protons scattered at an angle of 26^o to the left and right of the beamline simultaneously. The equations for the scattered intensity to the left (L) and right (R) are

$$L = I_o(\theta)\ (1 + P_B P(\theta)) \qquad 2.5.2$$

$$R = I_o(\theta)\ (1 - P_B P(\theta)) \qquad 2.5.3$$

from which one defines an asymmetry, ε,

$$\varepsilon = \frac{L - R}{L + R} = P_B P(\theta) \qquad 2.5.4$$

Thus a measurement of the asymmetry, ε , leads to a value of P_B if $P(\Theta)$ is known. The monitor of beam polarization had been previously calibrated to give beam polarizations to ±1.5% (2.12).

The monitor of beam polarization also measures beam intensities, the sum, L + R, being proportional to the beam rate.

2.6 Beam Rates

Two factors determined the acceptable beam rate for the experiment. The first was the rate at which the scintillator counters monitoring the beam incident upon, and transmitted by, the target could count. The expected maximum beam rate these counters could tolerate was $\sim 10^6$ protons per second.

The other limiting factor was the random correction to the transmission. The target cell was approximately 2.4cm long with an expected hydrogen density of $0.07 g/cm^3$. Using $P_T = P_B = 65\%$ and $\bar{t} = 1.0$, then from equation 2.1.7 a value of $\Delta\sigma = 0.2mb$ corresponds to a Δt of one part in 10^5. It was therefore necessary that corrections to the transmission for accidental coincidences could be made to at least this precision.

The overriding majority of accidental coincidences between the counters monitoring the beam incident upon, and transmitted by, the target occur due to beam bursts containing two protons. The TRIUMF cyclotron produced a beam burst every 43nS. At a beam rate of $10^5 sec^{-1}$

there was a 1 in 230 chance of a proton in each beam burst. The probability of two protons in a radiofrequency bucket is 1 in 5.3×10^4. In one second there are therefore, approximately 430 double proton events, and 10^5 single proton events. The correction to the transmission, t, for randoms is r(1-t), where r is the ratio of the random rate to the incident beam rate; the transmission was expected to be approximately 97%. The random correction to the transmission was, therefore, expected to be approximately 1×10^{-4}.

Previous experience at TRIUMF had shown calculated and measured randoms to be in agreement to $<1\%$. To keep random corrections to an acceptable level, therefore, beam rates of approximately 10^5 sec^{-1} were required. The TRIUMF polarized ion source was adjusted to supply similar beam currents for both up and down polarization. The random corrections to transmissions for up and down were, therefore similar, and thus had a smaller effect on the transmission difference, Δt, than on the individual transmissions.

The minimum stable intensity of the polarized H^- beam in the TRIUMF cyclotron was approximately 10^{11} sec^{-1}. By using a thin wire stripper 0.1% of the circulating beam can be extracted, giving a beam rate of 10^8 sec^{-1}. It was therefore necessary to incorporate a collimator in BL4C to reduce the beam rate by a factor of 10^{-3}.

CHAPTER 3 EXPERIMENTAL APPARATUS

3.1 The TRIUMF Cyclotron

The TRIUMF laboratory (3.1) has a six sector focussing cyclotron, which accelerates H^- ions, fig 3.1 (3.2) The ions are injected at 300KeV. Inside the cyclotron the ions are accelerated by an 85KV radiofrequency field operating at 23.05MHz, leading to a beam burst every 43nS. The radiofrequency field is applied via 80 sections of $\frac{1}{4}$ wave length resonators; the total radiofrequency power dissipated is 1.2MW.

The H^- ions are used for ease of extraction, which is the usual problem in circular accelerators. Extraction from the TRIUMF accelerator is by insertion of a carbon or aluminium foil into the circulating beam at the orbit corresponding to the required extracted energy. The foil strips the electrons from the H^- ion to leave a proton which is bent out of the accelerator. Using this method TRIUMF is able to extract two independent beams from the cyclotron by using two strippers placed 180^o apart. One beam is directed to the Meson hall, and used for π production, the other to the Proton hall. The energy of the beam is determined to approximately 1MeV by an accurate field map and the (r,θ) position of the stripper foil.

The second electron, in the H^- ion, with a binding energy of 0.75eV, is easily stripped by collisions with residual gas molecules and by the effect of strong magnetic fields. The vacuum of the

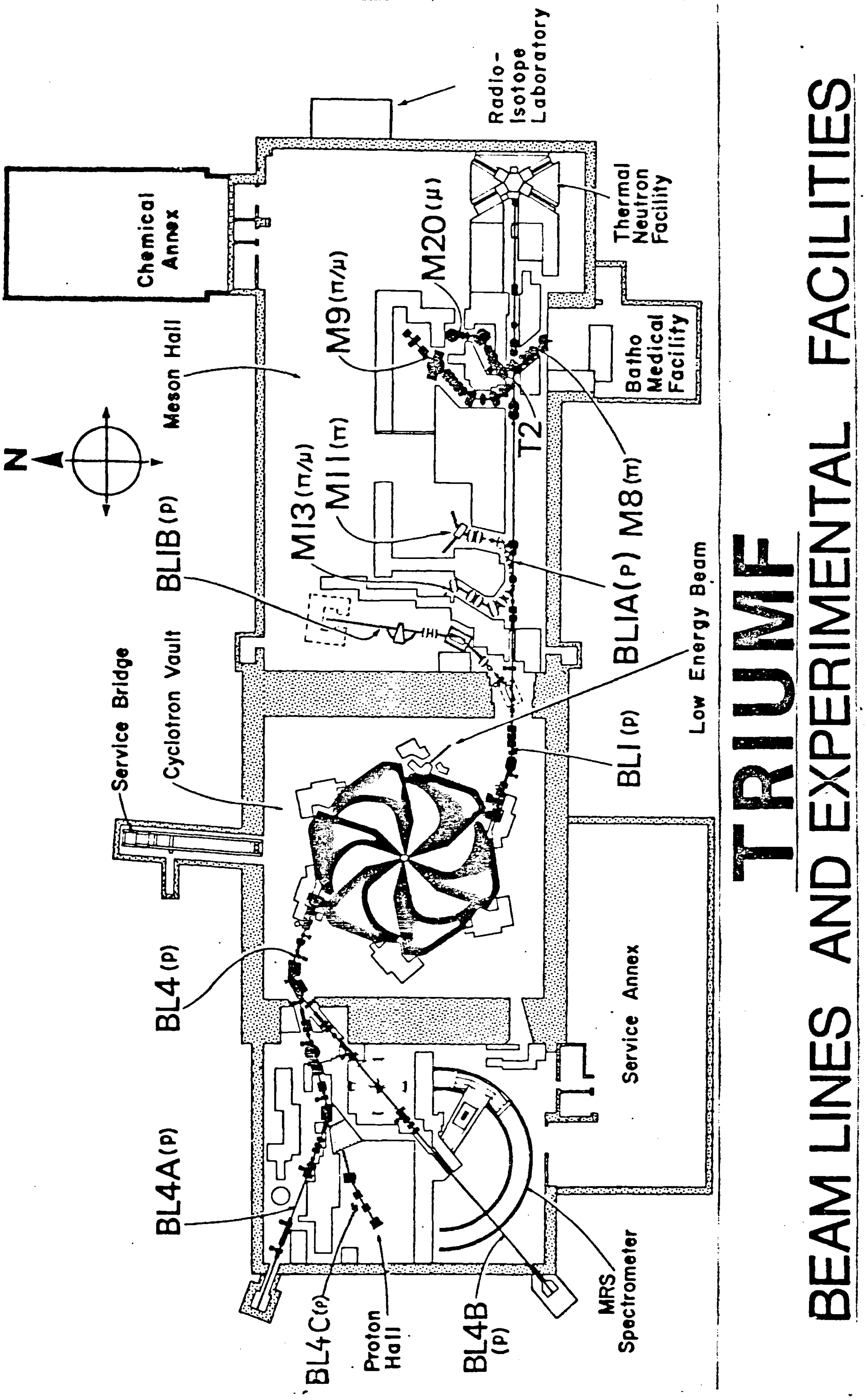
TRIUMF
BEAM LINES AND EXPERIMENTAL FACILITIES
N
Chemical Annex
Radio-Isotope Laboratory
Meson Hall
Thermal Neutron Facility
M20(μ)
M9(π/μ)
Batho Medical Facility
T2
M8(π)
M13(π/μ)
M11(π)
BL1B(P)
BL1A(P)
Low Energy Beam
BL1(P)
Service Bridge
Cyclotron Vault
Service Annex
BL4(P)
BL4A(P)
BL4C(P)
Proton Hall
BL4B(P)
MRS Spectrometer

FIGURE 3.1

accelerator's cavity (17m in diameter x 0.5m) is kept at 10^{-7} torr. The magnetic field is kept at less than 0.58T leading to a physically large radius magnet.

Each of the cyclotron's sections weighs 610 metric tonnes. Despite this weight the entire upper half of the cyclotron can be elevated 1.2m allowing access into the vacuum tank. Above and below the vacuum tank are 54 concentric trim coils which are used to correct the magnetic field.

The $\Delta\sigma_L$ and $\Delta\sigma_T$ experiments were to be performed in the Proton hall. Beamline 4 (BL4) which supplies the Proton hall, is split into two experimental beamlines, BL4A and BL4B. The special requirements of the $\Delta\sigma_L$ and $\Delta\sigma_T$ experiments required the installation of a new beamline, BL4C, which was to use elements of BL4A. This beamline, BL4A, used a 35° bending magnet which if not energised directs the beam through a large neutron collimator. BL4C was to be built onto the exit of this collimator.

3.2 TRIUMF Polarized Ion Source

The TRIUMF polarized ion source (POLISIS) (3.3) produces 500eV H^- ions. These are supplied to a 300KV injection line which takes the beam to the main accelerator.

POLISIS operates using the Lamb-shift method (3.4) employing Sona crossing (3.5) to enhance polarization.

The polarized source is constructed of four modules, each one being 25cm square and serviced by a 15cm diffusion pump.

In the first module, incident protons enter a caesium oven at $85^{\circ}C$. A fraction of them undergo a resonant charge exchange to produce a neutral metastable hydrogen atom in the $2S_{1/2}$ state.

$$Cs + H^{+} \rightarrow Cs^{+} + H(2S_{1/2})$$

Situated at the exit of module 1 is a solenoid which produces an axial field of 0.0575T. In this field the $2S_{1/2}$ state splits into four separate energy states. The two lowest energy states are at the same energy as the $2P_{1/2}$ highest energy states. Application of a crossed electric field of 10V/cm produces the transition $2S_{1/2} \rightarrow 2P_{1/2}$. The $2P_{1/2}$ state quickly decays to the ground state hydrogen atom.

Module 2 contains a similar solenoid and crossed electric field . The second solenoid produces a field of 0.0575T in the opposite direction to the first. This rapid reversal of fields causes the hydrogen atoms with both electron and nuclear spins aligned along the field direction, to flip and align antiparallel to the new applied field. At the full field of 0.0575T the $2S_{1/2}$ and $2P_{1/2}$ states mix and the antiparallel states are quenched. This now leaves only one species of metastable hydrogen with electron magnetic moment parallel and nuclear magnetic moment antiparallel to the applied field. There also exist a large number of ground state hydrogen atoms.

In module 3 the beam passes through argon contained in a solenoid. The effect of the argon is to produce a resonant charge exchange.

$$H(2S_{1/2}) + Ar \rightarrow H^{-} + Ar^{+}$$

The H^{-} ions then enter module 4. This final module contains lenses to adjust the phase space of the H^{-} beam to that required by the 300KV acceleration tube.

The acceleration tube contains only electrostatic elements apart from a Wein filter. The stray fields from the cyclotron rotate the polarization vector of the H^{-} beam . This rotation is compensated for by the Wein filter which uses crossed magnetic and electric fields. The protons reach the accelerator with their polarization orientated vertically. The direction of orientation can be either up or down, reversal of polarization is acheived by solenoid field reversals and takes approximately one second. The polarization orientation can be controlled manually or POLISIS can be programmed to deliver a set sequence of polarized and unpolarized beam.

3.3 Monitor of Beam Polarization

The primary beam polarization monitor had been designed for use in a double scattering experiment(2.12) to determine the P-P polarization parameter, P, at 24^{o} LAB with an absolute normalization of 1.5% at five energies between 200 and 520MeV.

The monitor used scintillator counters to detect protons scattered elastically from the hydrogen in a polythene film. The scattered protons were detected in coincidence with the target recoil proton. Although the calibration of P was performed at 24° LAB the polarimeter monitors forward scattered protons at 26°, however, phase shift analysis can be used to predict P at this angle with an uncertainty of < 0.001.

Each detector arm consisted of a scintillator telescope, an elastic hydrogen scattered event being signalled by a four fold coincidence in the forward and recoil arms. The polarimeter is shown schematically in fig 3.2, the electronic logic used to derive the scaler outputs from the polarimeter is depicted in fig 3.3. The signals from the photo multiplier tubes were routed to the BASQUE experimental trailer which was situated just outside the Proton hall. Here the signals were discriminated before entering the fast logic circuits.

The forward arms used 32 x 30mm scintillators in the front, and 51 x 20mm in the rear, separated by 250mm. The recoil arms used 41 x 49mm and 99 x 70mm in front and rear respectively, with the same separation. All scintallators were 1.5mm thick. The solid angle of acceptance was determined by the forward telescope of each arm, whose centre line made an angle of 26° with respect to the beam line axis. Recoil protons were detected at the conjugate angle.

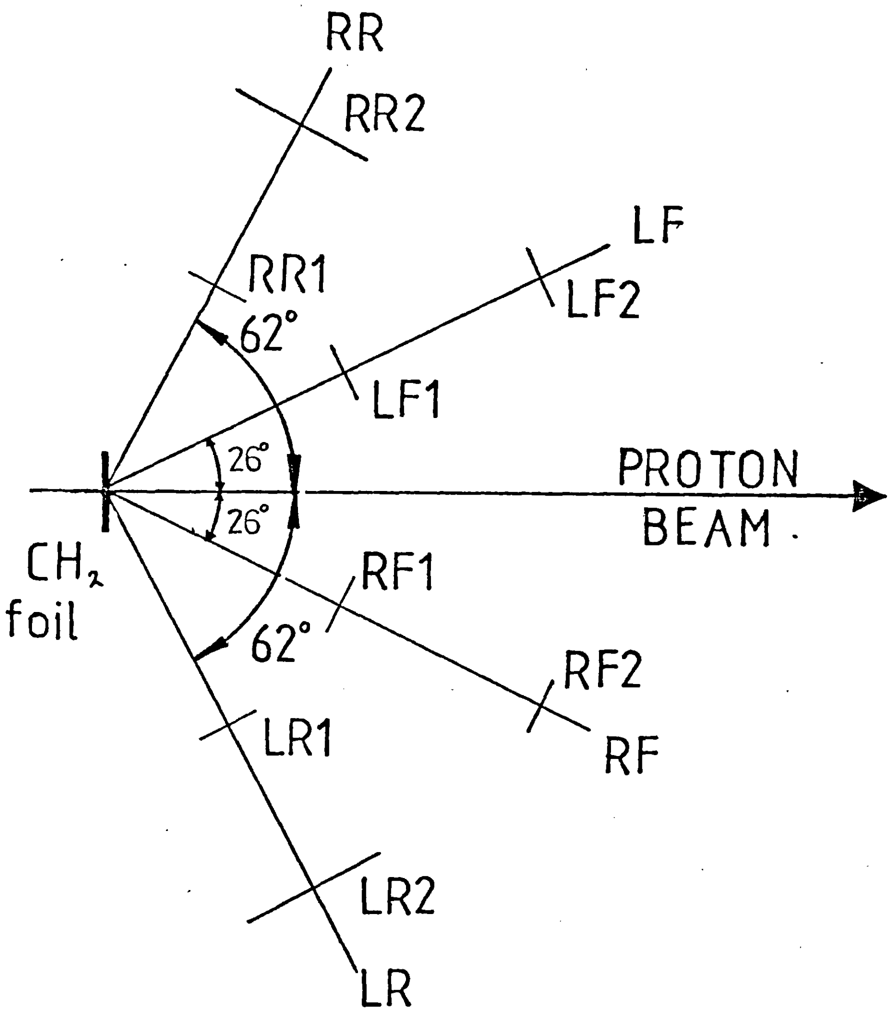

Scintillator Notation

1st letter	2nd letter	Number
L left	F front	1 front
R right	R recoil	2 back

FIGURE 3.2 SCHEMATIC OF BEAM POLARIZATION MONITOR

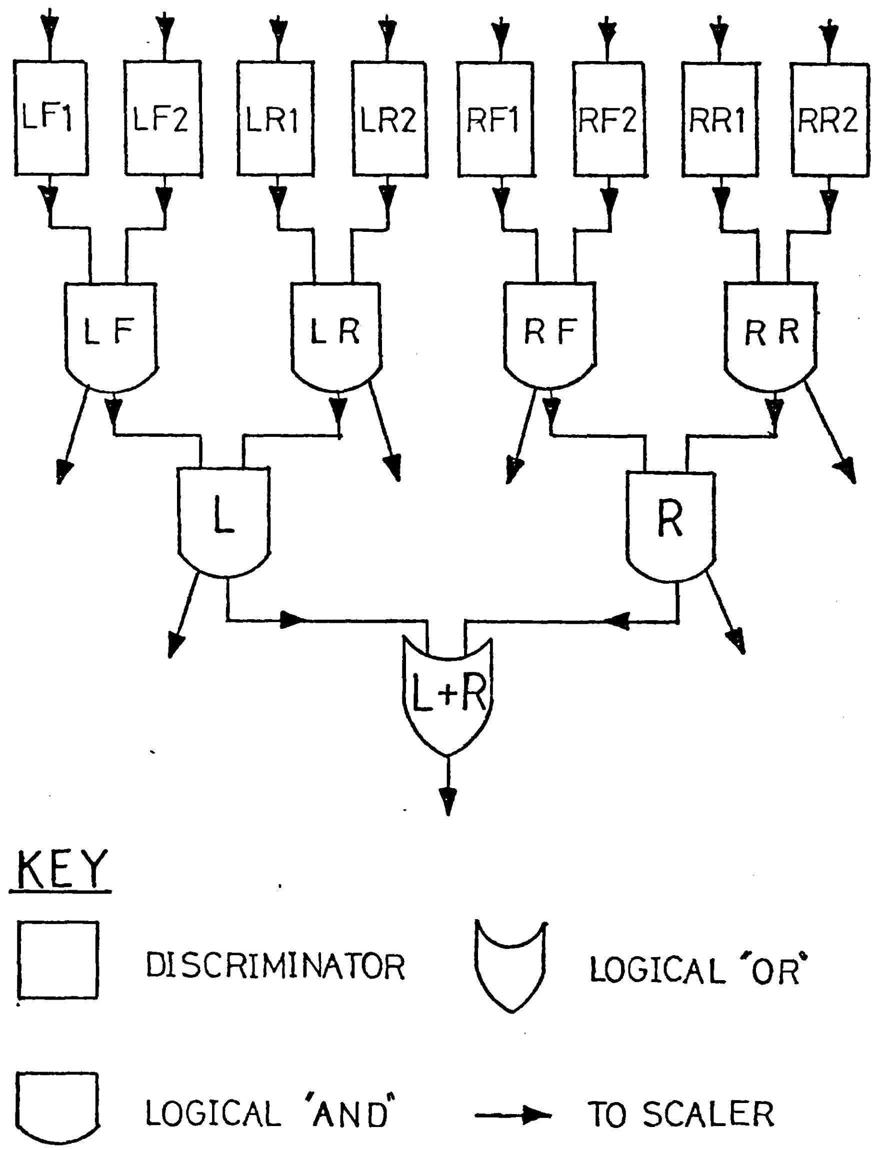

FIGURE 3.3 ELECTRONIC LOGIC OF BEAM POLARIZATION MONITOR

Beam polarizations were calculated using

$$P_B = \frac{\mathcal{E}\ fc}{P(26^o)} \qquad 3.3.1$$

which is equation 2.5.4 incorporating a factor fc to allow for contamination due to background events arising from carbon. This factor is always less than 6%, the correction factor, for the run energies is listed in table 3.1, together with values of $P(26^o)$.

Previous experiments had determined the constant of proportionality between the incident beam rate and the sum of left and right events. A beam rate of 1nA, using 1.6mm thick polythene foil, gave a $(L + R)$ count rate of 1.2×10^4/sec.

3.4 Superconducting Solenoid

The superconducting solenoid was constructed for use in earlier BASQUE experiments and is well described by G. Gallagher Daggett and others [3.6]. It consists of five individual windings giving a total length of 1m with a bore of 14cm, fig 3.4.

The solenoid is supported inside a helium cryostat, which in turn is supported by a liquid nitrogen bath and a vacuum vessel. Pre-cooling to LN_2 temperatures takes approximately ten hours, a further seven hours is required to cool to operating temperatures. It uses about two litres of helium an hour, and a further one litre for each current reversal, an operation taking less than one minute.

T (MeV)	$P(26^o)$	fc
209.0	0.268	1.031
330.1	0.331	1.050
379.2	0.342	1.054
423.7	0.353	1.056
459.8	0.367	1.056
501.0	0.397	1.056

TABLE 3.1 $P(26^o)$, THE P-P POLARIZATION PARAMETER, AND THE CARBON BACKGROUND CORRECTION FACTOR, fc, AS A FUNCTION OF PROTON LAB. ENERGY T

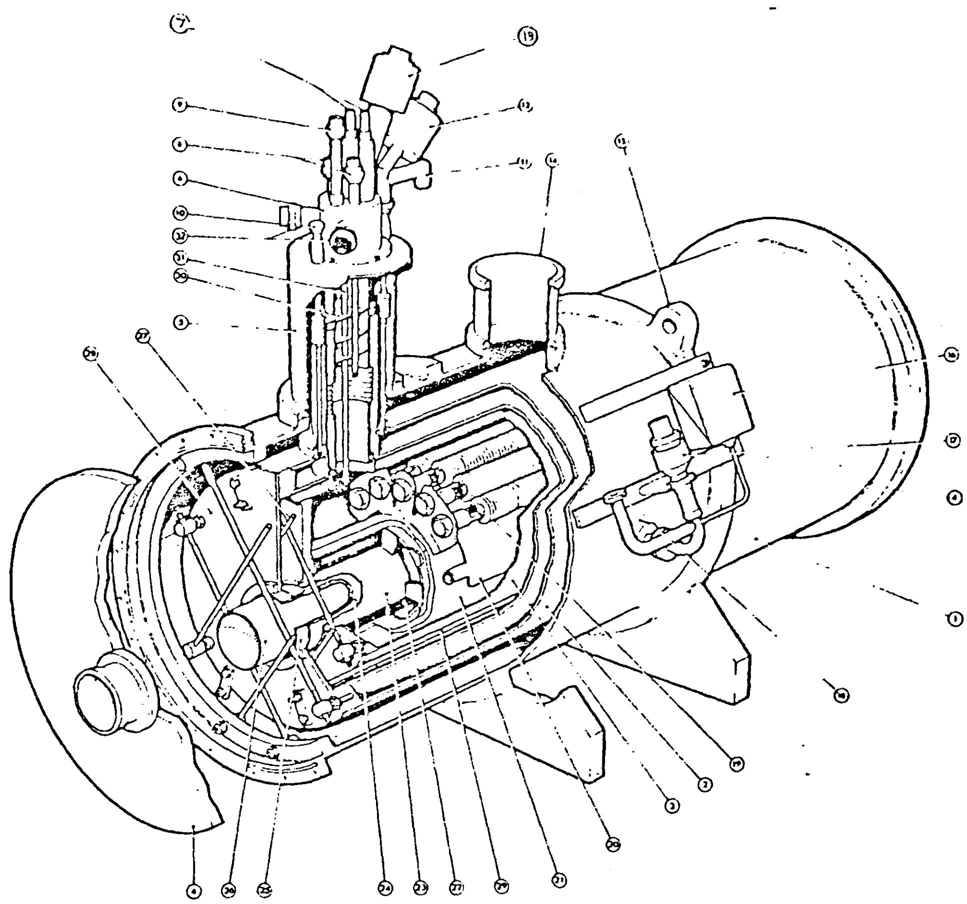

1. CRYOSTAT VACUUM VESSEL
2. LN_2 COOLED RADIATION SHIELD
3. HELIUM VESSEL
4. VACUUM VESSEL END PLATES
5. SERVICES TURRET
6. SERVICE TURRET TOP HAT
7. CURRENT LEADS
8. NITROGEN PRE-COOLER INLET/OUTLET
9. LIQUID HELIUM TRANSFER ENTRY
10. LIQUID NITROGEN TRANSFER ENTRY
11. NITROGEN VENT-RADIATION SHIELD
12. INSTRUMENTATION CONNECTOR-LN_2 COOLED RADIATION SHIELD
13. INSTRUMENTATION CONNECTOR-He VESSEL
14. VACUUM VESSEL PUMPING PORT
15. LIFTING EYES ON CRYOSTAT REINFORCING HOOP
16. PRESSURE SWITCH
17. PRESSURE BURSTING DISC
18. PRESSURE RELIEF VALVE (NOT SHOWN)
19. PROTECTION RESISTORS
20. PRE-COOLING HEAT EXCHANGER
21. SOLENOID (AL. ALLOY) SUPPORT CYLINDER
22. SOLENOID WINDING (FIRST OF 5 SECTIONS)
23. HELIUM VESSEL INNER CYLINDER
24. SUPER INSULATION IN VACUUM SPACE
25. LN_2 COOLED RADIATION SHIELD INNER CYLINDER
26. VACUUM VESSEL INNER CYLINDER
27. HELIUM VESSEL SUPPORT STRUTS
28. LN_2 COOLED SHIELD END PLATE SHOWING SUPPORT STRUTS
29. LN_2 COOLED RADIATION SHIELD OUTER CYLINDER
30. RADIATION SHIELDS
31. CURRENT LEADS-VAPOUR COOLED-OTHER SERVICES NOT SHOWN
32. HELIUM VENTS

FIGURE 3.4 BASQUE SUPERCONDUCTION SOLENOID

The path integral had been evaluated as 5.919298T at 210A. Equation 2.2.1 can be rewritten to relate the current required to precess the proton spin through 90° to the lab momentum

$$I = 0.06656\, p_{LAB} \tag{3.4.1}$$

where I is in amps and p_{LAB} is in units of MeV/c. The maximum proton energy of 520 MeV (1116MeV/c) requires an excitation current of 74.28 amps to precess the spin by 90°. The current was remotely controlled from the electronics trailer.

3.5 Bending Magnet

The bending magnet used for these experiments was originally designed at the University of California, Los Angeles (UCLA), as a cyclotron magnet to accelerate protons to a maximum of 50MeV.(3.7)

The magnet has a total weight of 40 tonnes and overall dimensions 2.7m x 1.6m x 1.4m, with a pole diameter of 1.2m and normal pole gap of 20cm.

Test of the UCLA magnet showed its path integral to be too small to bend beams above 375MeV by the 35° required. The maximum central field was measured as 1.35T with the power supply running at its maximum of 2400 amps. The section of beam pipe running through the UCLA magnet was 15cm in diameter, 2.5cm thick shims where attached to the magnet around the beam pipe. These shims raised the central field to 1.8T at full power supply output, sufficient to bend a beam of 520MeV.

3.6 Polarized Target

The dynamically polarized target was designed and built at Liverpool University. It had previously been used to investigate neutral pion production (3.8)(2.9).

The large magnetic field required by the target, approximately 2.5T, was obtained by using two superconducting coils in a Helmholtz configuration. By employing this arrangement, access to the target is acheived both axially and in the median plane between the coils. To keep the coil supports as small as possible, stainless steel was employed in their construction. The coil geometry showing the available access to the target is shown in fig 3.5. The target design allowed for the coils to be rotated to give a field orientated vertically or horizontally, a process taking a couple of days to complete. The compressive forces generated by the superconducting coils were contained by three aluminium wedges, positioned between them. Additionally, in the $\Delta\sigma_T$ arrangement, the external target structure was supported by a number of moveable brass posts.

To acheive the required central magnetic field of approximately 2.5T, currents of 52A were required. To keep the magnetic absorption on resonance throughout the target, the magnetic field must be kept constant across the target volume. This requirement is met if the variation in field is no greater than apporximately 1 part in 10^4. Calculation and measurement had shown this requirement to be fulfilled for approximately ± 0.75cm along the

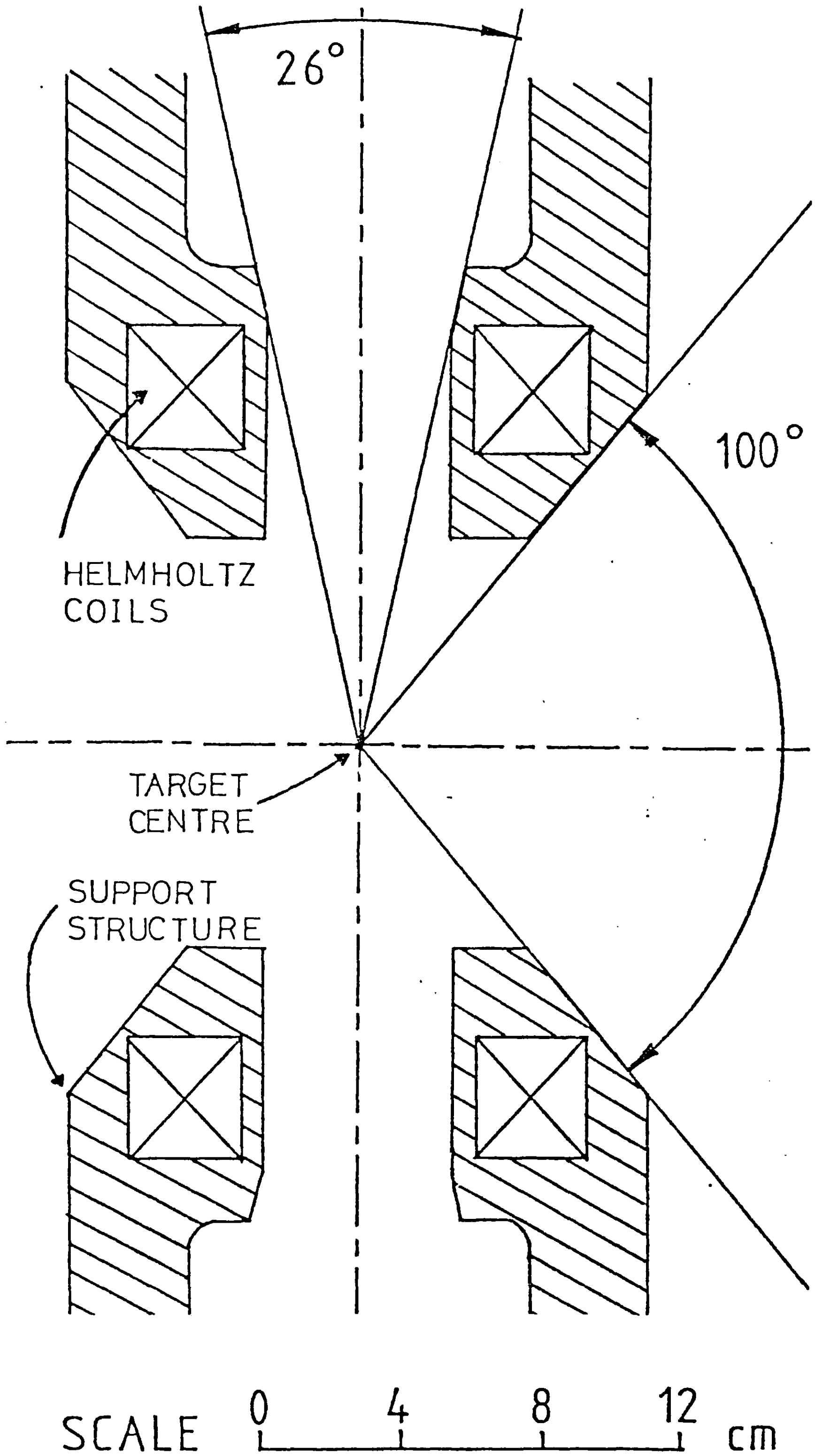

FIGURE 3.5 TARGET STRUCTURE SHOWING ACCESS TO TARGET, VIEWED ALONG HELMHOLTZ COILS

magnet axis from its centre, and approximately $\pm$ 1.2cm along a trajectory perpendicular to the magnet axis. This therefore defines the maximum target dimensions as being a cylinder 2.4cm in length and 1.5cm in diameter [3.9].

The target employs a He^3 evaporation refrigerator to achieve its working temperature of approximately 0.9K, which is measured by the monitoring of helium vapour pressure. The refrigerator and the superconducting coils are thermally isolated from the ambient temperature by a LN_2 bath and a vacuum chamber. To miminise the amount of material in the beam path, the functions of microwave cavity and vacuum isolation tube for the He^3 refrigerator were combined in a single aluminium alloy tube, 0.2mm thick. Beam access to the target's vacuum chamber was via 0.03cm mylar windows. Great care had to be employed with the magnet energised to ensure that loose pieces of steel and tools did not rupture the mylar windows. When the magnet was energised a yellow flashing warning light was activated. A section through the polarized target is given in fig 3.6.

At a temperature of 0.5K and a static field of 2.5T microwave frequencies of 70 and 70.2GHz are required to polarize the target. The microwave power generated by a klystron was supplied to the target via a waveguide with a variable attenuator. Provision was made for the output of the klystron to be dumped.

The target was supported by an aluminium table bringing the target cell up to beamline level, 1.37m above the floor. The magnet's

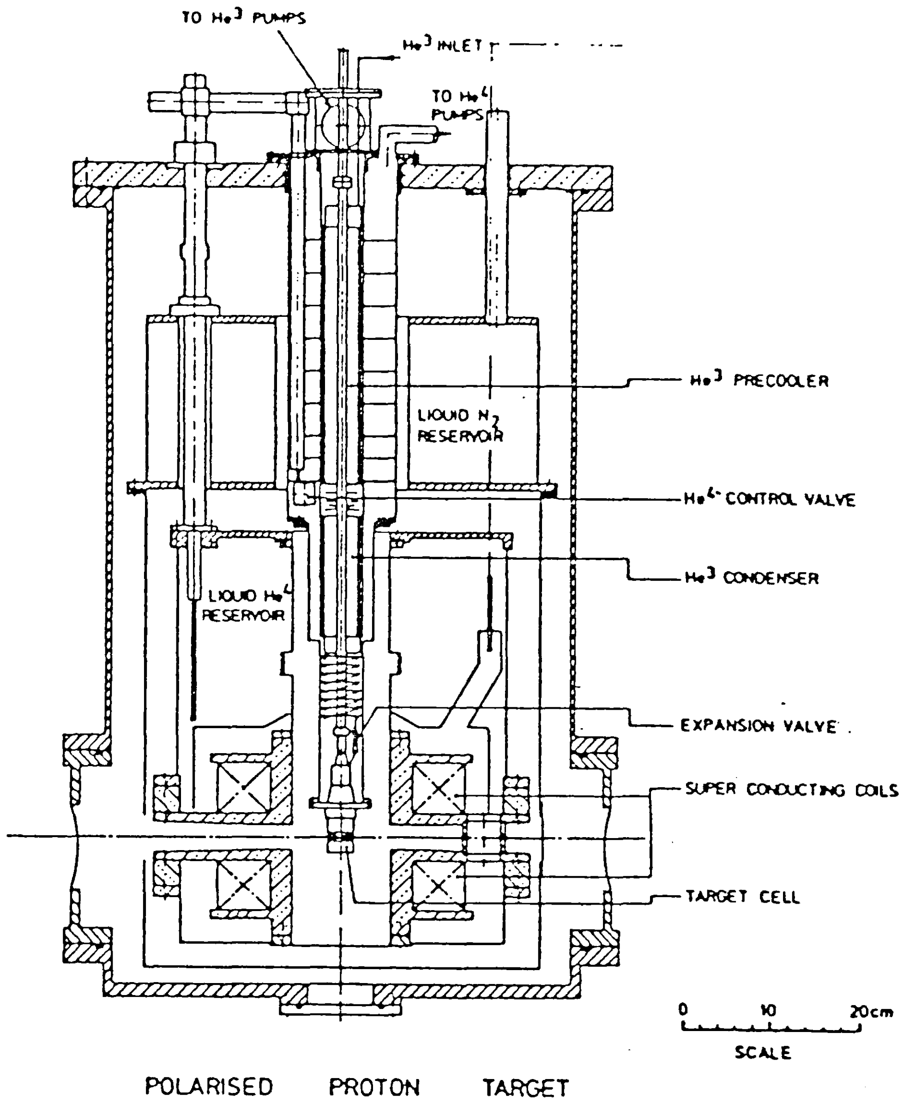

FIGURE 3.6 SECTION THROUGH THE POLARIZED TARGET

power supply and the klystron were mounted next to the target and any adjustments to them had to be made from inside the Proton hall. Visual indicators of helium and nitrogen bath levels, together with an audible warning for low levels, were mounted in the trailer. The time between refils varied according to the amount of microwave power input to polarize the target, but was generally required at twelve hourly intervals.

A close up view of the target cell is shown in fig 3.7. The target was contained in a fluorinated ethylene-propylene copolymer, (FEP) casing. FEP is used as it contains no hydrogen. As the target was operated with the magnetic field in two orthogonal directions, two NMR coils were needed to satisfy the requirement that the radiofrequency magnetic field direction should be perpendicular to the static field. In the $\Delta\sigma_T$ configuration, a solenoid type NMR coil, with its axis parallel to the beam direction was used. For $\Delta\sigma_L$ a saddle shaped coil was used. The NMR coils were mounted outside the target cell on a perforated FEP former of 20mm in diameter. The coils were made of 0.05mm copper foil, 2mm wide.

3.7 Butanol As A Target Material

1- Butanol ($C_4H_{10}O$) is a widely used target material due to its high free to bound proton ratio (3.2), its relatively high resistance to radiation damage and short polarizing times.(3.10)(3.11)(3.12)

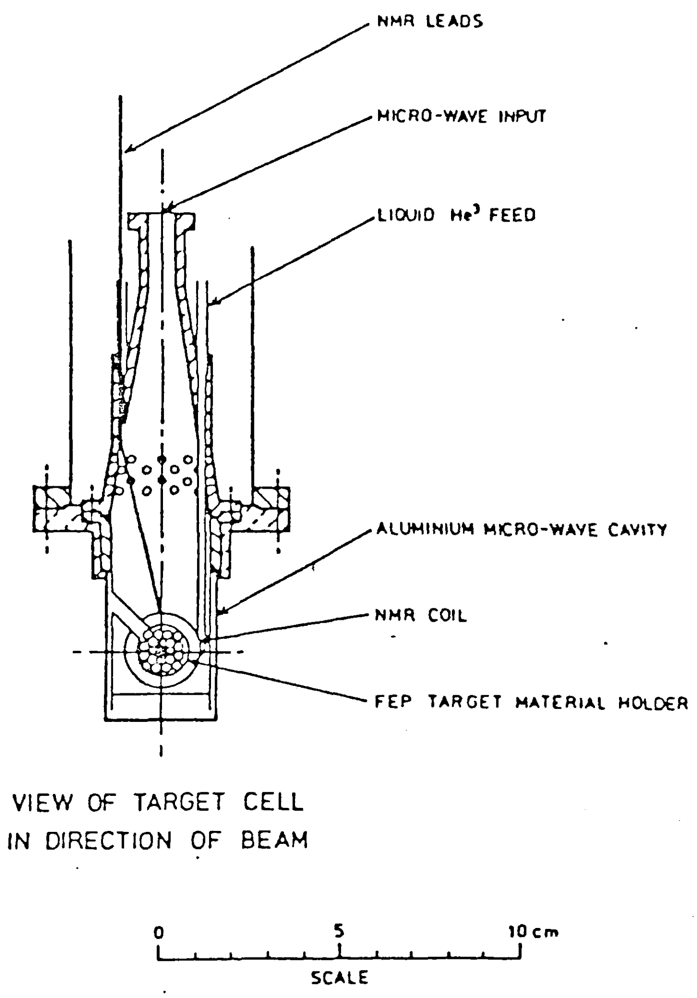

FIGURE 3.7 CLOSE UP VIEW OF THE TARGET CELL

Two target dopants were used, porphyrexide, fig 3.8 ,and sodium bis (2-ethyl-2-hydroxybutyrate) oxochromate (V), fig 3.9 (Cr(V)EHBA), the latter giving better radiation resistance. In the initial test runs the target was doped with porphyrexide. A saturated solution of porphyrexide was prepared by adding ..

3% by weight to the butanol. Dissolved oxygen can interfere with spin dynamics, its concentration is reduced by a factor of approximately 10 by bubbling dry nitrogen through the solution. Addition of 5%, by weight, of water to the mixture increases the acheiveable polarization by increasing the amount of porphyrexide that can be dissolved in solution. In later runs the butanol water mixture was doped with Cr(V)EHBA in a manner similar to that above.

The proton polarization and relaxation rates are both temperature dependent. To keep thermal gradients to a minimum, the target material is produced in beads of diameter 1.0 - 1.7mm. The target beads were manufactured following the procedure laid out in the paper by Ash [3.13]. The target material was driven through a hyperdermic needle using dry nitrogen gas. The drops had an additional force applied to them by a voltage of approximately 2.5KV. For a fixed gas pressure, variation of the voltage controls the size and rate of production of the drops. The beads fall from the needle into a liquid nitrogen bath. The beads retain some of their charge and repel each other while freezing on the surface. As the hyperdermic needle is held approximately 4.5cm above the liquid nitrogen, the flow rate is critical as too slow a rate can lead to the mixture freezing in the needle. The correct

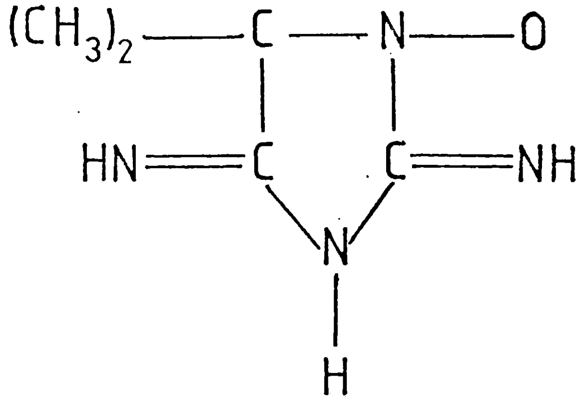

FIGURE 3.8 PORPHYREXIDE

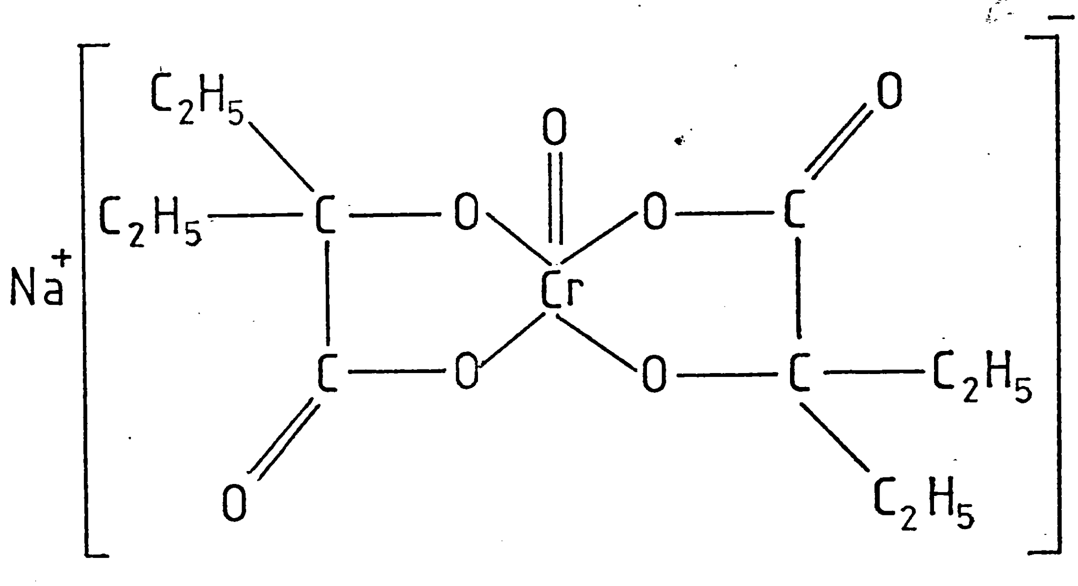

FIGURE 3.9 Cr(V)EHBA

size of beads are obtained with nitrogen pressure of 30-50cm of water with a voltage of 2-2.5KV.

After sufficient beads have been produced they are left for 15 - 20 minutes to lose their static charge, which makes them easier to handle. The beads are collected on the top of two sieves, the top one lets through beads of less than 1.7mm. The beads are gently brushed across the sieve as they need encouragement to pass through the mesh. The top sieve is then removed and the beads brushed across the lower sieve, which lets through beads of less than 1.0mm diameter. It is important to keep the equipment as free from frost as possible so as not to contaminate the target material. The beads are loaded into the target holder through the filling tube, using a funnel.

3.8 NMR Monitor

3.8.1 NMR Module

The NMR module was designed as a complete low noise, high quality, detection and amplification unit. The whole system is mounted inside a copper box to minimise pick up, and maintain a constant operating temperature. The module is split into five separate units to isolate the individual detection and amplification systems. Each unit is mounted on a separate PCB inside the copper box, fig 3.10.

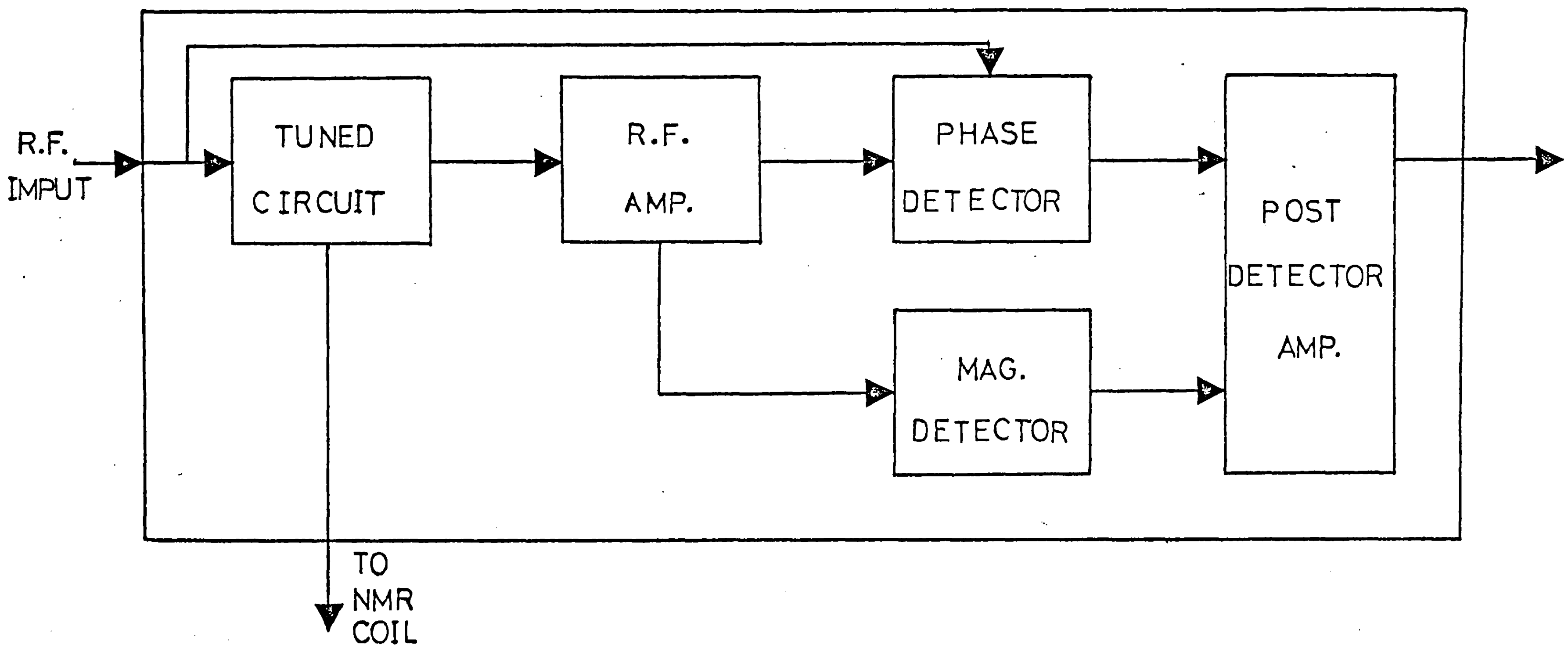

FIGURE 3.10 NMR DETECTION AND AMPLIFICATION UNIT

3.8.2 Microprocessor Based NMR System

The NMR module was incorporated in a complete digital microprocessor based NMR system. (3.14)

The radiofrequency source, used for exciting the NMR probe, was a remotely programmed Rockland frequency synthesiser, with a frequency range of 1KHz to 170MHz, and a variable output level. The control system was set to sweep the radiofrequency applied to the NMR probe, around a central frequency in ± 127 steps, with step intervals variable from 1 - 99KHz. When the sweep has finished the Rockland's output is automatically switched to its lowest level, one complete scan takes 80 microseconds. The voltage levels at each sampled frequency, or the phase difference are converted via an ADC to a 256 word array. The array was displayed on a CRT to show the variation of voltage, or phase difference, in the circuit, with changing frequency. There is provision for up to sixteen individual sweeps to be performed and averaged to produce one output. If the noise in the input is random in nature, then averaging the data over sixteen sweeps increases the signal to noise ratio.

3.8.3 NMR Polarization Measurements

The system was set up initially using the magnitude detector. At the normal target operating field and temperature, the nuclear magnetic resonance frequency was $\sim$109MHz, this was set as the centre frequency for the sweeps. With the target polarized, the magnetic field was adjusted so that the nuclear resonance frequency was moved outside the range of the radiofrequency sweep. A frequency sweep now shows the Q curve of the NMR tuned circuit. The tuning capacitor in this circuit was then adjusted to give a symmetric Q curve centred on the centre frequency, which was marked by a cursor on the display. The system was then switched to monitor the phase sensitive output, the capacitor was then tweaked to again centre the Q curve. This was the final value of the tuning capacitor. A sixteen sweep averaged Q curve was then recorded and stored. The target field was then restored to its normal value and a sixteen sweep averaged Q curve recorded.

The polarization is proportional to the area under the absorption curve. This area is given by the difference between the stored background Q curve taken off resonance, and the Q curve taken on resonance, the raw data. The subtraction is performed digitally by the software to give the extracted data, which can be displayed. The area of the extracted data is called the NMR integral.

Any random DC drift in the amplifier results in the raw data curve moving vertically away from the stored Q curve, and this will affect the result of the subtraction. To correct for this, a proportion of the difference between the curves at the fringes is used to adjust the raw data curve before the NMR integral is finally computed.

As with Q curves, the NMR integral can be computed from the average value of up to sixteen evaluations. This averaged value can be updated every 2 - 99 seconds. The last 301 integrals are stored and can be displayed.

To cover the large range of target polarizations, from thermal equilibrium values of approximately 0.3% up to the dynamically enhanced values of approximately 65%, the amplifier was equipped with three gain settings, 1x, 10x and 100x. The amplifier gain, the polarization direction and the NMR integral were transmitted in binary code to the electronics trailer, where there was also a CRT display of the raw data.

In fig 3.11 a raw data sweep, taken at thermal equilibrium, gain x100 is shown. A raw data sweep for a positive enhanced target polarization, gain x1, is shown in fig 3.12. Superimposed upon these figures are the stored background Q curves.

3.9 Beamline Counters

The beam incident upon the target was counted by three scintallator counters. A coincidence between all three counters defined an incident proton, the threefold coincidence effectively removes accidental coincidences. The small size of the target required the beam spot and divergence to be kept as small as possible. The counters were, therefore, placed as close as possible to the target and made of 1mm thick scintillator.

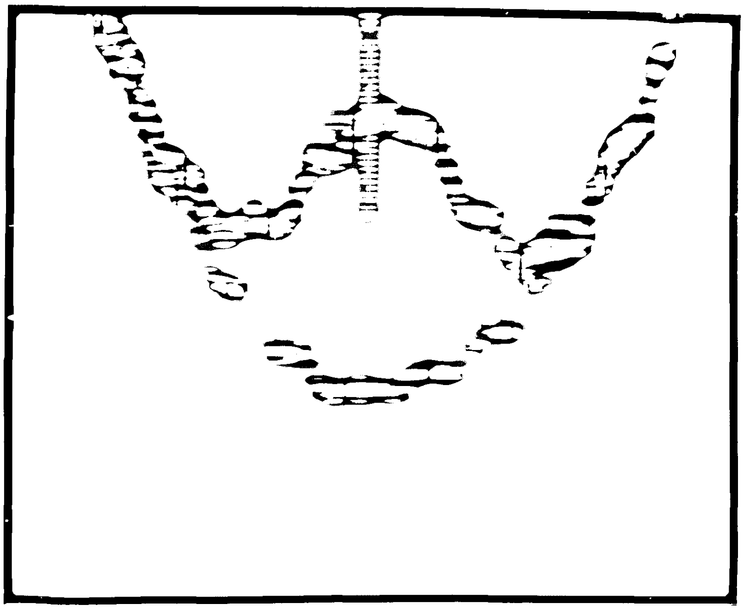

FIGURE 3.11 THERMAL EQUILIBRIUM SIGNAL, TOP TRACE;
Q CURVE, BOTTOM TRACE

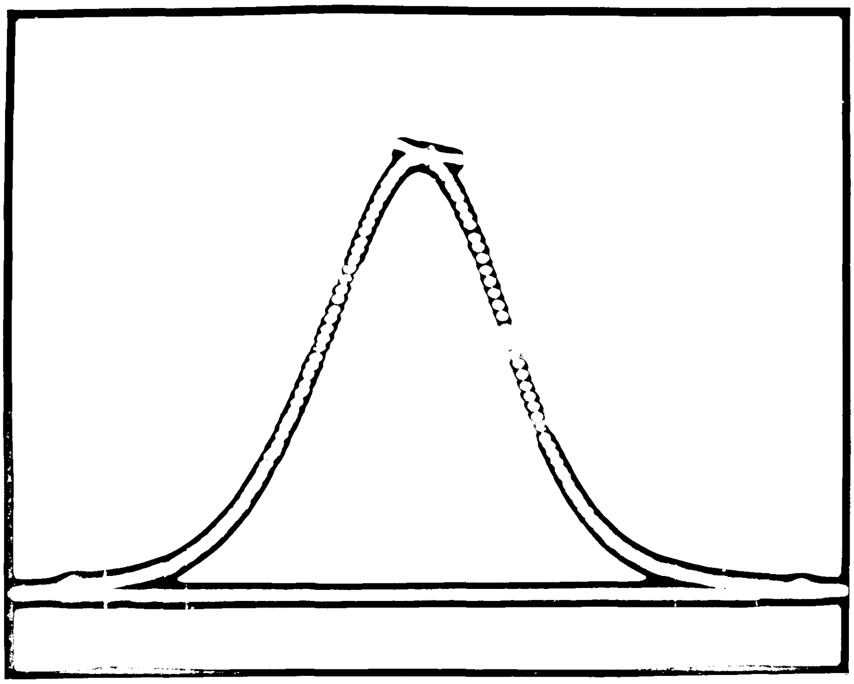

FIGURE 3.12 ENHANCED POSITIVE POLARIZATION SIGNAL, TOP TRACE; Q CURVE, BOTTOM TRACE

The three counters were placed at the end of the evacuated beamline in an air gap of approximately 25cm before the target housing. The counter furthest upstream, S1, and the middle counter, S2, were 1cm apart. S3 was 10cm downstream of S2. The separation of counters S1 and S2 from S3 removed first order cosmic counts.

The counter S1 consisted of two scintillators, each 2.5cm x 1.3cm x 1mm. These were mounted in separate lucite light guides giving a separation of approximately 65cm between the scintillator and the photo multiplier tube (PMT) base. This large separation was required to keep the PMT base away from the high magnetic fields produced by the polarized target coils. The scintillators were individually wrapped and butted together, separated by 0.25mm of double aluminised mylar and 0.13mm of opaque black plastic. Once butted, they were held in clamps which allowed fine horizontal and vertical movement. The counters were surveyed into the beamline with one counter above (S1U), and one below (S1D) the beamline axis. Counter S2 was constructed in exactly the same way, the only difference being that S2 was surveyed into position with one counter to the left, looking down the beamline (S2L), and one to the right, (S2R) of the beamline. Counters 1 and 2 were split to aid centring of the beam and to monitor any beamshifts.

The last counter, S3, was the smallest counter and thus defined the beam. It consisted of a 1cm diameter x 1mm scintillator viewed by an air light guide, to stop false Cerenkov counts. The air light guide was constructed from 5cm diameter black plastic pipe, the inside of which was lined with 0.13mm aluminised mylar. The light pipe was 65cm long to keep the PMT in a low magnetic field region. S3 was supported 3cm above the end of the pipe by a thin wire frame. Various reflective end caps, forming an optical coupling between the scintillator and the light pipe, were tested. One set of tops used 0.025mm aluminised mylar supported by wire frames of various geometries. The most successful designs were self-supporting tops, made from 0.13mm aluminised mylar. The best design was found to be a 10cm high cone with a 2.5cm diameter flat top. S3 was 42cm from the target centre.

The counters S1U, S1D, S2L, S2R and S3 were used to define an incident proton. A count, S123B, defined a good event.

$$S123B = (S1U + S1D) . (S2L + S2R) . S3 \qquad 3.9.1$$

(where + = OR and . = AND)

Monitors of two protons events, S123A, and accidental coincidences, S123C, were incorporated in the electronic logic, fig 3.13.

$$S123A = (S1U . S1D) + (S2L . S2R) . S3 \qquad 3.9.2$$

$$S123C = (S1U + S1D) . (S2L + S2R) . \widetilde{S3} \qquad 3.9.3$$

Where $\widetilde{S3}$ is the signal from S3 delayed from the previous beam burst by 43nS.

At a beam rate of 10^5 s^{-1} the probablilty of a proton in a given radiofrequency pulse is given by beam rate / frequency = 4.3×10^{-3}. The probability of 2 protons in one radiofrequency pulse is approximately 1.9×10^{-5}. This gives a rate of approximately 430 per second. The monitor S123A indicates the number of double proton

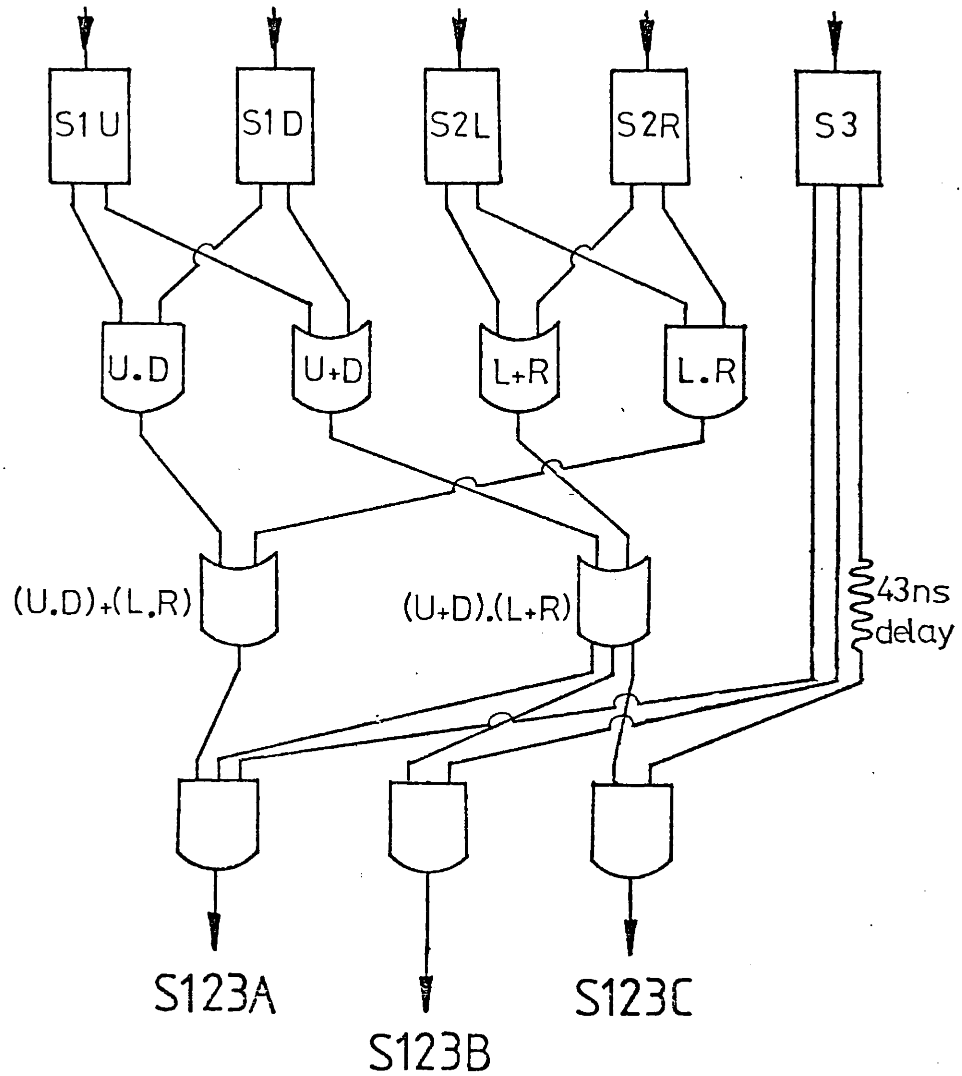

FIGURE 3.13 ELECTRONIC LOGIC OF BEAMLINE COUNTERS

events. For a perfectly circular beam, centred on counters S1 and S2, the monitor S123A will indicate $\frac{3}{4}$ of the double events.

The monitor S123C effectively monitors all counts arising from double proton and noise coincidences, as the probability of two protons in one radiofrequency pulse is the same as the probability of two protons in consecutive pulses.

3.10 Target Monitor Chambers

Four delay line chambers were used to record the position of both the forward and recoil protons emerging from the target. The chambers, designed and manufactured by the University of Alberta, (Canada), (3.15) had an active area of 20cm x 20cm surrounded by a 4cm wide aluminium frame. The wire separation was 2mm in both the horizontal and vertical planes. Each chamber was equipped with four preamplifier units, one for each end of the two delay lines, these were mounted externally on the aluminium frames. The power for the monitoring electronics was supplied from a custom-made module. This module also received the delay line outputs and level shifted them to standard NIM logic levels. The unit included a variable threshold discriminator and was designed to fit into a standard NIM bin. The chambers were designed to run on an EHT of 4.5 - 4.7KV and used a magic gas mixture (69.7% Argon, 30% Isobutane and 0.3% Freon).

The chambers were mounted onto the target structure, using an aluminium framework, at an average distance of approximately 37cm from the target centre. They were mounted such that the pre-amplifiers were not accesible to any scattered beam. A NIM bin was mounted underneath the targets support table and housed the four preamplifier power supply - NIM level output units. The EHT supplies were controlled from the electronics trailer. It was found necessary to shape the delay line output prior to routing them to the electronics trailer. Once in the trailer the outputs were all delayed by 64nS before being reshaped. The sixteen delay line outputs were used as stops for sixteen TDCs.

Mounted behind each chamber was a scintillator. The PMT bases for the scintillators were mounted approximately 1m from the scintillators to keep them in a region of low magnetic field. The chambers were positioned to cover both forward and recoil protons around approximately 33° LAB for $\Delta\sigma_L$ and approximately 24° LAB for $\Delta\sigma_T$. A coincidence between the forward and recoil scintillators occuring together with a S123B was registered as an event. An event generated a NIM output. This was used to start the sixteen TDCs monitoring the delay lines, the stop being the arrival of the delayed delay line output. Thus for each event an output of sixteen TDC numbers were generated.

3.11 Transmission Array

The transmission array used for this experiment was originally used to measure π -nucleus cross sections [3.16]. The array consists of six concentrically mounted plastic scintillators, T1 - T6, the dimensions of which are given in table 3.2.Each scintillator was enclosed in its own light tight chamber. The chambers were constructed of 0.13mm double aluminised mylar, stretched across circular aluminium frames, fig 3.14.The scintillators were glued to the mylar. A strip of aluminised mylar was arranged so as to reflect the scintillations to the PMT. The air light guides avoid false Cerenkov counts. The six chambers were clamped together and then enclosed in a large aluminium casing, 1.2m in diameter. The rear of the casing supported two 5cm square scintillators, E1 and E2, which were used to monitor the efficiency of the counters.

The transmission array was positioned such that the first counter subtended an angle of approximately 4°. This angle is approximately 5 times the multiple scattering angle caused by the target at 200MeV. It was found that an approach much closer than this resulted in the targets magnetic field affecting the PMT of the first counter.

In the $\Delta\sigma_T$ configuration the polarized target's magnetic field was orientated vertically and thus deflected the proton beam. The amount of deflection depends on the proton's momentum. The transmission array, therefore, had to be moveable so it could be

Scintillator	Radius (cm)	Thickness (cm)	Distance from scintillator 1 (cm)
1	9.01	0.91	0
2	12.00	0.92	1.24
3	16.50	0.94	10.00
4	19.99	0.97	11.28
5	25.46	0.99	20.01
6	29.50	1.23	21.44

TABLE 3.2 DIMENSIONS OF TRANSMISSION ARRAY COUNTERS

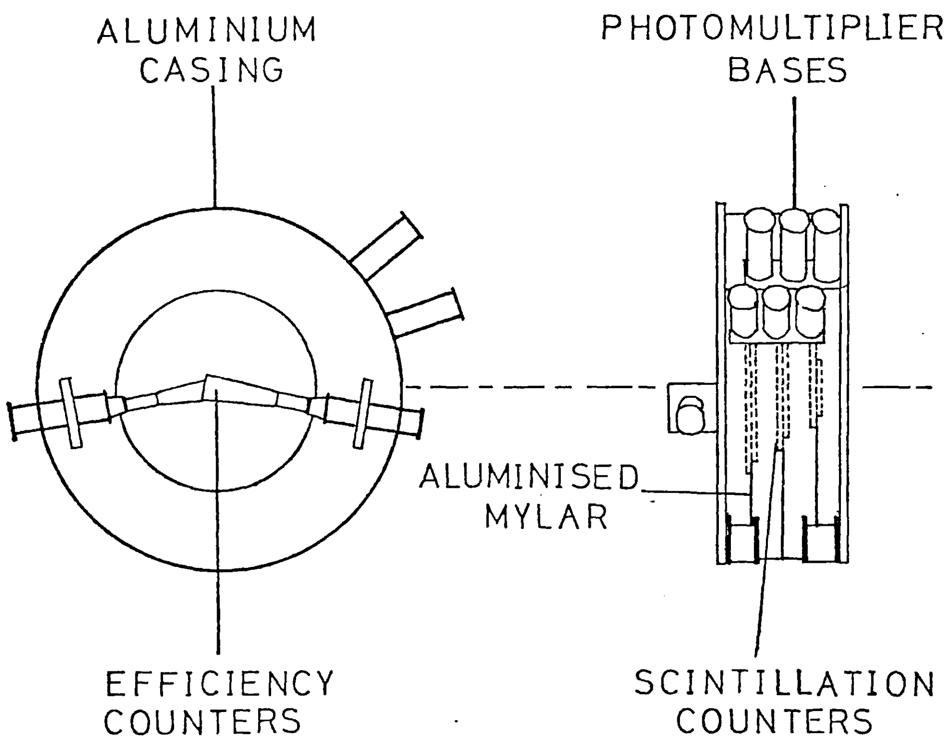

FIGURE 3.14 CONSTRUCTION OF TRANSMISSION ARRAY

centred on the transmitted beam at the various energies. The transmission array was mounted on a sledge of 2.5cm thick aluminium via four height adjusting bolts. The underneath of the sledge was faced with 1.3cm thick Teflon. The whole assembly was supported on an aluminium table 1.5m square. This was polished and oiled, and in this way the transmission array, mounted on the sledge, could be moved by one person. In the $\Delta\sigma_L$ target configuration the 12° rotation of the magnetic field resulted in a small vertical deflection of the beam. The transmission array was centred on this deflected beam using the height adjusting bolts.

To minimise random counts, consecutive transmission array counters were joined in coincidence with one another as well as S123B. The efficiency of the counters was measured by monitoring a further conicidence between E1 . E2 and Ti . Ti+1 . S123B, for i = 1 to 5. As a useful monitor in the overall efficiency of the array, the single coincidence,

E1 . E2 . S123B . T1 . T2 . T3 . T4 . T5 . T6 was produced. It was important to scale the random coincidence defined as $\widetilde{S123B}$. Ti . Ti+1, where $\widetilde{S123B}$ is the S123B output delayed by 43nS, to enable random corrections to be made to the transmissions. Fig 3.15 shows the full logic used for the transmission array.

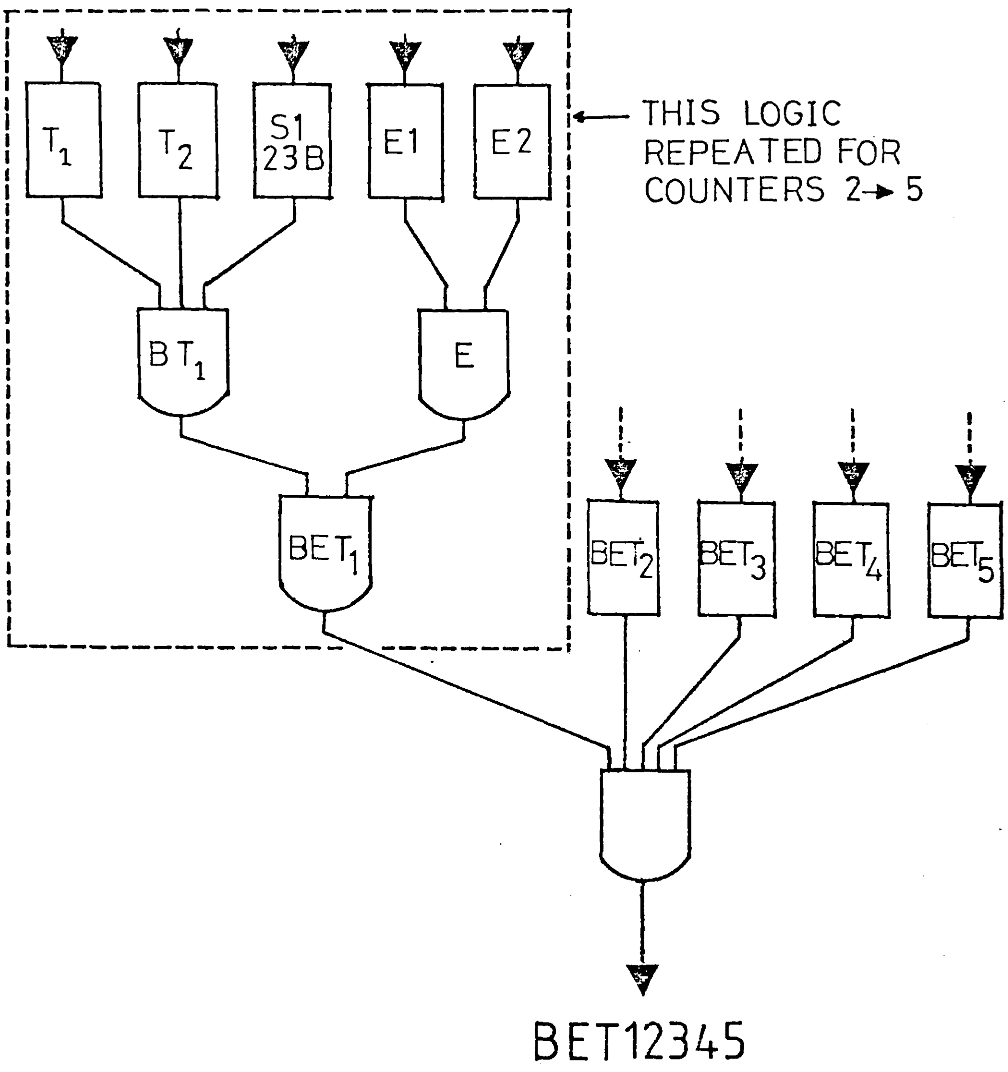

FIGURE 3.15 ELECTRONIC LOGIC OF THE TRANSMISSION ARRAY

3.12 Data Acquisition

Data Acquisition was under the control of an online program running in a PDP11/34 computer situated in the electronics trailer. The PDP11/34 was interfaced to a CAMAC system receiving input from fast NIM logic electronics. The PDP11/34's tasks were to accumulate data, give online checks on this data and buffer the data to tape. The data acquisition consisted of two separate tasks, that of reading the scaler and the delay line chamber data.

The scintillator counter outputs were all discriminated at 100mV, output widths were set at approximately 10nS, to be much less than the cyclotron's radiofrequency period of 43nS. The appropriate discriminated outputs and the required logical combinations were recorded by twelve Hex CAMAC scalers. These were read and stored by the PDP11/34 when requested by a generated 'look at me' signal. The scaler data, recorded over one period of a particular beam spin, was written to tape on receipt of the 'spin busy signal' from the polarized ion source.

The receipt of a trigger from the target monitor chamber scintillators generated a start for the TDCs monitoring the delay lines. The trigger also generated a computer busy, used to inhibit scalers and further data acquisition until the computer had read and stored the event data. The event data was recorded in a 368 bit word. It contained bits set by the beam spin orientation followed by the sixteen TDC generated numbers, the NMR integral, the S123B scaler and output from a 1MHz clock started at the beginning of the run. After all the event data had been stored by the PDP11/34, a 'busy clear signal' was generated, which restarted data acquisition.

Data blocks buffered to tape by the PDP11/34 were 3584 bytes long. One tape write, therefore, was required for every 77 chamber triggers. A clock gated by the computer busy signal gave a measure of the system workload.

CHAPTER 4

DESIGN, INSTALLATION AND OPERATION OF BEAMLINE 4C

4.1 Beamline Design

During the summer of 1979 a series of computer simulations of the proposed beamline were undertaken (4.1). These simulations were to investigate the effect of the small bore collimator on beam quality and rate. The simulations were also to ensure that a suitable beam spot of approximately 3mm diameter and small divergence (~5mrad) could be acheived at the proposed target position. Two computer programs were used to simulate the beamline, these were TRANSPORT and REVMOC.

4.1.1 TRANSPORT

An interactive version of TRANSPORT (4.2) was available at TRIUMF. TRANSPORT represents beamline elements by matrices, and the passage of beam through a beamline by a process of matrix manipulations.

The effect of a beamline component on an incident beam particle can be represented by a square transformation matrix, R

$$X(1) = R\,X(0) \tag{4.1.1}$$

where X(1) is the final state beam particle vector and X(0) the incident vector. The state vector representing any arbitrary beam particle is six dimensional,

$$X = (x, \theta, y, \psi, l, \Delta) \qquad 4.1.2$$

where $x(y)$ is the horizontal (vertical) displacement of the arbitrary particle with respect to the central trajectory. θ (ψ) is the angle this particle ray makes in the horizontal (vertical) plane with respect to the central trajectory. l is the path length difference between the arbitrary ray and the central trajectory, Δ is the fraction momentum deviation of the ray from the central trajectory's momentum.

The traversing of several elements is described by replacing R in equation 4.1.1 by the product matrix R_{TOT}, of the elements. For N elements,

$$R_{TOT} = R(N)\, R(N-1) \ldots R(1)\, R(0) \qquad 4.1.3$$

TRANSPORT represents the beam by an ellipsoid in the six dimensional coordinate space. The particles in a beam are assumed to occupy the volume enclosed by the ellipsoid, each point representing a possible ray.

The equation of the six dimensional ellipsoid may be written,

$$X(0)^t \text{ SIGMA } (0)^{-1}\, X(0) = 1 \qquad 4.1.4$$

where $X(0)^t$ is the transpose of the coordinate vector X(0). After passing through a beamline element with transformation matrix R, the equation representing the new ellipsoid becomes,

$$X(1)^t \text{ SIGMA } (1)^{-1}\, X(1) = 1 \qquad 4.1.5$$

where

$$\text{SIGMA } (1) = R \text{ SIGMA}(0) R^t \qquad 4.1.6$$

The diagonal terms of the SIGMA(1) matrix give the size of the emergent beam. The off-diagonal elements determine the orientation of the ellipsoid in the 6 dimensional space.

To use TRANSPORT, a beamline file is created. This file contains details of all the constituent elements of the beamline. The SIGMA matrix is supplied for the start of the beamline. In the case of this design work, the SIGMA matrix defines the parameters of the beam emergent from the TRIUMF cyclotron. The TRANSPORT program then computes the cummulative transformation matrix for the whole, or any desired section , of the beamline. The SIGMA matrix, giving the beam parameters may be outputted at any point along the beamline.

The TRANSPORT program also offers graphical output of beam parameters along the beamline, in two different formats, envelope and ellipse. In the envelope mode the output plots the variation of any of the six beam parameters along the beamline. The ellipse mode depicts the cross sectional ellipse of the six dimensional beam ellipsoid, eg x vs θ or y vs ψ for any point along the beamline.

From the initial SIGMA matrix and the beamline file, TRANSPORT calculates the beam parameters along the beamline. If the predicted beam parameters are not as required, then the beamline file needs to be changed. It is possible to set, as a constraint, the required value of a parameter, such as x, at a certain point. One element in the beamline file may then be set as a variable, eg a quadruple field. The program now endeavours, by adjusting the variable, to obtain the required preset value of the parameter. A check must be made on the final fit to ensure that parameters such as quadrupole fields have not exceeded their maximum values.

4.1.2 REVMOC

REVMOC (4.3) is a Monte Carlo program which calculates the probability that a particle, in traversing the beamline, will be lost by means of scattering or absoprtion by material in the particle's path or due to the effects of active elements.

A beamline file is prepared in much the same manner as for TRANSPORT, as is the initial six dimensional beam ellipsoid. Initial parameters for each particle tracked through the beamline are selected at random from the beam ellipsoid. The particle is then traced through the system. At the end of each element, a test is made to see if the particle's parameters fall within preset limits. If they do not, the particle is rejected and another particle chosen and tracked through the system.

After tracking a preset number of particles through the beamline the number of particles which fail to negotiate the full beamline were output. The reason for their rejection was given, together with the number and final parameters of all the transmitted beam.

The REVMOC program was used in conjunction with the TRANSPORT beamline tunes as a check on their validity. There are no facilities in REVMOC for beamline fits. To obtain good statistics in order to predict final beam phase space parameters, large numbers of protons have to be tracked through the beamline. The REVMOC program, therefore, used a large amount of CPU time compared with TRANSPORT.

4.1.3 Beam Tunes

The beamline, BL4C, was to use part of the existing BL4A. The first elements in BL4A, outside the cyclotron vault shielding was a quadrupole doublet, fig 4.1. This doublet was followed by the monitor of beam polarization. There were then a further two quadrupoles. The superconducting solenoid was positioned downstream of this doublet and was followed by a neutron collimator[1.9]. The neutron collimator, 330cm long, was made of steel and lead. It provided a good location, and biological shielding for the small bore collimator. Beamline files for use in TRANSPORT and REVMOC were created for BL4A, including a 20cm long copper collimator, situated at the upstream end of the neutron collimator. The smallest acheivable bore in the collimator was thought to be approximately 3mm, and this was used in the simulations. It was, however, found possible to make a 1mm diameter bore collimator which was used in the actual experiments.

The BL4A beamline files were extended to include the elements required for BL4C. The 35^{o} bending magnet was positioned approximately 2m downstream of the neutron collimator exit. After the

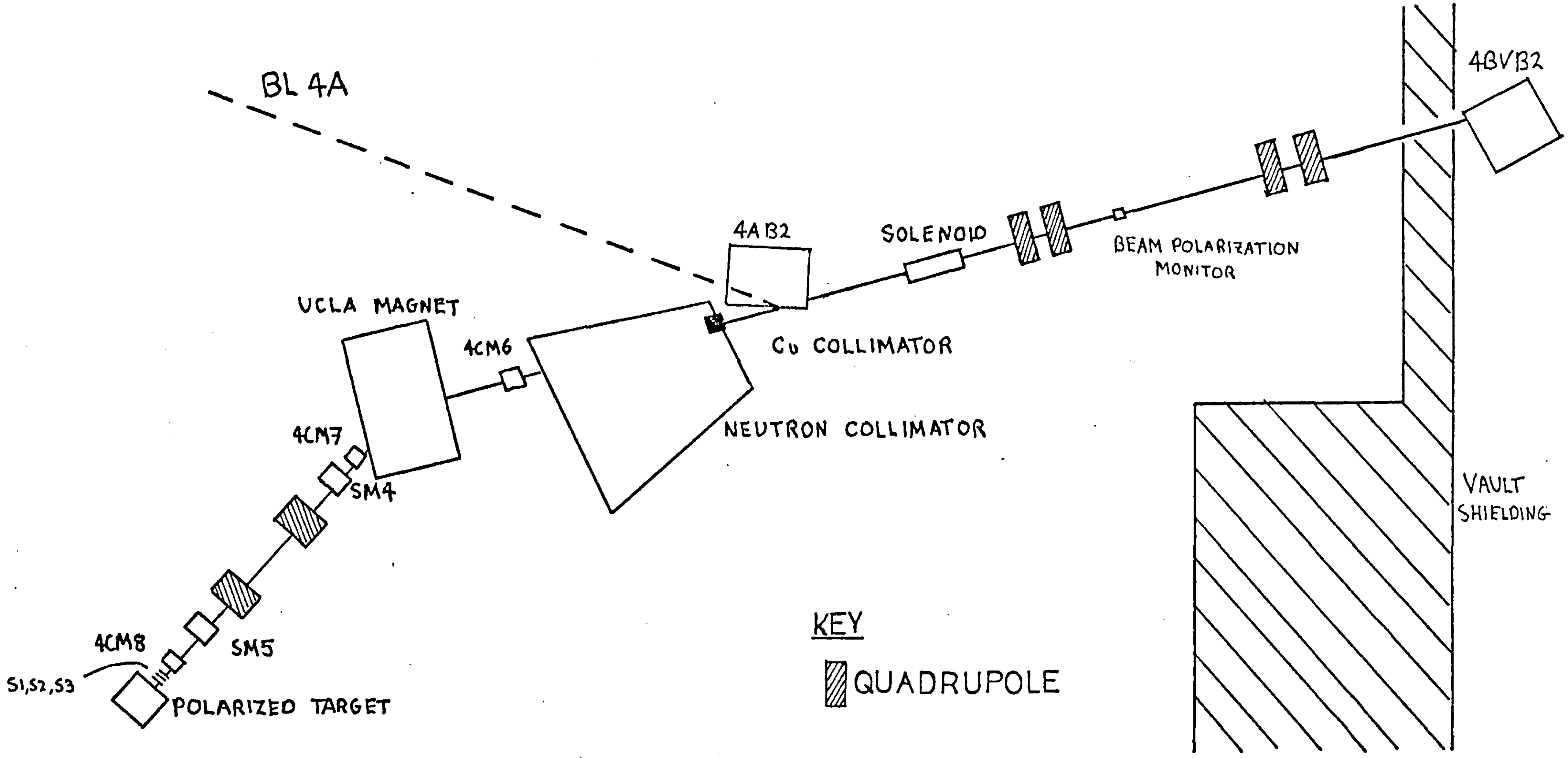

FIGURE 4.1 EXPERIMENTAL BEAMLINE

bend magnet, a quadrupole doublet was included for final beam ellipsoid manipulation. The use of several quadrupole types for use as the final doublet was investigated; Alberta (QP-405837), Rutherford Model IV, TRIUMF (4Q14(1a)/8) and Bellona. The characteristics of these quadrupoles, their maximum gradients, operating currents and voltages corresponding to the available TRIUMF standard power supplies of 11 and 25KW, are listed in table 4.1. The positions of all the elements and drift lengths downstream of the solenoid exit, used in the final computer simulations, are listed in table 4.2.

A set of initial tunes on the beamline, ignored the effects of the beam polarization monitor target and the small bore collimator. The only beamline obstruction considered in these provisional fits were two mylar windows 2.5 x 10^{-5}cm thick, one at the beam pipe end and one at the entrance of the polarized target.

Beamline simulations were performed at four energies 200, 300, 400 and 500MeV using TRANSPORT. At all energies beam spots of full width, approximately 3mm and divergences of approximately 6 mrads were acheived in both horizontal and vertical planes at all energies. The beam envelope, variation of x and y along the beamline, for the 200 and 500MeV tunes are shown in fig 4.2 and fig 4.3. REVMOC checks were not carried out on these provisional simulations.

The effect of the small bore collimator and a 3mm target foil of polythene, used in beam polarization monitor, were investigated

TYPE	EFFECTIVE POLE LENGTH (m)	GRADIENT x EFFECTIVE LENGTH(T) 11kW SUPPLY	25kW SUPPLY
ALBERTA QP-405837	0.36	2.23	3.59
RUTHERFORD MODEL IV	0.85	1.98	4.12
TRIUMF 4Q14(1a)/8	0.41	6.56	6.56
BELLONA	0.50	1.58	2.34

TABLE 4.1 CHARACTERISTICS OF VARIOUS QUADRUPOLES

ELEMENT	DISTANCE FROM STRIPPER FOIL (m)	OPTICAL LENGTH (m)
SOLENOID	20.18	1.0
DRIFT LENGTH		
35^{o} BENDING MAGNET	31.10	1.4
DRIFT LENGTH		
QUADRUPOLE	33.74	0.36
DRIFT LENGTH		
QUADRUPOLE	35.10	0.36
DRIFT LENGTH		
MYLAR WINDOW	36.91	2.54×10^{-5}
DRIFT LENGTH		
MYLAR WINDOW	37.01	2.54×10^{-5}
DRIFT LENGTH		
TARGET	37.56	

TABLE 4.2 THE INPUT PARAMETERS USED IN THE TRANSPORT CALCULATIONS USING ALBERTA QUADRUPOLES

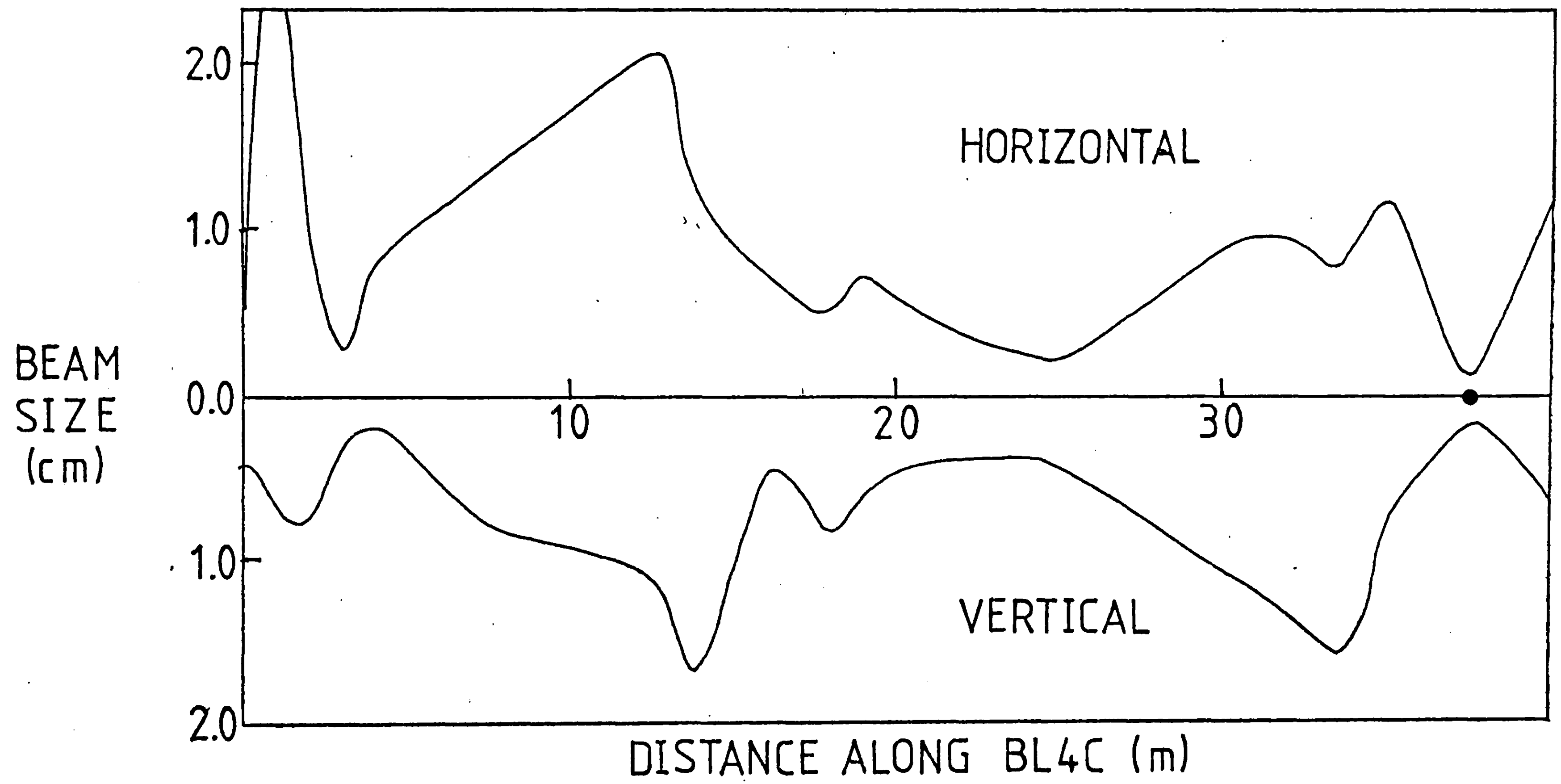

● TARGET CENTRE

FIGURE 4.2 BEAM ENVELOPE AT 200MeV

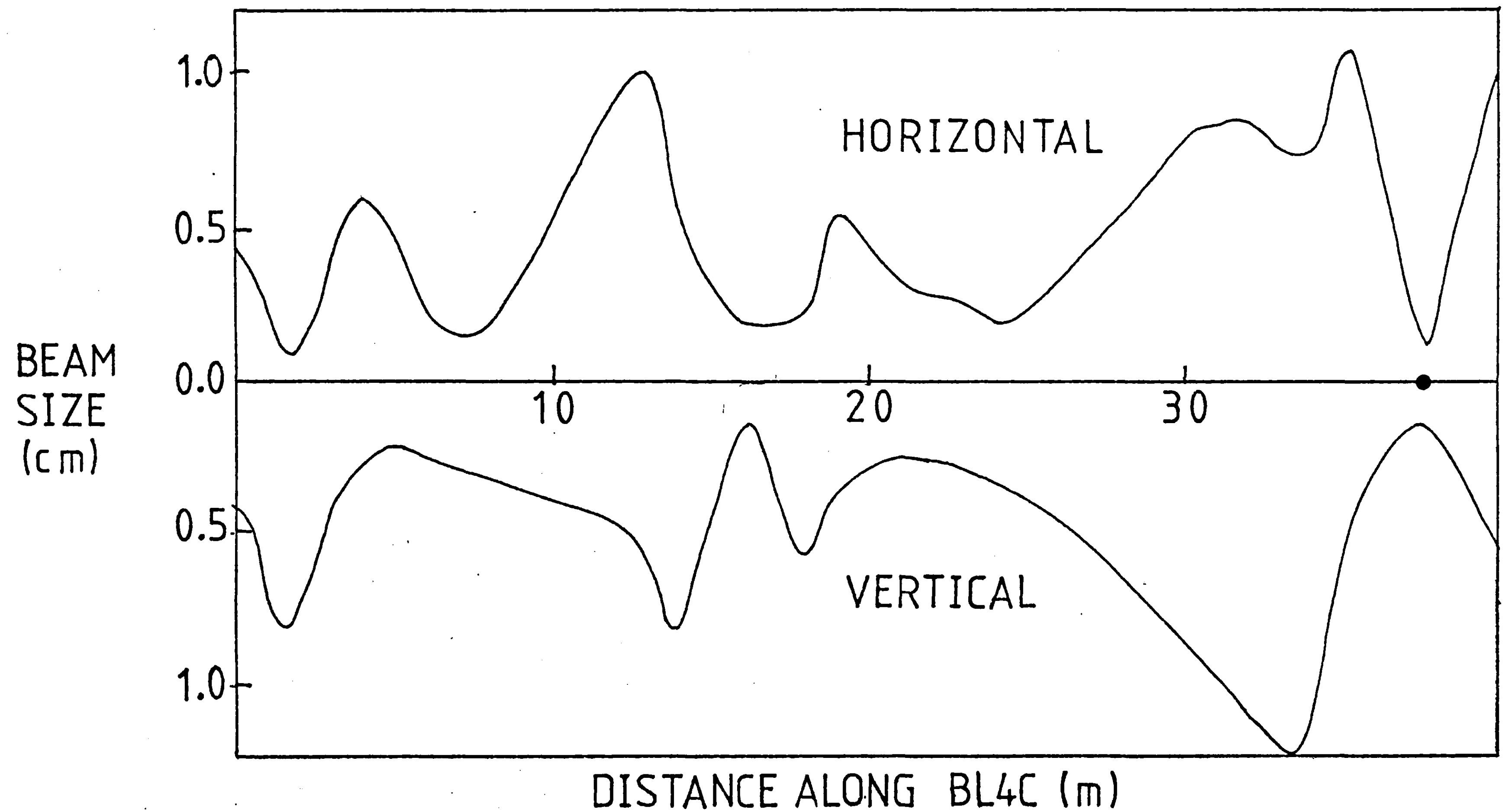

● TARGET CENTRE

FIGURE 4.3 BEAM ENVELOPE AT 500MeV

using both TRANSPORT and REVMOC at two energies, 200 and 500MeV.

The TRANSPORT program was used for the initial tunes. The additional divergence, introduced into the beam by the polarimeter foil, is kept to a minimum by demanding a beam spot focus at this point. The inclusion of the small bore collimator in TRANSPORT was acheived by redefining the beam to be $\pm$ 1.5mm at its exit.

Estimates of transmission through the collimator were made using outputs of x vs θ and y vs ψ produced by TRANSPORT at the collimator. The transmission was estimated by the ratio of the area of the ellipse contained within $\pm$ 1.5mm around the central trajectory, to the total area of the ellipse. It was found that by adjustments of the quadrupole doublet upstream of the collimator, a large range of transmission could be acheived. Beamline settings were optimized for a transmission of 1 in 10^3. In figs 4.4 and 4.5 the beam envelopes for 200 and 500MeV are shown.

The REVMOC program was then used to check the TRANSPORT predictions and validate the approach adopted to incorporate the collimator. The reduction in the beam intensity caused by the collimator resulted in REVMOC being very expensive, in CPU time, to use in order to obtain good statistics at the target position. REVMOC predictions of transmission were in broad agreement with those estimated by TRANSPORT, of 1 / 1000, being 1 in 670 (500) at 200 (500)MeV. REVMOC beam spot predictions were in good agreement with those of TRANSPORT. The beam spot parameters obtained from both TRANSPORT and REVMOC at 200 and 500MeV are listed in table 4.3.

		200MeV		500MeV	
		TRANSPORT	REVMOC	TRANSPORT	REVMOC
X	(mm)	4.2	3.9	2.6	2.7
θ	(mr)	7.3	6.6	4.2	3.7
Y	(mm)	3.6	2.2	3.6	1.6
ψ	(mr)	0.3	0.3	0.3	0.3

TABLE 4.3 CHARACTERISTICS OF THE BEAM SPOT AT THE TARGET POSITION PREDICTED BY TRANSPORT AND REVMOC

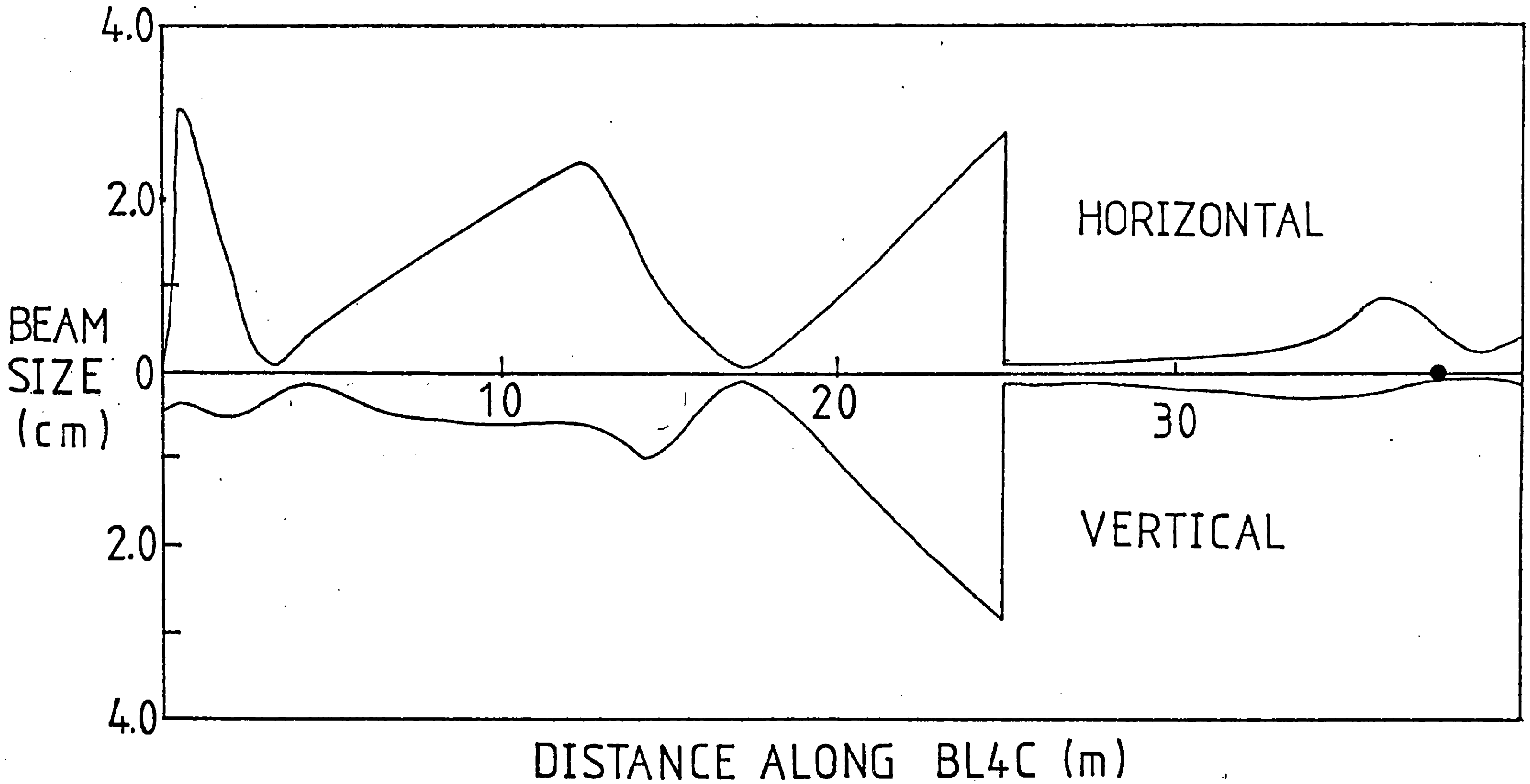

● TARGET CENTRE

FIGURE 4.4 BEAM ENVELOPE AT 200MeV INCLUDING THE EFFECTS OF THE POLARIMETER FOIL AND COLLIMATOR

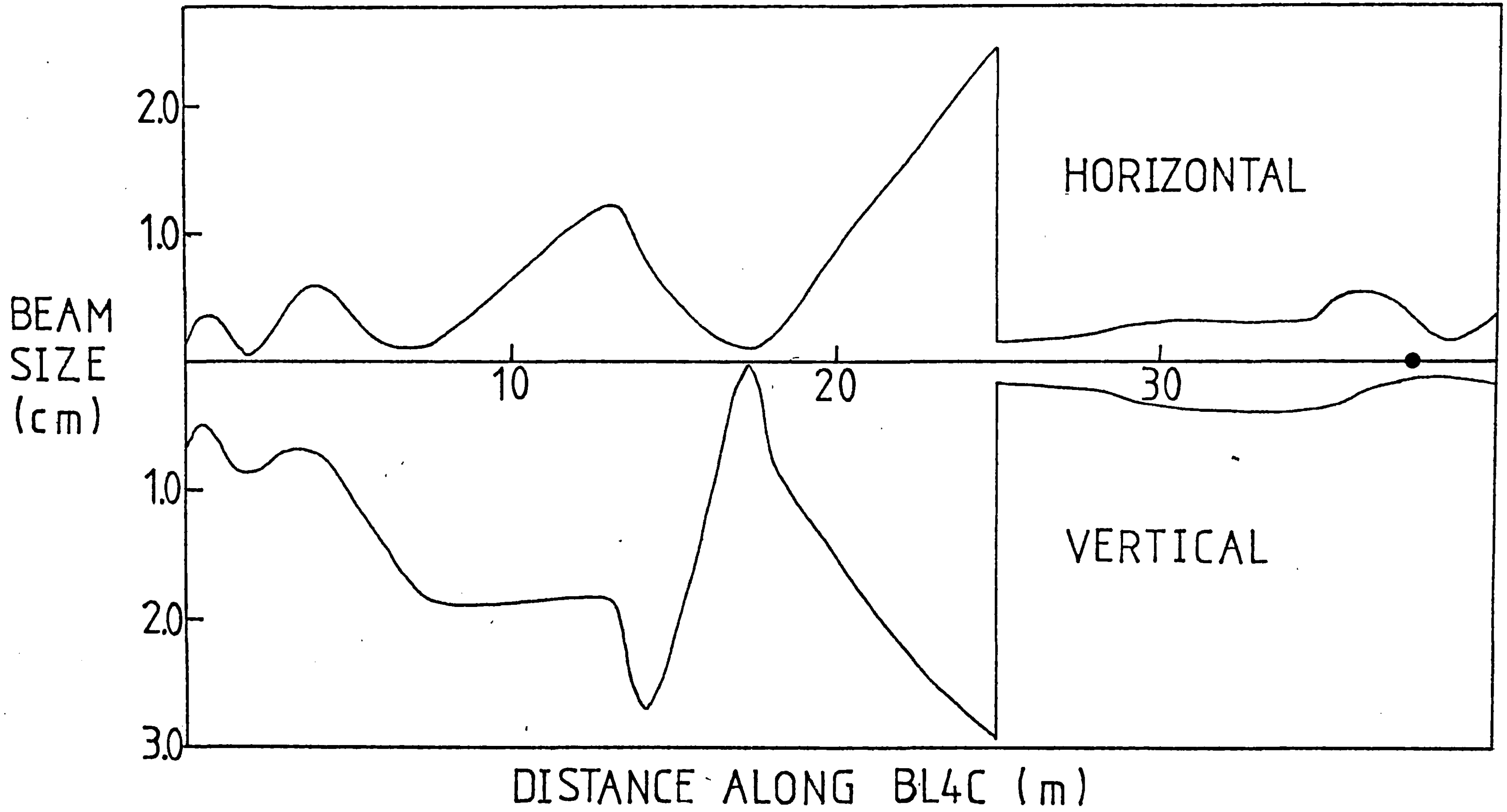

● TARGET CENTRE

FIGURE 4.5 BEAM ENVELOPE AT 500MeV INCLUDING THE EFFECTS OF THE POLARIMETER FOIL AND COLLIMATOR

The multiple coulomb scattering in the cyclotron's stripper foil affects the extracted beam's quality. The lowest energy, 200MeV, is affected most, equation 2.1.2, this results in the beam spot parameters being worse than those at 500MeV. The six dimensional ellipsoid, SIGMA matrix, used to represent the beam emergent from the cyclotron was, however, expected to be improved by the use of a wire stripper, used to produce low extracted beam currents. This was smaller and thinner than the standard high beam rate foil stripper, from which the SIGMA matrix elements were measured. The final beam spot parameters were therefore expected to be better than those predicted.

The energy dispersion of the beam, after passing through the beam line, was increased due to the combined effects of the collimator, polarimeter target foil and mylar windows. The REVMOC predictions were that the expected extracted beam energy dispersion of $\pm$ 360 (800)KeV would increase to $\pm$ 1.0 (1.1)MeV at 200 (500)MeV.

In conclusion, at 200 and 500MeV, the desired beam spot parameters at the target position were found to be acheivable. The collimator was able to provide a beam reduction of 1 per 10^3 by manipulation of the beam spot at its entrance.

4.2 Magnetic Deflection

In the $\Delta\sigma_T$ configuration, the target field is perpendicular to the proton momentum and thus deflects the beam.

The beam deflection was studied using computer simulations to aid the experimental design. The magnetic field from the target's Helmholz coils was generated by using a Rutherford lab. program, Solfield. The field was generated and stored for only one octant of space. The spacing of the calculated field points was one every 1cm out to a distance of 150cm. The central field value was normalized to a value of 2.53T. The calculated field in the central plane, aligned along the Helmholz coil axis, B_S, and transverse to it, B_L, are plotted on fig 4.6.

A TRIUMF routine was used in conjunction with OPDATA, an interactive data manipulation program, to study beam trajectories. The beam was tracked through the field using a path step length of 1mm through where necessary an interpolated field.

The trajectory of beams with energy of 210 and 515MeV near the target region are shown in fig 4.7 . These beams were incident upon the reference beamline trajectory. The plots show that maximum deflections of approximately 3.5 (2.0)mm occur at 210 (515)MeV at 8cm from the target centre. A close-up of these plots in the target volume in shown in fig 4.8 . It is seen that for a beam steered to pass through the exact target centre, the magnetic field causes a displacement of approximately 1mm off the beamline at the edge of the target volume, for a 210MeV beam (the worst case).

In order to determine the position and the amount of movement required for the Transmission Array beams of 210, 270, 325, 380,

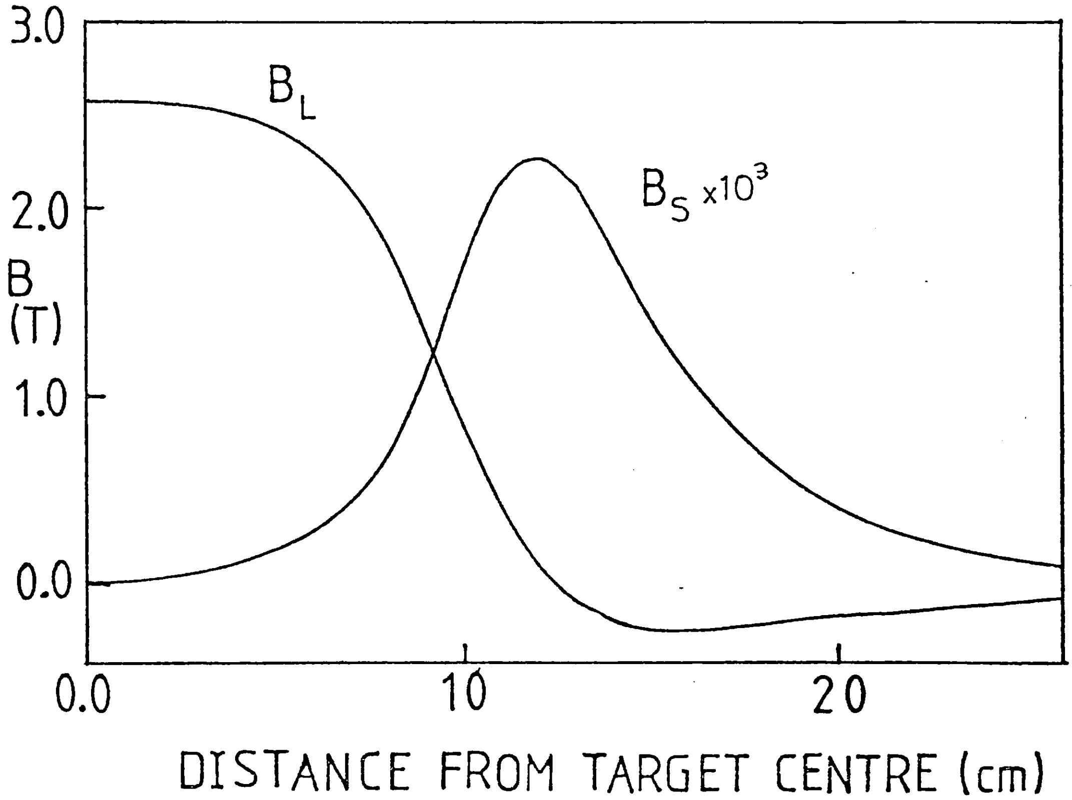

B_S, Field aligned along Helmholz coils axis

B_L, Field perpendicular to B_S

FIGURE 4.6 POLARIZED TARGET'S MAGNETIC FIELD, IN THE CENTRAL PLANE

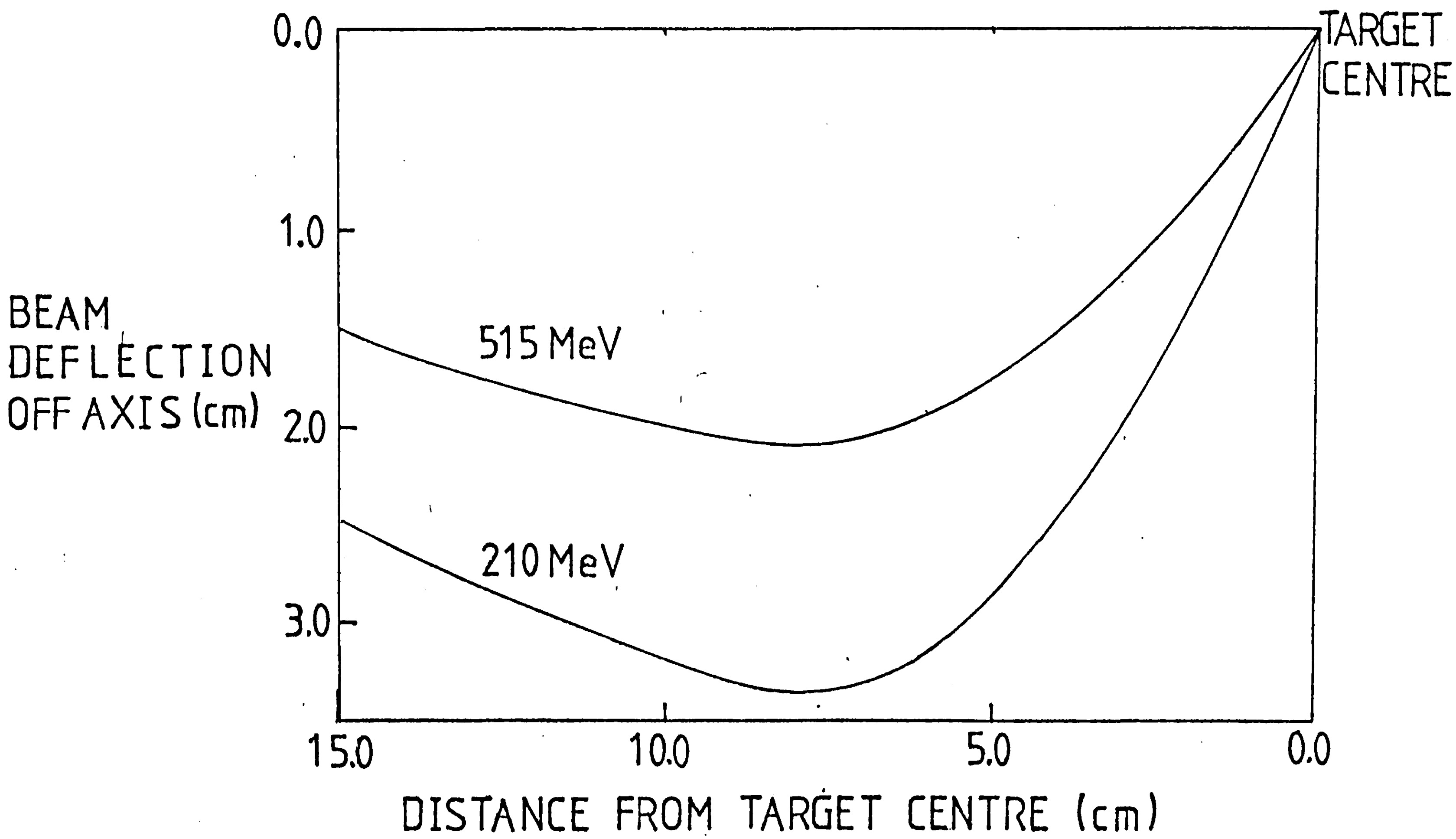

FIGURE 4.7 BEAM DEFLECTION CAUSED BY TARGET'S MAGNETIC FIELD

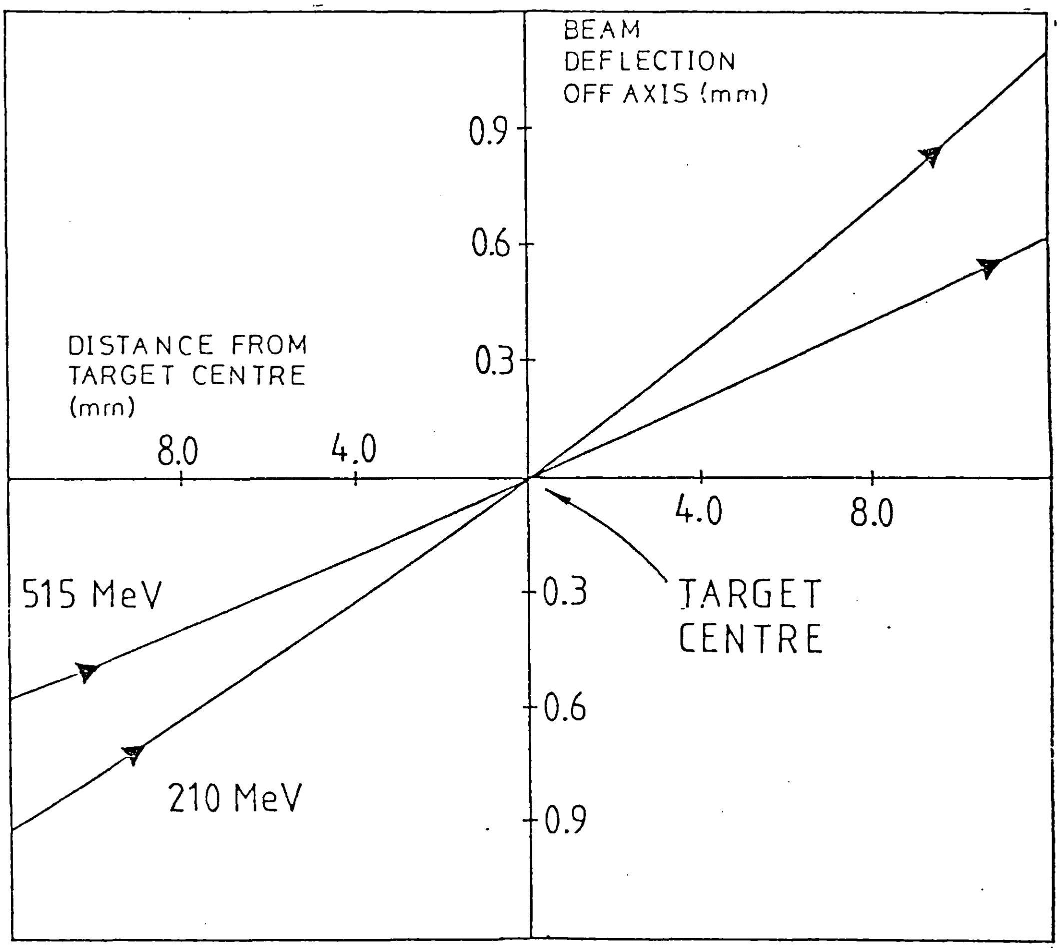

FIGURE 4.8 BEAM TRAJECTORIES THROUGH TARGET VOLUME FOR BEAMS OF INCIDENT ENERGY 210 AND 515MeV

425, 470 and 515MeV, were tracked through the target field to determine the total bend angle. The total angular deflections relative to the central beamline axis are plotted in fig 4.9 for a central field normalized to 2.53T. Deflections of approximately 10.0° (6.0°) were predicted for 210 (515)MeV.

A set of calculations were also performed to determine the vertical angular deflection of the beam, caused by the 12° rotation of the magnetic field in the $\Delta\sigma_L$ configuration.

The target monitor chambers in the $\Delta\sigma_T$ configuration were to monitor scattered protons around 24°_{LAB}. The monitor chambers were not to be moved for each incident energy and thus had to cover the full range of the scattered and recoil protons from 200-520MeV. The scattered and recoil protons were tracked through the magnetic field for 210 and 520MeV out to a radius of 38cm, to determine where to mount the chambers.

4.3 Installation of Beamline 4C

In December 1979, a 1mm diameter bore, 20cm long copper collimator was installed at the upstream end of the neutron collimator. It was optically aligned along the beamline. The first beam was run through the collimator on 7th December. This beam was used to measure transmission through the collimator. The beam current incident upon the collimator was measured by the monitor of beam polarization. The transmitted beam was counted by a set of

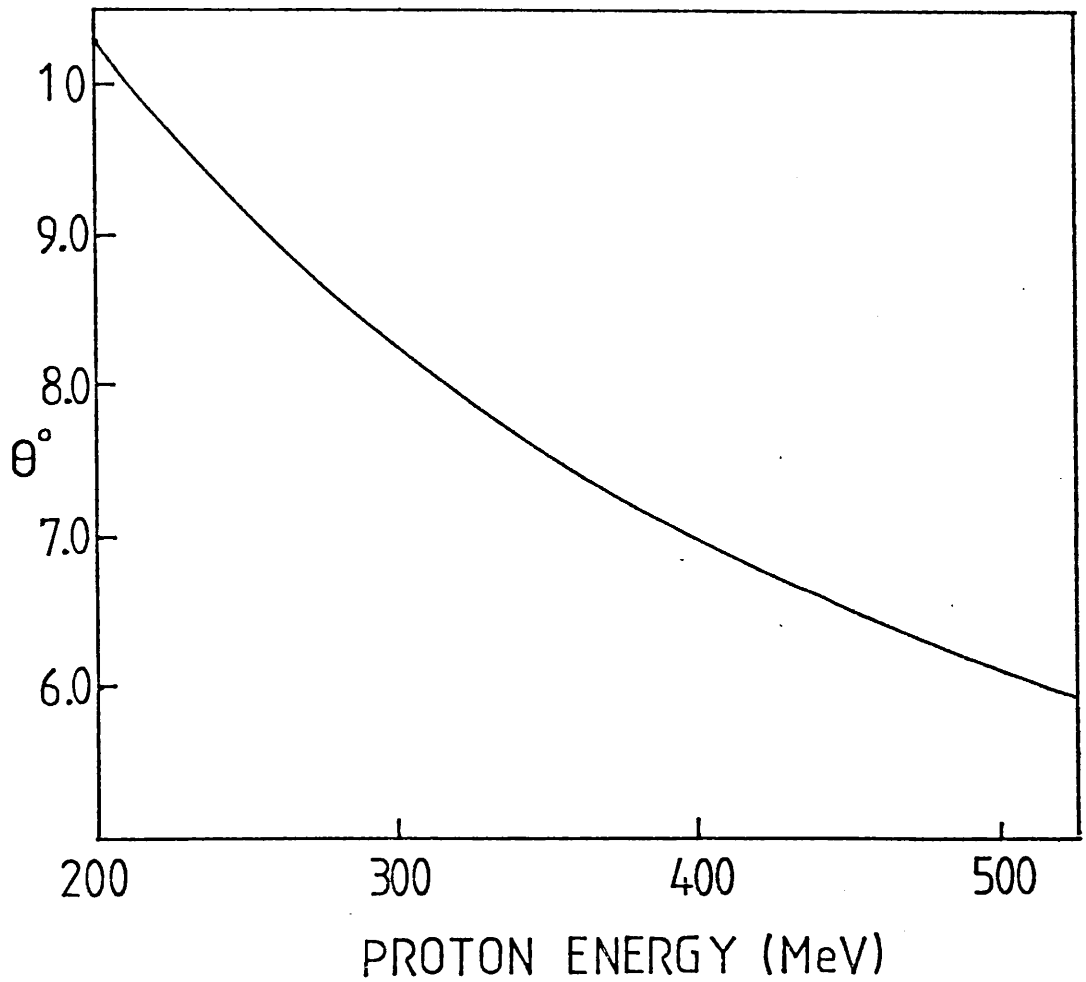

FIGURE 4.9 TOTAL ANGULAR DEFLECTION OF PROTON BEAMS IN THE RANGE 200 - 520MeV, TRAVERSING THE COMPLETE TARGET MAGNETIC FIELD

scintillation counters positioned on the beamline axis at the neutron collimator exit. Using a 500MeV incident beam transmission ratios varying from $1:5 \times 10^2$ up to $1:10^3$ were obtained by changing the beam's phase space at the collimator entrance, using upstream quadrupoles.

The complete evacuated section of the beamline was installed in January and February of 1980, fig 4.1 . An automatic gate valve was positioned at the exit of the neutron collimator, this protected beamline 4A against a sudden vacuum failure in BL4C. The evaculated section of BL4C was terminated just after 4CM8, by a stainless steel end cap, 0.0025cm thick. Beam profile monitors 4CM6 and 4CM7 were standard TRIUMF monitors with a 3mm wire spacing in both horizontal and vertical planes. The monitors were remotely rotated in and out of the beam, readout was by CRT display, with a hardcopy facility. These standard monitors were not sensitive enough to give beam profiles at normal running rates of 10^5/sec. They were intended for use in preliminary setting-up of beam tunes where high currents could be used. The final monitor, 4CM8, was the MWPC chamber, constructed by the University of Alberta. Monitor 4CM8 was rotated in and out of the beamline by hand. The Bellona quadrupoles were used for the final quadrupole doublet. Two steering magnets, SM4 and SM5, were incorporated in the beamline for accurate alignment of the beam onto the target. SM4 (SM5) steered vertically (horizontally).

The first beam was run down the complete evacuated sections of BL4C on 28th February 1980. Beamline tests were made using a 330MeV beam. Various tunes were able to vary the transmission through the collimator from $1:2 \times 10^2$ to $1:1.1 \times 10^4$, acceptable spots of 6mm full width were seen at 4CM8.

In April 1980, the five counters comprising S1, S2 and S3 were installed, together with the polarized target and the transmission array. The bending magnet was also shimmed allowing beams of 520MeV to be bent through the required 35^o bend.

4.4 Data Taking

4.4.1 Test Runs

During May 1980, a set of beamline tests were carried out, in the $\Delta\sigma_T$ experimental configuration. For these test runs, the target was polarized vertically downwards. The NMR system software was not complete, and NMR integrals were not available. There were, however, CRT displays of the Q curves which indicated a sizeable polarization. The seven required incident energies were all successfully tuned and beam spots at 4CM8 of approximately 6mm FW were routinely obtained.

The online data acquisition program, running in the PDP11/34, provided a number of online checks on both the scaler and TDC data, which were both stored separately for the three beam polarization states. The scaler data from the twelve Hex scalers could be displayed in table form on a Tectronix 4010 terminal for any of the beam polarization states. A table of pre-programmed scaler ratios was also available. If these ratios drifted outside acceptable values, the data acquisition could be paused or stopped. A list of the scaler ratios that were evaluated is given in table 4.4.

Information from the target monitor chambers was displayed in the form of sixteen, 256 bin, histograms. The two TDC numbers, X1 and X2, from each end of the delay lines were combined to form X1 + X2 and X1 - X2, both these combinations of X1 and X2 being histogrammed. If the TDC number received no stop, eg the chamber did not record an event, then the TDC number overflowed. The number of overflows was recorded in bin 256 of each histogram. The histograms could be viewed on the Tectronix terminal. A check on the efficiency of the chambers was provided by an output of the sum of contents of each chamber histogram, excluding bin 256.

For these test runs and all other runs, the polarized ion source was programmed to supply five mintues of down polarization,

COUNTERS	ONLINE SCALER RATIOS
BEAMLINE	S1U.(S2R+S2L)/S1D.(S2R+S2L) S2R.(S1U+S1D)/S2L.(S1U+S1D) (S1U+S1D).(S2L+S2R)/S123B
TRANSMISSION ARRAY	S123B.E1.E2.T1.T2.T3.T4.T5.T6/S123B.E1.E2 S123B.E1.E23S123B
BEAM POLARIZATION MONITOR	LF/LR RF/RR (L-R)/(L+R) S123B/(L+R)

TABLE 4.4 ONLINE SCALER RATIOS

followed by one minute of spin off, and then five minutes of up polarization in a continuous cycle. The beam polarization state was signalled by a NIM level supplied to the electronics trailer. This was used by the PDP11/34 to split the data acquisition into the three beam polarization states. Whilst the polarized ion source was changing spin state, a 'spin busy signal' was received in the trailer.

The beamline was tuned using high beam rates so beam profiles could be viewed on all the monitor boxes before and after the collimator. The beam was steered onto the beam polarization monitor's target foil to ensure that the measured asymmetry for beam spin off was small, in practice $|\varepsilon| < 0.018$. The beam parameters at the collimator entrance were then adjusted to give a transmission of 1 in 10^3. In both the $\Delta\sigma_L$ and $\Delta\sigma_T$ experiments, it was found unnecessary to energise the final quadrupoles (apart from 200MeV) to acheive the required beam spot size at 4MC8. The TRANSPORT and REVMOC beam simulations had both found it necessary to have an excited quadrupole doublet after the collimator. The installed collimator, however, had a ninth of the area of the one used in the beam simulations and defined a much superior beam phase space.

During these test runs, checks were carried out on the rate dependence of the transmission array efficiency and the dependence of the transmission on beam rate, steering and size. For these runs, the transmission array was supported on a temporary moveable trolley.

In the test runs, the beam was centred on the target cell by monitoring the change in transmission, during horizontal and vertical scans of the beam across the target cell. The small counter, S3, was switched out of the S123B coincidence and a horizontal scan of the target made using the large 35° bending magnet while monitoring the scaler ratio, S12B.T5T6 / S12B, which gives the transmission of beam through the target. When the beam was passing through the target cell, the transmission dropped by 3%. From the horizontal scan, the power supply setting for the bending magnet to steer the beam onto the target cell, was found. A similar vertical scan was then performed. The values of the scaler ratios U/D and L/R corresponding to the beam passing through the target cell were recorded and at each energy the beam was steered to obtain these ratios.

The efficiency of the transmission array's counters were monitored by the two counters E1 and E2. The efficiency of the i^{th} counter, Ei , is defined as

$$\mathrm{Ei} = \frac{\mathrm{S123B.E1.E2.Ti.Ti+1}}{\mathrm{S123B.E1.E2}}$$

The efficiency was generally about 99.9%. It was, however, found to have a small rate dependence. For example, the efficiency of counter pair 1-2 fell from 99.94% to 99.88% when the beam rate was increased from 30 to 300k/sec.

The effect of an increase in beam rate is an increase in the measured transmission. This arises due to the increased chance of there being two protons accelerated and extracted in one radio-frequency pulse. The component of the transmission arising from double events, t_{ri}, in the i^{th} counter is,

$$t_{ri} = RT(1-t_i) \qquad 4.4.1.$$

where t_i is the transmission measured by the i^{th} counter, R is the beam rate, and T is the cyclotron's radiofrequency period, 43ns. A check was made to see if calculated and measured changes in transmission, due to changes in beam rate, were in agreement. The change in transmission on increasing the beam rate from 60 to 350k/sec was measured as $5.15 \pm 0.22 \times 10^{-4}$. The calculated random contribution to the transmission at 60k/sec is 1.05×10^{-4}, whereas at 350k/sec this contribution is 6.06×10^{-4}, leading to an expected change in transmission of 5.01×10^{-4}, in good agreement with the measured change.

The dependence of the transmission on the beam size, position and rate was investigated. A set of transmission test data was taken with the beam centred on the target cell and at a beam rate of 300k/sec. Four sets of data were then taken with deliberate beam steers of $\pm$ 2mm at the target position in the vertical and horizontal plane. The final quadrupoles were then used to overfocus and underfocus the beam spot by 10%. A final set of data was then taken at a halved beam rate of 150k/sec. It was found that the results were all consistent, within errors.

At the end of the test runs the transmission array support table was installed and the NMR system was made fully operational.

A readout of the NMR integral in binary code was available in the electronics trailer as well as by request, in decimal format, through the PDP11/34. As an aid to centring of the transmission array on the transmitted beam, cross wires marking the centre of the counters, were mounted on its entrance and exit, together with holders for polaroid film. Immediately before developing the exposed polaroid film, the position of intersection of the cross wires was marked onto the film package. A small hole was punched through the film at the intersection. In this way, the mis-alignment of the transmission array, relative to the transmitted beam, was found and the array moved accordingly.

4.4.2 $\Delta\sigma_T$ Data

On June 12 1980, beam was run down the now fully operational BL4C. An incident beam energy of 500MeV was tuned and a beam spot of 6mm x 6mm was produced at 4CM8. This was confirmed by two other sources, exposed polaroid film and from scaler information from the split scintillators, S1 and S2.

The final monitor box, 4CM8, had 1mm wire spacing and was therefore able to monitor beam movements of this order. In this way, it was possible to calibrate the power supplies of the steering magnets, SM4 and SM5, for beam movements at 4CM8 and further downstream, by distance ratios. From plots of the log ratio of counts in the right counter to that in the left, as a function of horizontal beam movement, the size of the horizontal beam envelope encompassing a certain percentage of the beam can be obtained. This plot for the $\Delta\sigma_T$ 500MeV tune is shown in fig 4.10. 90% of the beam is seen to be contained within a diameter of 6.2mm. A similar plot obtained for the vertically split counter gave a 90% vertical beam envelope of 4mm diameter.

Beam scans across counter S3 lead to plots from which beam profiles as well as size information, can be extracted. In figs 4.11 and 4.12 the scaler ratio S123B.T5.T6 / S12B is plotted for both horizontal and vertical scans. Superimposed on the figs is the variation of the scaler ratio, assuming a gaussian beam profile of σ = 3(2)mm for the horizontal (vertical) plot. The gaussian distribution is a good representation of the beam profile apart from the down side of the vertical plot. This deviation from the fit shows the beam to have a halo on the up side.

Using the calibrated SM4 and SM5, the alignment of the beamline counters and of the target cell, were checked. The beam was initially centred, horizontally, by the large bending magnet with SM5 off, by maximising the counts in the S123B coincidence. The beam was then centred vertically using SM4. The counter S3 was then switched out of this coincidence and a horizontal scan performed across the target using SM5. The change in transmission through the target was monitored using the scaler ratio S12B.T5.T6 / S12B. An example of one of these plots is shown in fig 4.13. The fig shows the 3% attenuation dip corresponds to all the beam traversing the target cell. Also recorded during these scans, were S2R.S1 and S2L.S1, a plot of the ratio as a function

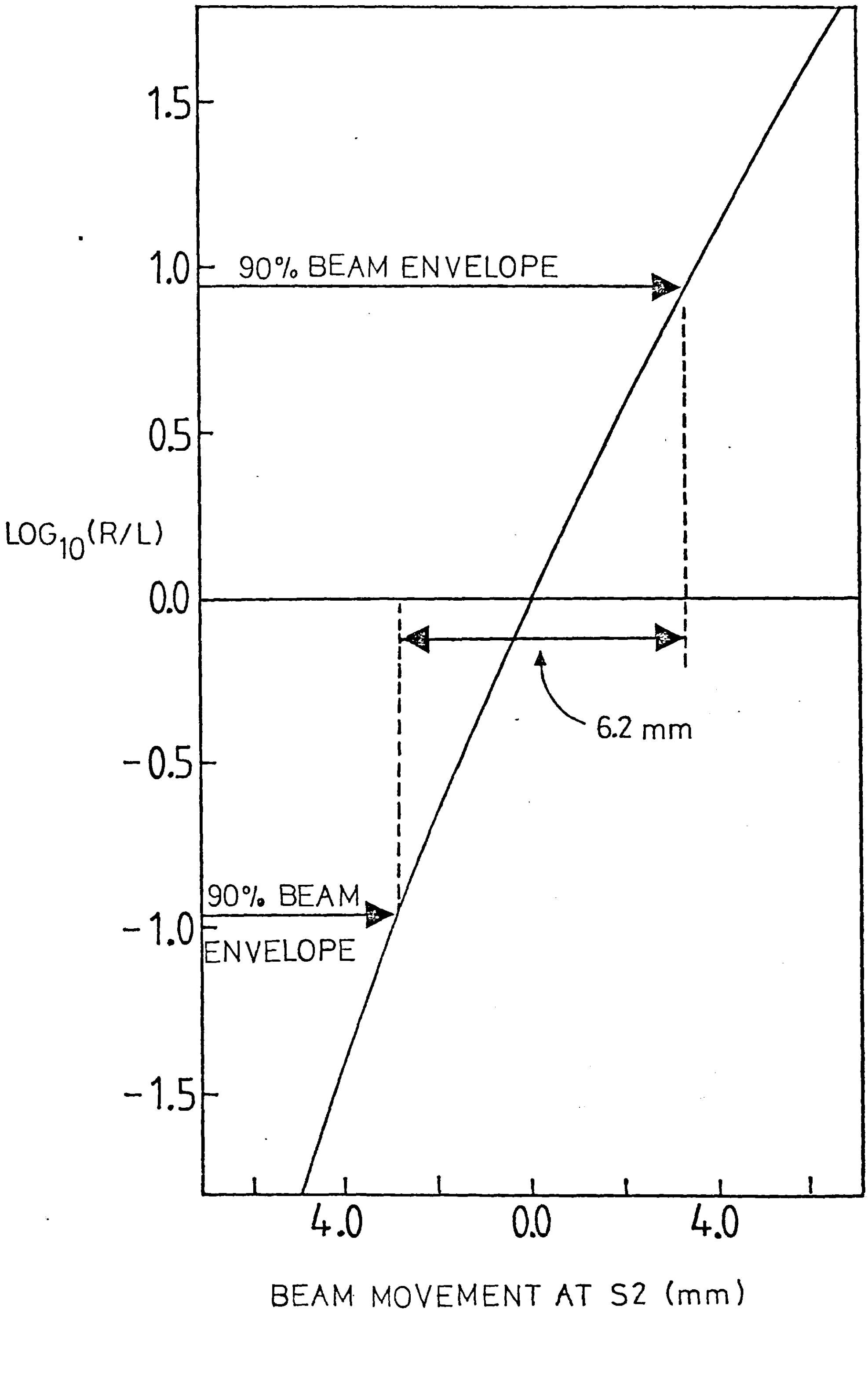

FIGURE 4.10 LOG RATIO OF COUNTS IN S2's RIGHT COUNTER TO THE COUNTS IN THE LEFT AS A FUNCTION OF HORIZONTAL BEAM MOVEMENT AT S2

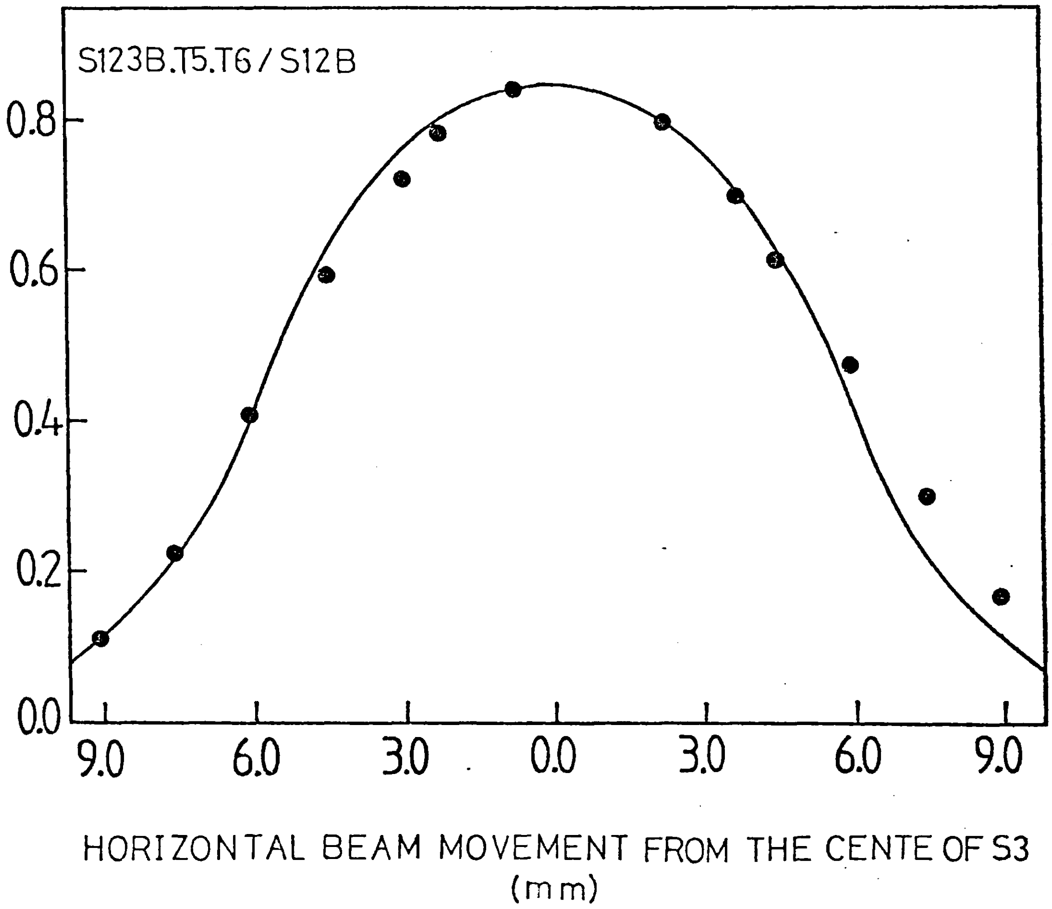

● EXPERIMENTAL POINT

—— VARIATION OF SCALER RATIO ASSUMING A GAUSSIAN BEAM PROFILE WITH σ = 3mm

FIGURE 4.11 THE SCALER RATIO S123B.T5.T6/S12B AS A FUNCTION OF HORIZONTAL BEAM MOVEMENT AT S3

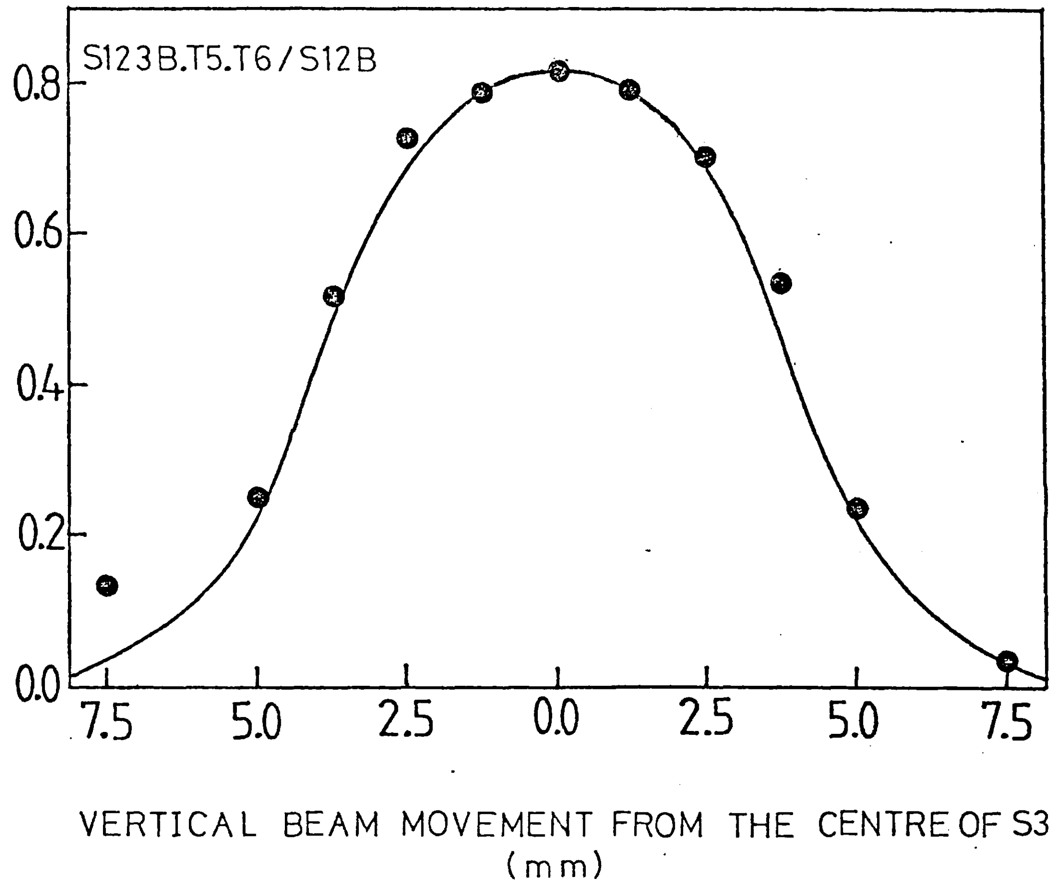

● EXPERIMENTAL POINT

—— VARIATION OF SCALER RATIO ASSUMING A GAUSSIAN BEAM PROFILE WITH $\sigma = 2$mm

FIGURE 4.12 THE SCALER RATIO S123B.T5.T6/S12B AS A FUNCTION OF VERTICAL BEAM MOVEMENT AT S3

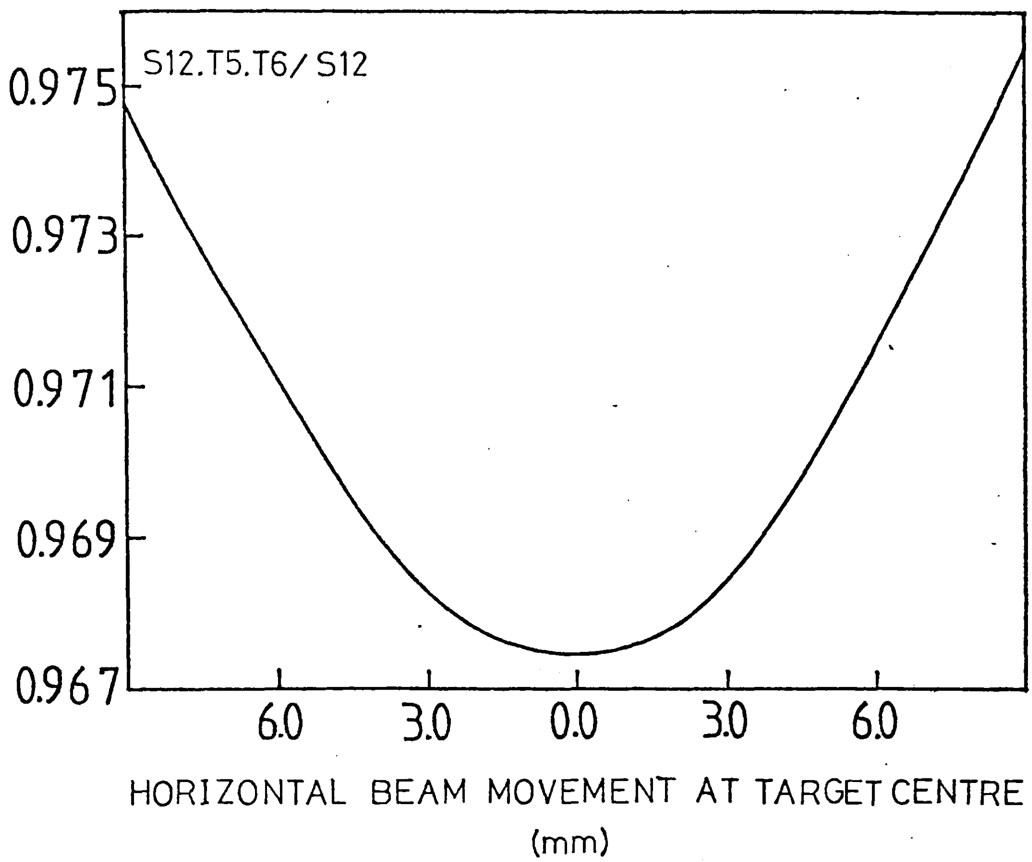

FIGURE 4.13 VARIATION OF TRANSMISSION THROUGH THE TARGET AS A FUNCTION OF THE HORIZONTAL BEAM MOVEMENT AT THE TARGET CENTRE

of power supply setting determined the setting corresponding to the beam being equally spread over both S2R and S2L. The horizontal scans were then repeated after switching S3 back into the S123B coincidence. The variation of the scaler ratio S123B.T5.T6/S123B revealed the centre of S3. A similar set of scans in the vertical plane were performed using SM4. These scans showed the counters were aligned to within 0.3mm horizontally and 0.5mm vertically. The polarized target was found to be 1.3mm to the left and 0.5mm up, with respect to the centre of S3.

The collimator, far from degrading the beam quality, was in fact found to enhance it, by transmitting only the central paraxial protons. At the 325MeV tune, the beam spot at the target was clearly seen to have two distinct images on both 4CM8 and on the exposed polaroid film. These images were thought to have arisen from stripping of adjacent and partially separated turns within the cyclotron. The energy resolution of the extracted beam was thus determined to be of the order of $\pm$100keV, as each separated turn has an energy resolution of $\pm$50keV. Indications of a double beam spot were also seen at 360 and 425MeV.

In these data acquisition runs, the beam was steered onto the target cell for each individual energy. At all energies with the beam centred on the target, the small counter, S3, was found to count 85% of the beam registered by the S1.S2 coincidence. Once tuned and centred on the target cell, polaroid film was exposed at the majority of energies. This was used as a final visual check on the beam spot quality and also to check the centring of the transmission array on the transmitted beam. It was found that at 500MeV, and subsequently at the other energies, the transmission array had to be placed at a 5% greater angle to the beamline than that calculated by the computer simulations. This discrepancy was partially due to using magnetic fields approximately 2 - 3% higher in the target than in the computer simulations, and partially from using a magnetic field interpolated from a $1cm^2$ grid, a smaller grid would have given a more precise value. Once positioned accurately, the efficiency counters E1 and E2 counted approximately 85% of the beam registered by the S123B coincidence.

The systematic checks on the transmission of deliberate changes in beam spot, position and size, and beam ratios, performed in the test runs, were repeated with the same result. With these systematic tests completed data was taken at the seven energies.

The data acquisition was split into a number of runs, each consisted of 2×10^8 protons incident upon the target. This determined $\Delta\sigma_T$ to a statistical precession of approximately ± 0.7mb. At each energy there were approximately six data taking runs, three taken with each target polarization.

At 210MeV, where the beam is deflected most, the transmission through the target was approximately 4% less than expected. This was found to be caused by the beam transmitted by the target cell, glancing a brass support post, part of the target structure. The variation of transmission during a horizontal scan across the target cell showed the obstruction to be to the left, looking down the beamline. Exposed polaroid film revealed the shape of the obstruction. The post was removed and data was then successfully taken.

4.4.3 $\Delta\sigma_L$ Data

During July and August 1980, BL4C was prepared for the $\Delta\sigma_L$ run. The target coils were rotated through 90° to give longitudinal polarization, the coils were surveyed into the beamline at an angle of 12° and the monitor chambers were secured to the target structure. The BASQUE superconducting solenoid was installed into it's position in BL4A.

The $\Delta\sigma_L$ run started on 2nd September 1980 with a beam of 500MeV. The final quadrupole doublet was again only energised at 210MeV and for some runs at 330MeV. Similar beam spots to those obtained for $\Delta\sigma_T$, 6 - 7mm FW were obtained at all energies.

The first few runs at 500MeV were used for checking the solenoid. During these runs it was found that the solenoid steered the beam and thus the beam had to be recentred onto the target for any change in the solenoid current. Online values of the transmission showed the change in transmission between beam spin up and down to be equal, within errors, with the solenoid unpowered. The online checks in Δt also showed the expected sine curve for the partially powered solenoid. The data was also checked for any dependence on small beam steers approximately $\pm$2mm horizontally and vertically. With these systematic checks completed data was taken at 210, 325, 420, 500 and 515MeV. Time did not allow for any data taking at 360MeV. Generally data was taken with both target polarizations, both solenoid power supply polarities, and at least one run was carried out with the solenoid unpowered.

A considerable number of runs were performed at 330MeV after Δt's recorded with the solenoid off were found to be approximately 1/3 of Δt measured with the solenoid on. Beam steering was not found to change the result, neither did the beamline tunes, one with the final quadrupole doublet energised, one without.

The 12° rotation of the target field resulted in a vertical deflection of the transmitted beam. The transmission array had to be jacked up to centre it on the beam. The maximum deflection was approximately 2° at 210MeV.

4.5 Beam Energy

The energy of the beam extracted from the cyclotron was determined, to better than 1MeV, by a TRIUMF routine. This used an accurate field map of the accelerator's magnet, and from the location of the stripper foil calculated the beam energies.

The energies of the beams, extracted from the cyclotron and at the target centre, are listed in table 4.5. From the energy of the

EXPERIMENT	EXTRACTED BEAM ENERGY(MeV)		BEAM ENERGY AT TARGET CENTRE	
	$\Delta\sigma_L$	$\Delta\sigma_T$	$\Delta\sigma_L$	$\Delta\sigma_T$
	520.7	520.8	516.5	516.6
	501.4	501.8	497.1	497.5
	460.2	460.1	455.8	455.7
	424.1	424.0	419.5	419.4
		379.7		374.8
	330.6	330.3	325.4	325.1
	209.8	209.9	202.7	202.8

TABLE 4.5 BEAM ENERGIES

beam at the 35^{o} bending magnet the angle, ϕ_B , was found. These are given in table 4.6.

BEAM ENERGY (MeV)	ϕ_B (DEG)
208.2	76.7
329.6	84.8
423.3	91.1
459.4	93.5
500.7	96.2
519.5	97.5

TABLE 4.6 POLARIZATION PRECESSION ANGLE ϕ_B CAUSED BY A 35° BEND

CHAPTER 5

EVALUATION OF TARGET POLARIZATION

This chapter is concerned with the offline evaluation of the target polarization. This analysis was performed initially on the Amdahl 470/V6 computer at the University of British Colombia. The majority of the data analysis was, however, performed on the IBM 195s at the Science and Engineering Research Council's (SERC) Rutherford and Appleton Laboratory (RAL) at Chilton, Oxfordshire. The tapes produced by the PDP11/34 were at a density of 800bpi. These rather numerous data tapes were copied to new tapes at a higher density, 62500bpi, to ease data handling and transport.

The chapter is split into four sections. The first section deals with the performance and results obtained from the NMR monitor. The further three sections of the chapter are concerned with the analysis of the monitor chamber data. The second section covers the analysis of the TDC data and procedures common to both the $\Delta\sigma_L$ and $\Delta\sigma_T$ experiments, eg event reconstruction and subtraction of background events. The final two parts deal separately with obtaining target polarization data for $\Delta\sigma_L$, and for $\Delta\sigma_T$, from the p-p data extracted from the chamber data.

5.1 NMR Target Polarization Evaluation

5.1.1 $\Delta\sigma_L$ NMR Results

In the $\Delta\sigma_L$ experiment the NMR system worked faultlessly. Values of the NMR integral were computed and updated every five seconds during the data acquisition runs. The integrals were evaluated from the average of sixteen radiofrequency sweeps. These sweeps were centred on a frequency of 108.8MHz, using a step length of 1kHz.

The NMR integral was appended to the end of each event word written to tape. Using these values the mean NMR integral and its standard deviation were calculated for each run. The stability of the NMR system was such that the NMR integral only fluctuated by approximately 0.06% over the duration of an average run, which was approximately 40 minutes.

The reversal of the target polarization involved a change of the microwave pumping frequency supplied to the target cell. The new polarization grew very rapidly on changing the frequency. The NMR integral values showed the polarization to have achieved approximately 97% of its maximum value 60 minutes after changing the microwave frequency.

During the course of the experiment the maximum achievable target polarization was seen to fall by approximately 10%. This was thought to be caused by radiation damage of the target. The maximum values of target polarization for both positive and negative orientation were seen to be broadly similar, and both showed the trend of decreasing maximum achievable polarization with increasing time.

The ratio of the calculated target polarization at thermal equilibrium to the NMR integral measured at thermal equilibrium (NMR_{TE}), gave the calibration factor relating the enhanced target polarization to the enhanced NMR integral (NMR_{ENH}). Two measurements were made of NMR_{TE}, one before and one after the $\Delta\sigma_L$ experiment.

The thermal equilibrium measurements were both performed at a temperature of 0.935 ± 0.015K, measured by He^3 vapour pressure. At this temperature the target needs to be left for one and a half to two hours to stabilize to its thermal equilibrium polarization.

Measurements of NMR_{TE} were made using a centre sweep frequency of 108.8MHz, with a 1kHz step size. The integral was evaluated every 60 seconds from the average of sixteen radiofrequency sweeps. The PDP11/34 was used to read and produce a hardcopy, via a line printer, of these integrals. The measurements at the start of the experiment recorded 65 values of NMR_{TE}, the measurements at the end of the experiment took a total of 360 integrals. The integrals obtained showed two things. Firstly, no trend of increasing or decreasing during the period of the measurement, and secondly the points were randomly distributed above and below the mean value. This behaviour showed the target to be at thermal equilibrium and the variation in the integrals to be due to noise and random fluctuations.

The average value of the thermal equilibrium integrals from the two measurements were in excellent agreement. The two values were used to produce a weighted mean value for NMR_{TE} of 2751 ± 168. These values were obtained using an amplifier gain of 100. The thermal equilibrium target polarization was calculated using equation 5.1.1, which is obtained from equation 2.3.1,

$$P_{TE} = \tanh \left(\frac{h\nu_0}{2KT} \right) \qquad 5.1.1$$

where ν_0 is the centre frequency of the radiofrequency sweep. At an operating temperature of 0.935K and with a ν_0 of 108.8MHz, $P_{TE} = 0.279\%$. The expression relating the enhanced target polarization, P_T, to NMR_{ENH}, is,

$$P_{T(\Delta\sigma_L)} = NMR_{ENH} \left(\frac{0.279}{2751} \right) \left(\frac{100}{A} \right) \qquad 5.1.2$$

where the factor (100/A) allows for the different amplifier gains. A is set to the amplifier gain at which the NMR_{ENH} measurement was made.

The error in P_T was calculated using,

$$\left(\frac{\Delta P_T}{P_T} \right)^2 = \left(\frac{\Delta NMR_{ENH}}{NMR_{ENH}} \right)^2 + \left(\frac{\Delta NMR_{TE}}{NMR_{TE}} \right)^2 + \left(\frac{\Delta P_{TE}}{P_{TE}} \right)^2 \qquad 5.1.3$$

The first term on the right hand side of equation 5.1.3 was found to be typically 3.6×10^{-5}, the last term was 3.2×10^{-2}. The majority of the error in P_T arises from the poor signal to noise ratio encountered in determining NMR_{TE}, leading to a value for $\left(\frac{\Delta NMR_{TE}}{NMR_{TE}} \right)^2$ of 37.21. The total error in P_T from all three terms was 6.4%.

Using the NMR_{ENH} calibration factor for determining P_T , from equation 5.1.2, the maximum and average values for P_T $(\Delta\sigma_L)$ were obtained.

	$P_T(\Delta\sigma_L)$	
TARGET POLARIZATION	MAXIMUM	AVERAGE
NEGATIVE	$-66.8 \pm 4.3\%$	-63%
POSITIVE	$65.5 \pm 4.3\%$	64%

5.1.2 $\Delta\sigma_T$ NMR Results

In the $\Delta\sigma_T$ configuration the NMR pick up coil was in the shape of a solenoid. This geometry gave a greater coupling to the target volume than that provided by the saddle coil used for the $\Delta\sigma_L$ experiments. This increase in coupling showed itself by an increase in output, reducing by a factor 3 the signal to noise ratio in determining NMR_{TE} compared to the $\Delta\sigma_L$ determination.

As in the $\Delta\sigma_L$ experiment, thermal equilibrium integrals were measured before and after the experiment. An additional set of data was also taken at a much lower temperature in the middle of the experiment.

The data taken at the start and finish of the experiment was recorded at a temperature of 0.875 ± 0.005K around a central radiofrequency of 109.1MHz, using 1kHz steps. Two sets of data were taken at the start of the run using gain x1 and gain x10 settings on the amplifier. Both sets of data were found to be consistent, showing the linearity of the amplifier over these two settings. The data taken at the end of the experiment was split into three separate evaluations of NMR_{TE}. The values obtained were all consistent within errors. All five sets of data were combined to give a weighted mean value for NMR_{TE} of 13431 $\pm$262 at an amplifier gain of 100. The calculated thermal equilibrium polarization, from equation 5.1.1, is P_{TE} = 0.299% $\pm$0.002%. The $\Delta\sigma_T$ target polarizations were obtained from the enhanced NMR integrals using the following equation,

$$P_{T(\Delta\sigma_T)} = NMR_{ENH} \left(\frac{0.299}{13431}\right) \left(\frac{100}{A}\right) \qquad 5.1.4$$

The percentage error in P_T is again obtained using equation 5.1.3. The dominant term in the expression arises from the uncertainty in NMR_{TE}, 1.95%, the error in P_{TE} contributes 0.67%. For $\Delta\sigma_T$ the enhanced NMR integral was found to be not as stable as for $\Delta\sigma_L$. The average percentage error in NMR_{ENH} was approximately 1.0 (0.3)% for negative (positive) target polarizations.

During the experiment the target was maintained at 0.490 $\pm$0.005K, at which P_{TE} = 0.534 $\pm$ 0.005%, for a period of approximately seven hours. At this temperature the target takes around three hours to reach thermal equilibrium. At the lower temperature, the value of NMR_{TE} was 24293 $\pm$275. The expected value for NMR_{TE} at 0.49K can be calculated from the NMR_{TE} value obtained at 0.875K, using the ratio of the temperatures. This calculated value of 23987 $\pm$540 is in agreement with the measured value. This agreement confirms the correct evaluation of these low temperatures.

During the course of the experiment it was found that for positive target polarization the NMR integrals were only approximately 60% of those obtained for the target negatively polarized.

The reason for the difference in the magnitude of the two NMR integrals was explained as occuring due to a saturation effect of the positive NMR signal. This had the effect of levelling off the positive NMR integral at a fixed ceiling of P_T at approximately 45%. The data to back up this reasoning came from three independent sources of information outlined below.

Firstly, the maximum achievable target polarizations in the $\Delta\sigma_L$ experiment had showed a trend of an approximate 10% decrease during the course of the experiment. In the $\Delta\sigma_T$ experiment, the negative polarization showed this trend. However, the positive polarization showed no such trend, instead it remained small and approximately constant.

The second piece of supportive evidence came from the target polarization times. The target polarization grew rapidly once the microwave power was applied. The negative polarization carried on growing rapidly for approximately one hour and then tailed off, reaching full polarization only after approximately two hours. The positive polarization grew rapidly, and then only after fifteen to twenty minutes, the rate of increase tailed off dramatically, indicating a possible amplifier saturation.

Thirdly, the fluctuation, or jitter, of the NMR integral was found to be the same order of magnitude for both target polarization orientations in the $\Delta\sigma_L$ experiment. In the $\Delta\sigma_T$ experiment, however, the fluctuation was a factor of five less for positive than for the negative polarization. This suggested that the true fluctuations in the target polarization were being compressed for the positive polarization by the NMR amplifier.

In total this information suggested that the amplifier used for the positive polarization was saturating. The input signal was overloading the amplifier once the target polarization reached 45% and the NMR integral produced did not represent a true target polarization.

During data acquisition for $\Delta\sigma_T$ at 500MeV, the saturation effect occured for both positive and negative polarizations. The saturation effect of the NMR for negative polarization only was able to be removed during a maintainence period after the 500MeV data taking, and before taking subsequent data at the other energies.

The maximum and average values of P_T, derived using the thermal equilibrium calibration for negative target polarization, were,

	$P_T(\Delta\sigma_T)$	
TARGET POLARIZATION	MAXIMUM	AVERAGE
NEGATIVE	$-75.5 \pm 1.9\%$	-67%

In conclusion, the NMR system worked faultlessly during the $\Delta\sigma_L$ run, but for $\Delta\sigma_T$ the NMR integrals produced for positive polarizations were being truncated. The NMR evaluations of the target polarization were to be compared with those obtained by the completely independent monitor chambers.

5.2 Analysis of Target Monitor Chamber Data

5.2.1 TDC(SUM)

The pulses from both ends of the delay lines in the chambers were used as stops for TDCs. The trigger used to start the TDCs was the detection of a coincidence occuring in the scintillators monitoring the forward and recoil chambers. In an ideal situation the sum of the two numbers generated by the two TDCs, one monitoring each end of the delayline. is a constant TDC(CONST). This constant is the delay line length in TDC units plus a timing constant. The TDCs used had a calibration of 5 TDC counts per nanosecond. There are, however, a number of reasons why the sum of the two TDC numbers,TDC(SUM), is not a constant.

The positive ions formed by a proton traversing the chamber are accelerated towards the cathode wires to produce a pulse which is transmitted to a delay line. There is, therefore, a variable time component in TDC(SUM) dependent on the distance of the incident proton from the cathode wire. If the incident proton is adjacent to the cathode wire then TDC(SUM) is equal to TDC(CONST). If the ionizing event occurs a finite distance from the cathode wire, then each TDC number contains a term arising from the finite collection time of the event. TDC(SUM) is now larger than TDC(CONST).

A delay line pulse can also be created by sparking, caused by dirt on the chamber wires. Pulses created in this way are called hot wire pulses. If a TDC trigger occurs about the time of a hot wire fire, then one TDC can be stopped by the arrival of the hot wire pulse. This has the effect of decreasing TDC(SUM) and rendering the recorded TDC data, for that trigger, useless.

A TDC(SUM) histogram is shown in fig 5.1. This histogram was produced by a chamber having a hot wire. The shape of the histogram is explained by considering the effects mentioned in the previous paragraphs. The events, occuring adjacent to the cathode wire, produce a narrow peak centred on TDC(CONST). This peak will have a finite width due to electronic noise. The component in the TDC(SUM) histogram arising from these events is represented, schemeatically by the solid line on fig 5.2. Events with a finite collection time produce a high end tail on the peak, the dashed line on fig 5.2. The effect of one or more hot wires is to introduce a low end tail into the histogram, the dotted line on fig 5.2. The TDC(SUM) histogram from a chamber in good condition is shown in fig 5.3.

Histograms of TDC(SUM) were produced for a number of runs at different energies. From these histograms cuts were chosen so as to remove of the small number of background events, and hot wire contaminated data. These cuts were then applied to all runs to exclude this data from further analysis.

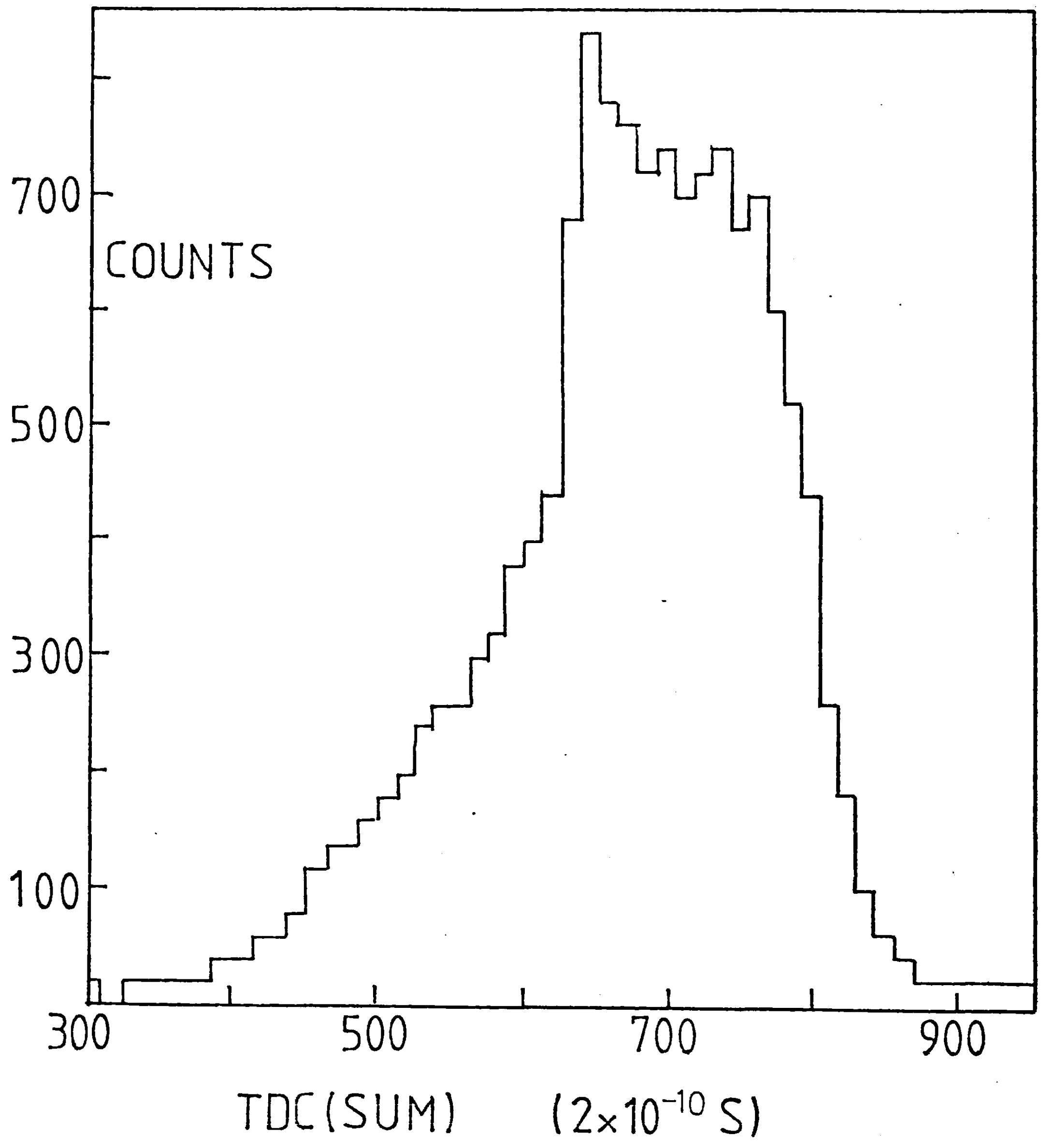

FIGURE 5.1 TDC(SUM) HISTOGRAM, OBTAINED FROM A DELAY LINE CHAMBER WITH A HOT WIRE

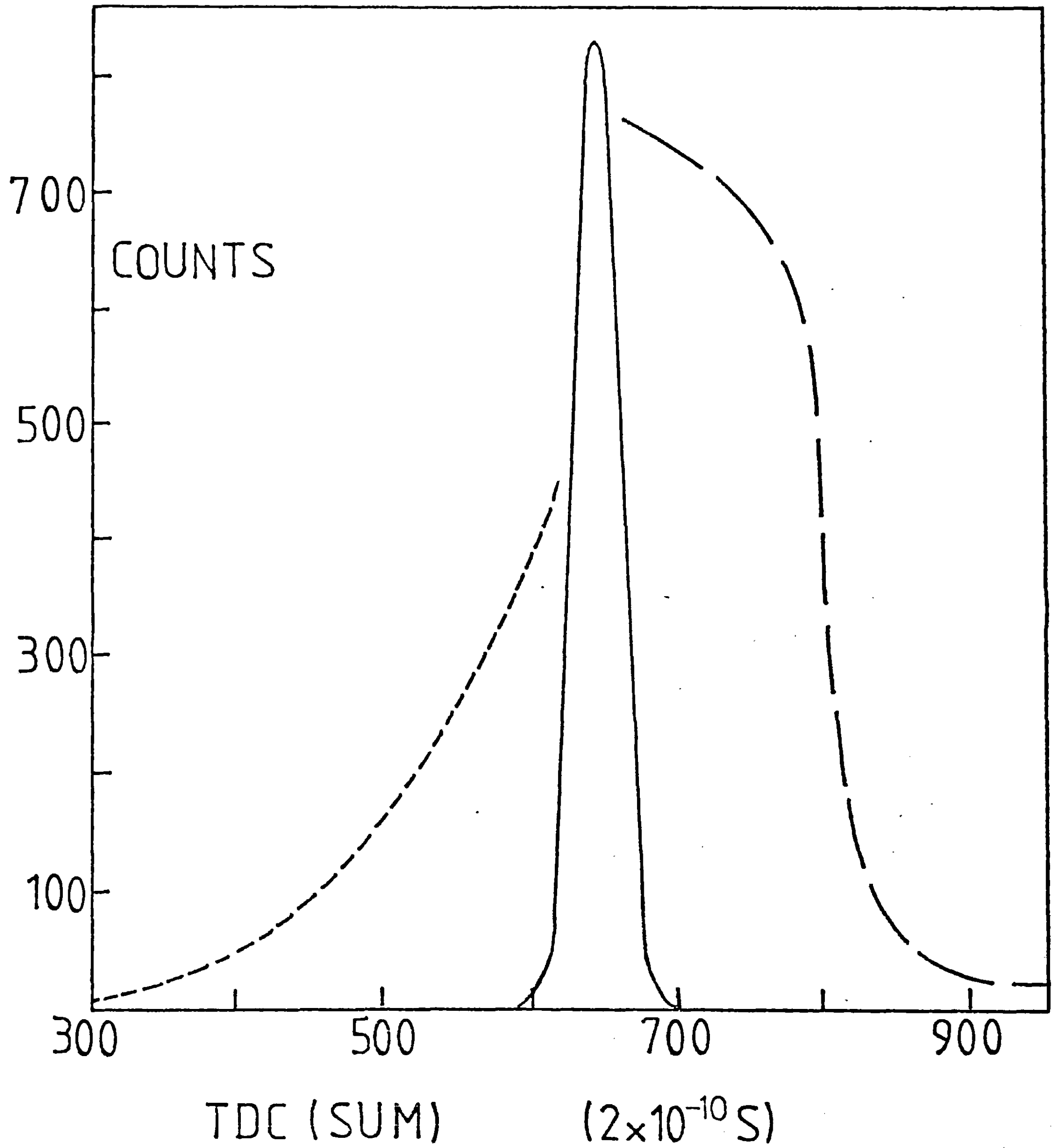

FIGURE 5.2 SCHEMATIC HISTOGRAM SHOWING CONSTITUENT COMPONENTS OF FIG. 5.1

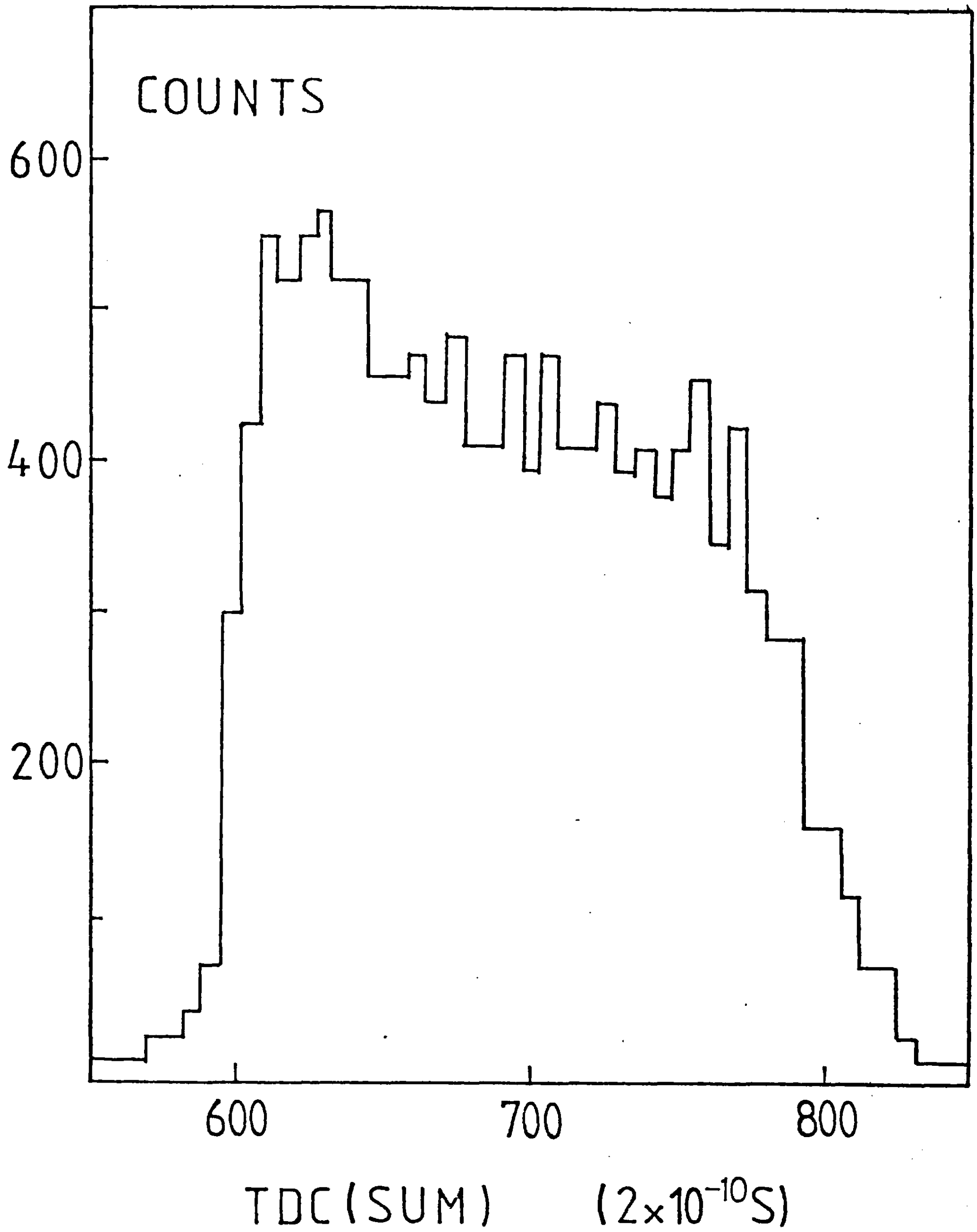

FIGURE 5.3 TDC(SUM) HISTOGRAM OBTAINED FROM A DELAY LINE CHAMBER IN GOOD CONDITION

5.2.2 TDC(COORD)

A coordinate for the position of a signal reaching a delay line is produced by subtracting one TDC number from the other, giving TDC(COORD). For a general event, one TDC records a time, TDC1 + C, where C is the charge collection time. The other records a time, TDC2 + C. The coordinate of this event is TDC1 - TDC2, thus TDC(COORD) is independent of the charge collection time C.

Having first applied TDC(SUM) cuts to the data histograms of TDC(COORD) were produced for a number of runs at all energies. These histograms showed the distribution of events across the chamber. The chamber triggering scintillators were placed approximately 5cm behind the monitor chambers. They did not completely cover the chamber's active area. The TDC(COORD) histograms were, therefore, composed of a well-defined central region of dimensions given by the projection of the triggering scintillators, as seen from the target, onto the wire planes. There were also a small number of background events extending to the edge of the chamber's active area. TDC(COORD) cuts were introduced to remove these background events. The upper and lower edges of the central regions of the TDC(COORD) histograms were expanded to find the exact position to apply the cuts. An example of a magnified upper edge histogram is shown in fig 5.4. From the measured position of the target centre, the triggering scintillators and the chambers; the dimensions of the trigger region at the chamber wire plane, the effective trigger size, were calculated. The distances of the chamber wire planes from the target centre, together with the

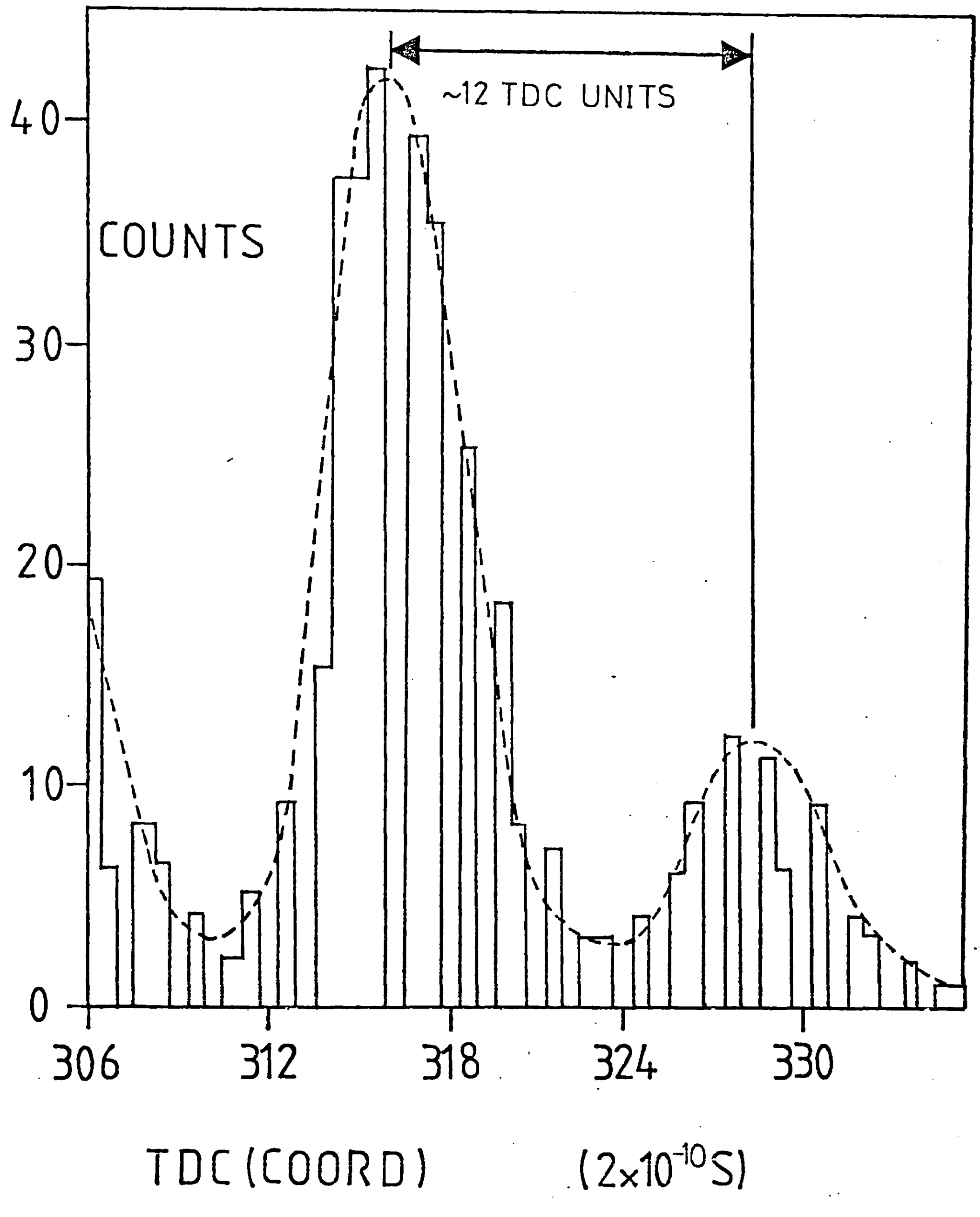

FIGURE 5.4 TDC(COORD) HISTOGRAM, SHOWING INDIVIDUAL WIRES

effective trigger sizes and the angle subtended by the centre of the triggering scintillators to the beamline, are listed in table 5.1. The nomenclature used to lable the chambers and scintillators is shown in fig 5.5.

The histogram in fig 5.4 was taken from the horizontal plane of the right recoil chamber in the $\Delta\sigma_L$ experiment, where the trigger length was 13.58cm, the full TDC(COORD) histogram had a range of 822 TDC units. In fig 5.4 two individual wires can be seen. The separation between these wires was approximately 12TDC units, the cathode wire separation is given by (12/822) x 13.58 $\sim$ 0.2cm.

The large monitor counters detected both elastic p-p scattering and background events scattered from non-hydrogenous material in the target. It was necessary to remove this contaminating data. For pure p-p elastic scattering the incident, scattered and recoil protons are all coplanar and thus a deviation from coplanar scattering is an indication of a non p-p event. The opening angle can also be different for p-p scattering and non-hydrogenous scattering events.

The TDC(COORD) data from the forward and recoil chambers was used to constructan opening and a coplanarity angle for each event.

EXPERIMENT	CHAMBER	DISTANCE FROM TARGET CENTRE (CM)	TRIGGER SIZE(CM) HORIZONTAL PLANE	VERTICAL PLANE	ANGLE BETWEEN TRIGGER CENTRE AND BEAMLINE
$\Delta\sigma_L$	RR′ 1	35.0	12.0	13.3	53.6°
	RR′ 2	39.7	13.6	15.1	53.6°
	RF1	34.4	11.9	12.9	31.1°
	RF2	39.1	13.5	14.6	31.1°
$\Delta\sigma_T$	RR′	34.5	13.9	9.4	69.6°
	LF	39.1	15.3	10.7	30.1°
	RF	38.2	17.1	10.4	21.8°
	LR′	34.5	14.1	9.4	52.6°

TABLE 5.1 GEOMETRY OF MONITOR CHAMBERS

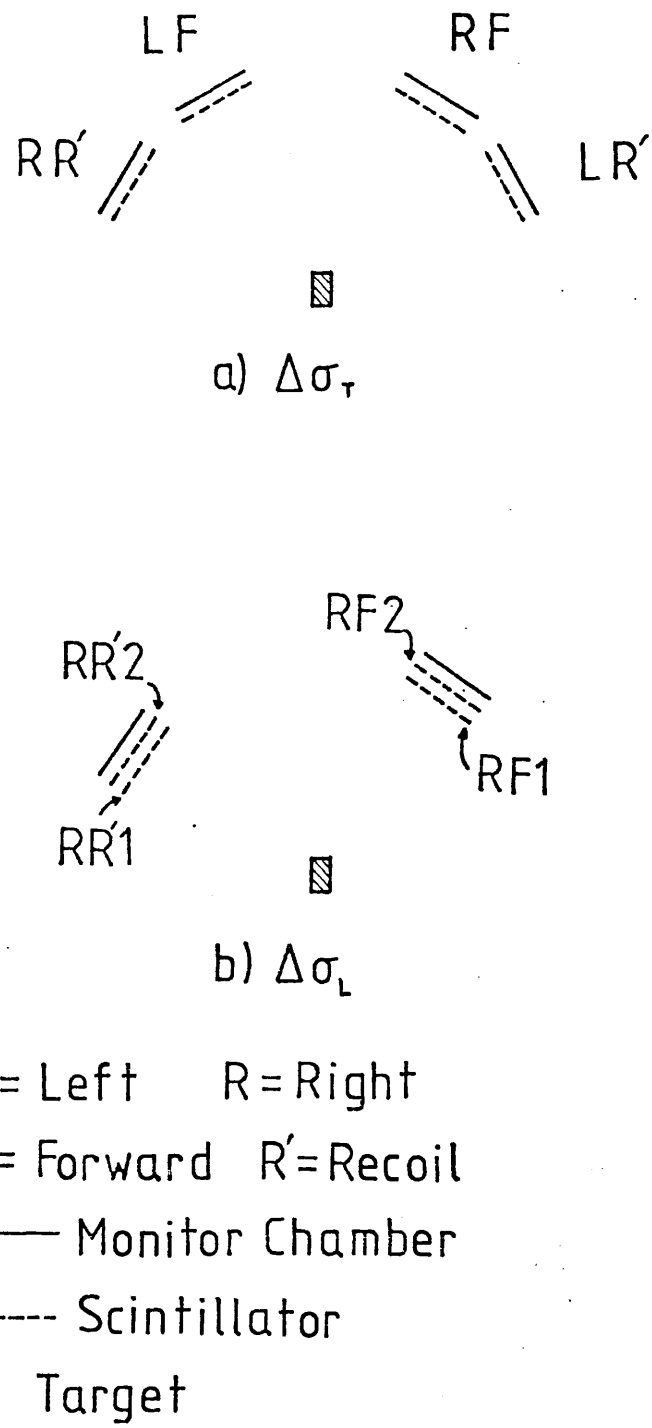

FIGURE 5.5 SCHEMATIC DIAGRAM OF MONITOR CHAMBERS AND SCINTILLATORS FOR A) $\Delta\sigma_T$ AND B) $\Delta\sigma_L$, VIEWED FROM ABOVE. THE BEAM APPROACHES FROM THE BOTTOM OF THE PAGE

5.2.3 Event Reconstruction

To reconstruct a detected event, a vertical and horizontal impact coordinate for each chamber was produced. The positions of the impacts were defined using an axis set XY, for each chamber. The axes were centred at the centre of the trigger area of the chamber. The axes were defined such that negative X(Y) was in the right (upper) section of the chamber as viewed from the target.

To produce coordinates from the TDC data on the axes set XY, a constant OFFSET had first to be added to each value of TDC(COORD). The value of OFFSET depended on the difference in path length that the two TDC stop signals had to travel to reach the TDC units in the electronics trailer. The value of OFFSET was found from the histograms of TDC(COORD). OFFSET was the difference between zero and the centre of the histogram. Once determined, the impact coordinates, COORD, were obtained from TDC(COORD) using equation 5.2.1.

$$\mathrm{COORD} = \frac{\text{TRIGGER LENGTH}}{\begin{array}{l}\text{RANGE OF TDC(COORD)}\\ \text{HISTOGRAM}\end{array}} \Big(\mathrm{TDC(COORD)} + \mathrm{OFFSET}\Big) \qquad 5.2.1$$

The horizontal plane scattering angle of the proton, relative to the centre of the scintillator, was obtained from COORD and the distance between the target and the chamber wire plane, L. The total horizontal plane scattering angle, θ_{HSCAT}, was then the addition of this and the angle the centre of the scintillator makes with the beamline axis, θ_{SCI}. For scattering to the right of the beamline,

$$\theta_{HSCAT} = \theta_{SCI} - \mathrm{Tan}^{-1}\ (\mathrm{COORD/L}) \qquad 5.2.2$$

and for scattering to the left of the beamline,

$$\theta_{HSCAT} = \theta_{SCI} + \mathrm{Tan}^{-1}\ (\mathrm{COORD/L}) \qquad 5.2.3$$

where θ_{HSCAT} were calculated to always be positive. From the vertical coordinates a vertical plane scattering angle, θ_{VSCAT}, was calculated. The vertical and horizontal plane scattering angles were combined to give a total scattering angle θ_{SCAT},

$$\theta_{SCAT} = \mathrm{Cos}^{-1}\left[\mathrm{Cos}\ (\theta_{VSCAT})\ \mathrm{Cos}\ (\theta_{HSCAT})\right] \qquad 5.2.4$$

The target's magnetic field, however, caused a deflection of the incident and scattered protons. To obtain the true scattered angles, these magnetic deflections must be considered.

5.2.4 Magnetic Deflections

In the $\Delta\sigma_T$ configuration the magnetic field associated with the target deflects the beam in the horizontal plane.

The magnetic deflection contribution to the scattering angle can be split into two components. The first is the magnetic angular deflection caused to the incident beam in reaching the target centre. This deflection is half the deflection of a beam traversing the complete field. This had been previously calculated , see fig 4.9. These calculated deflections needed scaling by 5% to agree with experimentally measured values. The half field deflections were simply subtracted from the measured horizontal scattering angle, θ_{HSCAT}, to give the new horizontal scattering angle, θ'_{HSCAT}.

The angle, θ'_{HSCAT}, was composed of two terms, the true horizontal scattering angle, θ''_{HSCAT}, and the second magnetic deflection component, arising from the magnetic deflection of the scattered proton. The momentum of the scattered proton is dependent on the angle of scatter and the incident proton momentum. Thus, for a given scattering angle, the momentum of the scattered proton is known and the magnetic deflection can be calculated. In this way the two components of θ'_{HSCAT}, the true scattering angle θ''_{HSCAT}, and the magnetic deflection were determined.

The momentum of the recoil proton could then be calculated, as the scattering angle of the forward proton had been determined. The magnetic deflection of the recoil proton was calculated and subtracted from its measured recoil angle to give the true recoil angle.

In the $\Delta\sigma_L$ configuration, the 12° rotation of the target's magnetic field introduces a vertical deflection of the proton beam. This was treated in a similar manner to that described for $\Delta\sigma_T$, to obtain the true scattering and recoil angles.

The vertical deflection caused to the beam in reaching the target centre had previously been calculated, see section 4.2. This was subtracted from the measured vertical angle. The ray tracing program, section 4.2, was used to find the path integral for a proton traversing the magnetic field at a range of angles, corresponding to the angular range covered by the monitor chambers. It was found that the path integral in this angular range could be parameterised by,

$$\int B_T dl = 0.003712\alpha - 0.01516 \text{ (Tm)} \qquad 5.2.5$$

where α is the angle, in degrees, between the magnetic field axis and the proton trajectory. B_T is perpendicular to the momentum.

With a knowledge of the path integrals, the magnetic deflection caused to the scattered and recoil protons was calculated. The detected chamber position of the protons was then corrected for this magnetic deflection in the manner described for $\Delta\sigma_T$, to obtain the true scattering and recoil angles.

5.2.5 Coplanarity and Opening Angles

From the true scattering and recoil angles, the equation of two unit vectors, $\underline{S}$ and $\underline{R}$ aligned in the direction of the scattered and recoil protons travelling from the target centre, were formed. A unit vector $\underline{I}$ aligned along the direction of the incident beam was also constructed.

The cross product of the incident and scattered vectors was used to define a unit normal to the scattering plane. The angle between the recoil vector and this normal, defined the coplanarity angle. An angle of 90° showing the scattering to be coplanar, that is the vectors $\underline{I}$, $\underline{S}$ and $\underline{R}$ are all contained in a plane.

The opening angle was defined by the angle between the scattered and recoil proton vectors.

5.2.6 Selection of Hydrogen Events

For each run, the coplanarity and opening angles for each event were formed and histogrammed. This was done separately for data from each of the three beam polarization states. The information to be extracted from these histograms was the number of p-p elastic events scattered into the monitor chambers.

Opening angle histograms obtained for $\Delta\sigma_L$ and $\Delta\sigma_T$ were similar. They consisted of a central peak with a full width at half maximum (FWHM) of approximately $3.5 - 4.5^{\circ}$. This peak was superimposed upon a broad background of events occuring over an angular range of approximately 35°. An example of a typical opening angle histogram is shown in fig 5.6. This was produced from a $\Delta\sigma_L$ run at ~460MeV. The width of the central p-p peak arises from the effects of the finite target and beam size, together with a smearing caused by beam divergence. The background events arise from scattering of protons from nuclei other than hydrogen.

The coplanarity histograms had a similar structure to the opening angle histograms, that of a central p-p peak superimposed on

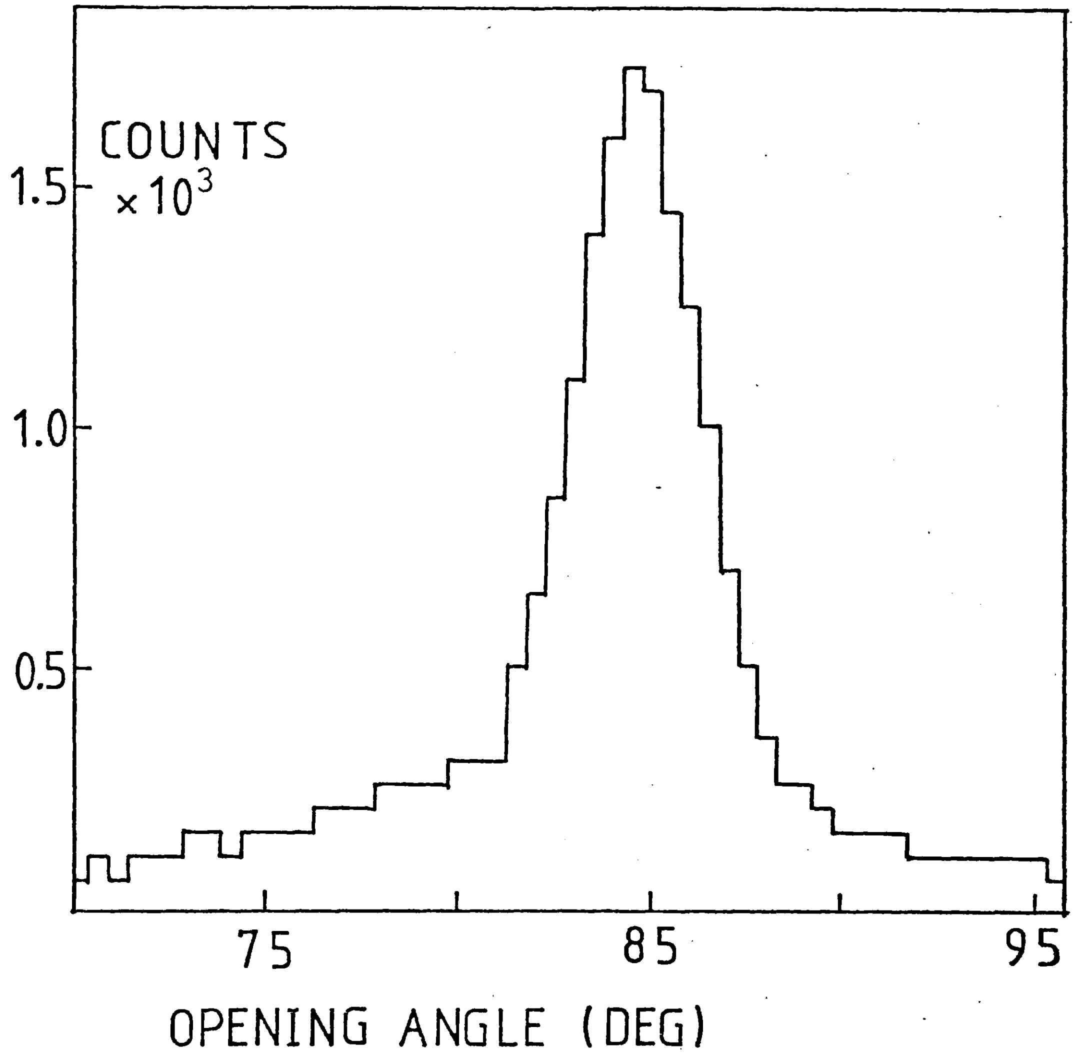

FIGURE 5.6 OPENING ANGLE HISTOGRAM PRODUCED FROM DATA TAKEN IN A $\Delta\sigma_L$ RUN AT 455.8 MeV

background events covering a large angular range. The coplanarity plots were symmetric about the p-p peak. The p-p data was extracted from these histograms. An example coplanarity histogram is shown in fig 5.7, taken from a $\Delta\sigma_T$ run at 325MeV.

The opening angle information was used to improve the p-p to background event ratio by applying a weight to events used to fill the coplanarity histograms. An exponential weighting function was used, given by

$$\mathrm{EXP}\ -\left[\frac{(\overline{\theta}-\theta)^2}{X^2}\right]$$

where $\overline{\theta}$ is the average opening angle, θ is the opening angle of the individual event, X is the variable weighting parameter. The average opening angle, $\overline{\theta}$, was evaluated from opening angle histograms. A value of $\overline{\theta}$ was evaluated for each energy, for each chamber set, for each experiment. It was found that with X set to 5° the background events were reduced by approximately 50%. Using a value of X much smaller than this was found to substantially reduce the number of p-p events. The effect of the weighting function on the coplanarity histogram is seen by comparing fig 5.7 with 5.8. Fig 5.8 was produced using the same data as 5.7, only the opening angle weighting function was applied to the data before histogramming.

The proceedure adopted to extract the pure p-p events from the background was by the use of a double function fit to the coplanarity histogram, using a least squares fitting routine.

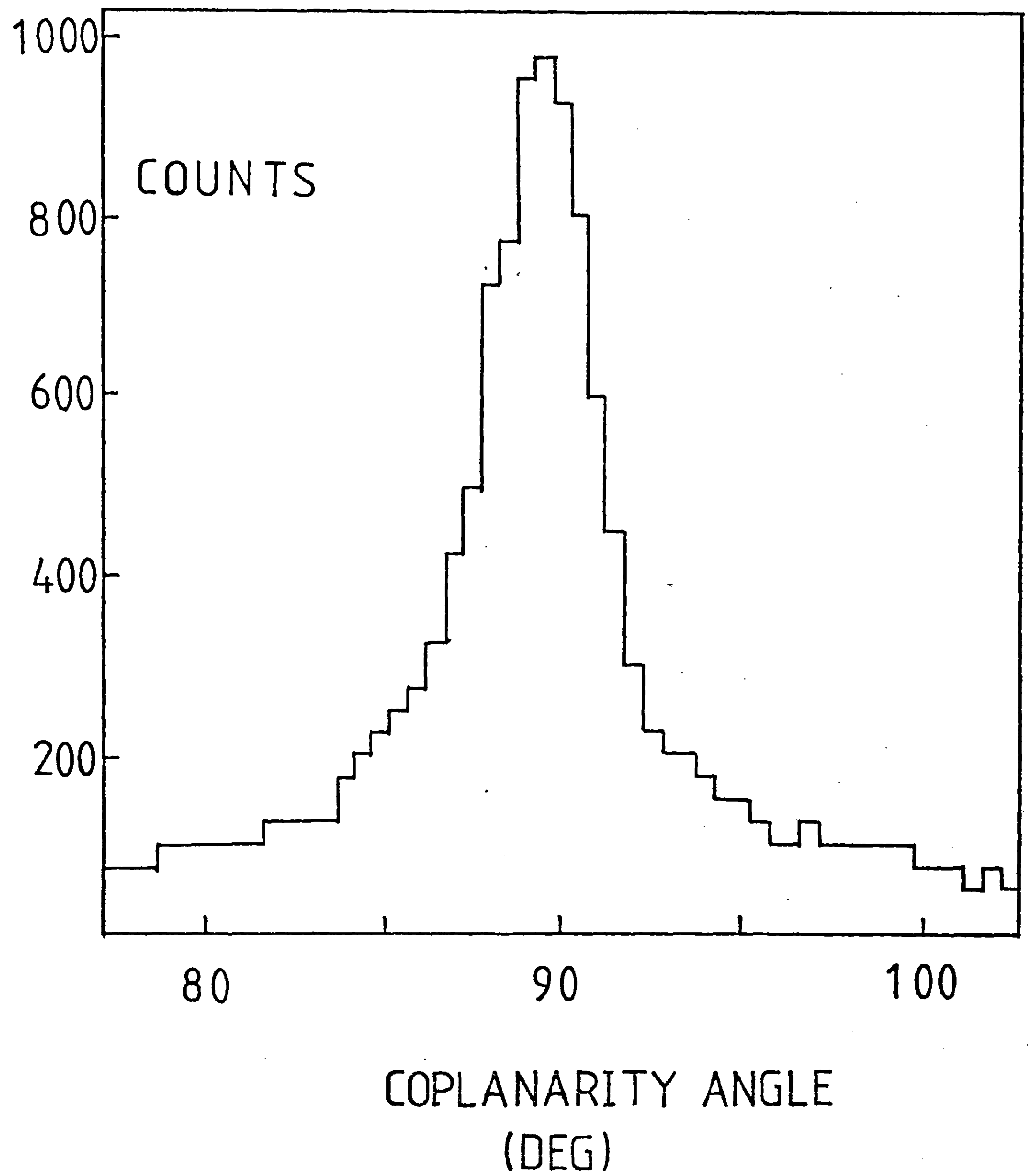

FIGURE 5.7 COPLANARITY HISTOGRAM, PRODUCED FROM DATA TAKEN IN A $\Delta\sigma_T$ RUN AT 325.1 MeV

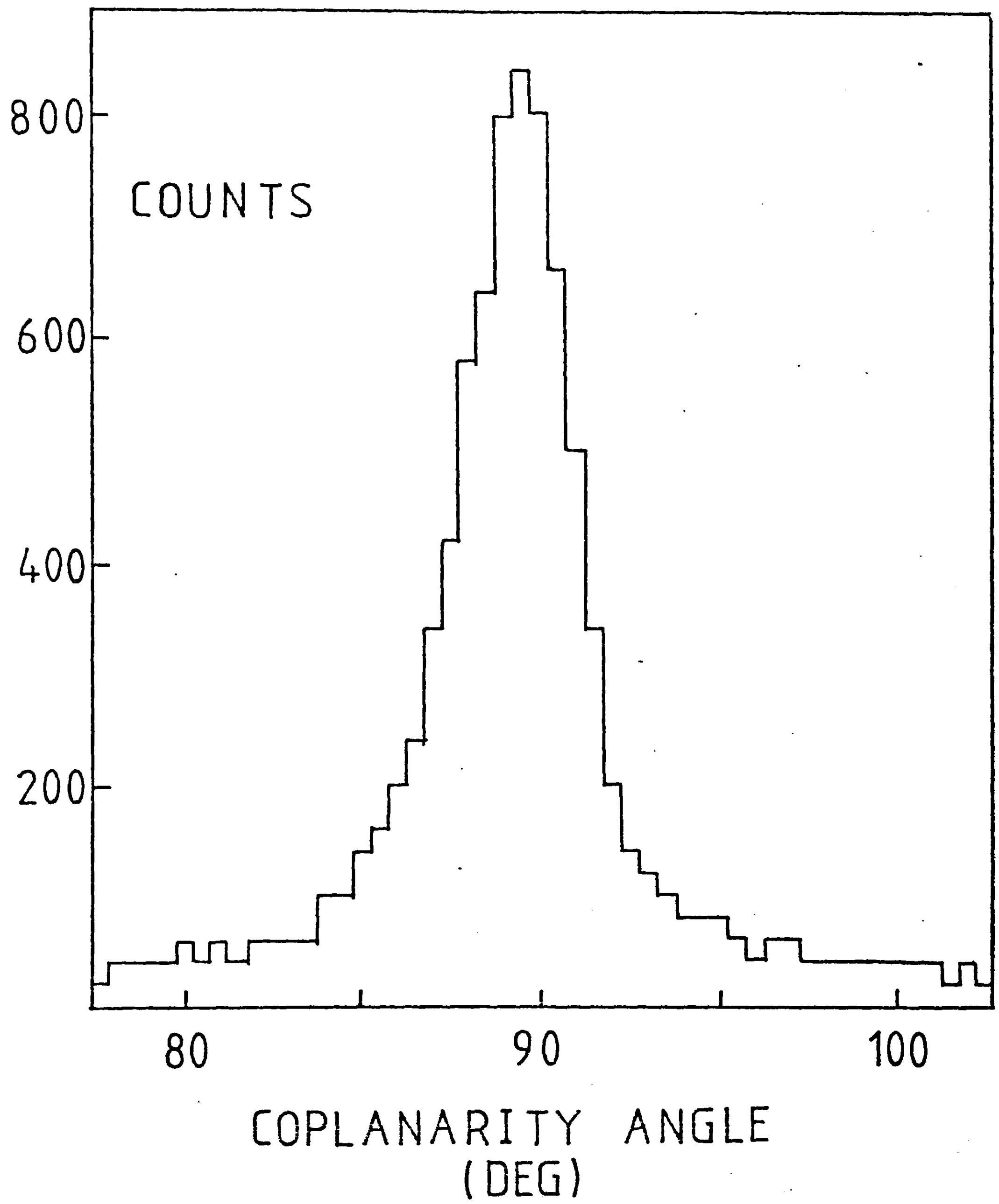

FIGURE 5.8 WEIGHTED COPLANARITY HISTOGRAM PRODUCED FROM THE SAME DATA AS THAT USED IN FIGURE 5.7

Initially, a fit using a central gaussian, superimposed upon a quadratic background was tried. It was found that this was a poor representation of the histogram's shape. The quadratic did not fit the background well. A second fit used a double gaussian function, and this was found to give good fits to the histograms.

This distribution of events around the mean coplanarity angle was symmetric for both the background and p-p events. The double gaussian function used to fit the histograms used five variable parameters, P(1) - P(5), given by

$$P(1)\ \mathrm{EXP}\left[\frac{-(X - P(2))^2}{2P(3)^2}\right] + P(4)\ \mathrm{EXP}\left[\frac{-(X - P(2))^2}{2P(5)^2}\right]$$

Estimates for the widths of the distributions, P(3) for p-p and P(5) for the background, were input as a starting point for the fitting routine.

An example of the double gaussian fit for ~460MeV taken from the left monitor, $\Delta\sigma_T$, is shown in fig 5.9 for both beam polarized up and down, with P_T fixed.

Although the gaussian fitted the central peak well at all energies for both experiments, the area under the peak, the p-p signal, was taken from the subtraction of the fitted background gaussian from the coplanarity histogram. This subtraction method allowed for any deviation of the central peak from a true gaussian shape. The region of the subtraction was defined by $P(2) \pm 5P(3)$. This subtraction region incorporated essentially all the p-p peak.

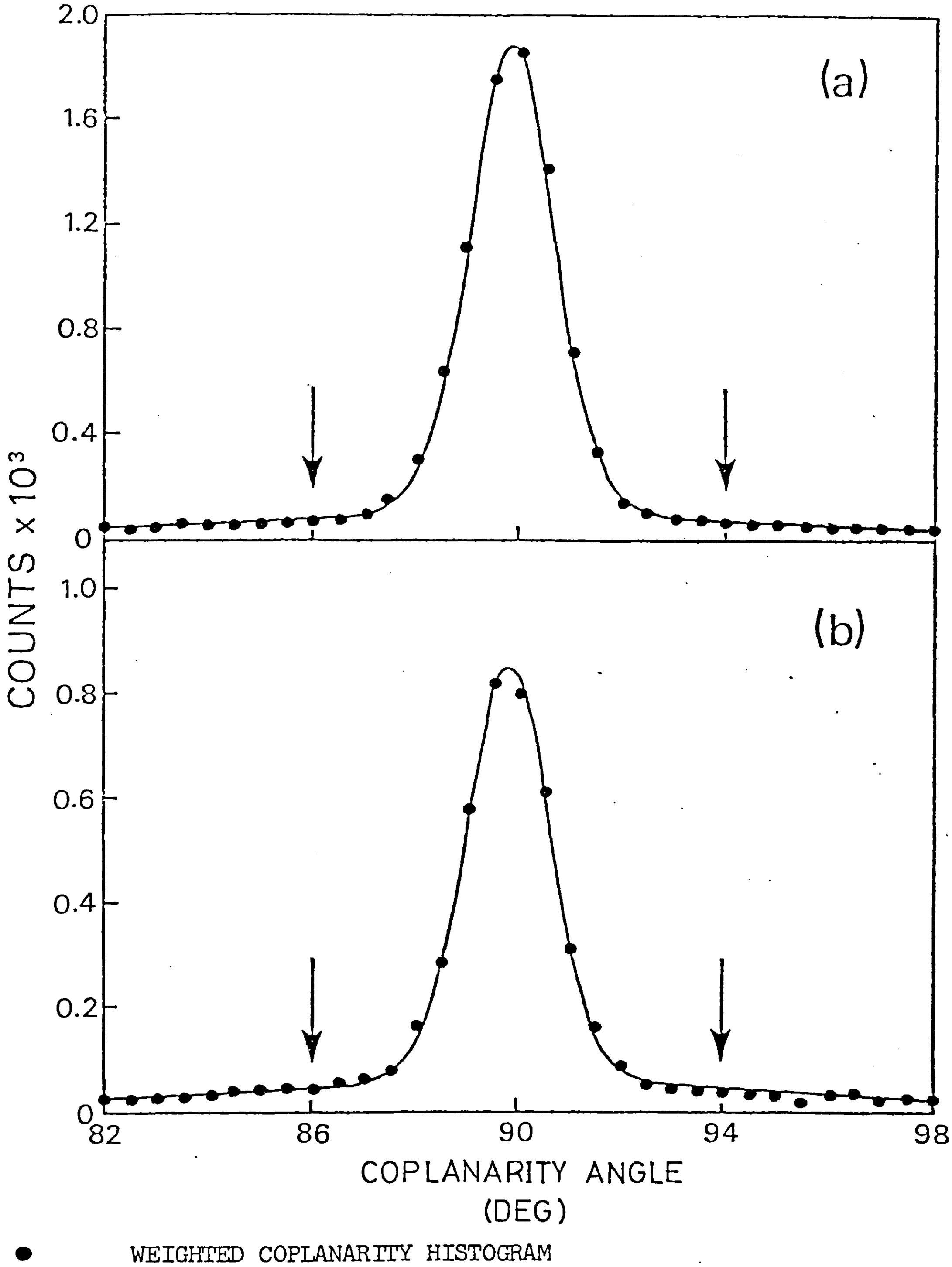

● WEIGHTED COPLANARITY HISTOGRAM

— FITTED DOUBLE GAUSSIAN

FIGURE 5.9 WEIGHTED COPLANARITY HISTOGRAM, PRODUCED FROM DATA TAKEN IN A $\Delta\sigma_T$ RUN AT 455.8 MeV, SHOWING THE DOUBLE GAUSSIAN FIT TO a) BEAM POLARIZATION POSITIVE DATA b) BEAM POLARIZATION NEGATIVE DATA. THE RANGE OVER WHICH THE FITTED BACKGROUND WAS SUBTRACTED IS BETWEEN THE ARROWS

Subtraction of the background gaussian from the whole histogram would only introduce noise into the data.

The evaluation of the p-p signal by the subtraction method required a good background gaussian fit. To this end the double gaussian was fitted to the histogram data assuming an equal weight for all bins independent of their statistics. This allowed the function to fit the central high statistics region with equal quality as the low statistics wings.

5.2.7 Chamber Efficiencies

The p-p data extracted from the monitor chamber information was corrected for the inefficiency of the detection system. A successful $\Delta\sigma_T$ event trigger was accompanied by eight stops arriving at the TDCs: four from the forward and four from the recoil monitor chambers. The efficiency of the chamber system was defined as, the ratio of events with eight stops arriving to the number of event triggers. This efficiency was calculated for each beam spin state for each run, from which the extracted p-p signals were corrected.

In the $\Delta\sigma_T$ experiment the right monitor had an efficiency of 98% for the majority of the runs. However, it fell to near zero for two runs at 202.8MeV, after which it was replateaued and it returned to its high efficiency. The left monitor's efficiency varied but had an average efficiency of approximately 85%.

In the $\Delta\sigma_L$ configuration one of the forward chambers had an efficiency which fell to zero for most of the runs, however each arm consisted of two monitor chambers giving redundant information. The remaining chambers had an efficiency of approximately 98% for all runs.

5.3 $\Delta\sigma_L$ Chamber Analysis

Target polarizations were evaluated using the p-p signals extracted from the coplanarity histograms. The number of protons elastically scattered by the hydrogen in the target, into the monitor chambers, was dependent on the magnitude and sign of P_B and P_T and the analysing power of the target, M. The analysing power is from equation 2.4.7,

$$M = \alpha A_{LL}(\theta) - \beta A_{SS}(\theta) + \gamma A_{SL}(\theta) \qquad 5.3.1$$

The coefficients α, β and γ are defined in section 2.4.2. From the p-p data obtained in one run with a fixed orientation of P_T but two orientations of P_B, an asymmetry ε_H was calculated, where ε_H is given by,

$$\varepsilon_H = \frac{\left(\frac{N}{N_o}\right)(\rightrightarrows) - \left(\frac{N}{N_o}\right)(\rightleftarrows)}{\left(\frac{N}{N_o}\right)(\rightrightarrows) + \left(\frac{N}{N_o}\right)(\rightleftarrows)} \qquad 5.3.2$$

where N is the number of p-p events and N_o is the number of protons incident upon the target. The three equations, 2.4.7, 5.3.1 and 5.3.2 can be solved to give an expression for P_T

$$P_T = \frac{2\ \varepsilon_H}{\left[P_B(+)M(+) - P_B(-)M(-)\right] - \varepsilon_H\left[P_B(+)M(+) + P_B(-)M(-)\right]} \qquad 5.3.3$$

The second term in the denominator is small as $P_B(+) \sim -P_B(-)$, $M(+) \sim M(-)$ and $\varepsilon_H < 1$.

5.3.1 Target Analysing Power

The analysing power of the target, M, is a function of energy and scattering angle. Values of the component parts of M, namely A_{LL}, A_{LS} and A_{SS}, were evaluated using the BASQUE phase shift program. The predicted values of these parameters over the centre of mass range $45 - 90^{\circ}$ are given in appendix B , together with values of M. In fig 5.10 the variation of M as a function of the centre of mass scattering angle for the six run energies is plotted.

In order to estimate the error in the analysing power, phase shifts were fitted to four different data bases:

1) Fits to only p-p data
2) Fits to p-p and n-p data
3) Calculations from phase shifts smoothed as a function of energy.
4) A set of fits omitting individual data sets.

The error was assessed from the maximum change in calculated M values for all these changes, plus the statistical error. The errors are listed in appendix B . It is seen from the table of M that the small angles and low energies carry the most information.

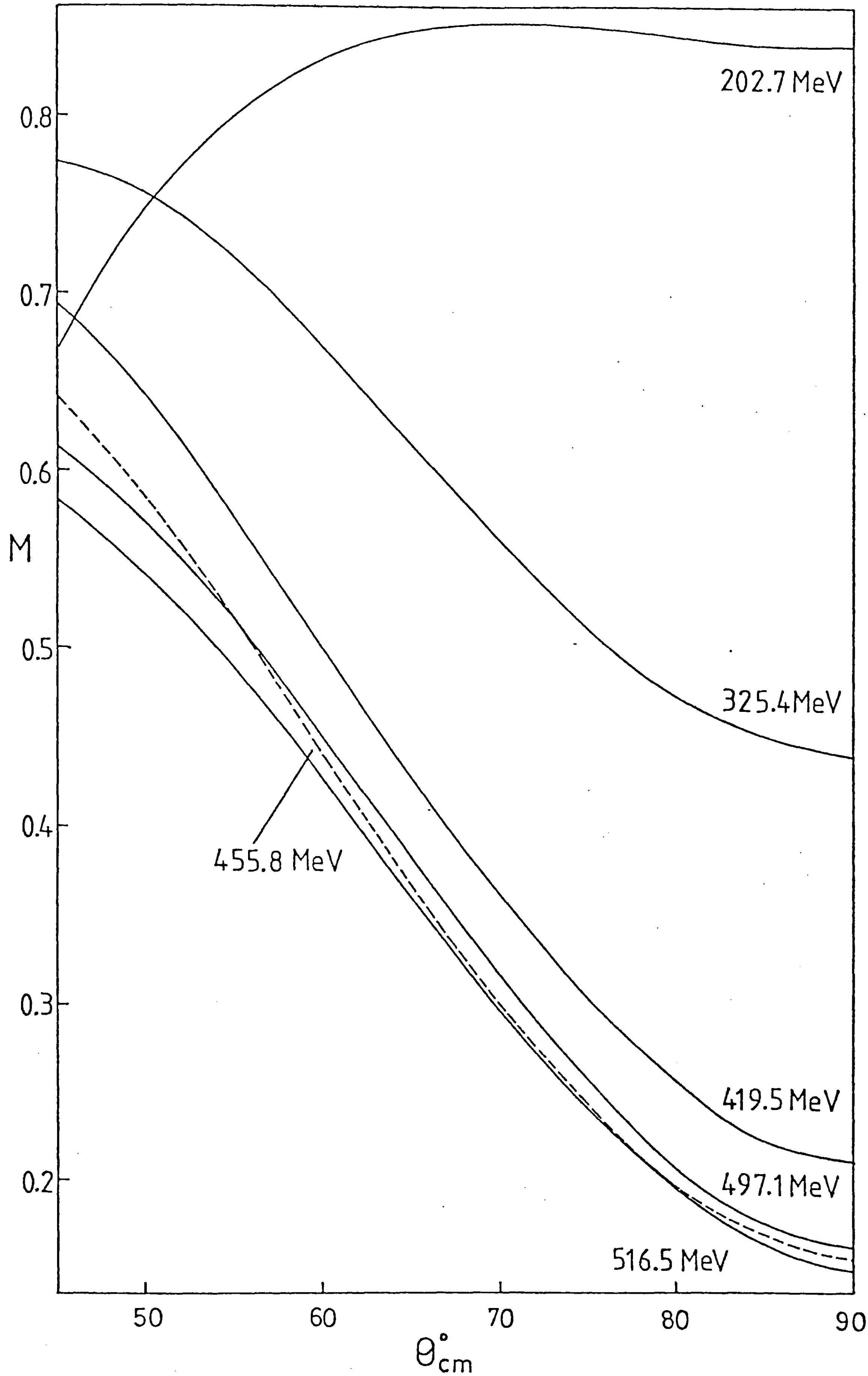

FIGURE 5.10 TARGET ANALYSING POWER, M, AS A FUNCTION OF CENTRE OF MASS SCATTERING ANGLE, θ_{cm}

The monitor chambers detected events over a large angular range. The true scattering angle of the events, transformed into the centre of mass, were histogrammed for both the forward and recoil chambers. The histograms were filled with events which were weighted by the exponential opening angle function, see section 5.2.5. A representative histogram is shown in fig 5.11, taken from the forward chamber at 455.8MeV, similar plots were obtained at all energies.

The average scattering angle obtained from each histogram were further averaged over all runs and energies giving a value of 69.1°_{CM}. The average from the recoil chamber was approximately 0.5° less than that obtained from the forward chamber. This difference indicates the accuracy to which the detector geometry was known.

Values of A_{LL}, A_{LS} and A_{SS} were available at intervals of 2.5° from $42.5 - 90^{\circ}_{CM}$. A linear interpolation was used to calculate a value of the parameters at the central value of each histogram bin, which covered $\frac{1}{2}^{\circ}$. From these values and the contents of the histograms a weighted value of each parameter was produced and the corresponding value of M was then calculated. A straight average was taken over the forward and recoil results to produce a value of $M(+)$ and $M(-)$ for each run.

5.3.2 Asymmetry Evaluation

Asymmetries were calculated for all runs using equation 5.3.2. A tabulation of this data showed a number of runs with anomalous values.

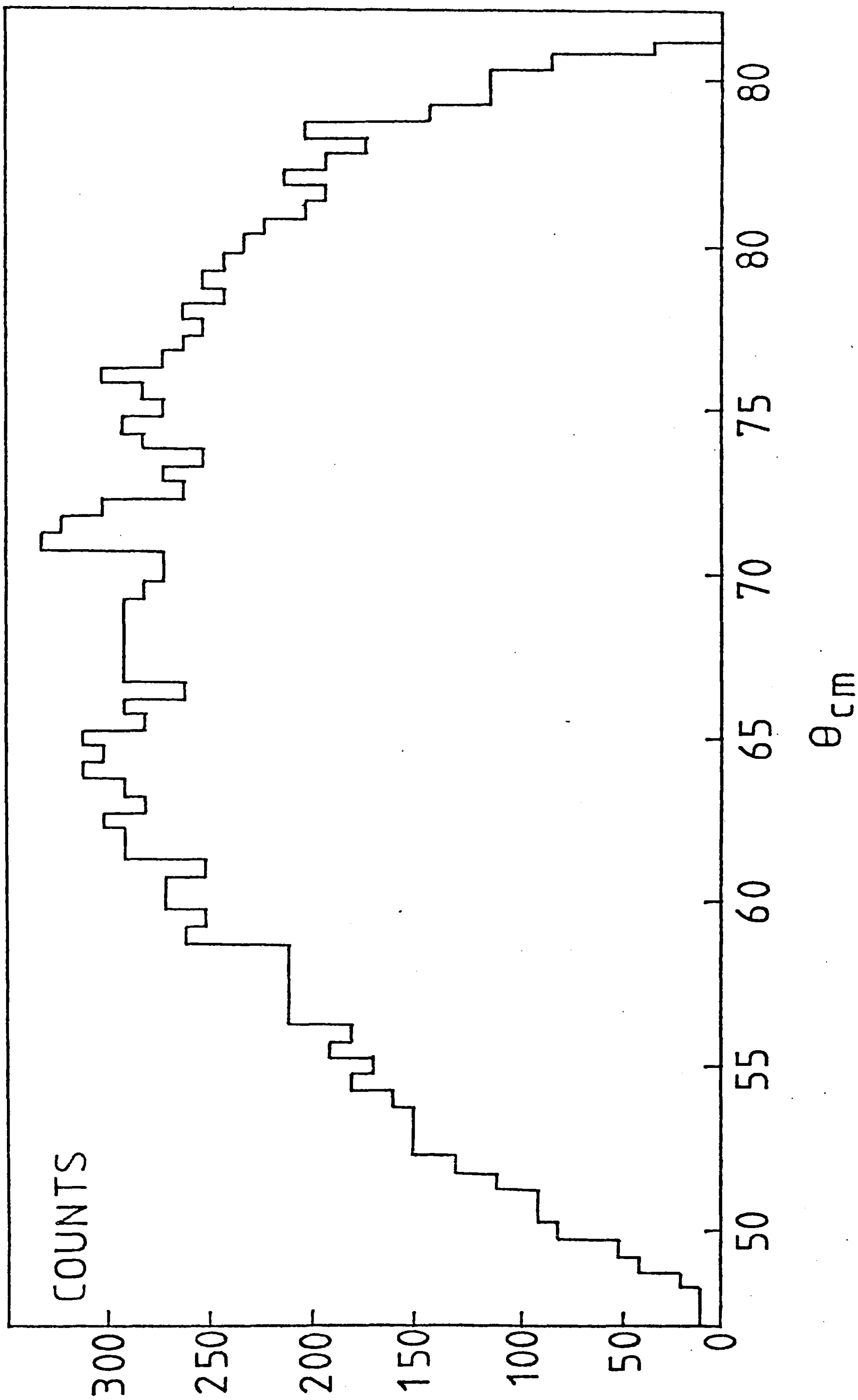

FIGURE 5.11 HISTOGRAM OF THE CENTRE OF MASS SCATTERING ANGLE, θ_{cm}, PRODUCED FROM DATA OBTAINED FROM THE FORWARD CHAMBER IN A $\Delta\sigma_L$ RUN AT 455.8 MeV

Checks on the data recorded during these runs revealed a problem in the online data acquisition program. If data collection was 'paused', using the online program, during a beam polarization change, this change was not registered. On restarting data acquisition scaler data from the new polarization state was combined with the scaler information of the previous polarization state. The offline data analysis program was modified to remove this corrupted data and correct asymmetries were then obtained.

Asymmetries obtained for each combination of target polarization and solenoid precession angle are listed in table 5.2. A positive precession is defined as a right handed screw travelling along $\underline{I}$. The errors are statistical arising from the p-p signal, N, and B, the background signal, (obtained by integrating the background gaussian). Errors were evaluated using equation 5.3.4, which is derived in appendix C.

$$\Delta\varepsilon_H^2 = \frac{4}{\left[r(+)+r(-)\right]^4}\left\{\left[\frac{r(-)}{N_o(+)}\right]^2\left[N(+)+2B(+)\right] + \left[\frac{r(+)}{N_o(-)}\right]^2\left[N(-)+2B(-)\right]\right\} \qquad 5.3.4$$

where +(-) denotes positive (negative) beam polarization and $r = N/N_O$.

An inspection of the asymmetries at 325MeV revealed two unexpected results. The asymmetry for runs with the solenoid off, changed in magnitude on reversal of the target polarization. With the solenoid energized the asymmetry was obviously different for each target polarization. These occurences suggested that the beam polarization extracted from the cyclotron contained a spin component in a direction other than vertical. The effect of non-vertical beam polarization components on the beam polarization at the target is discussed in detail in appendix D.

TARGET POLARIZATION	SOLENOID PRECESSION	ENERGY (MeV)					
		202.7	325.4	419.5	455.8	497.1	516.5
POSITIVE	POSITIVE	0.399 $\pm$0.008	0.228 $\pm$0.010	0.190 $\pm$0.010	0.138 $\pm$0.008	0.124 $\pm$0.008	0.128 $\pm$0.009
POSITIVE	NEGATIVE		-0.227 $\pm$0.013	-0.157 $\pm$0.012	-0.134 $\pm$0.009		-0.118 $\pm$0.009
NEGATIVE	POSITIVE	-0.438 $\pm$0.012	-0.332 $\pm$0.011	-0.136 $\pm$0.010		-0.142 $\pm$0.004	-0.096 $\pm$0.009
NEGATIVE	NEGATIVE	0.472 $\pm$0.016	0.322 $\pm$0.008	0.183 $\pm$0.009	0.139 $\pm$0.010		0.127 $\pm$0.010
POSITIVE	OFF	-0.103 $\pm$0.009	-0.220 $\pm$0.016	-0.155 $\pm$0.014	-0.157 $\pm$0.012		-0.170 $\pm$0.011
NEGATIVE	OFF		-0.057 $\pm$0.008		-0.177 $\pm$0.020	-0.147 $\pm$0.006	-0.136 $\pm$0.015

TABLE 5.2 ASYMMETRIES, ε_H, OBTAINED FROM MONITOR CHAMBER DATA AT EACH ENERGY FOR EACH COMBINATION OF TARGET AND SOLENOID SETTINGS.

The important results are summarised here.

The beam polarization $\underline{P}_b$ incident into the solenoid is defined as,

$$\underline{P}_b = P_B\underline{n} + T\underline{r} + L\underline{l} \qquad \text{D.1}$$

where $\underline{n}$ is vertically upwards, $\underline{r}$ is to the right as seen by the beam and $\underline{l}$ is along the beam direction. The interaction of the beam polarization with the magnetic fields of the solenoid, 35° bend magnet and the polarized target changed the beam polarization, which at the target centre was given by,

$$\underline{P}_b' = A'\underline{n} + B'\underline{r} + C'\underline{l} \qquad \text{D.6}$$

where

$$A' = A\cos\chi - (B\cos\theta_{TGT} + C\sin\theta_{TGT})\sin\chi \qquad \text{D.6.1}$$

$$B' = \left[A\sin\chi + (B\cos\theta_{TGT} + C\sin\theta_{TGT})\cos\chi\right]\cos\theta_{TGT} - \sin\theta_{TGT}(C\cos\theta_{TGT} - B\sin\theta_{TGT}) \qquad \text{D.6.2}$$

$$C' = \left[A\sin\chi + (B\cos\theta_{TGT} + C\sin\theta_{TGT})\cos\chi\right]\sin\theta_{TGT} + \cos\theta_{TGT}(C\cos\theta_{TGT} - B\sin\theta_{TGT}) \qquad \text{D.6.3}$$

$$A = P_B\cos\phi_s - T\sin\phi_s \qquad \text{D.3.1}$$

$$B = (P_B\sin\phi_s + T\cos\phi_s)\cos\phi_B - L\sin\phi_B \qquad \text{D.3.2}$$

$$C = (P_B\sin\phi_s + T\cos\phi_s)\sin\phi_B + L\cos\phi_B \qquad \text{D.3.3}$$

ϕ_s and χ are the spin precession angles produced by the solenoid and target's magnetic fields. They are defined as positive for a right handed screw travelling along the beam direction. ϕ_B is the polarization precession caused by the 35° bend magnet, values of which are listed in table 4.6 . θ_{TGT} is the 12° angle that the target's magnetic field makes to the beamline.

From the p-p data obtained from one run an asymmetry, ε_H , was evaluated. During a run the target polarization direction and the solenoid power supply polarity were kept constant. The asymmetries were labelled to show the target polarization direction and the solenoid precession angle, at which they were measured, $\varepsilon_H(\overset{+}{\underset{-}{o}}, \pm)$, where the first term in the bracket refers to the solenoid setting, precessing the beam polarization by $+90^{o}$, -90^{o} or 0^{o}. The second term in the bracket refers to the target polarization direction.

From equation 1.8.1 and 2.4.7 the general expression for the monitor asymmetry for a polarization $\underline{P}_0'$ given by equation D.6 is,

$$\varepsilon_H = -PA' + P_T(B'B'' + C'C'') \qquad 5.3.5$$

where

$$B'' = A_{LS}\cos\theta_{TGT} - A_{SS}\sin\theta_{TGT}$$
$$C'' = A_{LL}\cos\theta_{TGT} - A_{LS}\sin\theta_{TGT}$$

In the experiment the value of P_B is measured, T and L are unknowns. The value of P_T is derived from ε_H using equation 5.3.3. It was therefore desirable to eliminate as completely as possible, any effects on ε_H arising from non zero values of T and L. To this end the asymmetry at each energy, was averaged over solenoid precession angle and target polarization to give $\overline{\varepsilon}_H$,

$$\overline{\varepsilon}_H = \left[\tfrac{1}{2}\left[\varepsilon_{H(+,+)} - \varepsilon_{H(-,+)}\right] - \tfrac{1}{2}\left[\varepsilon_{H(+,-)} - \varepsilon_{H(-,-)}\right]\right]/2 \qquad 5.3.6$$

which using the results in sections 2 and 3 of appendix D can be shown to be given by,

$$\overline{\mathcal{E}}_H = P_T \left\{ \left[-T\sin\chi + P_B\cos(\phi_B - \Theta_{TGT})\cos\chi\right]\left[\cos\Theta_{TGT}B'' + \sin 12C''\right] + P_B\sin(\phi_B - \Theta_{TGT})\left[\cos\Theta_{TGT}C'' - \sin\Theta_{TGT}B''\right]\right\} \quad 5.3.7$$

From equation 5.3.7 it is seen that even after averaging over solenoid and target settings, a term dependent on T still survives. To remove this term, one would have to average over the target field direction. However, during this experiment the target field direction was fixed. Certain combinations of asymmetries allow terms dependent on T and L to be separated out.

$$\tfrac{1}{2}\left[\varepsilon_{H(+,+)} - \varepsilon_{H(-,+)}\right] + \tfrac{1}{2}\left[\varepsilon_{H(+,-)} - \varepsilon_{H(-,-)}\right] = 2P\left[T\cos\chi + \sin\chi\, P_B\cos(\phi_B - \Theta_{TGT})\right] \quad 5.3.8$$

$$\tfrac{1}{2}\left[\varepsilon_{H(+,+)} + \varepsilon_{H(-,+)}\right] + \tfrac{1}{2}\left[\varepsilon_{H(+,-)} + \varepsilon_{H(-,-)}\right] = L\left[-2P\sin\chi\,\sin(\phi_B - \Theta_{TGT})\right] \quad 5.3.9$$

It was possible, therefore, at energies where measurements of $\Delta\sigma_L$ were made with the four combinations of solenoid precession angle and target polarization, to calculate values of T and L. From the calculated value of T, the solneoid and target averaged asymmetry $\overline{\mathcal{E}}_H$ can be corrected for the term $T\sin\chi$.

5.3.3 Evaluation of Beam Spin Contamination

Values of asymmetries for all four combinations of solenoid and target settings were available at 325.4, 419.5 and 516.5MeV, enabling values of T and L to be evaluated . It was, however, only at 325.4MeV where large changes of asymmetries were seen.

Values of χ were determined from the path integral, $\int B.dl$ evaluated by computer simulation, for a proton travelling at 12^{o} to the magnetic field axis. The component of the target's magnetic field along the beamline was aligned in the direction of the beam momentum. This field alignment precessed the beam polarization perpendicular to the magnetic field, in the direction of a left handed screw travelling in the direction of the beam momentum. Values of χ for the run energies are listed in table 5.3 . Values of P and P_B for use in equations 5.3.8 and 5.3.9 were averaged values obtained from all the runs used at each energy. The calculated values of T and L are listed in table 5.4.

The errors quoted include phase shift normalisation errors and a component which allows for the uncertainty in the detector geometry. The results are subject to systematic errors, eg due to the difference between $P_B(+)$ and $P_B(-)$. Consequently, results differing from zero by 2-3 standard deviations should not have much reliance placed upon them. Bearing this in mind, all L values were consistent with zero. The T value at 325.4MeV was, however, approximately 6 standard deviations from zero.

5.3.4 NMR Calibration Factor

The target monitor chambers were included in the experiment to provide an independently normalized evaluation of the target

BEAM ENERGY (MeV)	χ (DEG)
203	26.5
325	20.1
420	17.3
456	16.5
497	15.7
517	15.3

TABLE 5.3 BEAM POLARIZATION PRECESSION ANGLE, χ , CAUSED BY THE TARGET'S MAGNETIC FIELD

BEAM ENERGY (MeV)	T	L
325.4	-0.176 ± 0.029	-0.033 ± 0.077
419.5	0.072 ± 0.025	0.308 ± 0.084
516.5	0.041 ± 0.018	0.124 ± 0.067

TABLE 5.4 VALUES OF THE BEAM POLARIZATION COMPONENTS T AND L EVALUATED FROM MONITOR CHAMBER DATA

polarization. The NMR integral was shown to provide a monitor of the target polarization with a statistical accuracy of 0.06%, and could thus be relied upon to show the time dependence of the polarization. The monitor data was used to derive a target polarization for each run $P_{T(MON)}$, using equation 5.3.2. This polarization was then used to produce a calibration factor C_{NMR}, which related the NMR integral for that run to $P_{T(MON)}$.

$$P_{T(MON)} = C_{NMR} NMR \times \left[\frac{100}{A} \right] \times 10^{-4} \qquad 5.3.10$$

The calibration factors from all the runs at one energy were combined. Firstly, calibration factors from runs with the same target and solenoid settings were combined to produce a weighted mean value, using the statistical precision of the runs. The calibration factors were then averaged over all available combinations of target and solenoid settings. The individual calibration factors for each solenoid and target setting are given in table 5.5 , the final averaged calibration factor at each energy is listed in table 5.6 , ΔC_{STAT} quoted in this table arises from a quadratic addition of the component errors.

There are two further errors to take into account for the calibration factor obtained at each energy. These arise from the uncertainty in the exact position of the chamber wire planes and from the normalisation uncertainty in the phase shift predictions of the components used to produce values of the target's analysing power, M.

TARGET POLARIZATION	SOLENOID PRECESSION	ENERGY (MeV)					
		202.7	325.4	419.5	455.8	497.1	516.5
POSITIVE	POSITIVE	1.049 $\pm$0.018	0.871 $\pm$0.037	1.208 $\pm$0.066	1.207 $\pm$0.058	0.953 $\pm$0.060	1.069 $\pm$0.073
POSITIVE	NEGATIVE		0.725 $\pm$0.050	1.113 $\pm$0.087	1.238 $\pm$0.112		1.004 $\pm$0.080
NEGATIVE	POSITIVE	1.086 $\pm$0.020	1.238 $\pm$0.042	0.978 $\pm$0.072		1.096 $\pm$0.028	0.877 $\pm$0.083
NEGATIVE	NEGATIVE	1.210 $\pm$0.038	1.196 $\pm$0.033	1.218 $\pm$0.062	1.189 $\pm$0.072		1.008 $\pm$0.089

TABLE 5.5 NMR CALIBRATION FACTOR, C_{NMR} , AT EACH ENERGY FOR EACH COMBINATION OF TARGET AND SOLENOID SETTINGS

BEAM ENERGY (MeV)	C_{NMR}	ΔC_{STAT}	ΔC_{GEOM}	ΔC_{PSA}	ΔC_{TOT}
202.7	1.104	0.015	0.001	0.036	0.039
325.4	1.011	0.021	0.002	0.050	0.054
419.5	1.132	0.036	0.011	0.101	0.108
455.8	1.182	0.048	0.016	0.114	0.125
497.1	1.026	0.032	0.010	0.107	0.112
516.5	0.991	0.041	0.014	0.112	0.120

TABLE 5.6 AVERAGED VALUES OF C_{NMR} AND IT'S ERROR, ΔC_{TOT}, AT EACH ENERGY. COMPONENT ERRORS ARISING FROM STATISTICS ΔC_{STAT}, PHASE SHIFT PREDICTIONS, ΔC_{PSA}, AND GEOMETRY UNCERTAINTIES, ΔC_{GEOM}, ARE LISTED

To a good approximation the target polarization derived from the monitor asymmetry is from equation 5.3.3 given by

$$P_{T(MON)} \sim \frac{\overline{\mathcal{E}}_H}{P_B M} \qquad 5.3.11$$

from which a simple expression for the error in C_{NMR} arising from an error in M is obtained,

$$\Delta C_{NMR} \sim \frac{C_{NMR}\,\Delta M}{M} \qquad 5.3.12$$

The phase shift normalisation errors were estimated as described in section 5.3.1. The chamber geometry error was estimated by the change in the weighted values of A_{LL}, A_{LS} and A_{SS} produced by the forward and recoil arms. The errors in C_{NMR} arising from the geometry uncertainties, ΔC_{GEOM} and from the phase shift uncertainties, ΔC_{PSA}, are given in table 5.6. The total error in C_{NMR}, ΔC_{TOT}, at each energy was obtained from a quadratic addition of the three independent errors, listed in table 5.6.

The value of C_{NMR} at all energies was combined to give a weighted mean value, C_{NMR}, using the error ΔC_{TOT}, $C_{NMR} = 1.074 \pm 0.028$.

In section 5.3.2 it was shown that averaging over all target and solenoid settings still left a term $T\sin\chi$ in the asymmetry expression, see equation 5.3.7. The averaged asymmetry needed to be corrected for this remaining T term. The only energy where this correction is significant was at 325.4MeV. In section 6.2.1 values of T are evaluated at all energies from transmission data, these results confirmed the values of T obtained using the asymmetry data. A scaling factor applied to the asymmetry, $\overline{\varepsilon}_H$, to allow for non zero T values, was obtained from equation 5.3.13 which considers the change in the averaged asymmetry caused by the T term.

$$[\varepsilon_H(\text{WITH T}) - \varepsilon_H(\text{WITHOUT T})] / \varepsilon_H(\text{WITHOUT T}) = -T \sin\chi \, BC_1 \Big/ P_B [\cos\chi \cos(\phi_B - \theta_{TGT}) BC_1 + \sin(\phi_B - \theta_{TGT}) \, BC_2]$$

Where
$$BC_1 = \cos\theta_{TGT} B'' + \sin\theta_{TGT} C''$$
$$BC_2 = \cos\theta_{TGT} C'' - \sin\theta_{TGT} B'' \qquad 5.3.13$$

Using equation 5.3.13 the scaling factors to apply to the calibration factors were obtained. The values of T, the scaling factors and the new calibration factors are listed in table 5.7. The scaling changes the weighted mean value of the calibration factor, C_{NMR}, to 1.070 ± 0.028.

The value of C_{NMR} can be compared and combined with the independently derived calibration obtained from the thermal equilibrium measurements. This value is, from equation 5.1.2, 1.014 ± 0.065, which combined with the chamber evaluation gives a final weighted mean value of $C_{NMR} = 1.061 \pm 0.026$.

5.3.5 Solenoid Unpowered Monitor Data

Asymmetries evaluated from the chamber data taken during runs when the solenoid was unpowered could be compared with phase shift predicted values.

Using the results from section 3 of appendix D it can be shown that the asymmetry, with the solenoid unpowered, averaged over

BEAM ENERGY (MeV)	T	SCALING FACTOR	SCALED C_{NMR}
325.4	-0.16	-1.61%	0.995
419.5	0.06	0.87%	1.142
516.5	0.04	0.75%	0.998

TABLE 5.7 VALUES OF C_{NMR} SCALED TO ALLOW FOR NON ZERO COMPONENTS OF T BEAM POLARIZATION, SHOWING VALUES OF T AND THE CORRESPONDING SCALING FACTORS USED ON VALUES OF C_{NMR} IN TABLE 5.6

target polarization is given by,

$$[\varepsilon_{(0,+)} + \varepsilon_{(0,-)}]/2 = -PL\sin\chi\sin(\phi_B - \theta_{TGT})$$
$$-PP_B\cos\chi + PT\sin\chi\cos(\phi_B - \theta_{TGT}) \qquad 5.3.14$$

The SECOND term on the right hand side was directly calculable and could be compared with the averaged asymmetry once this had been corrected for any T and L beam polarization components.

Data taken with the solenoid unpowered and with both target polarizations, was available at 325.4, 455.8 and 516.5MeV. The magnitude of T had been calculated at 325.4 and 516.5MeV, using monitor chamber data. It was also possible to calculate T at all energies using transmission data, see section 6.2.1. The value of T at 325.4 and 516.5MeV was taken as the average of the two evaluations. The magnitude of T at 455.8MeV was consistent with zero.

Values of L had been calculated at 325.4 and 516.5MeV. A further evaluation was, however, possible. Using the results in sections 2 and 3 of appendix D an asymmetry proportional to L was formed.

$$[\varepsilon_{(+,+)} + \varepsilon_{(-,+)}]/2 - [\varepsilon_{(+,-)} + \varepsilon_{(-,+)}]/2 =$$
$$2LP_T[-\sin(\phi_B - \theta_{TGT})\, BC_1\cos\chi + \cos(\phi_B - \theta_{TGT})\, BC_2] \qquad 5.3.15$$

Using equation 5.3.15, L was evaluated at 325.4, 419.5 and 516.5MeV. The results obtained are given in table 5.8.

All the results were consistent with zero, in broad agreement with the previous evaluations.

BEAM ENERGY (MeV)	L
325.4	0.06 ± 0.12
419.5	0.12 ± 0.17
516.5	0.06 ± 0.08

TABLE 5.8 VALUES OF THE BEAM POLARIZATION COMPONENT, L, DERIVED FROM MONITOR CHAMBER DATA RECORDED WITH THE SOLENOID UNPOWERED

Equation 5.3.14 was rewritten assuming L = 0 at all energies to define the ratio, R, which is given by ,

$$R = \frac{\frac{1}{2}\left[\mathcal{E}_{(o,+)} + \mathcal{E}_{(o,-)}\right] - PT\sin\chi\cos(\phi_B - \theta_{TGT})}{-P\,P_B\cos\chi} \qquad 5.3.16$$

The values of R obtained at the three energies, 325.4, 419.5 and 516.5MeV are given in table 5.9 , which also lists the values of T used.

The error in R includes both statistical and phase shift components. The weighted mean value of R, 0.996 $\pm$ 0.046 showed that there was excellent agreement between the measured and calculated asymmetries. This gave an absolute check on P_B to $\pm$ 4.6%.

5.4 $\Delta\sigma_T$ Chamber Data Analysis

In the $\Delta\sigma_T$ experimental configuration two double arm monitors were incorporated. These detected scattered and recoil protons to the left and right of the beamline, see fig 5.5 . After applying corrections to the proton trajectories for magnetic field deflections, the chambers were found to monitor scattered protons centred on approximately 50°cm (63°cm) to the left (right) of the beamline, as seen by the beam.

For $\Delta\sigma_T$ the count rate, N, of p-p events detected by a counter monitoring at an angle θ is from equation 1.8.1.

$$N(\theta) = N_o\alpha\left[1+P_BP(\theta) + P_TP(\theta) + P_TP_BA_{NN}(\theta)\right] \qquad 5.4.1$$

BEAM ENERGY (MeV)	R	T
325.4	0.998 $\pm$0.075	-0.163
455.8	0.980 $\pm$0.089	0.0
516.5	1.005 $\pm$0.075	0.042

TABLE 5.9 VALUES OF THE RATIO,R, DEFINED BY EQUATION 5.3.16 AND THE VALUES OF T USED TO OBTAIN IT

where N_o is the beam rate incident upon the target and α is a geometric constant dependent on the size and position of the monitor counters.

Data for $\Delta\sigma_T$ was taken in runs where the beam polarization was reversed while keeping the direction of target polarization constant. It was, however, inappropriate to derive a value for P_T from data obtained from individual runs. The change in intensity of p-p events on reversing the beam polarization, while keeping P_T fixed, was determined by $P_B P(\theta)$ and $P_T P_B A_{NN}(\theta)$, these terms being similar in magnitude. The intensity change had, therefore, a sizeable dependence on the term $P_B P(\theta)$ which was independent of P_T.

The analysis proceedure adopted was to combine data taken with both target orientations, while keeping the orientation of P_B constant. Combining data in this way produced an intensity difference dependent purely on terms involving P_T.

The target polarization was obtained from the data with fixed beam spin polarization and two target polarization orientations by first forming an asymmetry, ε_T,

$$\varepsilon_T = \frac{\frac{N}{N_o}(\uparrow\uparrow) - \frac{N}{N_o}(\downarrow\uparrow)}{\frac{N}{N_o}(\uparrow\uparrow) + \frac{N}{N_o}(\downarrow\uparrow)} \qquad 5.4.2$$

Substitution of equation 5.4.1 into equation 5.4.2 , assuming $P_T(+) = -P_T(-) = \overline{P}_T$, leads to,

$$\overline{P}_T = \frac{\varepsilon_T\left[2 + P^{(+,\pm)}P_B^{(+,\pm)} + P^{(-,\pm)}P_B^{(-,\pm)}\right] - P^{(+,\pm)}P_B^{(+,\pm)} + P^{(-,\pm)}P_B^{(-,\pm)}}{\left[C^{(+,\pm)} + C^{(-,\pm)}\right] - \varepsilon_T\left[C^{(+,\pm)} - C^{(-,\pm)}\right]} \qquad 5.4.3$$

where $C^{(\pm,\pm)} = P^{(\pm,\pm)} + P_B^{(\pm,\pm)} A_{NN}^{(\pm,\pm)}$. The first sign in the bracketed suffix refers to target polarization, the latter to the beam polarization. The angular distribution of p-p events changes on reversal of the target or beam spin, because of the terms $P_T P(\Theta)$, $P_B P(\Theta)$ and $P_T P_B A_{NN}(\Theta)$. This, therefore, changed the mean value of P and A_{NN} obtained from the histograms of the scattering angles. This effect changed values of P and A_{NN} by only 1 - 2% on reversal of P_B or P_T, therefore $C^{(+,\pm)} \sim C^{(-,\pm)}$. Using the approximation that A_{NN}, P and P_B are equal for both target polarization orientations, equation 5.4.3 reduces to,

$$P_T \sim \frac{\varepsilon_T\left[1 + P_B P\right]}{P + P_B A_{NN}} \qquad 5.4.4$$

For the case of positive (negative) beam polarization and forward scattering into the right (left) chambers, the two terms in C act destructively. For these cases the denominator in equation 5.4.3 becomes small and the results obtained for P_T unreliable. Data taken where this occured was not used in the final evaluation of P_T.

As an independent check on the assumption, used in deriving equation 5.4.3, that $P_T(+) = -P_T(-)$, the data obtained from individual runs, (where the beam polarization was reversed and P_T was kept fixed), was used to determine P_T for each run.

The asymmetry ε_B was formed.

$$\varepsilon_B = \frac{\frac{N}{\bar{N}_o}(\uparrow\uparrow) - \frac{N}{\bar{N}_o}(\uparrow\downarrow)}{\frac{N}{\bar{N}_o}(\uparrow\uparrow) + \frac{N}{\bar{N}_o}(\uparrow\downarrow)} \qquad 5.4.5$$

Substitution of equation 5.4.1 into equation 5.4.5 leads to,

$$P_T^{(\pm)} = \frac{\varepsilon_B\left[2 + P_B^{(\pm,+)}P^{(\pm,+)} + P_B^{(\pm,-)}P^{(\pm,-)}\right] - P_B^{(\pm,+)}P^{(\pm,+)} + P_B^{(\pm,-)}P^{(\pm,-)}}{\left[C^{(\pm,+)} - C^{(\pm,-)}\right] - \varepsilon_B\left[C^{(\pm,+)} + C^{(\pm,-)}\right]} \qquad 5.4.6$$

Making the assumption that P, A_{NN} and P_B are equal for both beam polarization orientations reduces equation 5.4.6 to,

$$P_T = \frac{\varepsilon_B - P_B P}{P_B A_{NN} - \varepsilon_B P} \qquad 5.4.7$$

Values of P_T were calculated using equation 5.4.6 for both left and right chamber sets for all runs.

For these evaluations of P_T values of P and A_{NN} were obtained using weighted scattering angle histograms in an analogous manner to which values of A_{LL}, A_{LS} and A_{SS} were produced for $\Delta\sigma_L$. The values of P and A_{NN} used in this evaluation are tabulated, in the centre of mass angular range $45 - 90^o$, in appendix B.

The evaulations of P_T from each run for each energy were combined to give two mean values of P_T, weighted by the statistics of the component values, one for each chamber set. Two further error components were then incorporated in these values of P_T. The first arose from phase shift normalization uncertainties, these were estimated by changing the data base that the phase shift analysis program used to predict values of P and A_{NN} using the proceedure given in section 5.3.1. The second additional error component came from the uncertainty in the exact chamber position. As for $\Delta\sigma_L$ this was estimated from the difference between values of P and A_{NN} obtained from the scattering angle histograms from the forward and recoil chambers.

The evaluations of the target polarization from the left and right chamber sets were combined to give a weighted mean value of P_T at each energy. These results are listed in table 5.10. The error quoted for P_T in table 5.10 is the error of the weighted mean value or the dispersion of the two chamber evaluations, which ever was larger. The results showed the magnitude of the target polarization to be of the same order for both orientations. This was in sharp contrast to the NMR evaluation. The result thus verified that the positive NMR signal was being truncated as discussed in section 5.1.2.

At 202.8MeV the right monitor efficiency fell to zero for all runs with the target negatively polarized. Also the beam polarization monitor recorded polarizations of approximately 23% for beam polarization off for all runs. This large value for $P_{B(OFF)}$ could have introduced systematic errors into an evaluation of P_T from the chamber data. Consequently the chamber data at 202.8MeV was not used.

BEAM ENERGY (MeV)	$-P_T(-)$	$P_T(+)$
325.1	0.59 ± 0.04	0.61 ± 0.04
374.8	0.65 ± 0.04	0.67 ± 0.03
419.4	0.64 ± 0.04	0.67 ± 0.04
455.7	0.58 ± 0.03	0.62 ± 0.04
497.5	0.62 ± 0.03	0.66 ± 0.03
516.5	0.57 ± 0.04	0.63 ± 0.03

TABLE 5.10 VALUES OF THE TARGET POLARIZATION, FOR BOTH ORIENTATIONS

Although each value of P_T negative was smaller than P_T positive, the errors were such that the two values of the target polarization were consistent. This data was, therefore, interpreted as showing the positive and negative target polarizations to be equal in magnitude.

The target polarization $\overline{P}_T$ was obtained from equation 5.4.3 using data obtained from the left (right) chamber set with the beam polarization up (down). The two results for $\overline{P}_T$, one from each chamber set, were combined to give a mean value, weighted by the statistical error and the small chamber geometry uncertainty error. The total error in the weighted mean was obtained by adding the phase shift normalization error in quadrature. These values of $\overline{P}_T$ and their errors are listed in table 5.11

The chamber evaluation of target polarization was to be compared with the NMR evaluation of P_T negative. An average NMR integral was produced for all runs with negative target polarization at one energy. This integral was converted into a target polarization using the thermal equilibrium calibration. The ratio of target polarization calculated from the chambers to that derived from the NMR was formed to give a calibration factor for use on the NMR evaluations. The values of P_T (NMR) obtained from the NMR and the ratio of this to $\overline{P}_T$ obtained from the chambers are given in table 5.11 . These ratios at the five available energies were combined to give a weighted mean value for use at all energies. To cover the spread of the results, the standard deviation of the data was used as the error, giving a final ratio of 0.944 ± 0.030.

BEAM ENERGY (MeV)	$\overline{P}_T$	$P_{T(NMR)}$	R'
325.1	0.664 ± 0.011	0.718	0.924 ± 0.016
374.8	0.662 ± 0.011	0.677	0.978 ± 0.016
419.4	0.626 ± 0.011	0.692	0.905 ± 0.016
455.7	0.627 ± 0.011	0.649	0.966 ± 0.017
516.5	0.581 ± 0.013	0.611	0.950 ± 0.021

TABLE 5.11 VALUES OF THE TARGET POLARIZATION, $\overline{P}_T$, AND THE RATIO, R', OF THIS TO THE NEGATIVE TARGET POLARIZATION, $P_{T(NMR)}$, DERIVED FROM THE NMR

The chamber data was used to normalize the NMR system, as a saturation problem could have led to misleading results if the thermal equilibrium signal had also been used.

The value of P_T for all runs at 497.5MeV was set to the value obtained from the chambers. This was because the NMR signal was seen to saturate for both target polarization orientations.

CHAPTER 6

$\Delta\sigma_L$ AND $\Delta\sigma_T$ RESULTS

6.1 Evaluation of $\Delta\sigma_L$ and $\Delta\sigma_T$

Values of $\Delta\sigma_L$ and $\Delta\sigma_T$ are calculated using equation 2.1.7. The transmissions $t(\pm +)$ and $t(\pm -)$ were evaluated by an offline analysis of the scaler data for each run. The transmission, t_i' of the beam, by the target, was evaluated for each consecutive counter pair of the transmission array,

$$t_i' = \frac{S123B.Ti.Ti{+}1}{S123B} \qquad 6.1.1$$

for i = 1-5. The transmission was corrected for random coincidences between the beamline and transmission counters. This random correction, r_i, to the t_i' th transmission is,

$$r_i = \frac{\widetilde{S123B}.Ti.Ti{+}1}{S123B}\left(1 - t_i'\right) \qquad 6.1.2$$

($\sim$ ≡ delayed by 43ns)

The efficiency of the transmission array's ith counter is,

$$\varepsilon_i = \frac{S123B.E1.E2.Ti.Ti{+}1}{S123B.E1.E2} \qquad 6.1.3$$

The final transmission, t_i, corrected for both random events and the inefficiency of the transmission counter is given by,

$$t_i = \frac{t_i' - r_i}{\varepsilon_i} \qquad 6.1.4$$

Values of Δt and $\bar{t}$, equation 2.1.8, were obtained using transmissions evaluated from equation 6.1.4. Generally, the random corrections were $\sim$0.03% of the magnitude of t_i. Beam rates for both beam polarizations were such that the random correction to t_i beam polarization up, and t_i beam polarization down, differed by less than 10%. The efficiency of the transmission array for all data acquisition runs was generally $\sim$99.98%, it never fell below 99.9%.

Beam polarizations were obtained using equation 3.3.1, for all three conditions of beam polarization. The value of fc and P (26^{o}) used are listed in table 3.1. The asymmetry, ε_o, measured when the ion source was supplying unpolarized beam, was subtracted from the asymmetries measured when the beam was polarized. This subtraction removed instrumental asymmetries. The beam polarization was given by,

$$P_B = \frac{(\varepsilon - \varepsilon_o)\, fc}{P(26^o)} \qquad 6.1.5$$

In almost all runs $|\varepsilon_o| < 0.018$. The value of P_B, for use in equation 2.1.7, was obtained from the average of the two beam polarizations, and was thus independent of instrumental asymmetries in the beam polarization monitor.

Values of P_T for use in the $\Delta\sigma_L$ calculations were obtained using equation 5.3.10, with the value of $C_{NMR} = 1.061 \pm 0.026$ as derived at the end of section 5.3.4. The value of the NMR integral used for each run was the average value of all the NMR integrals recorded for that run.

Obtaining the target polarization for $\Delta\sigma_T$ was complicated by the NMR saturating. The average NMR integral was evaluated for all runs where the target was negatively polarized, from which P_T was obtained using the thermal equilibrium calibration. The independent chamber calibration of 0.944 ± 0.030 was then used to produce final values of P_T. For runs where the target was positively polarized, the target polarization at each energy was taken to have a magnitude equal to the negative polarization, averaged over all runs at that energy, see section 5.4 . However, during the runs at 497.1MeV for $\Delta\sigma_T$ the NMR was producing truncated results for both target polarizations. At this energy, therefore, the target polarization was taken directly from the chamber results, and was found to be $P_T = 58.2 \pm 1.3\%$, see section 5.4

6.1.1 Target Hydrogen Density

The target beads consisted of 95% 1-butanol ($C_4H_{10}O$) by weight, and 5% water (H_2O), plus in all data taking runs, Cr(V)EHBA dopant ($NaCrC_{12}O_7H_{20}$). The actual recipe used to produce the target beads was 20ml of butanol (16.196g) with 0.8524ml of H_2O (0.8524g) and 0.5109g of Cr(V)EHBA. The percentage composition by weight of this mixture was butanol 92.2360%; H_2O, 4.8544% and Cr(V)EHBA, 2.9096%. The ratio by weight of hydrogen to all other constituents of each of the components in the mixture were, butanol, 0.1360; H_2O, 0.1119; and Cr(V) EHBA, 0.0574. In the quantities in which they were mixed the total density of hydrogen ρ_H was,

$$\rho_H = \left[(0.1360 \times 09224)+(0.1119 \times 0.0485)+(0.0574 \times 0.0291)\right] D$$

$$\rho_H = 0.1325D \qquad 6.1.6$$

where D was the measured density of the target.

The $\Delta\sigma_L$ and $\Delta\sigma_T$ experiments used two separate target bead containers, each fabricated from FEP. The containers were cylindrical in shape, of dimensions given in table 6.1.

The weight of the target material was found by filling the container with the target beads in a systematic way. The beads were then emptied into a container for weighing. The whole proceedure being carried out at LN_2 temperatures. To investigate the reproducibility of the filling factor of the target, a series of fillings and weighings were carried out on the $\Delta\sigma_T$ target container. Five measurements were made using target beads with diameters in the same range as those used in the experimental runs, namely 1.0 - 1.7mm. Two further measurements were made to investigate any effect of using beads with a different range of diameters, 1.0 - 1.4mm.

The stability of the individual weighings was found to be poor due to changing packing fractions of the target beads. For the series of five measurements, the target weights varied from 2.142 up to 2.375g, the average being 2.315g. The range of diameters of the beads made no systematic change to the weight of the target. Including results of measurements on the beads used in the $\Delta\sigma_T$ experiment gave an average weight of 2.3085g. The result of the measurement for the $\Delta\sigma_L$ beads used in the data acquisition runs was 1.719g. Unfortunately, the $\Delta\sigma_L$ target container was accidentally damaged and thus a set of systematic weighings could not be carried out on this target.

EXPERIMENT	LENGTH (mm)	DIAMETER (mm)	VOLUME (ml)
$\Delta\sigma_L$	20.79 $\pm$0.10	14.55 $\pm$0.15	3.457 $\pm$0.073
$\Delta\sigma_T$	23.68 $\pm$0.10	15.07 $\pm$0.10	4.224 $\pm$0.059

TABLE 6.1 TARGET CYLINDER DIMENSIONS AT 300K

The weighings gave target densities of 0.4973 (0.5466)gml^{-1} for $\Delta\sigma_L$ ($\Delta\sigma_T$). These two results combined statistically gave an average target density of 0.5411gml^{-1} giving a hydrogen density, from equation 6.1.6, of 0.0717gml^{-1}.

The error on the hydrogen density was assesed from the spread of the individual weigh ings and was $\pm$ 4.87%. The error in $\Delta\sigma_L$ or $\Delta\sigma_T$ arising from the combination of $\rho_H L$ is the error in (weight of target) / (area of target cylinder). The error in the area of the target, averaged over $\Delta\sigma_L$ and $\Delta\sigma_T$, was 1.69%. The quadratic addition of the two independent errors gave a normalization error on $\Delta\sigma_L$ and $\Delta\sigma_T$ of 5.2%.

The measurements of dimensions were performed at room temperature. However, the weighings were all carried out at LN_2 temperatures. In changing the temperature from 293 - 77K, the FEP contracts by 1.3%: the density of the target was therefore 0.0745gml^{-1}. The FEP container has a negligible contraction in the range 77 - 0K.

6.1.2 Extrapolation to Zero Detection Angle

In the $\Delta\sigma_L$ experiment the first counter in the transmission array of radius ~9.0cm was positioned ~1.3m from the target centre. At each energy in the $\Delta\sigma_T$ experiment the transmission array was moved to centre it on the beam which was deflected by the target field. These movements changed the separation of the first counter from the target by a few millimetres, the average separation was 1.184m. In table 6.2, the angles subtended by the first five counters to the target are given for $\Delta\sigma_L$ and $\Delta\sigma_T$. The solid angle covered by each counter is also listed, where the solid angle, Ω, is related to the detection angle ψ by.

$$\Omega = 2\pi(1 - \cos\psi) \qquad 6.1.7$$

In the centre of mass the angular range covered varied from 9.1° - 21.9° (9.8° - 20.4°) at the lowest (highest) energy for $\Delta\sigma_T$, and from 8.3° - 20.3° (8.9° - 21.7°) for $\Delta\sigma_L$.

Values of $\Delta\sigma_L$ and $\Delta\sigma_T$ were calculated for each of the five transmission array counter pairs. The values were to be extrapolated to zero detection angle.

6.1.3 Coulomb Corrections

To obtain values of $\Delta\sigma_L$ and $\Delta\sigma_T$ arising from purely nuclear effects, corrections for Coulomb contributions were evaluated and removed from the results.

The contribution to $\Delta\sigma_L$ and $\Delta\sigma_T$ from purely elastic scattering is,

$$\Delta\sigma_L^{EL} = -4\pi\int_0^{\pi/2} A_{LL}\left[\frac{d\sigma}{d\Omega}\right]^{EL}\sin\theta \, d\theta \qquad 6.1.8$$

EXPERIMENT	θ_1 (DEG)	Ω (msr)	θ_2	Ω_2	θ_3	Ω_3	θ_4	Ω_4	θ_5	Ω_5
	3.96	15.0	5.22	26.1	6.72	43.2	8.05	62.0	9.63	88.6
	4.35	18.1	5.73	31.4	7.33	51.3	8.77	73.3	10.4	104

TABLE 6.2 LABORATORY ANGLE, θ , AND SOLID ANGLE, Ω, SUBTENDED BY THE COUNTERS IN THE TRANSMISSION ARRAY, TO THE TARGET

$$\Delta\sigma_T^{EL} = -2\pi \int_0^{\pi/2} \left(A_{NN} + A_{SS}\right) \left[\frac{d\sigma}{d\Omega}\right]^{EL} \sin\theta \; d\theta \qquad 6.1.9$$

where $\left[\frac{d\sigma}{d\Omega}\right]^{EL}$ is the elastic differential cross section and θ is the centre of mass scattering angle. The Coulomb scattering and Coulomb-nuclear interference components contained in the measured value of $\Delta\sigma_L$ and $\Delta\sigma_T$ from counter i, were calculated by evaluating the appropriate integral over the angular range, $\theta_i \rightarrow \pi/2$, where θ_i was the maximum centre of mass angle subtended by the i^{th} transmission counter. The integrals were performed numerically using the BASQUE phase shift program. Two evaluations of these integrals were performed. Firstly, with all Coulomb amplitudes present, see section 1.6, and secondly with the Coulomb phase shift, ξ , set to zero, $f_c = 0$, (for both these integral evaluations the Coulomb barrier terms Δ and Φ were retained). The Coulomb-nuclear interference was taken as the difference between these two integral evaluations.

The BASQUE predictions of the Coulomb-nuclear terms were compared to values calculated using the phase shift analysis of Arndt. The two values differed by at most 0.06mb over the angular range and energy covered in the experiment. The error of the Coulomb-nuclear correction was taken as the maximum discrepancy between the two evaluations.

The Coulomb-nuclear corrections for $\Delta\sigma_L$ ($\Delta\sigma_T$) are plotted against θ_{CM}, for the approximate angular range covered by the transmission array counters, in fig 6.1 (6.2) . The corrections

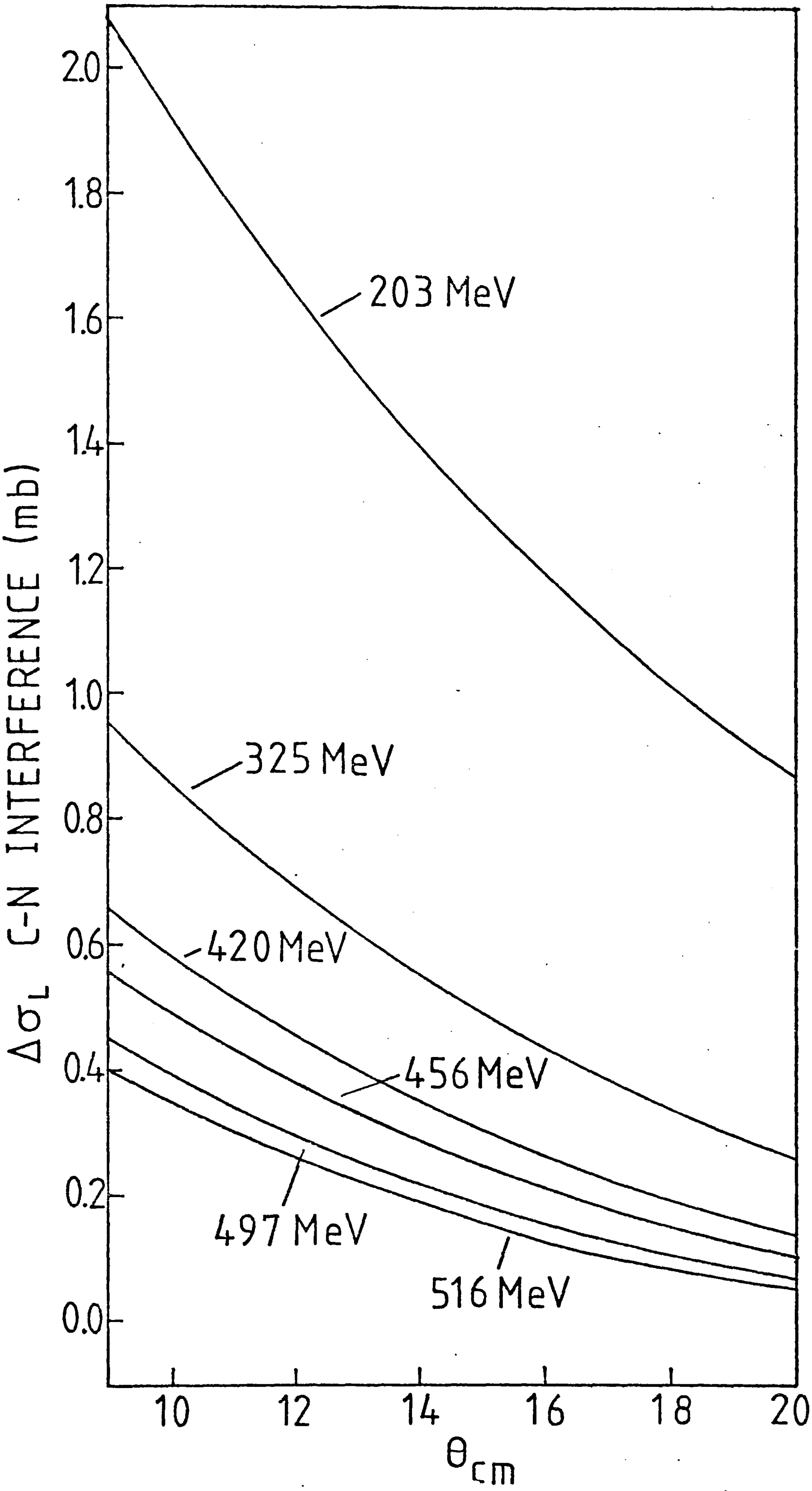

FIGURE 6.1 COULOMB-NUCLEAR INTERFERENCE TERMS, FOR $\Delta\sigma_L$, AS A FUNCTION OF CENTRE OF MASS ANGLE

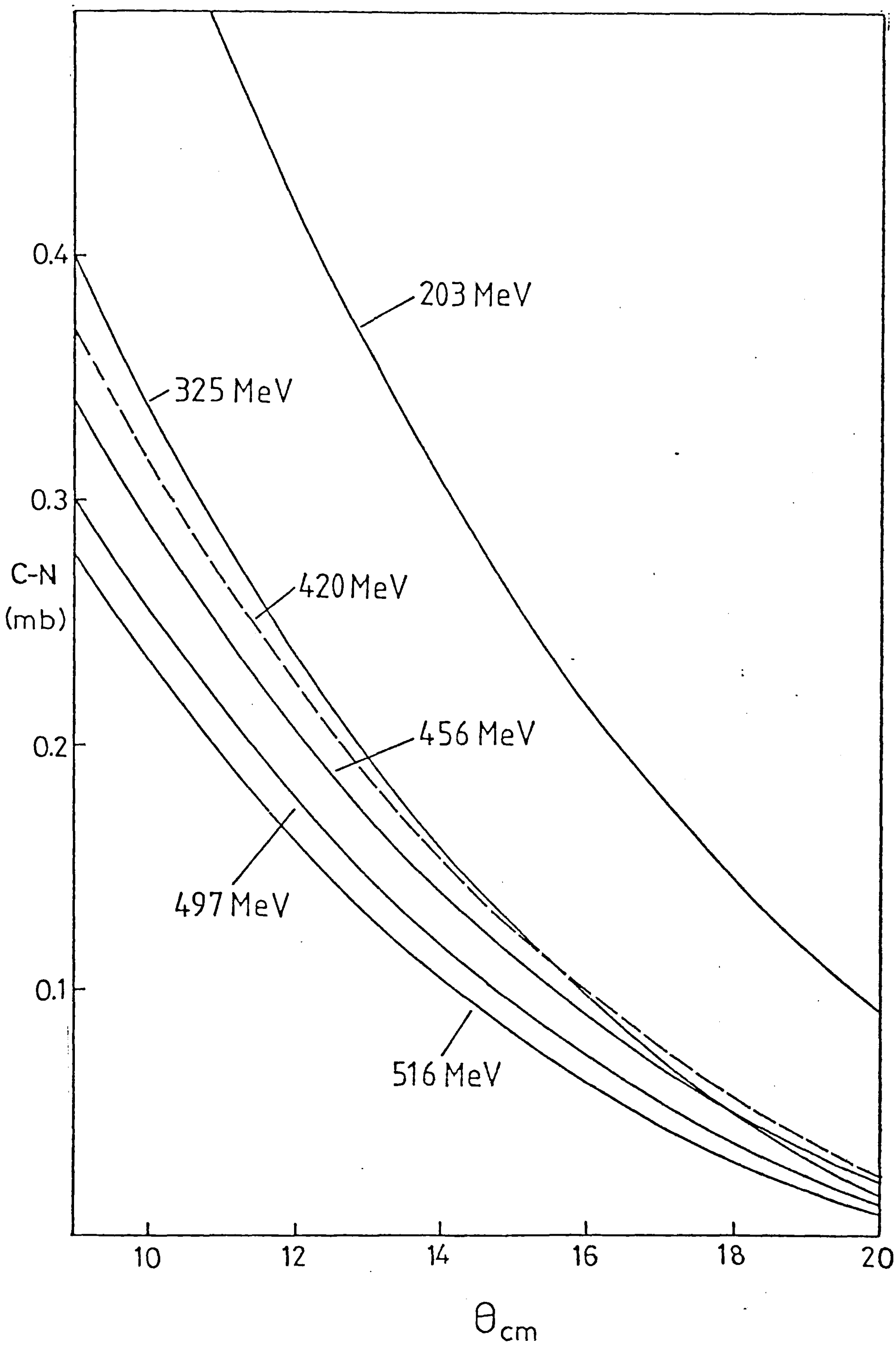

FIGURE 6.2 COULOMB-NUCLEAR INTERFERENCE TERMS, FOR $\Delta\sigma_T$, AS A FUNCTION OF THE CENTRE OF MASS ANGLE,

as a function of Θ_{CM} change rapidly, particularly at the lower energies. The corrections were, therefore, applied to the values of $\Delta\sigma_L$ and $\Delta\sigma_T$ before extrapolating them to zero detection angle. The corrections which were applied to each counter for both experiments are listed in table 6.3.

The largest Coulomb-barrier corrections are in low partial waves which produce effects varying only slowly with angle. The Coulomb-barrier could therefore be assesed by using the optical theorem. This relates the total cross section to the imaginary components of the scattering amplitudes at $\Theta = 0$. The correction was evaluated using normal values of Δ and ϕ and then re-evaluated setting $\Delta = \phi = 0$, ie switching off the Coulomb force. The difference in the two evaluations being the applied corrections. The corrections used for both experiments are listed in table 6.3. The error of the Coulomb-barrier correction was assesed by varying the phase shifts by the maximum reasonable amount.

Extrapolations of the $\Delta\sigma_L$ and $\Delta\sigma_T$ data were performed as a function of detector solid angle, by a least squares fit. Plots of the data, with Coulomb-nuclear corrections applied, showed it to require a quadratic fit, except at the lowest energy in both experiments.

The predominant error in the data arose from the statistical error in the number of protons counted by the transmission array. The binomial counting error in the transmission of the 5th counter, $t_{5,6}$, is given by $\left[N_o t_{5,6} \left(1-t_{5,6} \right)\right]^{1/2}$, where N_o is

EXPERIMENT	BEAM ENERGY (MeV)	CN_1 (mb)	CN_2	CN_3	CN_4	CN_5	CB
$\Delta\sigma_L$	202.7	2.20	1.76	1.37	1.08	0.82	-0.83 ± 0.22
	325.4	0.99	0.72	0.49	0.33	0.19	-0.35 ± 0.25
	419.5	0.67	0.46	0.29	0.17	0.06	-0.10 ± 0.27
	455.8	0.57	0.38	0.22	0.11	0.02	-0.06 ± 0.25
	497.1	0.45	0.29	0.15	0.07	-0.01	-0.06 ± 0.25
	516.5	0.39	0.25	0.13	0.05	-0.01	-0.04 ± 0.25
$\Delta\sigma_T$	202.8	0.65	0.42	0.25	0.16	0.08	-0.09 ± 0.01
	325.1	0.37	0.22	0.11	0.05	0.00	0.03 ± 0.05
	374.8	0.35	0.21	0.12	0.06	0.02	0.08 ± 0.13
	419.4	0.34	0.22	0.13	0.09	0.05	0.14 ± 0.20
	455.7	0.31	0.20	0.12	0.07	0.04	0.16 ± 0.18
	497.5	0.30	0.19	0.12	0.08	0.05	0.09 ± 0.16
	516.6	0.23	0.13	0.07	0.04	-0.01	0.10 ± 0.16

TABLE 6.3 COULOMB-NUCLEAR, CN_i, AND COULOMB-BARRIER, CB, CORRECTIONS APPLIED TO $\Delta\sigma_L$ AND $\Delta\sigma_T$ FOR THE i^{th} TRANSMISSION ARRAY COUNTER

the number of protons incident upon the target. This error is correlated and affects all counters pushing all t_i values up or down together. There is a further small statistical error arising from the different number of protons counted in each counter pair. The number of protons counted increased by $<0.1\%$ on going from counter pair 1-2 to counter pair 5-6. The least squares fitting routine, therefore, assumed an equal weight for all five points.

6.2 $\Delta\sigma_L$ Results

At an early stage in the data acquisition the effect of the solenoid precession angle on Δt was investigated. Data was taken at 497.1MeV. The solenoid was energised to produce beam polarization precessions of up to 180° in 30° steps. A polarization precession of ϕ_s produces a longitudinal beam component at the target of $P_B \sin\phi_s$, where P_B is the beam polarization component in the vertical plane incident into the solenoid.

Values of $\Delta\sigma_L$ were evaluated for each of the five counter pairs, using values of P_B obtained from the monitor of beam polarization. For these tests, Coulomb-nuclear corrections were not applied and the results were extrapolated assuming a linear relationship with solid angle.

The first set of data produced results inconsistent with the expected $\sin\phi_s$ dependence. The solenoid was found to be steering the beam. A further set of data was taken, recentring the beam on the target after each change in solenoid setting. The results from the second set of data, are presented in fig 6.3, the errors shown are purely statistical. The values of $\Delta\sigma_L$ have been normalized by the value obtained with $\phi_S = 90$, $[\Delta\sigma_L(90)]$. The results follow the expected sin ϕ_S dependence which is represented on the figure by a solid line.

Equation 2.1.7 assumes P_B and P_T are parallel to the beamline axis. However, P_T was aligned at 12° to the left, as seen by the beam, and P_B was affected by the fixed 35° bend and precession in the target's magnetic field. Values of the components of the beam polarization at the target centre are derived in appendix D

For the case where the solenoid is energised to produce $\phi_s = +90^\circ$, section 1 gives expressions for A', B', and C' the polarization components along $\underline{n}$, $\underline{r}$ and $\underline{l}$ respectively.

$$
\begin{aligned}
A' &= -T\cos\chi - \sin\chi\left[P_B\cos(\phi_B-\theta_{TGT}) - L\sin(\phi_B-\theta_{TGT})\right] \\
B' &= -\sin\theta_{TGT}\left[P_B\sin(\phi_B-\theta_{TGT}) + L\cos(\phi_B-\theta_{TGT})\right] \\
&\quad + \cos\theta_{TGT}\left\{-T\sin\chi + \cos\chi\left[P_B\cos(\phi_B-\theta_{TGT}) - L\sin(\phi_B-\theta_{TGT})\right]\right\} \\
C' &= \cos\theta_{TGT}\left[P_B\sin(\phi_B-\theta_{TGT}) + L\cos(\phi_B-\theta_{TGT})\right] \\
&\quad + \sin\theta_{TGT}\left\{-T\sin\chi + \cos\chi\left[P_B\cos(\phi_B-\theta_{TGT}) - L\sin(\phi_B-\theta_{TGT})\right]\right\}
\end{aligned}
$$

The longitudinal component of beam polarization at the target, C', setting T = L = 0, reduces to,

$$\frac{C'}{P_B} = \sin\phi_B - (1-\cos\chi)\sin\theta_{TGT}\cos(\phi_B-\theta_{TGT}) \qquad 6.2.1$$

The first term allows for the non-alignment of P_B arising from $\phi_B \neq 90^\circ$. The second term allows for the precession of the beam polarization in the target's magnetic field. The change in values

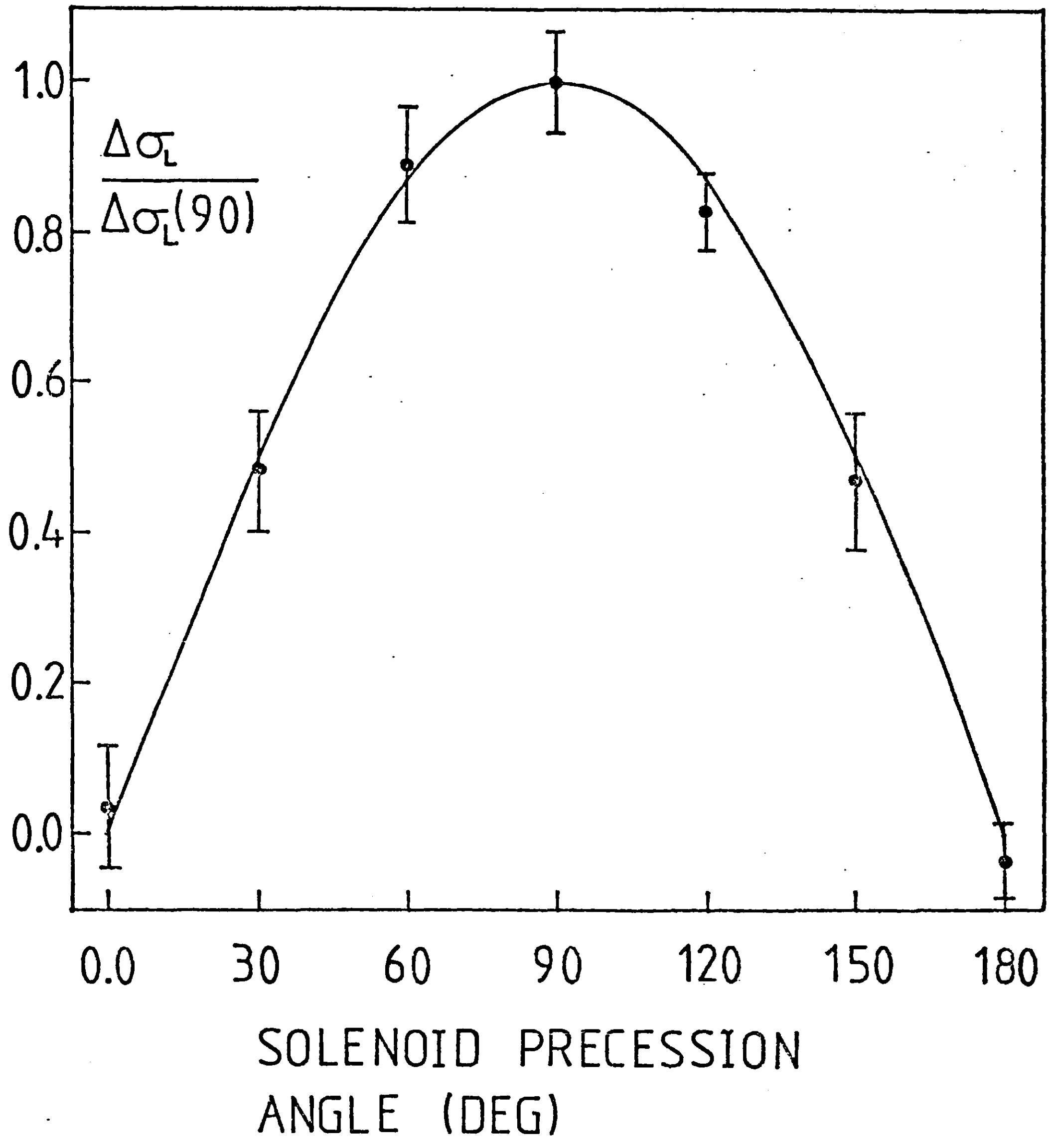

FIGURE 6.3 VARIATION IN THE MAGNITUDE OF $\Delta\sigma_L$ AS A FUNCTION OF SOLENOID PRECESSION ANGLE, ϕ_s. RESULTS ARE NORMALISED TO 1.0 AT ϕ_s=90°

of $\Delta\sigma_L$ due to the effect of the target field were small. The second term in equation 6.2.1 varied from 9.36×10^{-3} at 202.7MeV down to 5.8×10^{-4} at 516.5MeV.

The transverse component of the beam at the target, again setting $T = L = 0$, is,

$$\frac{B'}{\rho_B} = \cos\phi_B - (1-\cos\chi)\cos\theta_{TGT}\cos(\phi_B - \theta_{TGT}) \qquad 6.2.2$$

Allowing for the 12° target rotation, the transmission difference Δt is given by,

$$\Delta t = tL n_H \bar{P}_B P_T \left(C'\Delta\sigma_L \cos\theta_{TGT} - B'\Delta\sigma_T \sin\theta_{TGT} \right) \qquad 6.2.3$$

giving,

$$\Delta\sigma_L = \frac{\Delta t}{C' tL n_H \bar{P}_B P_T \cos\theta_{TGT}} + \Delta\sigma_T \frac{B'}{C'} \tan\theta_{TGT} \qquad 6.2.4$$

The above expression showed that values of Δt had a contribution from a term dependent on $\Delta\sigma_T$. Values of the coefficients $(C')^{-1}$ and $\frac{B'}{C'}\tan\theta_{TGT}$ for the run energies, are listed in table 6.4. This table shows that the coefficient of $\Delta\sigma_T$ in equation 6.2.4 is small for all energies. Using values of $\Delta\sigma_T$, given in section 6.4, corrections to $\Delta\sigma_L$ were evaluated. These are also listed in table 6.4.

To values of $\Delta\sigma_L$ calculated using equation 6.2.4, Coulomb-nuclear, $\Delta\sigma_T$, and Coulomb-barrier corrections were applied. The data was then extrapolated using a 3 variable quadratic function. There was found to be significant run-to-run jitter, at each energy, in the quadratic coefficient obtained from these fits. To smooth out

BEAM ENERGY (MeV)	$[C']^{-1}$	$[B'/C']\,\mathrm{TAN}\,\theta_{TGT}$	$[B'/C']\,\Delta\sigma_T\,\mathrm{TAN}\,\theta_{TGT}$
202.7	1.0037	0.0411	0.01
325.4	1.0078	0.0157	0.00
419.5	1.0020	-0.0079	-0.03
455.8	1.0031	-0.0142	-0.10
497.1	1.0068	-0.0240	-0.25
516.5	1.0099	-0.0287	-0.33

TABLE 6.4 VALUES OF THE COEFFICIENTS $[C']^{-1}$, $[B'/C']\,\mathrm{TAN}\,\theta_{TGT}$ AND $\Delta\sigma_T\,[B'/C']\,\mathrm{TAN}\,\theta_{TGT}$

this jitter, the coefficients at each energy were combined by firstly taking a weighted mean of values from runs with the same solenoid and target settings, and then averaging over all settings of solenoid and target.

Evaluation of the integral equations 6.1.8 and 6.1.9, including Coulomb effects, over the angular range covered by the counters, suggested that the extrapolations should be linear below the π production threshold. The curvature was thought to arise from $p\text{-}p - d\pi^+$. The quadratic coefficient was plotted as a function of incident proton energy, see fig 6.4. This showed that the coefficient followed a roughly linear trend of increasing,with increasing energy. The value at 202.7MeV was consistent with zero. Errors are not plotted on fig 6.4, however, the dispersion of the data was generally $\pm$75mb/msr. To smooth the coefficient, a linear function was fitted to data above 325MeV, assuming an equal weight for each point, the solid line on fig 6.4. The final values of the coefficient obtained from the fit, are given in table 6.5. Using these smoothed values of the quadratic coefficient, a two parameter linear fit was then used to repeat the extrapolation for each run.

A value of $\Delta\sigma_L$ was produced for each setting of target and solenoid by taking a weighted mean of $\Delta\sigma_L$ obtained from individual runs. For the error on the individual $\Delta\sigma_L$ value, the binomial counting error of the run was combined with an estimate of the error on the intercept from the least squares fit.

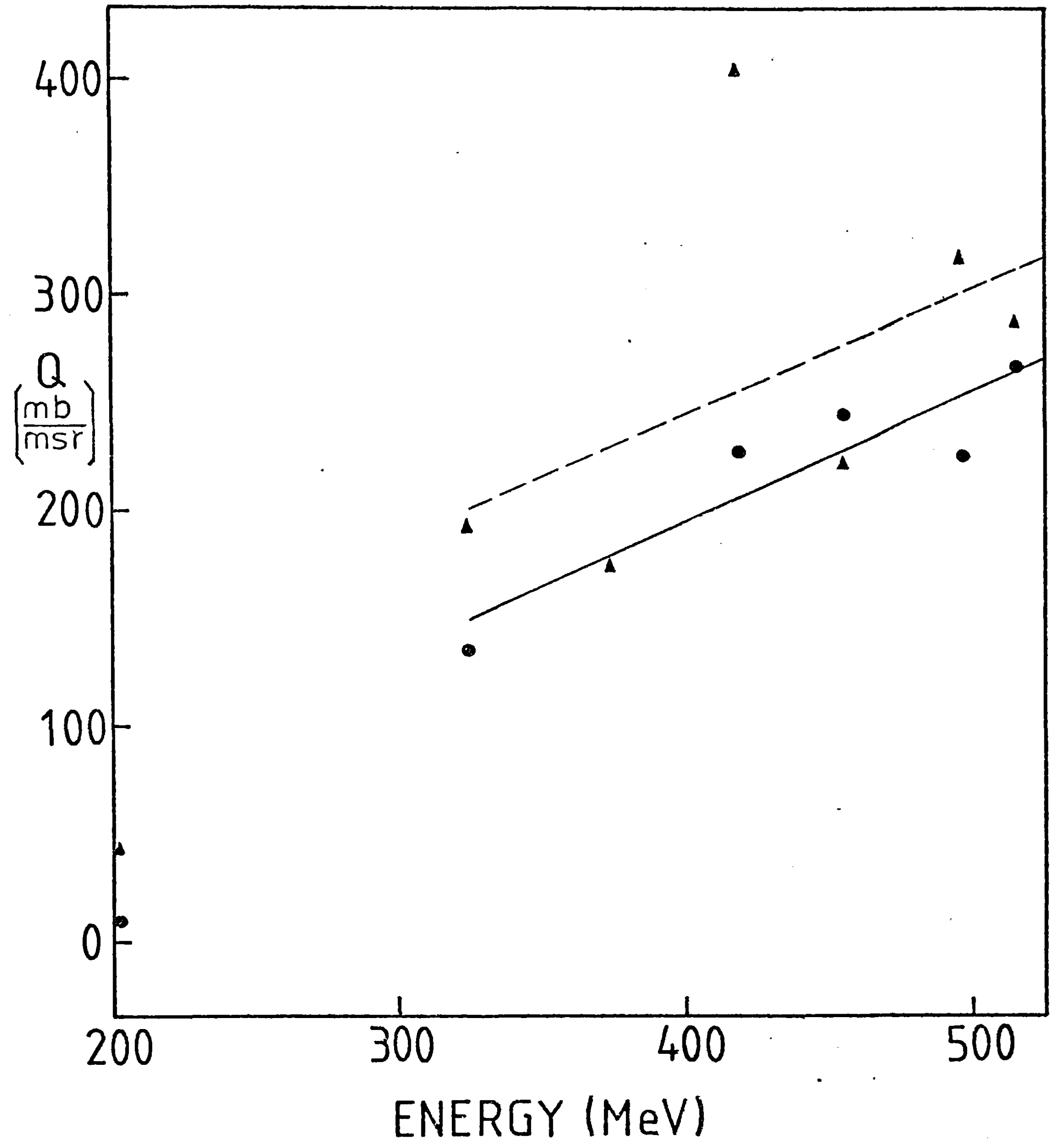

● $\Delta\sigma_L$ DATA ; ——— LINEAR FIT TO $\Delta\sigma_L$ DATA

▲ $\Delta\sigma_T$ DATA ; – – – LINEAR FIT TO $\Delta\sigma_T$ DATA

FIGURE 6.4 QUADRATIC COEFICIENT, Q, AS A FUNCTION OF ENERGY FOR FOR BOTH $\Delta\sigma_L$ AND $\Delta\sigma_T$

BEAM ENERGY (MeV)	Q (mb/msr)
202.7	0
325.4	151
419.5	206
455.8	228
497.1	252
516.5	264

TABLE 6.5 SMOOTHED QUADRATIC COEFFICIENT, Q, USED IN $\Delta\sigma_L$ EXTRAPOLATIONS. THE VALUE AT 202.8MeV HAS BEEN SET TO ZERO

These values of $\Delta\sigma_L$ were then averaged over positive and negative solenoid precession angle. This averaging removed any dependence of $\Delta\sigma_L$ on L components of beam polarization, see equation 6.2.4, and sections 1 and 2 of appendix D. As a further precaution, see section 6.4, the results were further averaged over target polarization.

The error on $\Delta\sigma_L$ was increased to allow for the spread of the component values being outside the assigned errors. The error was assessed using the expression,

$$\left[\frac{\sum_{i=1}^{N}\left(\Delta\sigma_{Li}-\overline{\Delta\sigma_L}\right)}{N-1}\right]^{1/2} \Bigg/ \left[N\right]^{1/2}$$

where $\Delta\sigma_{Li}$ is the individual, and $\overline{\Delta\sigma_L}$ the mean value, N is the number of available target and solenoid settings over which the result was averaged. However, at 497.1MeV, the two available values agreed within statistical errors and thus these were used to form the error on the mean Combined with these errors was the contribution from the Coulomb-nuclear and the Coulomb-barrier corrections. These were treated as independent and added in quadratature to give the final total error. These values of $\Delta\sigma_L$ and their errorsare given in table 6.6.

To show the extrapolation to zero solid angle, all the data was combined, by averaging over target and solenoid settings, and then fitted using a linear fit, incorporating the smoothed quadratic coefficient. The extrapolations are shown in fig 6.5, the errors show the spread in the component values.

BEAM ENERGY (MeV)	$\Delta\sigma_L$ (mb)
202.7	-30.28 ± 0.66
325.4	-25.55 ± 1.21
419.5	-21.39 ± 0.96
455.8	-16.90 ± 0.97
497.1	-14.69 ± 0.41
516.5	-12.87 ± 0.45

TABLE 6.6 $\Delta\sigma_L$ RESULTS AVERAGED OVER TARGET AND SOLENOID SETTINGS. COULOMB-NUCLEAR, COULOMB-BARRIER AND CORRECTIONS HAVE BEEN APPLIED

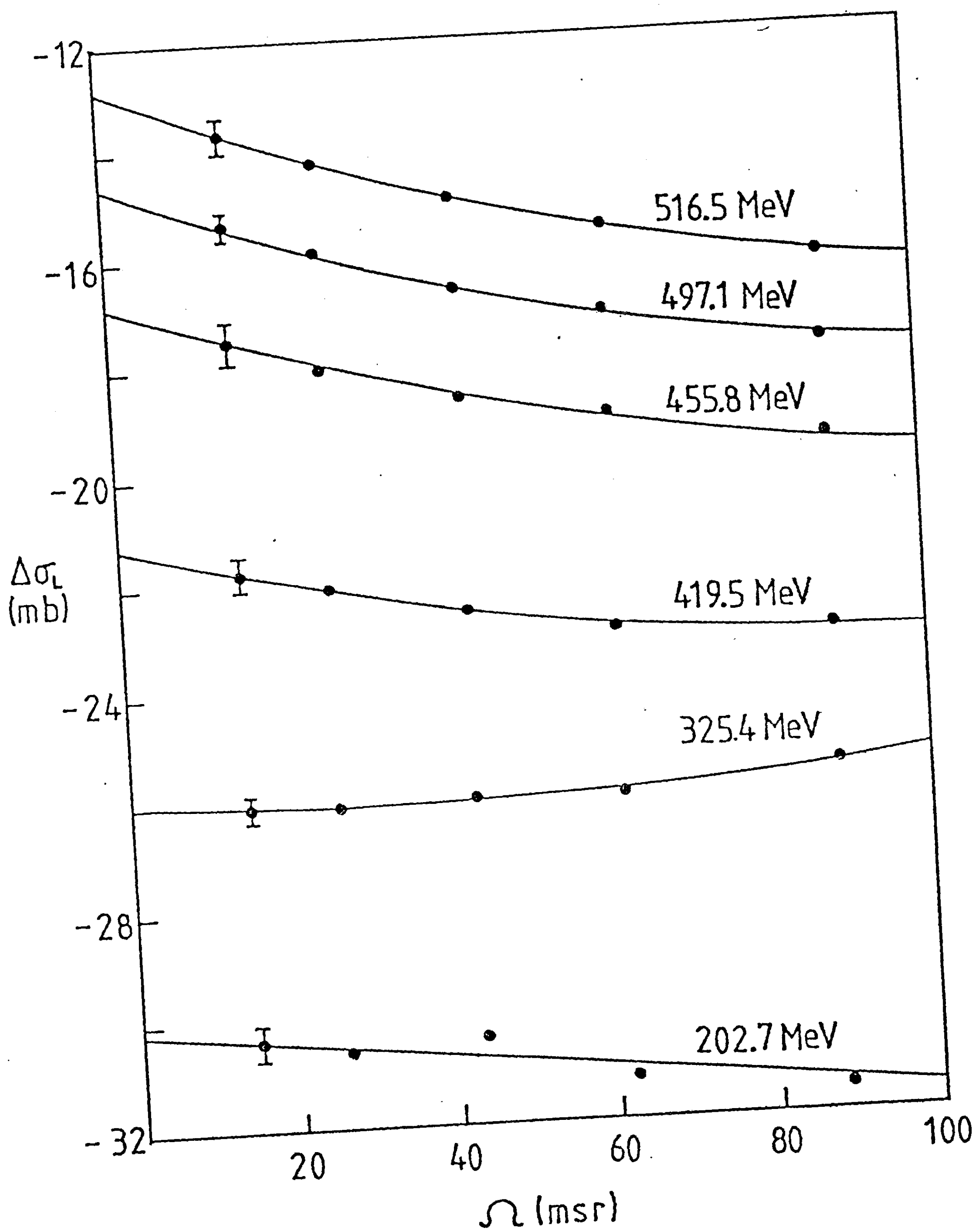

FIGURE 6.5 $\Delta\sigma_L$ EXTRAPOLATION TO ZERO SOLID ANGLE

6.2.1 Beam Spin Contamination

With the solenoid energised, averaging over both settings cancels L components in C' and B' giving $\bar{C}'$ and $\bar{B}'$,

$$\bar{C}' = -T\sin\theta_{TGT}\sin\chi + P_B\left[\cos\chi\sin\theta_{TGT}\cos(\phi_B-\theta_{TGT}) + \cos\theta_{TGT}\sin(\phi_B-\theta_{TGT})\right] \qquad 6.2.5$$

$$\bar{B}' = -T\cos\theta_{TGT}\sin\chi + P_B\left[\cos\chi\cos\theta_{TGT}\cos(\phi_B-\theta_{TGT}) - \sin\theta_{TGT}\sin(\phi_B-\theta_{TGT})\right] \qquad 6.2.6$$

Combining the above with equation 6.2.4, it is seen that the dominant term in the transmission arises from $P_T P_B \cos^2\theta_{TGT}\Delta\sigma_L \sin(\phi_B-\theta_{TGT})$, D ; extracting this as a factor,

$$\Delta t(\text{SOL,ON}) \propto D\left\{1+\frac{\Delta\sigma_T}{\Delta\sigma_L}\left[\tan^2\theta_{TGT} - \frac{\cos\chi\tan\theta_{TGT}}{\tan(\phi_B-\theta_{TGT})}\right] + \frac{\cos\chi\tan\theta_{TGT}}{\tan(\phi_B-\theta_{TGT})} - \frac{T\sin\chi\tan\theta_{TGT}}{P_B\sin(\phi_B-\theta_{TGT})}\left[\frac{\Delta\sigma_L-\Delta\sigma_T}{\Delta\sigma_L}\right]\right\} \qquad 6.2.7$$

A similar proceedure can be followed for the case of solenoid off. From section 3 of appendix D , equations for C' and B' are obtained for substitution into equation 6.2.4, giving the following

$$\Delta t(\text{SOL. OFF}) \propto D\left\{\frac{T}{P_B}\left[1+\frac{\tan\theta_{TGT}\cos\chi}{\tan(\phi_B-\theta_{TGT})} + \frac{\Delta\sigma_T}{\Delta\sigma_L}\left(\tan\theta_{TGT} - \frac{\cos\chi}{\tan(\phi_B-\theta_{TGT})}\right)\right] + \frac{L}{P_B}\left[\frac{1}{\tan(\phi_B-\theta_{TGT})} - \tan\theta_{TGT}\cos\chi + \frac{\Delta\sigma_T}{\Delta\sigma_L}\left[\frac{\tan\theta_{TGT}}{\tan(\phi_B-\theta_{TGT})}+\cos\chi\right]\right] + \left[1-\frac{\Delta\sigma_T}{\Delta\sigma_L}\right]\frac{\sin\chi\tan\theta_{TGT}}{\sin(\phi_B-\theta_{TGT})}\right\} \qquad 6.2.8$$

It was shown in section 5.3.5 that the L component was consistent with zero at the energies where measurements were made. Values of L were therefore assumed zero at all energies , in order that values of T could be obtained. Note that the coefficients of L/P_B in equation 6.2.8 are smaller than those for T/P_B.

To evaluate the magnitude of the T component values of Δt from each counter pair were extrapolated using a linear relationship with solid angle. The intercepts were averaged over solenoid and target settings for runs with the solenoid on, and over target polarization for runs with the solenoid off. The ratio of Δt (solenoid off)/Δt (solenoid on) is given in table 6.7. Using these ratios and equations 6.2.7 and 6.2.8, values of T were obtained, and are given in table 6.7. The errors quoted arise purely from statistics.

These values can be compared and combined with the independent evaluation of T from the monitor data, which is also listed in table 6.7. The values obtained from the two methods were in agreement at the three available energies, final values, $\overline{T}$, were taken as the average of the two evaluations. $\overline{T}$ was small at all energies except 325.4MeV where a value of -0.16 was found.

The effect of a non-zero T component on Δt can be evaluated using equation 62 .7,

$$\frac{\Delta t(T=0) - \Delta t(T\neq 0)}{\Delta t(T=0)} = \frac{T}{P_B}\left[\frac{\sin\chi \tan\theta_{TGT}}{\sin(\phi_B - \theta_{TGT})}\left(1 - \frac{\Delta\sigma_T}{\Delta\sigma_L}\right)\right] \left\{1 + \frac{\cos\chi \tan\theta_{TGT}}{\tan(\phi_B - \theta_{TGT})} + \frac{\Delta\sigma_T}{\Delta\sigma_L}\left[\tan^2\theta - \frac{\cos\chi \tan\theta_{TGT}}{\tan(\phi_B - \theta_{TGT})}\right]\right\}^{-1} \qquad 6.2.9$$

Values of T at 202.7, 455.8 and 497.1MeV were assumed to be zero. Values at the remaining three energies were set to values of $\overline{T}$. Using these values it was found that Δt had to be scaled by 1.0161, 0.9930 and 0.9924 at 325.4, 419.5 and 497.1MeV respectively.

BEAM ENERGY (MeV)	$\frac{\Delta t(\text{SOL OFF})}{\Delta t(\text{SOL ON})}$	T (TRANS)	T (MONS)	$\overline{T}$
202.7	-0.063 ± 0.012	0.024 ± 0.009		
325.4	-0.278 ± 0.011	-0.147 ± 0.007	-0.176 ± 0.026	-0.162
419.5	0.003 ± 0.030	0.051 ± 0.020	0.072 ± 0.025	0.062
455.8	-0.054 ± 0.029	0.017 ± 0.018		
497.1	-0.026 ± 0.043	0.049 ± 0.029		
516.5	-0.041 ± 0.039	0.042 ± 0.026	0.041 ± 0.019	0.042

TABLE 6.7 THE RATIO OF TRANSMISSION DIFFERENCES, Δt, RECORDED WITHOUT AND WITH THE SOLENOID ENERGISED AND VALUES OF T, T(TRANS), OBTAINED FROM THEM. VALUES OF T OBTAINED FROM THE CHAMBER MONITOR DATA, T(MONS), FROM TABLE 5.4 ARE ALSO LISTED. THE MEAN VALUE OF THESE TWO EVALUATIONS, $\overline{T}$, IS ALSO GIVEN

These scaling factors were incorporated into the data by firstly removing from $\Delta\sigma_L$ the Coulomb-nuclear, Coulomb-barrier and $\Delta\sigma_T$ corrections. These raw values were then scaled and the corrections were reapplied. A further correction was applied to the data to allow for the curved path that the beam travelled in the target volume, caused by the component of magnetic field transverse to the beam momentum. This increased the path length through the target by $\sim 0.09\%$ (0.02%) at 202.7(516.5)MeV. The largest correction was at 202.7MeV where $\Delta\sigma_L$ changed by only 0.03mb. Final values of $\Delta\sigma_L$, after applying the above corrections, are given in table 6.8.

6.3 $\Delta\sigma_T$ Results

Values of $\Delta\sigma_T$ were calculated for each counter pair for each run. Coulomb-nuclear and Coulomb-barrier corrections were applied and the results extrapolated to zero detector angle. The curvature, slope and intercept of these extrapolations were found to be dependent upon the orientation of the target polarization, but they did not correlate systematically with it. These differences were understood in a qualitative fashion to arise from small mis-alignments of the transmission array, coupled with the large differential cross section, 10^3mbsr^{-1}, and analysing power, $P(7)\sim 0.4$, of elastic scattering from carbon at small angles, which cause an asymmetry in scatters proportional to $P_B P_C(\theta)$.

BEAM ENERGY (MeV)	$\Delta\sigma_L$ (mb)
202.7	-30.25 ± 0.66
325.4	-25.98 ± 1.21
419.5	-21.23 ± 0.96
455.8	-16.90 ± 0.97
497.1	-14.69 ± 0.41
516.5	-12.77 ± 0.45

TABLE 6.8 FINAL $\Delta\sigma_L$ RESULTS CORRECTED FOR T COMPONENT BEAM POLARIZATION AND THE CURVED TRAJECTORY IN THE TARGET VOLUME

A transmission array misalignment introduces an additional component σ_{INST}, into equation 2.1.4 and 2.1.5, which ignoring the spin independent scattering, can be rewritten,

$$t(\uparrow\uparrow) = \mathrm{EXP}\left[\frac{n_H L P_B(\uparrow) P_T(\uparrow) \Delta\sigma_T}{2 \times 1.0079} - \sigma_{INST} P_B(\uparrow)\right] \tag{6.3.1}$$

$$t(\uparrow\downarrow) = \mathrm{EXP}\left[\frac{n_H L P_B(\downarrow) P_T(\uparrow) \Delta\sigma_T}{2 \times 1.0079} - \sigma_{INST} P_B(\downarrow)\right] \tag{6.3.2}$$

which leads to,

$$\Delta\sigma_T = \Delta\sigma_{TM} + \frac{2\sigma'_{INST}}{P_T(\uparrow)} \tag{6.3.3}$$

where

$$\Delta\sigma_{TM} = \frac{1.0079\,\Delta t}{\bar{t}\, n_H P_T \bar{P}_B L} \quad ; \quad \sigma'_{INST} = \frac{1.0079\,\sigma_{INST}}{n_H\, L}$$

Values of σ'_{INST} were evaluated from data contained in the paper of Besset et al [(6.1)], using equation 6.3.4,

$$\sigma'_{INST} = \frac{1.0079}{A}\frac{n_c}{n_H}\int_{\Delta\Omega} P_c \left(\frac{d\sigma}{d\Omega}\right)_{p\text{-}c} d\Omega \tag{6.3.4}$$

where the suffix p-c implies the elastic proton-carbon differential cross section and A is the atomic weight of carbon, $n_c = N_A \rho_c$ where N_A is the Avogadros number and ρ_c the density of carbon in the target. The integral was evaluated over the asymmetry in solid angle subtended by a counter displaced by 1cm. Five counters were considered which covered the angular range 2 - 5.5^{o}LAB. The data was then extrapolated linearly to zero solid angle, the results are listed in table 6.9.

Combining the data for $\Delta\sigma_T$ obtained with the target polarized up and down, ($\Delta\sigma_T(\uparrow)$ and $\Delta\sigma_T(\downarrow)$), values for σ'_{INST} can be

BEAM ENERGY (MeV)	σ'_{INST}(CALC) (mb)	σ'_{INST}(MEAS) (mb)
210	-0.84	-0.14
330	-0.72	0.96
380	-0.63	0.59
425	-0.63	0.61
460	-0.57	-0.46
500	-0.51	0.15
520	-0.51	1.17

TABLE 6.9 EVALUATION OF σ'_{INST} A) ARISING FROM INSTRUMENTAL ASYMMETRY, CAUSED BY A 1cm MISALIGNMENT OF THE TRANSMISSION ARRAY, σ'_{INST} (CALC), B) EVALUATED FROM EXPERIMENTAL RESULTS, σ'_{INST}(MEAS)

extracted from the experimental data, using equation 6.3.5,

$$\sigma'_{INST} = \frac{\Delta\sigma_{TM}(\uparrow) - \Delta\sigma_{TM}(\downarrow)}{-2\left[\frac{1}{P_{T(\uparrow)}} - \frac{1}{P_{T(\downarrow)}}\right]} \qquad 6.3.5$$

Values of $\Delta\sigma_{TM}$ were produced for each run by extrapolation using a 3 parameter quadratic least squares fit. All the results from one energy and one target polarization were combined to give a weighted mean value for $\Delta\sigma_{TM}$. From the value of $\Delta\sigma_{TM}$ from each target polarization orientation, values of σ'_{INST} were evaluated. These are listed in table 6.9. Comparison of the experimental and calculated values showed that a misalignment of the transmission array by $\sim$1cm was enough to explain the differences in $\Delta\sigma_{TM}$ found between the two target polarization orientations.

The results indicated that there was an average transmission array misalignment of $\sim$1cm. The position of the cross wires on the transmission array, with respect to the centre of array, was found to be good to $<$3mm, and the scintillators were positioned to $\pm$ 0.5mm with respect to the array's centre. A close examination of the setting-up at each energy, detailed in log books, suggested that misalignments of $\sim$1cm could have been present. The data at 516.5MeV, the last energy to be tuned, was rather hurriedly set-up and a transmission array misalignment of more than 1cm could have occured.

The experimental and calculated results for σ'_{INST} were taken as showing the dependence of $\Delta\sigma_T$ on the orientation of the target polarization to arise from the scattering of polarized beam from the carbon in the target, coupled with a transmission array misalignment. This being the case, the instrumental effect is removed by averaging $\Delta\sigma_T$ over both target polarizations. Extra care was taken during the $\Delta\sigma_L$ runs to align the transmission array, However, as the effect arises because of the transverse components of polarization, the effect is small for $\Delta\sigma_L$. Values of $\Delta\sigma_L$ were, however, averaged over target polarization in order to remove any instrumental effects.

The quadratic coefficient for the extrapolation to zero solid angle was dependent on the orientation of the target polarization. This coefficient was to be smoothed as a function of energy, to follow a similar proceedure as that adopted for $\Delta\sigma_L$. Values of $\Delta\sigma_T$ calculated from each counter pair, were averaged over all runs with the same target polarization at all energies. A three parameter quadratic extrapolation to zero solid angle was then performed. The quadratic coefficient and values of $\Delta\sigma_T$ from each counter pair were then averaged over target polarization. The averaged quadratic coefficients are plotted on fig 6.4.

The dispersion of the coefficient for each target setting was generally $\pm$ 120mb/msr. The coefficients are seen to be very similar to those obtained for $\Delta\sigma_L$, apart from the value at 419.4MeV which was anomalously high. The coefficient was smoothed by taking values from a linear fit to the data above 325MeV, the dashed line on fig 6.4. The value at 202.8MeV was taken to be zero as for $\Delta\sigma_L$. The smoothed coefficients are listed in table 6.10.

BEAM ENERGY (MeV)	Q (mb/msr)
202.8	0
325.1	201
374.8	230
419.4	256
455.7	278
497.5	302
516.5	314

TABLE 6.10 SMOOTHED QUADRATIC COEFFICIENT, Q, USED IN $\Delta\sigma_T$ EXTRAPOLATIONS. THE VALUE AT 202.8MeV HAS BEEN SET TO ZERO

All the $\Delta\sigma_T$ data from all runs at one energy was then combined and one extrapolation to zero solid angle was performed using a 2 parameter quadratic function, with smoothed quadratic coefficient. These extrapolations are shown in fig 6.6. The errors on this figure show the statistical error only. The final error in $\Delta\sigma_T$ needed to be increased at a few energies to allow for the run-to-run variation in $\Delta\sigma_T$ being higher than statistics. In these cases the errors were evaluated from the spread of $\Delta\sigma_T$ obtained from extrapolations performed on the data from each run. The final error was composed of this error plus estimates of errors in Coulomb-nuclear and Coulomb-barrier terms and a small error reflecting the uncertainty in the intercept of the extrapolations. These components were added in quadrature to give the final error.

In the $\Delta\sigma_T$ experiment the beam was deflected by the large component of magnetic field perpendicular to its momentum. As for $\Delta\sigma_L$ this increased the effective length of the target, for which corrections were applied ranging from 0 at 202.7MeV, up to -0.02mb at 516.5MeV. The final values of $\Delta\sigma_T$ are given in table 6.11.

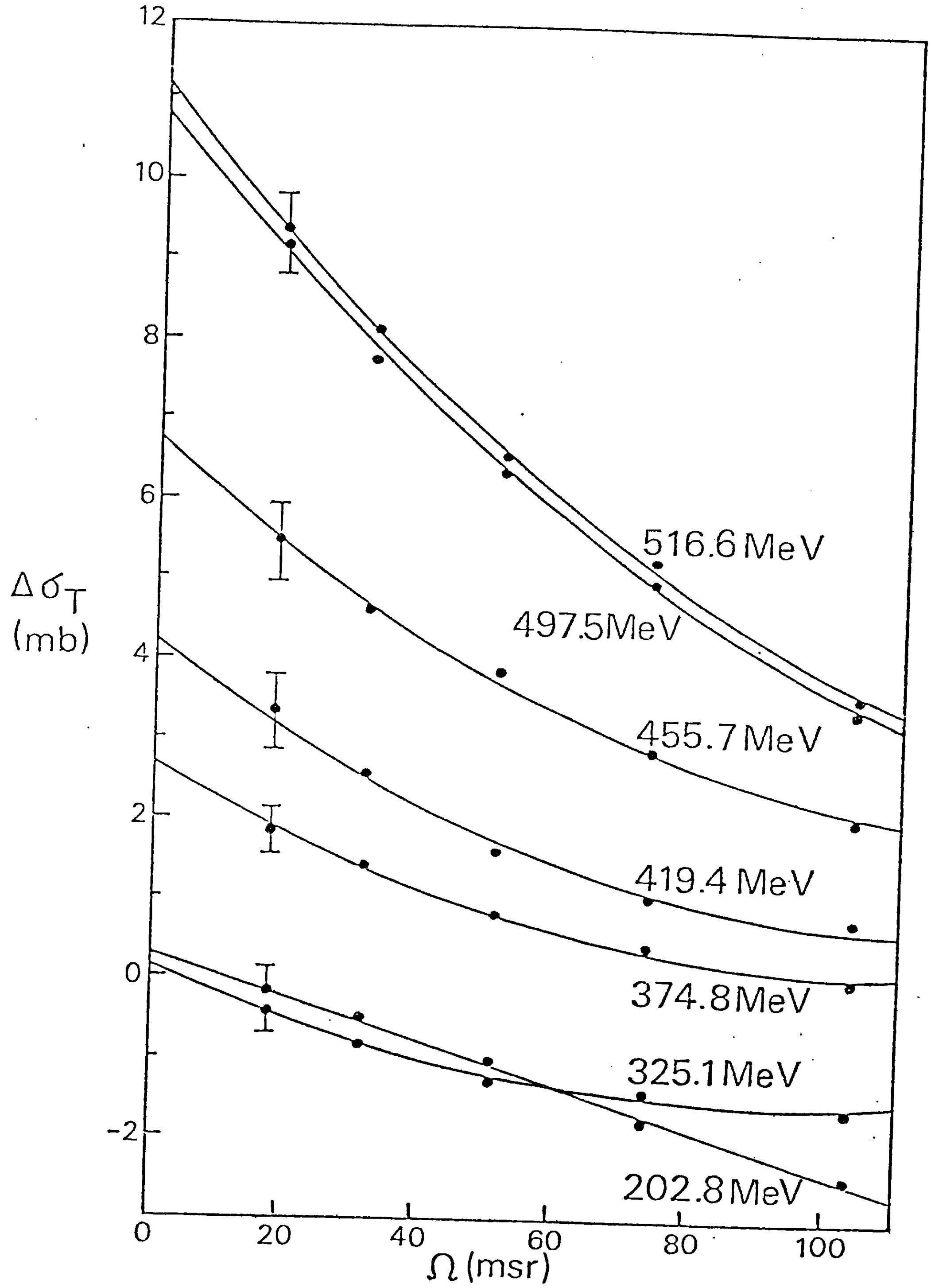

FIGURE 6.6 $\Delta\sigma_T$ EXTRAPOLATION TO ZERO SOLID ANGLE

BEAM ENERGY (MeV)	$\Delta\sigma_T$ (mb)
202.8	0.29 $\pm$0.38
325.1	0.16 $\pm$0.37
374.8	2.68 $\pm$0.33
419.4	4.20 $\pm$0.37
455.7	6.75 $\pm$0.50
497.5	10.82 $\pm$0.73
516.5	11.15 $\pm$0.64

TABLE 6.11 $\Delta\sigma_T$ RESULTS

CHAPTER 7

CONCLUSION

These experiments have measured $\Delta\sigma_L$ ($\Delta\sigma_T$) at six (seven) energies. The results are presented in tables 6.8 and 6.11 . An important improvement in these experiments over all previous measurements was the inclusion of a nuclear physics experiment to independently determine the target polarization. The evaluation of the target polarization from the NMR system agreed well with the result from the nuclear scattering detectors, see section 5.3.4. The results have an independent overall normalization uncertainty of $\pm$6.5(6.8)% for $\Delta\sigma_L$ ($\Delta\sigma_T$). This uncertainty arises from three sources.

1. The main contribution came from the variation in the packing fraction of the target beads. Repeated measurements showed a variation of $\pm$4.9%. As the two experiments used different targets this is an independent normalization on each experiment, which combined with the uncertainty in target dimensions, gives a normalization of $\pm$5.2%.

2. The target polarization for $\Delta\sigma_L$ was obtained from the NMR and the independent chamber evaluation to an accuracy of $\pm$2.5%. In the $\Delta\sigma_T$ experiment the target polarization was evaluated to an accuracy of $\pm$3.2% using only the monitor chamber data.

3. Lack of detailed knowledge for the precise function to fit the background in the monitor chambers was judged to introduce an uncertainty of $\pm$3% into the overall normalization.

The total normalization error was obtained from a quadratic addition of these three independent errors. The normalization uncertainty in the beam polarization, $\pm 1.5\%$, contributes very little to the experiment's overall normalization. $\Delta\sigma_L$ and $\Delta\sigma_T$ are both inversly proportional to $(P_B P_T)$. The target polarization was evaluated only by the monitor chambers for $\Delta\sigma_T$, and predominantly by them for $\Delta\sigma_L$. The evaluation of the target polarization from the chambers depends on a term $(P_B)^{-1}$. Thus P_B approximately cancels out in the evaluation of $\Delta\sigma_L$ and $\Delta\sigma_T$.

The values of $\Delta\sigma_L$ and $\Delta\sigma_T$ presented in this thesis and in Stanley et al[7.1] update those values given in Axen et al [7.2], which were evaluated using a linear extrapolation to zero detection angle, and a quadratic fit to the background in the monitor chambers. Errors on $\Delta\sigma_T$ in these earlier publications were inflated to cover the spread in the values obtained for each orientation of the target polarization. These differences have now been understood in terms of small misalignments of the transmission array, see section 6.3, and the errors reduced accordingly.

An independent check on the normalization of the $\Delta\sigma_L$ experiment was possible at the two lowest energies of 203 and 325MeV. The phase shift predictions at these energies are secure as inelasticities are zero or negligible, and the dominant phase shifts are accurately fixed by extensive data. At higher energies predictions are sensitive to the poorly determined elasticity parameters. The BASQUE phase shift analysis, excluding all $\Delta\sigma_L$ and $\Delta\sigma_T$ data , predicted values of -30.88 ± 0.32mb and -25.78 ± 0.63mb for 202 and 325MeV respectively. Similar predictions were obtained from the phase shift analysis of Arndt [7.3]. From a comparison of these predictions with the experimental results, a scaling factor for these results of 1.016 $\pm$0.023 is implied, which confirms the correct normalization of this experiment.

Results for $\Delta\sigma_T$ at the two lowest energies were also in agreement with phase shift predictions of 0.16 $\pm$0.3 (0.51 $\pm$0.59)mb at 203 (325)MeV. Owing to the near zero magnitude of these results no conclusion could be drawn as to the experiment's normalization.

Comparison of $\Delta\sigma_L$ is made in fig 7.1, with early Argonne [1.14-16] newer LAMPF [7.4] and preliminary SIN[7.5] results. Coulomb-nuclear and Coulomb-barrier corrections calculated by the method described in this thesis have been applied to these data. This has moved the early Argonne points around 500MeV more negative by $\sim$0.4mb. The early Argonne data point at 1.17GeV/c (560MeV) has now been withdrawn. The BASQUE results are consistently 3mb more negative than other data. If they are renormalized by 30%, so as to agree with other groups above 400MeV, χ^2 in the phase shift fits is found to increase by large amounts, $\sim$150(50) at 203(325)MeV.

Exhaustive discussions with the Argonne, LAMPF and SIN groups have been unable to account for the discrepancy in the $\Delta\sigma_L$ results. However, in the Argonne and LAMPF experiments the smallest counters in their ten counter transmission array, which are the most crucial in the extrapolation, were furthest away from the target. Deuterons

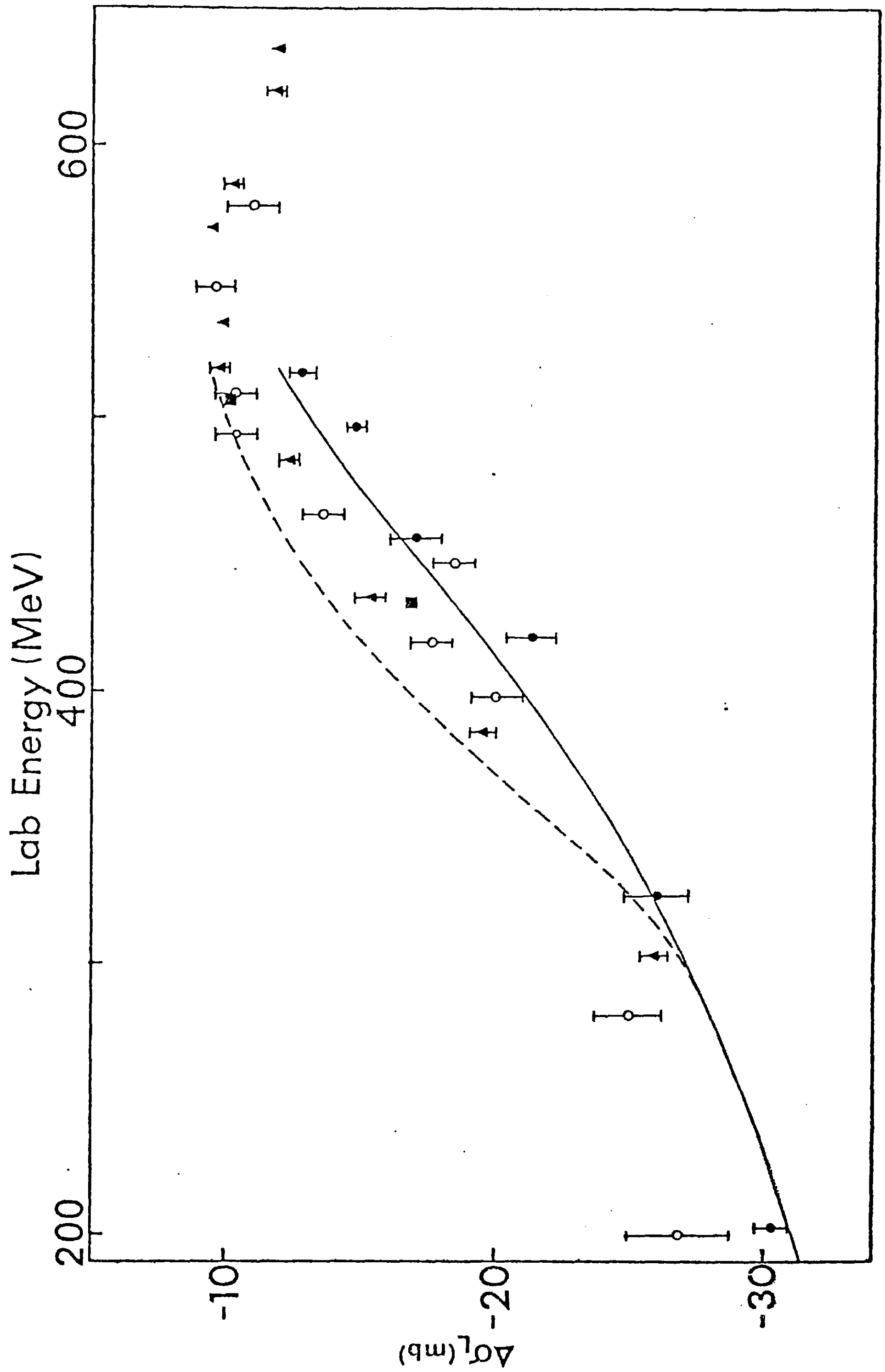

● BASQUE RESULTS : ▲ LAMPF RESULTS

o PRELIMINARY SIN RESULTS : ■ ARGONNE RESULTS

FIGURE 7.1 RESULTS FOR $\Delta\sigma_L$ COMPARED WITH THOSE OF OTHER GROUPS stopping in the array and not reaching the furthest counter, will change the extrapolation. However, this effect is too small to explain the discrepancy.

The solid line in fig 7.1 is the phase shift fit to all $\Delta\sigma_L$ data using the solution of Dubois et al [1.20]. The SIN data points below the π production threshhold are seen to disagree with the phase shift solution. As a positive bound for the phase shift predictions, values were recalculated using OPE predictions of elasticity parameters for partial waves with $J \geqslant 4$ and putting all other inelasticity into $^1D_2$ which contributes positively to $\Delta\sigma_L$, see equations 1.9.3 and 1.9.5. The implication of the BASQUE data, which lies away from the positive bound, is that the contribution from R_{JJ} (ie $^3P_1$ and/or $^3F_3$) is significant. This conclusion is in broad agreement with the limited data on pp-$d\pi^+$ [7.6], which shows that inelasticity starts at threshold in $^3P_1$, is overtaken at about 325MeV by $^1D_2$, and in the energy range 400-500MeV $^3F_3$ and $^3P_2$ inelasticity becomes significant. The Argonne, LAMPF and SIN data which lie near the positive bound require most of the inelasticity to be in $^1D_2$ and the contribution to $\Delta\sigma_L$ from R_{JJ} to be small, ie small inelasticity in the $^3P_1$ and $^3F_3$ partial waves, which is in contradiction to the pp-$d\pi^+$ data. Conversely, a component of inelasticity could be introduced into $^3F_3$ at the expense of a large inelasticity in $^3P_0$ which would be suprising as this wave is forbidden in pp-$d\pi^+$.

BASQUE $\Delta\sigma_T$ results are compared with data from Argonne[1.13] and Saclay [7.7] in fig 7.2. The BASQUE results at 497.5 and 516.5MeV

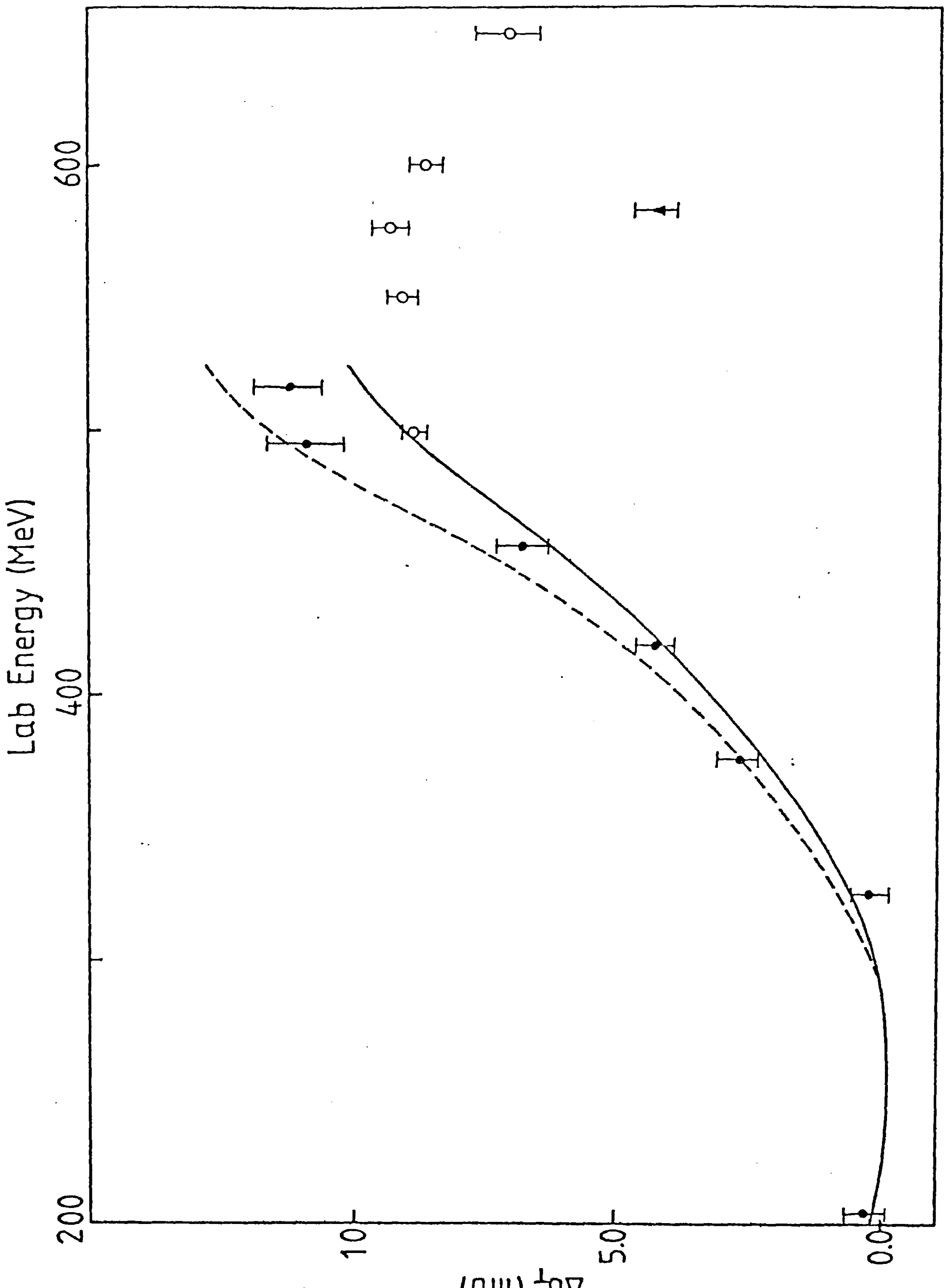

● BASQUE RESULTS : ○ SACLAY RESULTS

▲ ARGONNE RESULT :

FIGURE 7.2 RESULTS FOR $\Delta\sigma_T$ COMPARED WITH THOSE OF OTHER GROUPS are seen to be 2mb larger than the Saclay point at $\sim$500MeV. Shown on fig 7.2 is the phase shift solution (1.20), solid line, and the positive bound, dashed line, calculated using the method detailed for $\Delta\sigma_L$. The BASQUE data lies close to the positive bound, implying that contributions from R^J, $R_{J-1,J}$ and $R_{J+1,J}$ are small up to 515MeV, see equations 1.9.4 and 1.9.6. The best phase shift fit to the data is obtained with zero inelasticity in $^3P_2$ which is in contradiction to the pp-$d\pi^+$ data. The data is, however, in agreement, including normalization error, with the phase shift solution of ref 7.7 apart from at 497.5MeV.

The early Argonne data was used in a dispersion analysis by Grein and Kroll (1.28) to produce values of ReF_3 which were in conflict with phase shift predictions, see section 1.9. The dispersion analysis was re-evaluated (7.2) using the broken curves on fig 7.3, which were drawn through the phase shift solutions of ref1.20, up to 580MeV and which thereafter follow the curves drawn through LAMPF data. Much better agreement was found between ReF_3 obtained from phase shift analysis, and that obtained from this new dispersion analysis. The dispersion analysis is very little altered by the changes in $\Delta\sigma_L$ between those in ref 7.7 and results presented in this thesis. The most recent calculations by Grein and Kroll (7.8) report satisfactory agreement for ReF_2 and both BASQUE and Arndt phase shifts.

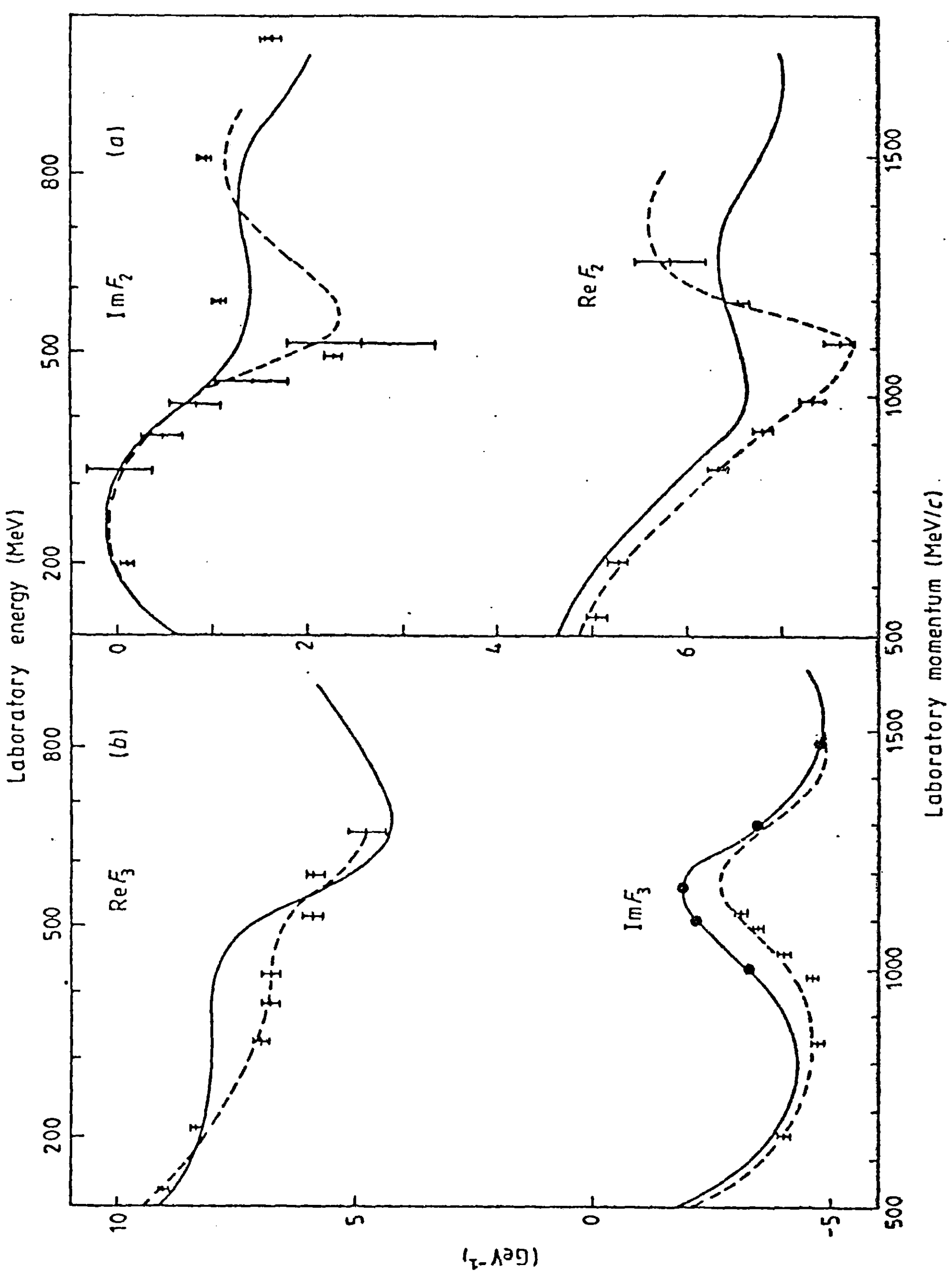

Ɪ BASQUE RESULTS

● ARGONNE RESULTS

--- CURVE DRAWN THROUGH THE PHASE SHIFT SOLUTION OF REF 7.7

— CURVE DRAWN THROUGH ARGONNE DATA, FROM REF 1.28

FIGURE 7.3 REAL AND IMAGINARY PARTS OF THE AMPLITUDES F_2 AND F_3

APPENDIX A

HELICITY AMPLITUDES

In this appendix the five independent helicity amplitudes, $\phi_1 - \phi_5$, (1.25) are given in terms of transition amplitudes, see section 1.4. This information was taken from table VIII in ref 1.24.

$$\phi_1 = \sum_{J,\,EVEN} \left[(2J+1)R_J + JR_{J-1,J} + (J+1)R_{J+1,J} + 2\sqrt{J(J+1)}R^J \right] P_J(x)$$

$$\phi_2 = \sum_{J,\,EVEN} \left[-(2J+1)R_J + JR_{J-1,J} + (J+1)R_{J+1,J} + 2\sqrt{J(J+1)}R^J \right] P_J(x)$$

$$\phi_3 = \sum_{J,\,EVEN} \left[(J+1)R_{J-1,J} + JR_{J+1,J} - 2\sqrt{J(J+1)}R^J \right] d^J_{11}(x) + \sum_{J,\,ODD} (2J+1)R_{JJ}\, d^J_{11}(x)$$

$$\phi_4 = \sum_{J,\,EVEN} \left[(J+1)R_{J-1,J} + JR_{J+1,J} - 2\sqrt{J(J+1)}R^J \right] d^J_{-1,1}(x) - \sum_{J,\,ODD} (2J+1)R_{JJ}\, d^J_{-1,1}(x)$$

$$\phi_5 = \sum_{J,\,EVEN} \left\{ \sqrt{J(J+1)}\,[R_{J-1,J} - R_{J+1,J}] + R^J \right\} d^J_{10}(x)$$

Where $x = \cos\Theta$, Θ is the centre of mass scattering angle.

$P_J(x)$ is the J^{th} order Legendre polynomial

$$d^J_{11}(x) = \frac{1}{(1-x)} \left[P_J(x) + \left(\frac{J+1}{2J+1}\right) P_{J-1}(x) + \left(\frac{J}{2J+1}\right) P_{J+1}(x) \right]$$

$$d^J_{-1,1}(x) = \frac{1}{(1-x)} \left[-P_J(x) + \left(\frac{J+1}{2J+1}\right) P_{J-1}(x) + \left(\frac{J}{2J+1}\right) P_{J+1}(x) \right]$$

$$d^J_{1,0}(x) = \frac{\sqrt{J(J+1)}}{(2J+1)} \; \frac{[P_{J+1}(x) - P_{J-1}(x)]}{\sqrt{1-x^2}}$$

APPENDIX B

PHASE SHIFT PREDICTIONS OF THE POLARIZATION PARAMETER, SPIN CORRELATION PARAMETERS AND THE TARGET ANALYSING POWER, M. The error in M, ΔM, was assessed using the method set out in section 5.3.1. θ_{cm} is the centre of mass scattering angle.

ENERGY, 202.7MeV

θ_{cm}	P	A_{NN}	A_{SS}	A_{LL}	A_{LS}	M	ΔM
45	0.298	0.752	-0.565	0.687	-0.512	0.670	0.047
50	0.282	0.826	-0.633	0.763	-0.480	0.746	0.040
55	0.259	0.877	-0.698	0.814	-0.433	0.799	0.032
60	0.231	0.910	-0.756	0.844	-0.376	0.831	0.023
65	0.198	0.928	-0.804	0.857	-0.314	0.848	0.019
70	0.162	0.936	-0.842	0.859	-0.249	0.852	0.029
75	0.123	0.937	-0.871	0.853	-0.185	0.850	0.040
80	0.083	0.934	-0.891	0.845	-0.122	0.845	0.050
85	0.042	0.932	-0.902	0.839	-0.060	0.841	0.056
90	0.000	0.931	-0.906	0.837	0.000	0.840	0.060

ENERGY, 325.1MeV

θ_{cm}	P	A_{NN}	A_{SS}	A_{LL}	A_{LS}	M	ΔM
45	0.400	0.783	-0.546	0.740	-0.359	0.773	0.007
50	0.371	0.798	-0.597	0.724	-0.318	0.754	0.009
55	0.335	0.792	-0.642	0.690	-0.272	0.716	0.012
60	0.293	0.772	-0.681	0.645	-0.225	0.668	0.017
65	0.248	0.745	-0.714	0.595	-0.179	0.615	0.022
70	0.200	0.715	-0.741	0.546	-0.137	0.562	0.029
75	0.151	0.686	-0.763	0.501	-0.099	0.515	0.036
80	0.101	0.663	-0.779	0.466	-0.064	0.476	0.042
85	0.050	0.648	-0.789	0.443	-0.031	0.450	0.045
90	0.000	0.643	-0.793	0.435	0.000	0.439	0.048

ENERGY 374.8MeV

θ_{cm}	P	A_{NN}
45	0.423	0.743
50	0.391	0.748
55	0.352	0.734
60	0.306	0.709
65	0.257	0.677
70	0.206	0.644
75	0.154	0.614
80	0.103	0.590
85	0.051	0.574
90	0.000	0.568

ENERGY, 419.5MeV

θ_{cm}	P	A_{NN}	A_{SS}	A_{LL}	A_{LS}	M	Δ M
45	0.445	0.698	-0.500	0.650	-0.267	0.694	0.011
50	0.410	0.694	-0.547	0.604	-0.228	0.640	0.019
55	0.368	0.673	-0.589	0.544	-0.187	0.572	0.025
60	0.320	0.643	-0.625	0.478	-0.149	0.499	0.030
65	0.268	0.608	-0.655	0.412	-0.114	0.426	0.033
70	0.215	0.573	-0.680	0.351	-0.083	0.359	0.034
75	0.161	0.542	-0.699	0.297	-0.058	0.301	0.035
80	0.107	0.517	-0.713	0.256	-0.036	0.256	0.034
85	0.053	0.501	-0.722	0.230	-0.017	0.226	0.033
90	0.000	0.496	-0.725	0.220	0.000	0.213	0.033

ENERGY, 455.7MeV

θ_{cm}	P	A_{NN}	A_{SS}	A_{LL}	A_{LS}	M	Δ M
45	0.464	0.661	-0.480	0.601	-0.235	0.643	0.010
50	0.429	0.656	-0.525	0.551	-0.199	0.584	0.018
55	0.385	0.635	-0.566	0.489	-0.162	0.514	0.025
60	0.336	0.604	-0.602	0.423	-0.127	0.440	0.030
65	0.282	0.571	-0.633	0.358	-0.097	0.367	0.032
70	0.226	0.537	-0.658	0.297	-0.070	0.301	0.033
75	0.170	0.507	-0.679	0.245	-0.048	0.243	0.033
80	0.113	0.483	-0.694	0.204	-0.030	0.199	0.033
85	0.056	0.468	-0.703	0.178	-0.014	0.169	0.032
90	0.000	0.463	-0.707	0.169	0.000	0.156	0.032

ENERGY, 497.1MeV

θ_{cm}	P	A_{NN}	A_{SS}	A_{LL}	A_{LS}	M	ΔM
45	0.495	0.621	-0.445	0.567	-0.226	0.612	0.043
50	0.463	0.624	-0.490	0.533	-0.193	0.568	0.048
55	0.421	0.611	-0.531	0.487	-0.157	0.511	0.038
60	0.370	0.591	-0.567	0.433	-0.121	0.446	0.041
65	0.314	0.567	-0.599	0.375	-0.089	0.379	0.041
70	0.254	0.544	-0.626	0.317	-0.062	0.313	0.037
75	0.191	0.524	-0.649	0.263	-0.040	0.253	0.036
80	0.128	0.508	-0.667	0.218	-0.024	0.205	0.049
85	0.064	0.498	-0.679	0.189	-0.011	0.172	0.055
90	0.000	0.495	-0.684	0.179	0.000	0.158	0.061

ENERGY, 516.3MeV

θ_{cm}	P	A_{NN}	A_{SS}	A_{LL}	A_{LS}	M	ΔM
45	0.499	0.596	-0.441	0.540	-0.210	0.581	0.044
50	0.467	0.600	-0.483	0.508	-0.177	0.538	0.040
55	0.425	0.590	-0.521	0.464	-0.143	0.484	0.038
60	0.375	0.574	-0.555	0.414	-0.109	0.423	0.041
65	0.319	0.556	-0.584	0.360	-0.079	0.360	0.039
70	0.259	0.538	-0.611	0.305	-0.054	0.297	0.036
75	0.196	0.523	-0.634	0.254	-0.035	0.240	0.037
80	0.131	0.511	-0.653	0.211	-0.020	0.193	0.048
85	0.066	0.504	-0.666	0.182	-0.009	0.161	0.055
90	0.000	0.502	-0.670	0.172	0.000	0.148	0.061

APPENDIX C   ERROR EXPRESSION FOR ε_H

The asymmetry, ε_H, is defined by equation 5.3.2. Simplifying the notation, in this equation, to show only the beam polarization, $+(-) = \rightarrow (\leftarrow)$. The number of incident protons, N_o, are counted explicitly and there is therefore no error in this term. Errors in ε_H arise from the terms N(+) and N(-),

$$\Delta^2 \varepsilon_H = \left[\frac{\partial \varepsilon_H}{\partial N(+)}\right]^2 \Delta^2 N(+) + \left[\frac{\partial \varepsilon_H}{\partial N(-)}\right]^2 \Delta^2 N(-) \qquad \text{C.1}$$

From equation 5.3.2

$$\frac{\partial \varepsilon_H}{\partial N(+)} = \frac{2}{N_o(+)} \frac{N(-)}{N_o(-)} \left[\frac{N(+)}{N_o(+)} + \frac{N(-)}{N_o(-)}\right]^{-2} \qquad \text{C.2}$$

$$\frac{\partial \varepsilon_H}{\partial N(-)} = \frac{-2}{N_o(-)} \frac{N(+)}{N_o(+)} \left[\frac{N(+)}{N_o(+)} + \frac{N(-)}{N(-)}\right]^{-2} \qquad \text{C.3}$$

Substitution of equations C.2 and C.3 into C.1 gives,

$$\Delta^2 \varepsilon_H = \frac{4}{[r(+) + r(-)]^4} \left\{ \left[\frac{r(-)}{N_o(+)}\right]^2 \Delta^2 N(+) + \left[\frac{r(+)}{N_o(-)}\right]^2 \Delta^2 N(-) \right\} \qquad \text{C.4}$$

where $r = N/N_o$.

The total area of the coplanarity histogram, T, is composed of two terms. The p-p, N, and the background,B, signals. The area B was assessed by integrating the background gaussian over the range of the coplanarity histogram. N was obtained by subtracting the background gaussian from the central section of the histogram.

$$T = N + B \tag{C.5}$$

Therefore

$$\Delta^2 N = \delta^2 T + \delta^2 B \tag{C.6}$$

The error in T is $T^{1/2}$, similarly for B, therefore

$$\Delta^2 N = N + 2B \tag{C.7}$$

Substitution of C.7 into C.4 leads to

$$\Delta^2 \varepsilon_H = \frac{4}{[r(+) + r(-)]^4} \left\{ \left[\frac{r(-)}{N_o(+)}\right]^2 [N(+) + 2B(+)] + \left[\frac{r(+)}{N_o(-)}\right]^2 [N(-) + 2B(-)] \right\} \tag{C.8}$$

APPENDIX D

BEAM POLARIZATION AT THE TARGET ALLOWING FOR NON-VERTICAL COMPONENTS IN THE POLARIZATION OF THE BEAM EXTRACTED FROM THE CYCLOTRON

Define the polarization of the beam incident into the solenoid as $\underline{P}_b$,

$$\underline{P}_b = P_B \underline{n} + T \underline{r} + L \underline{L} \qquad \text{D.1}$$

where $\underline{n}$ is vertically upwards, $\underline{r}$ is to the right, as seen by the beam, $\underline{L}$ is along the beam direction.

The solenoid precesses the polarization component perpendicular to the momentum vector by an angle ϕ_S, taken as positive for a right handed screw travelling along $\underline{L}$. After the solenoid the beam polarization is,

$$(P_B \cos\phi_s - T \sin\phi_s)\underline{n} + (P_B \sin\phi_s + T\cos\phi_s)\underline{r} + L\underline{L} \qquad \text{D.2}$$

The beam now traverses a 35 bending magnet.This precesses the beam polarization components along $\underline{r}$ and $\underline{L}$ through an angle ϕ_B, which is in the same sense as the beam momentum bend angle. After the magnet the beam polarization is,

$$A\underline{n} + B\underline{r} + C\underline{L} \qquad \text{D.3}$$

where,

$$A = P_B \cos\phi_S - T\sin\phi_S \tag{D.3.1}$$

$$B = (P_B \sin\phi_S + T\cos\phi_S)\cos\phi_B - L\sin\phi_B \tag{D.3.2}$$

$$C = (P_B \sin\phi_S + T\cos\phi_S)\sin\phi_B + L\cos\phi_B \tag{D.3.3}$$

The beam polarization of equation D.3 is incident upon the polarized target's magnetic field, B. This field is at an angle of 12° to the left as seen by the beam, Θ_{TGT}. The magnetic field precesses the beam. The angle of precession about B, χ, is taken as positive for a right handed screw travelling along $\underline{L}$. To accomodate this precession a new set of axes $\underline{L}'$ along B and $\underline{r}'$ at right angles to it are used. The incident polarization is now,

$$A\underline{n} + (B\cos\Theta_{TGT} + C\sin\Theta_{TGT})\,\underline{r}' + (C\cos\Theta_{TGT} - B\sin\Theta_{TGT})\,\underline{L}' \tag{D.4}$$

The field precesses this to,

$$\left[A\cos\chi - (B\cos\Theta_{TGT} + C\sin\Theta_{TGT})\sin\chi\right]\underline{n} + (C\cos\Theta_{TGT} - B\sin\Theta_{TGT})\,\underline{L}'$$
$$+\left[A\sin\chi + (B\cos\Theta_{TGT} + C\sin\Theta_{TGT})\cos\chi\right]\underline{r}' \tag{D.5}$$

Resolving back onto $\underline{r}$ and $\underline{L}$,

$$\underline{P}_b' = A'\underline{n} + B'\underline{r} + C'\underline{L} \tag{D.6}$$

where,

$$A' = A\cos\chi - (B\cos\Theta_{TGT} + C\sin\Theta_{TGT})\sin\chi \tag{D.6.1}$$

$$B' = \left[A\sin\chi + (B\cos\Theta_{TGT} + C\sin\Theta_{TGT})\cos\chi\right]\cos\Theta_{TGT}$$
$$- \sin\Theta_{TGT}(C\cos\Theta_{TGT} - B\sin\Theta_{TGT}) \tag{D.6.2}$$

$$C' = \left[A\sin\chi + (B\cos\theta_{TGT} + C\sin\theta_{TGT})\cos\chi\right]\sin\theta_{TGT}$$

$$+ \cos\theta_{TGT}(C\cos\theta_{TGT} - B\sin\theta_{TGT}) \qquad \text{D.6.3}$$

The three cases for $\phi_S = +90^\circ, -90^\circ$ and 0° are now dealt with.

D.1

$\phi_S = +90^\circ$

From equations D.3.1, D.3.2, and D.3.3 ,

$$A = -T\;;\; B = P_B\cos\phi_B - L\sin\phi_B\;;\; C = P_B\sin\phi_B + L\cos\phi_B$$

Hence from equations D.6.1, D.6.2 and D.6.3,

$$A' = -T\cos\chi - \sin\chi\left[P_B\cos(\phi_B - \theta_{TGT}) - L\sin(\phi_B - \theta_{TGT})\right]$$

$$B' = \cos\theta_{TGT}\left\{-T\sin\chi + \cos\chi\left[P_B\cos(\phi_B - \theta_{TGT}) - L\sin(\phi_B - \theta_{TGT})\right]\right\}$$

$$- \sin\theta_{TGT}\left[P_B\sin(\phi_B - \theta_{TGT}) + L\cos(\phi_B - \theta_{TGT})\right]$$

$$C' = \sin\theta_{TGT}\left\{-T\sin\chi + \cos\chi\left[P_B\cos(\phi_B - \theta_{TGT}) - L\sin(\phi_B - \theta_{TGT})\right]\right\}$$

$$+ \cos\theta_{TGT}\left[P_B\sin(\phi_B - \theta_{TGT}) + L\cos(\phi_B - \theta_{TGT})\right]$$

D.2

$\phi_S = -90^\circ$

$$A = T\;;\; B = -P_B\cos\phi_B - L\sin\phi_B\;;\; C = -P_B\sin\phi_B + L\cos\phi_B$$

Comparing the above equations with those in section D.1 one sees that terms involving T and P_B have changed sign, but terms involving L have remained unchanged.

$$A' = T\cos\chi + \sin\chi\left[P_B\cos(\phi_B - \theta_{TGT}) + L\sin(\phi_B - \theta_{TGT})\right]$$

$$B' = \cos\theta_{TGT}\{T\sin\chi + \cos\chi[-P_B\cos(\phi_B-\theta_{TGT}) - L\sin(\phi_B-\theta_{TGT})]\}$$
$$-\sin\theta_{TGT}[-P_B\sin(\phi_B-\theta_{TGT}) + L\cos(\phi_B-\theta_{TGT})]$$
$$C' = \sin\theta_{TGT}\{T\sin\chi + \cos\chi[-P_B\cos(\phi_B-\theta_{TGT}) - L\sin(\phi_B-\theta_{TGT})]\}$$
$$+\cos\theta_{TGT}[-P_B\sin(\phi_B-\theta_{TGT}) + L\cos(\phi_B-\theta_{TGT})]$$

D.3

$\phi_s = 0^\circ$

$$A = P_B \quad ; \quad B = T\cos\phi_B - L\sin\phi_B \quad ; \quad C = T\sin\phi_B + L\cos\phi_B$$
$$A' = P_B\cos\chi - \sin\chi[T\cos(\phi_B-\theta_{TGT}) - L\sin(\phi_B-\theta_{TGT})]$$
$$B' = \cos\theta_{TGT}\{P_B\sin\chi + \cos\chi[T\cos(\phi_B-\theta_{TGT}) - L\sin(\phi_B-\theta_{TGT})]\}$$
$$-\sin\theta_{TGT}[T\sin(\phi_B-\theta_{TGT}) + L\cos(\phi_B-\theta_{TGT})]$$
$$C' = \sin\theta_{TGT}\{P_B\sin\chi + \cos\chi[T\cos(\phi_B-\theta_{TGT}) - L\sin(\phi_B-\theta_{TGT})]\}$$
$$+\cos\theta_{TGT}[T\sin(\phi_B-\theta_{TGT}) + L\cos(\phi_B-\theta_{TGT})]$$

REFERENCES

1.1 YUKAWA, H., Proc. Phys. Math. Soc. Japan, 17, 48, (1935)

1.2 CONVERSI, M. et al, Phys. Rev., 71, 209, (1947)

1.3 SCOTTI, A. and WONG, D.Y., Phys. Rev., B145, 138, (1965)

1.4 BRYAN, R., in Lecture Notes in Physics, 87, 2 (Few Body Systems and Nuclear Forces, II), ZINGL, H., et al, eds., Springer-Verlag, Berlin, (1978)

1.5 MORAVCSIK, M.J., The Two Nucleon Interaction, Oxford U.P., (1963)

1.6 WILSON, R., The Nucleon-Nucleon Interaction, Wiley,New York, (1963)

1.7 BROWN, G.E. and JACKSON, A.D., The Nucleon-Nucleon Interaction North-Holland, Amsterdam, (1976)

1.8 BUGG, D.V. , Progr. Particle Nucl. Phys., 7, 47, (1981)

1.9 BUGG, D.V. , et al, J. Phys., G4, 1025, (1978);C21, 1004, (1980)

1.10 FERRARI, E. and SELLERI, F., Nuovo Cimento, 27, 1450,(1963)

1.11 PARKER, E. et al, Phys. Rev. Lett., 31, 12, (1973)

1.12 DE BOER. W. et al, Phys. Rev. Lett., 34, 558, (1975)

1.13 BIEGERT, K. et al, Phys. Lett., 73B, 235, (1978)

1.14 AUER, I.P. et al, Phys.Lett., 67B, 113, (1977)

1.15 AUER, I.P. et al, Phys. Lett. 70B, 475, (1977)

1.16 AUER, I.P. et al, Phys. Rev. Lett., 41,354, (1978)

1.17 MOTT, N.F. and MASSEY, H.S.W., Theory of Atomic Collisions, Clarendon Press, (1933)

1.18 MACGREGOR, M.H. et al, Ann. Rev. Sci., 10, 291, (1960)

1.19 STAPP, H.P. et al, Phys. Rev., 105, 302, (1957)

1.20 DUBOIS, R. et al, Nucl. Phys., A377, 554, (1982)

1.21 VINH MAU, R. et al, Phys. Lett., 44B, 1, (1973)

1.22 FROHLICH, J. and ZANKEL, H., Phys. Lett., 82B, 173, (1979)

1.23 GIBSON, W.M.,Nuclear Reactions, Penguin, Harmondsworth, (1971) 1.24 HOSHIZAKI, N., Suppl. Prog. Theor. Phys., 42, 107, (1968)

1.25 JACOB, M. and WICK, G.C., Ann. Phys., 7, 404, (1959)

1.26 KALLEN, G., Elementary Particle Physics, Addison-Wesley, (1964)

1.27 MURIHEAD.H., The Physics of Elementary Particles, Pergamon Press, (1965)

1.28 GREIN. W. and KROLL, P., Nucl. Phys., B137, 173, (1978)

1.29 ARNDT, R.A. et al, Phys. Rev., C15, 1002, (1978)

1.30 BUGG, D.V., J. Phys. G, 5, 1349, (1979)

1.31 BYSTRICKY. J. et al, Saclay Preprint D. Ph. P.E., 79-01, (1974)

1.32 HOSHIZAKI, N., Prog. Theor. Phys., 60, 1796, (1978); 61, 129, (1979)

1.33 ARNDT, R.A., Talk at LAMPF Nucleon-Nucleon Workshop, July 1978.

2.1 WOLFENSTEIN, L., Phys. Rev., 85, 947, (1952)

2.2 CLOUGH, A.S. et al, Phys. Rev., C21, 988, (1980)

2.3 AXEN, D. et al, Phys.Rev., 998, (1980)

2.4 KEELER, R.K. et al, Nucl. Phys., A377, 529, (1982)

2.5 KEELER, R.K., Neutron-Proton Cross Section Measurements in the Intermediate Energy Range, PhD, University of British Colombia, (1980)

2.6 ROSSI, B. and GREISEN, K.I, Rev. Mod. Phys., 13, 240, (1941)

2.7 BARGMANN, V. et al, Phys. Rev. Lett., 2, 435, (1959)

2.8 ROTH, R. et al, Phys. Rev., 140, B1533, (1965)

2.9 BOOTH, P.S.L. et al, Nucl Phys., B121, 45, (1977)

2.10 JEFFRIES, C.D., Dynamic Nuclear Orientation, Wiley, New York, (1963)

2.11 ABRAGAM. A., Principles of Nuclear Magnetism, Oxford U.P., (1961)

2.12 AMSLER, C. et al, J. Phys. G, 4, 1047, (1978) 3.1 TRIUMF Users Handbook, University of British Colombia, (1979)

3.2 RICHARDSON, J.R. et al, IEEE Trans., NS-22 (3), 1402, (1975)

3.3 BEVERIDGE, J.L. et al, IEEE Trans., NS-26 (3), 3215, (1979)

3.4 ENGLAND, J.B.A., Techniques in Nuclear Structure Physics, Part 2, Macmillan, London, (1974)

3.5 SONA, P.G., Energia Nucleare, 14, 295, (1967)

3.6 GALLAGHER-DAGGIT, G., Report on the BASQUE Superconducting Solenoid, Rutherford Laboratory, RL 75-008, (1975)

3.7 CLARK, D.J. et al, Nucl. Instr. Meth., 18-19, 1, (1962)

3.8 BUSSEY, P.J.,et al, Nucl. Phys., B159, 383, (1979)

3.9 COURT, G.R. et al, Proc. Fifth Int. Conf. Magnet Tech., Rome, 577, (1975)

3.10 MANGO, S. et al, Nucl. Instr. Meth., 72, 45, (1969)

3.11 HARTMANN, G. et al, Nucl. Instr. Meth., 106, 9, (1973)

3.12 Procedings of the Second Workshop on Polarized Target Materials, Rutherford Laboratory, RL-80-080, (1980)

3.13 ASH, W., Nucl. Instr. Meth., 134, 9, (1976)

3.14 COMYN. M. et al, in High Energy Physics with Polarized Beams and Polarized Targets, JOSEPH, C and SOFFER, J.,eds., Birkhauser, Basel, (1981)

3.15 LESOWAY, T. et al, Delay Line Wire Chambers, University of Alberta, TRI-DNA-80-1, (1980)

3.16 TURNER, G.K., Pion-Nucleus Total Cross-Sections from 86 - 860MeV, PhD, University of Surrey, (1974)

4.1 BENNETT, P. et al, Beamline 4C Studies, TRIUMF, TRI-DN-79-16, (1979)

4.2 BROWN, K.L., Transport 360, SLAC Report 91, (1970)

4.3 KITCHING. P., REVMOC, TRIUMF, TRI-71-2, (1971)

6.1 BESSETT, D. et al, Nucl. Instr. Meth., 166, 379, (1979)

7.1 STANLEY, J.P. et al, Nucl. Phys., (1983) (in press)

7.2 AXEN, D. et al, J. Phys. G., 7, L225, (1981)

7.3 ARNDT, R.A., Private communication

7.4 AUER, I.P. et al, Argonne Preprint, ANL-HEP-81-13, (1981)

7.5 APRILE, E. et al, in High Energy Physics with Polarized Beams and Polarized Targets, JOSEPH, G. and SOFFER, J., eds., Birkhauser, Basel, (1981)

7.6 JONES, G., in Nucleon-Nucleon Interactions, MEASDAY, D.F. et al, eds., American Institute of Physics, New York, (1978)

7.7 BRYSTRICKY, J. et al, Contribution to the Ninth ICOHEPANS, Versailles, July (1981)

7.8 GREIN, W. and KROLL, P., Nucl Phys., A377, 505, (1982)